R-05-60

Regional hydrogeological simulations for Forsmark – numerical modelling using DarcyTools

Preliminary site description Forsmark area – version 1.2

Sven Follin, SF GeoLogic AB

Martin Stigsson, Svensk Kärnbränslehantering AB

Urban Svensson, Computer-aided Fluid Engineering AB

December 2005

Svensk Kärnbränslehantering AB
Swedish Nuclear Fuel
and Waste Management Co
Box 5864
SE-102 40 Stockholm Sweden
Tel 08-459 84 00
+46 8 459 84 00
Fax 08-661 57 19
+46 8 661 57 19

ISSN 1402-3091
SKB Rapport R-05-60

Regional hydrogeological simulations for Forsmark – numerical modelling using DarcyTools

Preliminary site description Forsmark area – version 1.2

Sven Follin, SF GeoLogic AB

Martin Stigsson, Svensk Kärnbränslehantering AB

Urban Svensson, Computer-aided Fluid Engineering AB

December 2005

Summary

SKB is conducting site investigations for a high-level nuclear waste repository in fractured crystalline rocks in two coastal areas in Sweden. The two candidate areas are Forsmark and Simpevarp. The investigations started in 2002 and have been planned since the late 1990s. The site characterisation work is divided into two phases: an initial site investigation phase (ISI) and a complete site investigation phase (CSI). The results of the ISI phase are used as a basis for deciding on the subsequent CSI phase. On the basis of the CSI investigations, a decision is made as to whether detailed characterisation will be performed (including sinking of a shaft).

An integrated component in the site characterisation work is the development of site descriptive models. These comprise basic models in three dimensions with an accompanying text description. Central to the modelling work is the geological model which provides the geometrical context in terms of a model of deformation zones and the rock mass between the zones. Using the geological and geometrical description models as a basis, descriptive models for other disciplines (surface ecosystems, hydrogeology, hydrogeochemistry, rock mechanics, thermal properties and transport properties) will be developed. Great care is taken to arrive at a general consistency in the description of the various models and assessment of uncertainty and possible needs for alternative approaches.

A numerical model is developed on a regional-scale (hundreds of square kilometres) to study the zone of influence for variable-density groundwater flow that affects the Forsmark area. Transport calculations are performed by particle tracking from a local-scale release area (a few square kilometres) to test the sensitivity to different hydrogeological uncertainties and the need for far-field realism.

The main objectives of the regional flow modelling were to achieve the following:

I. *Palaeo-hydrogeological understanding*: An improved understanding of the palaeo-hydrogeological conditions is necessary in order to gain credibility for the site descriptive model in general and the hydrogeological description in particular. This requires modelling of the groundwater flow from the last glaciation up to present-day with comparisons against measured TDS and other hydro-geochemical measures.

II. *Simulation of flow paths*: The simulation and visualisation of flow paths from a tentative repository area is a means for describing the role of the current understanding of the modelled hydrogeological conditions in the target volume, i.e. the conditions of primary interest for Safety Assessment. Of particular interest here is demonstration of the need for detailed far-field realism in the numerical simulations. The motivation for a particular model size (and resolution) and set of boundary conditions for a realistic description of the recharge and discharge connected to the flow at repository depth is an essential part of the groundwater flow path simulations.

The regional flow simulations conducted started out with the second objective in mind. That is, a series of sensitivity cases are treated by means of particle tracking to study the need for detailed far-field realism. This to gain an understanding of how the uncertainty of different primary model parameter assumptions interplay with the low-conductive target volume, and ultimately to what extent these parameters contribute to a reasonable match to the field data (palaeo-hydrogeological understanding). Eventually, an attempt was made to achieve a reasonable matched flow model (first objective) despite the simplification associated with a multicomponent continuous porous media (CPM) flow model.

A number of new aspects to the scope of modelling have been included for model version 1.2 (Forsmark 1.2). One of the most important is the representation and treatment of uncertainty of the deformation zones. Three alternative geological models for the deterministically treated deformation zones were produced by geology for Forsmark 1.2 based on different levels of confidence in the interpretation. A *base model* was provided based on high confidence structures local to the site between the Singö and Eckarfjärden deformation zones. One of the key features of this model is the presence of several extensive gently dipping deformation zones within the candidate area. A *base variant model* was developed that considers an extension of some gently dipping deformation zones beyond the candidate area. Finally, an *alternative model* case was proposed with the inclusion of many low confidence steeply dipping lineaments outside the candidate area (mainly). In addition to these considerations of the sensitivity to various structural models, the concept that hydraulic properties for the deformation zones should vary with depth and according to the dip of structures was introduced.

Another key difference from model version 1.1 (Forsmark 1.1) is the increased effort invested in conditioning the hydraulic properties of the rock masses outside the deformation zones to the fracture Boremap and hydraulic data. A new methodology was developed and applied for interpreting the discrete fracture network (DFN) by integrating a global (average) geological description of the DFN (GeoDFN) with the hydraulic test data from Posiva Flow Log (PFL-f) to produce a conditioned hydrogeological DFN (HydroDFN) model that focussed on the connected fracture intensity (fracture surface area per unit volume). This was done in a systematic way that addressed uncertainties associated with the assumptions made in interpreting the data.

PFL-f data were available for five core drilled boreholes, KFM01A–KFM05A. Considerable spatial variations in fracture frequency and flow were observed within and between boreholes. Thus, it was believed important to differentiate rock mass properties inside rock domain RFM029 (the so-called ‘tectonic lens’ that spans the candidate area) from one another by means of subvolumes as well as from those outside.

Considerably more hydrogeochemical data were available for comparisons in the Data Freeze F1.2. Data were provided for four cored boreholes KFM01A–KFM04A and for a number of percussion drilled boreholes. The hydrogeochemical data were provided in terms of interpreted mixing fractions for four so-called reference waters, concentrations of major ions, stable isotope ratios and tritium concentrations in addition to ‘classic’ salinity data. This enabled a more elaborated comparison and discussion of the groundwater flow simulations than was previously the case.

However, hydrogeochemical data at elevations below –500 masl were still sparse and the samples taken for most parts gathered in the deterministically treated deformation zones. Moreover, the point of representation of the near-surface hydrogeochemical measurements was less certain (representative) due to the long open borehole sections and the large pumping-rates involved, and hence there remains uncertainty in interpreting and modelling both the deep and shallow groundwaters.

The numerical modelling was performed by two separate modelling teams, the *ConnectFlow Team* and the *DarcyTools Team*. The work presented in this report was based on the computer code DarcyTools developed by Computer-aided Fluid Engineering. DarcyTools is a kind of equivalent porous media (EPM) flow code specifically designed to treat flow and salt transport in sparsely fractured crystalline rock intersected by transmissive fractures. It comprises, among other things, a fracture network generator, algorithms for the computation of finite-volume (block-size) properties and a multi-rate diffusion model. It is noted that some of the components of DarcyTools are not used in the work reported here as they are still under development or subjected to testing and verification.

The main observations of the hydrogeological DFN and block-scale analyses with DarcyTools are as follows:

- There were several difficulties in applying the global geological DFN to the hydraulic tests. The main difficulty stemmed from significant variations in fracture intensities and the proportions of sets between boreholes making it difficult to use an averaged, global, geological DFN model when matching hydraulic tests in a specific borehole.

- Due to the spatial variability of the fracture properties and the few flow anomalies a number of bedrock volumes were defined jointly with the *ConnectFlow Team*. For the work presented in this report the following volumes were defined:

  Volume A – above the gently dipping deformation zone ZFMNE00A2 (A2) below c 100 m depth.
  Volume B – below A2 between 220–360 m depth.
  Volume C – below A2 between 100–220 m depth.
  Volume D – below A2 below c 360–400 m depth (target volume).

- A major observation from the hydrogeological DFN analysis of Volumes A–D is that it is possible to come to different results concerning the connected fracture area per unit volume when calibrating against the measured borehole fracture intensity depending on the value used for the minimum fracture size of the power-law size distribution. In conclusion, the reference fracture size is a key parameter of considerable importance for the outcome of the approach used.

- A direct correlation between transmissivity and length appears to be a workable hypothesis but the simulations conducted suggest a considerable variability between different volumes as well as between realisations within a fixed volume due to the spatial variations in fracture intensity and number of flow anomalies. Although the final model in each realisation has unique values of *a* and *b* a semi-correlated model could in fact be produced as an alternative.

- Block properties were estimated for Volume B and a block size of 20 m using different methods. The calculations suggest a low geometric mean of c $(1–5)\cdot10^{-11}$ m/s.

The significant differences in connected fracture intensity, number of flow anomalies and transmissivity magnitudes have implications for the application of an EPM approach of groundwater flow through RFM029. Different hydrogeological DFN models may be advocated depending on the volume of rock considered. For example, Volume D may be described as an almost impermeable rock mass characterised by a very sparsely connected and low-transmissive DFN, Volume C as a pretty conductive rock mass characterised by a well connected and moderately-transmissive DFN and Volume A as moderately conductive rock mass characterised by a sparsely connected but a pretty high-transmissive DFN.

The choice of flow model approach is also related to the scale of the flow problem, i.e. the size of the flow domain considered and the resolution of the computational grid. On a regional scale it is generally necessary to use some kind of continuum approach and a more or less coarse computational grid in order to relax the computational constraints. For the same reason fully discrete approaches of high resolution are generally limited to much smaller model domains.

Due to the large number of uncertainties associated with the application of the EPM approach to the low-conductive and sparsely fractured conditions in Forsmark it was decided to carry out the intended regional variable-density flow simulations and advective particle tracking with DarcyTools using a simple continuous porous media (CPM)

model. The working hypothesis used simplifies the local representation of the rock mass heterogeneity between the Eckarfjärden and Singö deformation zones by using a few fairly low-conductive CPMs. The spatial dimensions and equivalent properties of the multicomponent CPM were based on the hydrogeological DFN analysis of Volumes A–D. The rest of the regional model domain was suggested to be characterised as a single CPM because there were little data from outside the 'tectonic lens' with which to parameterise a more sophisticated model.

The working hypothesis implies that there is little flow through the deeper parts of RFM029, in particular below the gently dipping deformation zone ZFMNE00A2, and that the bulk of the groundwater flow through the candidate area is governed by the connectivity and hydraulic properties of the deterministically treated deformation zones. Whether this approach is right or wrong requires comparisons with both field data and simulations with alternative modelling approaches.

The main objectives of the multicomponent CPM model were to provide: (i) a bounding check on the more complex EPM model treated by the *ConnectFlow Team*, (ii) a comprehensible assessment in which the effects of specific assumptions are easily traced, and (iii) identification of key sources of uncertainty. However, the comparison of the results produced by the two modelling teams will be carried out by SKB's Site Analysis Team for Forsmark. This report considers the results obtained by the *DarcyTools Team* only.

The regional variable-density flow simulations and advective particle tracking were used to study the sensitivity to various regional hydrogeological uncertainties such as:

- the size and shape of the Forsmark 1.2 regional model domain,
- the different deformation zone models,
- the initial and boundary conditions associated with the palaeo-hydrogeological time frame,
- and the transient nature of the shoreline displacement process.

The variable-density flow simulation period was performed between 8,000 BC and 2,000 AD. The particle tracking was carried out with stationary boundary conditions representing the present-day position of the shoreline. The particles were released in a specified release area located at c 400 m depth within the target volume (Volume D) below the gently dipping deformation zone ZFMNE00A2 and traced until they reached ground surface. The objective of the advective particle tracking was to provide a means for simple relative comparisons of the sensitivity to different regional hydrogeological uncertainties.

Given the aforementioned working hypothesis, the main observations of the palaeo-hydrogeological simulations and the advective particle tracking of this study are that:

- The initial conditions for the salt water distribution and water types at the end of the last glaciation are unknown and different assumptions are tested. A tentative fit of simulated results to available measurements was obtained by assuming freshwater conditions down to c 450 m depth, with a linear increase of saline groundwater below that to 10% by weight at a depth of c 1,950 m. This gradient is perhaps too large as it gives an over-prediction of salinity at the bottom of borehole KFM03A, which is located above the gently dipping deformation zone ZFMNE00A2. The hydrogeochemical conditions below this important deformation zone, as well as outside the candidate area, are essentially unknown.

- In contrast, the model under-predicts salinity in the upper parts of the flow system. This creates a conceptual problem since it is difficult to have sufficient hydraulic conductivity to allow for a percolation of Littorina Sea water without a substantial subsequent flushing of freshwater once the site is exposed to Meteoric precipitation beginning at 1,000 AD. This may just be a question of having to fine-tune surface hydraulic, transport properties and boundary conditions to obtain a good match. For instance, a possible explanation is that the thickness of low-conductive sediments, such as postglacial clay and gyttja, increased after the Littorina pulse, thereby reducing the meteoric flushing of the superficial rock. Another possible explanation is that the high-transmissive horizontal fractures encountered a few metres below the bedrock surface are very extensive, thereby reducing the flushing of the superficial rock beneath.
- The assumed initial salinity distribution was stable during the simulation time. This is probably due to the low rock mass hydraulic conductivity at depth and the imposed depth dependency in the deformation zone transmissivity that approach the rock mass hydraulic conductivity below c 700 m depth. Thus, the simulation results outside the deformation zones will merely reflect the initial conditions. This does not imply, however, that all deformation zones become impervious at greater depth. There may still be several transmissive zones at depth, e.g. below the base of the existing boreholes or below the 'tectonic lens'.
- It was somewhat easier to match the hydrogeochemistry measurements at depth by conditioning particular deformation zones to their measured transmissivity and thickness values at the borehole intersection (where the groundwater water was sampled) instead of using a generalised trend model for the deformation zone properties. This suggests that the hydrogeochemical measurements at depth, available for an integrated interpretation by hydrogeology, may reflect a flow system governed by deformation zone heterogeneity.
- The assumption that the initial salinity conditions in the kinematic porosity were in equilibrium with those in the matrix porosity at the start of the simulation period influences the particle tracking. The simulations suggest that present-day groundwater chemistry in the advective (fracture) system may not be similar to that in the matrix. However, the absence of pore water hydrogeochemistry data in Forsmark 1.2 means that it is not possible to make judgements regarding the role of matrix diffusion in a low-conductive rock mass.
- The upstream artificial no-flux hydraulic boundary of the rectangular regional model domain is probably sufficiently far away from the groundwater flow within the target volume of RFM029.
- The presence of low confidence deformation zones upstream of the candidate area had little effect on the flow path simulations inside the target area vis-à-vis the presence of low confidence deformation zones inside the candidate area.
- Transmissivity heterogeneity among the *base model* deformation zones within the candidate area had a clear effect on the flow path simulations.
- Since the shoreline displacement is still ongoing, the real hydrogeological conditions within the candidate area are continuously changing. The basic picture using the multi-component CPM model is that the locations of the exit positions of future advective flow paths will follow the position of the moving shoreline. However, a substantial amount will discharge within the Forsmark candidate area also in the future.

This study identifies areas of concern to be considered in the planning of the forthcoming site investigations:

- To improve the understanding/description of the initial conditions it is desirable to learn more about the salinity profile in the matrix and in the rock mass fracturing both within and outside RFM029.
- The combination of PFL and PSS data is necessary for the uncertainty assessment of the reported PFL transmissivity data. It is recommended that future boreholes are investigated in a similar fashion. However, the uncertainty in the interpretation of PSS data remains to be treated, e.g. by means of a generalised radial flow model analysis.
- The description of the local deformation zones is vital. This may involve more boreholes to confirm seismic reflectors and to establish the extent of zones, and also interference tests within zones to investigate large scale flow and connectivity.
- Hydraulic and hydrogeochemical measurements in the top 100 m are uncertain as open percussion drilled boreholes together with large pumping rates are used. To improve our understanding/description of the near surface hydrogeology, hydraulic tests and hydrogeochemical measurements between packers in shallow (~ 200 m long) core drilled boreholes would be useful.
- The hydrogeochemistry data available for Forsmark 1.2 were very limited, particularly at or below the provisional repository depth. Additional data would assist constraining the hydrogeological models.
- Offshore conditions need to be considered as the shoreline displacement continuously modifies the hydraulic gradients. This calls for an improved description of the hydraulic properties of the Singö deformation zone as a boundary fracture for the ‘tectonic lens’. Hydrogeochemical measurements below the Baltic Sea would also improve the understanding/description of the Littorina Sea as reference water.

Contents

1 Introduction

1.1 Background

SKB is conducting site investigations for a high-level nuclear waste repository in fractured crystalline rocks in two coastal areas in Sweden. The two candidate areas are Forsmark and Simpevarp. The investigations started in 2002 and have been planned since the late 1990s. The site characterisation work is divided into two phases: an initial site investigation phase (ISI) and a complete site investigation phase (CSI). The results of the ISI phase are used as a basis for deciding on the subsequent CSI phase. On the basis of the CSI investigations, a decision is made as to whether detailed characterisation will be performed (including sinking of a shaft).

An integrated component in the site characterisation work is the development of site descriptive models. These comprise basic models in three dimensions with an accompanying text description. Central to the modelling work is the geological model which provides the geometrical context in terms of a model of deformation zones and the rock mass between the zones. Using the geological and geometrical description models as a basis, descriptive models for other disciplines (surface ecosystems, hydrogeology, hydrogeochemistry, rock mechanics, thermal properties and transport properties) will be developed. Great care is taken to arrive at a general consistency in the description of the various models and assessment of uncertainty and possible needs for alternative approaches.

A numerical model is developed on a regional-scale (hundreds of square kilometres) to study the zone of influence for variable-density groundwater flow that affects the Forsmark area. Transport calculations are performed by particle tracking from a local-scale release area (a few square kilometres) to test the sensitivity to different hydrogeological uncertainties.

1.2 Scope and objectives

The main objective of this study is to support the development of a Preliminary Site Description of the Forsmark area on a regional-scale (model version 1.2) based on the available data of 30 June 2004 (Data Freeze F1.2) and the previous Site Description (model version 1.1). Figure 1-1 shows a schematic geological map of the Forsmark area. The candidate area is located between the Singö and Eckarfjärden deformation zones and consists mainly of a single rock domain denoted by RFM029, see Figure A-1 in Appendix A. The Data Freeze F1.2 comprises data from five core drilled and 19 percussion drilled boreholes.

A more specific objective of this study is to assess the role of certain and uncertain hydrogeological conditions for the present-day distribution of saline groundwater in the Forsmark area on a regional scale. An improved understanding of the palaeo-hydrogeology is necessary in order to gain credibility for the Site Description in general and the hydrogeological description in particular. The latter will serve as a basis for describing the present-day hydrogeological conditions on a local scale as well as predictions of future hydrogeological conditions. Finally, this study aims to identify some of the issues that may impact the safety assessment project SR-Can, and where possible provide a preliminary evaluation of sensitivities to such issues. In particular, recommendations are made as to which uncertainties need to be addressed as part of SR-Can.

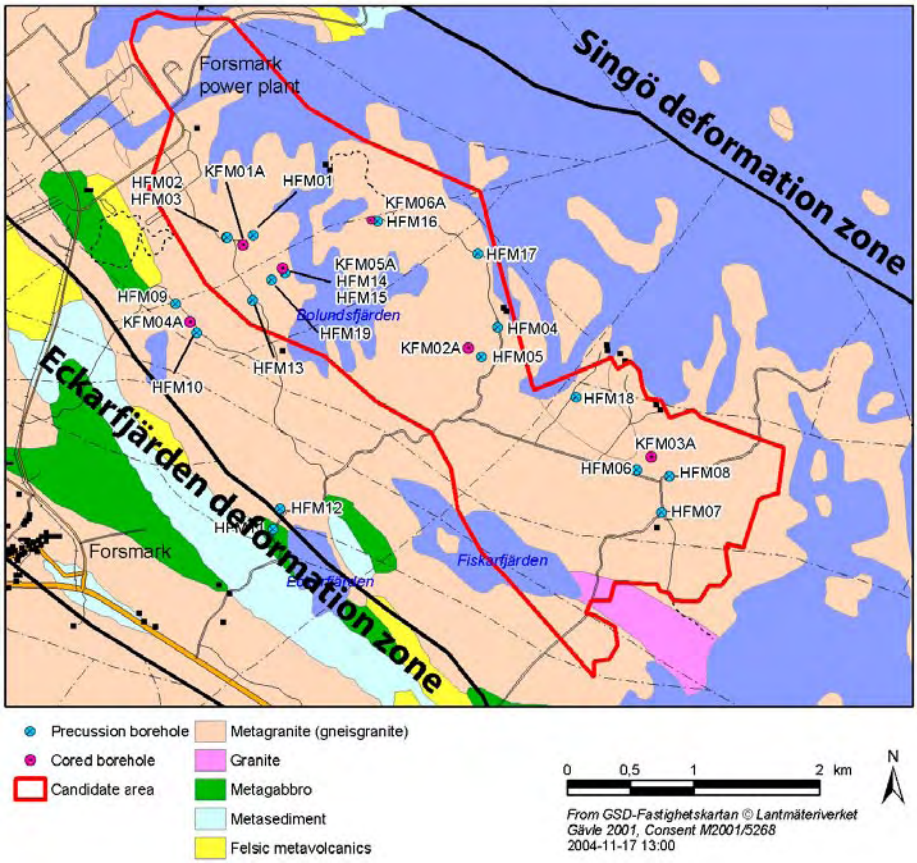

Figure 1-1. *Schematic geological map of the Forsmark area. The candidate area is located between the Singö and Eckarfjärden deformation zones and consists mainly of a single rock domain denoted by RFM029, see Figure A-1 in Appendix A. The Data Freeze F1.2 comprises data from five core drilled and 19 percussion drilled boreholes.*

1.3 Setting, assumptions and limitations

A number of new aspects to the scope of modelling have been included for model version 1.2 (Forsmark 1.2). One of the most important is the representation and treatment of uncertainty of the deformation zones. Three alternative geological models for the deterministically treated deformation zones were interpreted by geology for Forsmark 1.2 based on different levels of confidence in interpretation, see Figure 1-2 and Figure A-2 in Appendix A:

- A *base model* was provided based on 44 high confidence structures local to the site between the Singö and Eckarfjärden deformation zones. One of the key features of this model is the presence of several extensive gently dipping deformation zones within the candidate area, see Figure 1-3.
- A *base variant model* was developed that considers an extension of some gently dipping base model deformation zones beyond the candidate area.
- Finally, an *alternative model* case was proposed with the addition of 171 low confidence steeply dipping lineaments. Thus, this model consists of 215 deformation zones in total. The body of these are geophysical anomalies (magnetic mainly).

In addition to these considerations of the sensitivity to various structural models, the concept that hydraulic properties for the deformation zones should vary with depth and according to the dip of structures was introduced. The rationale for this assumption is indicated in Figure 1-4 and commented on in Chapter 4.

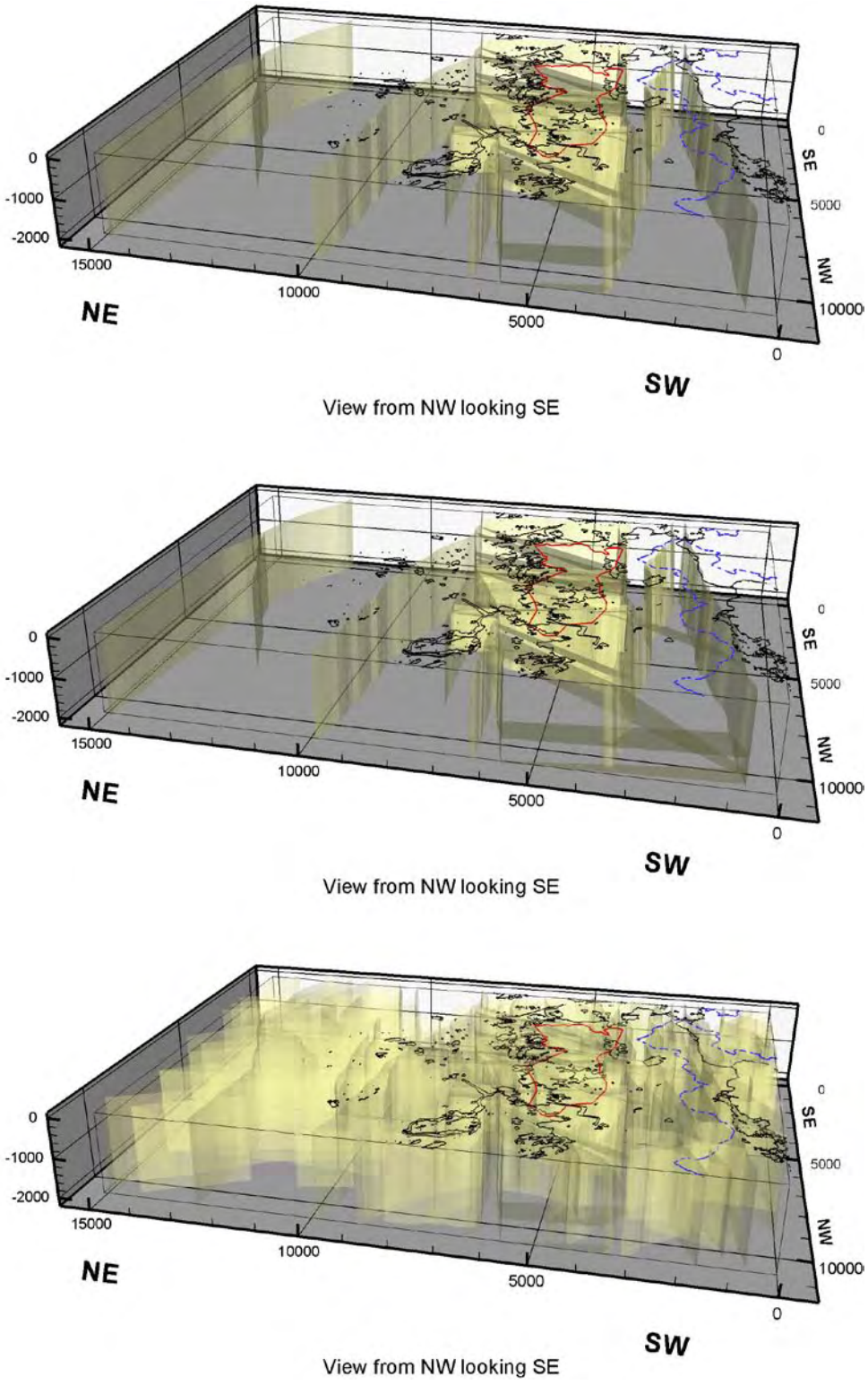

Figure 1-2. *Top: The base model consists of high confidence structures essentially local to the site between the Singö and Eckarfjärden deformation zones. One of the key features of this model is the presence of several extensive gently dipping deformation zones within the candidate area (red line). Middle: The base variant model considers an extension of four gently dipping deformation zones beyond the candidate area. Bottom: An alternative model case was proposed with the inclusion of many steeply dipping lineaments of low confidence as deformation zones. The body of these are geophysical anomalies (magnetic mainly).*

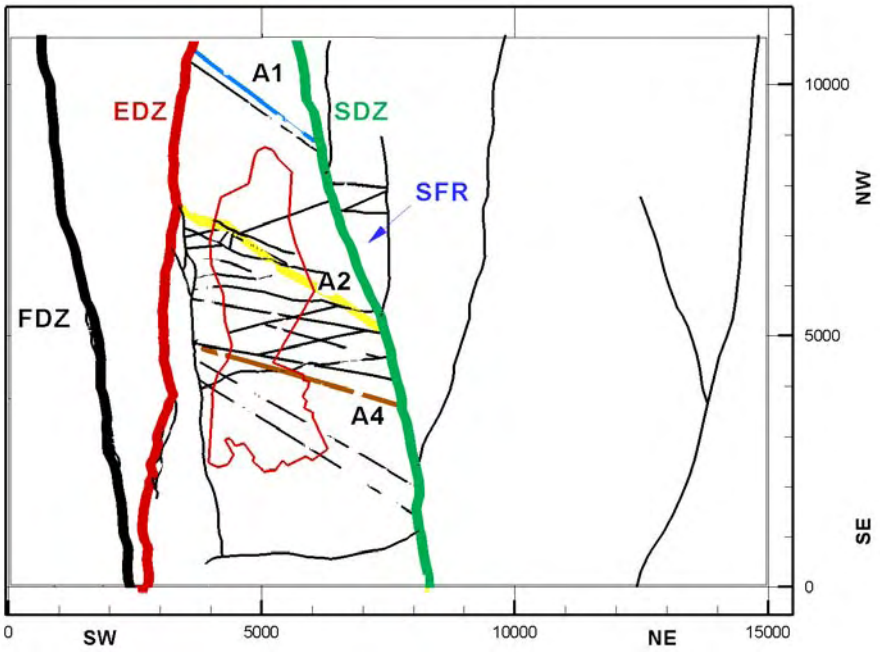

Figure 1-3. *Base model traces at ground surface. The candidate area (red) and the location of the SFR facility are also shown. The regional steeply dipping deformation zones have geographical the names of Forsmark (FDZ), Eckarfjärden (EDZ) and Singö (SDZ). A key feature of this model is the presence of several extensive gently dipping deformation zones between the Singö and Eckarfjärden deformation zones, some of which are highlighted in the figure, ZFMNE00A1 (blue), ZFMNE00A2 (yellow), and ZFMNE00A4 (brown).*

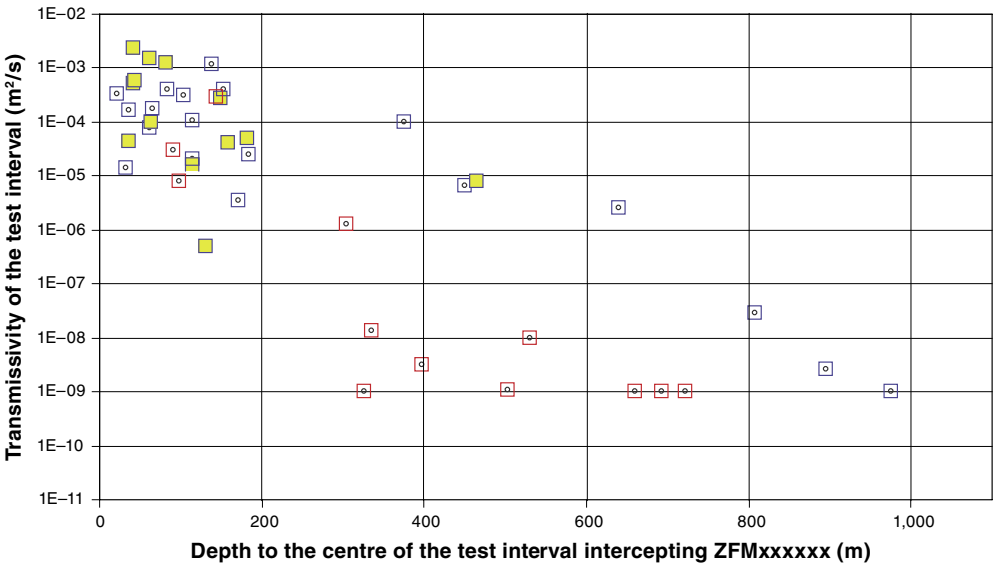

Figure 1-4. *Scatter plot of single-hole transmissivities associated with the base model deformation zones. The red squares indicate steeply dipping deformation zones, and the blue squares gently dipping. The blue squares with a yellow infilling refer to transmissivities associated with the gently dipping deformation zone ZFMNE00A2. The data behind this plot are considered in Chapter 4.*

The suggested regional model area in Figure 1-3 is oriented NE and has an area of 15 km by 11 km. The suggested thickness is 2.1 km. Figure 1-5 shows an excerpt of the regional model domain with the Forsmark candidate area in the centre. The major nearby deformation zones, present-day shoreline, lakes and the regional surface water divides are also shown as well as the locations of the five one kilometre long core-drilled boreholes KFM01A–KFM05A and the release area[1] used for the particle tracking. To address the aforementioned new issues it is necessary not only to consider sensitivities to the deformation zones themselves, but also the size and discretisation of the model required to accurately represent them.

Another key difference from model version 1.1 (Forsmark 1.1) is the increased effort invested in conditioning the hydraulic properties of the rock domains to the gathered fracture Boremap and hydraulic test data. A new methodology was developed and applied for interpreting the discrete fracture network (DFN) by integrating a global (average) geological description of the geological DFN (GeoDFN) with the hydraulic test data from Posiva Flow Log (PFL) to produce a conditioned hydrogeological DFN (HydroDFN) model that focussed on the connected fracture intensity (connected fracture area per unit volume). This was done in a systematic way that addressed uncertainties associated with the assumptions made in interpreting the data.

PFL data were available for the five core drilled boreholes, KFM01A–KFM05A shown in Figure 1-5. Considerable spatial variations in fracture frequency and flow were observed within, and between, boreholes. Hence, it was believed important to differentiate rock mass properties inside rock domain RFM029 (the so-called ‘tectonic lens’ that spans the candidate area) from one another by means of subvolumes as well from those outside.

Considerably more hydrogeochemical data were available for comparisons in the Data Freeze F1.2. Data were provided for cored boreholes KFM01A–KFM04A and for a number of percussion drilled boreholes. Figure 1-1 shows the locations of the different boreholes within the candidate area together with the traces of the aforementioned Singö and Eckarfjärden deformation zones. The hydrogeochemical data were provided in terms of interpreted mixing fractions for four so-called reference waters, concentrations of major ions, stable isotope ratios and tritium concentrations in addition to the ‘classic’ salinity data. This enabled a better comparison and discussion of the groundwater flow simulations than was previously the case.

However, hydrogeochemical data at elevations below –500 masl were still sparse and the samples taken for most parts gathered in the deterministically treated deformation zones. Moreover, the point of representation of the near-surface hydrogeochemical measurements was less certain (representative) due to the long open borehole conditions and the large pumping-rates involved, and hence there remains uncertainty in interpreting and modelling both the deep and shallow groundwaters.

Finally, the number of modelling cases that can be considered has to be limited so the reporting can be made according to the time schedule with the Oskarshamn and Forsmark site-investigation modelling projects (denoted by POM and PFM, respectively).

[1] The shape and elevation of the release area used for the particle tracking in the work reported here is symbolic. At this point there is no specific information on the exact location of a deep repository. However, the rock mass in the NW part of the candidate area between the two gently dipping deformation zones ZFMNE00A1 and ZFMNE00A2 is considered the target volume by SKB. SKB’s definition of a “repository depth” is in general terms 400–700 m below ground surface. In the work reported here we assumed a repository elevation of –400 and a rectangular shape according the specifications made by SKB. If the elevation of the release area is changed, e.g. to –700 or –200, or its horizontal position is moved the particle tracking simulations need to be rerun.

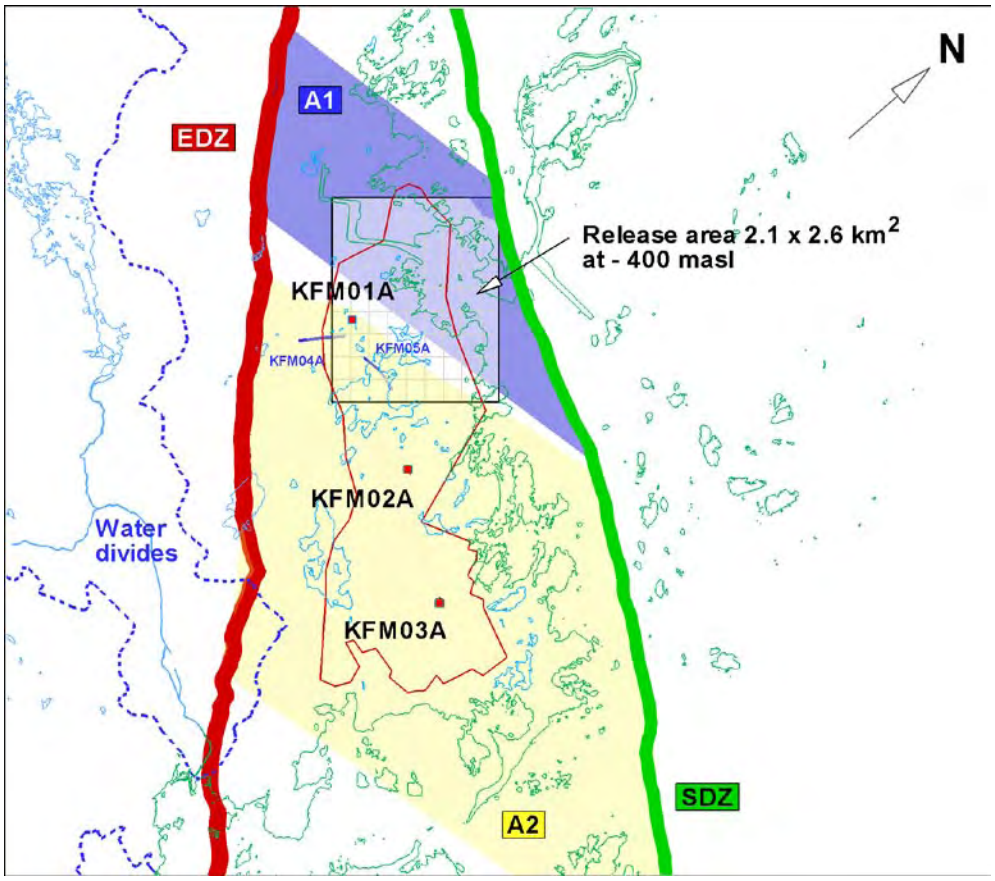

Figure 1-5. *Excerpt of the regional model domain with the Forsmark candidate area in the centre. The major nearby deformation zones Eckarfjärden (EDZ), Singö (SDZ), ZFMNE00A1 (A1; blue) and ZFMNE00A2 (A2; yellow), present-day shoreline, lakes and the regional surface water divides are shown together with the locations of the one kilometre long core-drilled boreholes KFM01A–KFM05A and the release area used for the particle tracking. The horizontal resolution of the computational grid is 100 m by 100 m (cf the red squares). The vertical discretisation is 100 m below 400 m depth and c 30 m above. KFM01A–KFM03A are essentially vertical, whereas KFM04A and KFM05A are inclined (60°).*

1.4 Organisation of work and structure of report

The numerical modelling was performed by two separate modelling teams. The focus of the simulations is in part different between the two modelling teams, ConnectFlow (CF) and DarcyTools (DT), although both teams have agreed a common initial regional model setup (Task Description). While exploring the sensitivity of simulated hydrogeochemistry distributions to different geometric alternatives, variations in the initial and boundary conditions and parameter uncertainties, CF has concentrated on confidence issues relating to the needs of Safety Performance, whereas DT has focused on confidence issues of general hydrogeological character, e.g. model domain size and boundary conditions. It is recognised, however, that there is an overlap between the two foci. Indeed, it is necessary to maintain some overlap on behalf of the objectives of the Site Descriptive Model. The work presented in this report was conducted by the DarcyTools Team involving hydrogeologists from SF GeoLogic and Swedish Nuclear Fuel and Waste Management Company. The DarcyTools code is developed and maintained by Computer-aided Fluid Engineering /Svensson et al. 2004, Svensson and Ferry 2004, Svensson 2004a/.

This report presents the analyses undertaken for the development of a HydroDFN for rock domain RFM029 in Forsmark. Based on the observations made, a simplistic flow model is developed and simulations of regional-scale variable-density groundwater flow are compared with measured hydrogeochemical data from deep core-drilled boreholes. Flow paths from a tentative repository area are simulated by means of particle tracking as a means of describing the role of the modelled regional hydrogeological conditions for the current understanding of the conditions in a particular part of the model domain denoted as the 'target volume'. Of particular interest here is the demonstration of the need for detailed far-field realism in the numerical simulations. The motivation for a particular model size and set of boundary conditions for a realistic description of the recharge and discharge connected to the flow at repository depth is an essential part of the groundwater flow path simulations.

Many variants were considered for the regional-scale groundwater flow to investigate the influence of conceptual and parameter uncertainties relating to initial and boundary conditions, DFN data interpretation, and background rock properties including some of the properties known to affect the rock matrix diffusion. Chapter 2 presents the overall modelling methodology, the model specifications and the deliverables on groundwater flow and particle tracking. Chapter 3 presents the data from the hydraulic tests available for bedrock hydrogeological modelling. Chapters 4, 5 and 6 present the assignment of hydraulic properties to the deformation zones, the rock mass between the deformation zones and the overburden, respectively. Chapter 7 presents the results from the flow simulations and particle tracking. Finally, Chapter 8 concludes the study.

2 Model set-up and specifications

2.1 Systems approach and modelling methodology

The systems approach presented in /Rhén et al. 2003/ describes how different modelling concepts, field investigations, and interpretation techniques come into play depending on the nature of the geological and hydraulic domains considered. Regional groundwater flow models are constructed from the following three hydraulic domains:

HCD Hydraulic Conductor Domains – deterministically treated deformation zones of high or relatively high confidence;

HRD Hydraulic Rock Domains – the sparsely fractured rock mass between the deterministically treated deformation zones. (The HRDs generally coincide with the lithological rock domains defined by geology (cf Figure A-1 in Appendix A). Several rock domains may be merged into one HRD or one rock domain may be divided into several HRDs depending on the structural and hydrogeological complexities.)

HSD Hydraulic Soil Domains – the overburden (Quaternary deposits mainly) on top of the bedrock.

The regional-scale modelling presented in this report is based on the three alternative geological models for the deterministically treated deformation zones produced by geology for model version 1.2 (cf Figure 1-2), i.e. the *base model* (BM), the *base variant model* (BVM) and the *alternative model* (AM).

The Forsmark candidate area consists predominantly of one rock domain, RFM029. Chapter 4 presents an assessment of hydraulic properties of the HCDs, Chapter 5 the hydraulic properties of the HRDs and Chapter 6 the properties of the HSDs as used in the regional modelling.

The uncertainties in the HRD properties are of key importance and may be modelled with alternative approaches. The simplest case is perhaps that of a low-conductive uniform Continuous Porous Medium and the most complex case is a heterogeneously fractured rock mass, where the geometric and hydraulic properties do not lend themselves to be characterised and simulated by means of simple statistical distributions. The moderately complex case can be more or less elaborated ranging from stochastic Channel Network (CN) or Discrete Fracture Network (DFN) realisations or Equivalent Porous Media representations thereof (EPM), as a Stochastic Continuum (SC) representation, or simply as a composite system consisting of several different Continuous Porous Media (CPM). The premises of different model representations (CN, DFN, EPM, SC or multicomponent CPM) is an essential part of the overall hydrogeological uncertainty assessment and different approaches may or may not be used in parallel dependent on the objectives and scale of the flow problem treated. Figure 2-1 illustrates schematically the different modelling approaches and the kind of flow fields these may treat. It is noteworthy that all approaches are based on the same constitutive parameters time, pressure and flow rate. Hence, they are not true alternative models but alternative approaches rather.

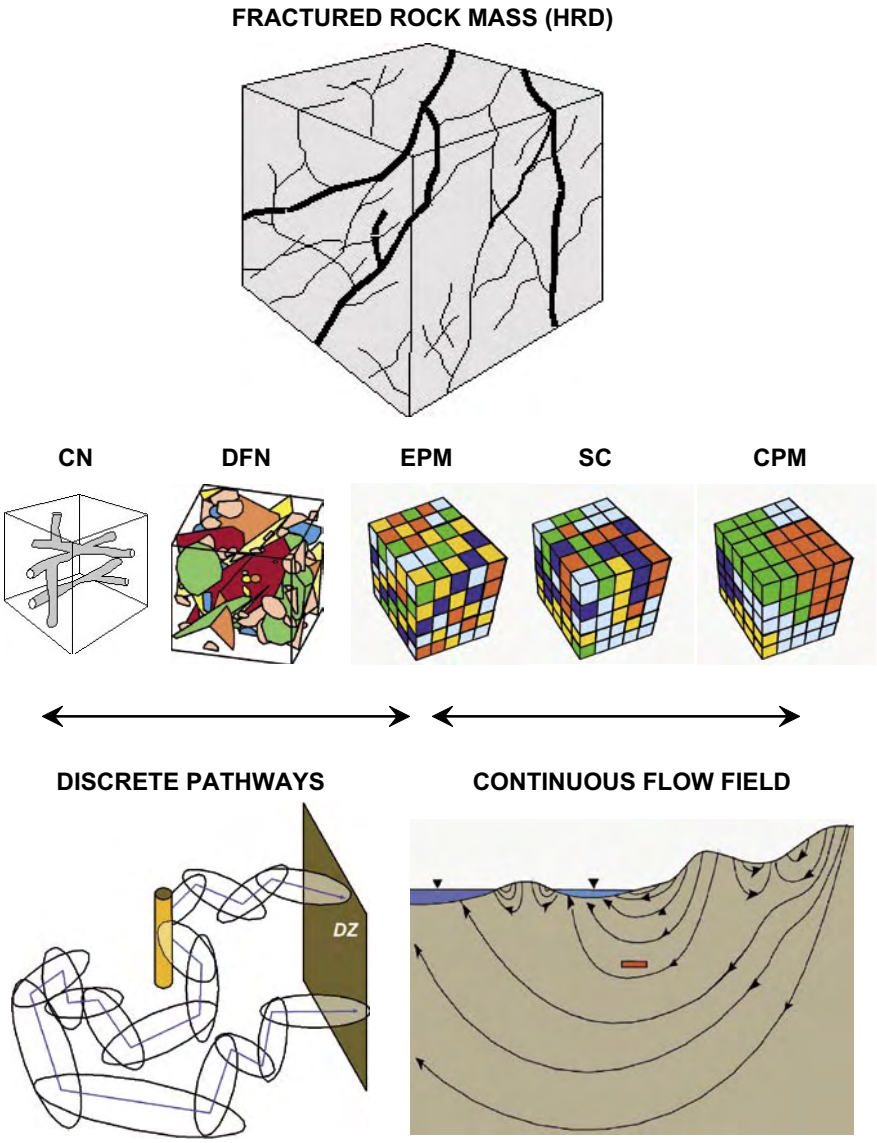

Figure 2-1. *Different modelling approaches to groundwater flow in crystalline rock and the kind of flow fields these may address. It is noteworthy that all approaches are based on the same constitutive parameters time, pressure and flow rate. Hence, they are not true alternative models approaches but alternative variants rather. CN = Channel Network, DFN = Discrete Fracture Network, EPM = Equivalent Porous Medium, SC = Stochastic Continuum, CPM = Continuous Porous Media (single-component or multi-component), DZ = Deformation Zone.*

Figure 2-2 illustrates the work flow of hydrogeological modelling envisaged for modelling stage 1.2. The details of the work flow may be described as follows:

- A hydrogeological DFN (HydroDFN) analysis is carried out based on core mapping data, PFL and PSS test data. The hydrogeological DFN modelling is underpinned by the geological DFN modelling. Uncertainties in the geological DFN modelling, e.g. the power-law size distribution, need to be scrutinised in detail in the hydrogeological DFN modelling.
- The output parameters (connected fracture intensity and fracture transmissivity) are applied to a structural DFN model (characterised by fracture orientation, size, geological intensity and spatial distribution) to estimate block size properties (EPM) and to analyse possibilities for anisotropy in flow.

- The EPM block size calculations are requested by Repository Engineering, but are useful also for the inclusion of the hydrogeological DFN findings into a regional scale groundwater flow model, cf Figure 2-1. The computation of EPM grid block tensors from a regional hydrogeological DFN simulation is a vital step in the flow modelling and the hydraulic properties derived are sensitive to the properties of the DFN model and to the chosen resolution of the grid blocks. The approach taken in DarcyTools is to discard stochastic features smaller than the grid size and treat the processes on scales smaller than the grid resolution analytically, cf /Svenson et al. 2004/. The basis for this approach is an assumed power-law correlation between fracture transmissivity and fracture size, cf Equation (2-10).
- The EPM model is combined with the models defined for the HCDs and HSDs and calibrated against hydraulic test data and hydrogeochemical data, e.g. chemical composition (salinity), water types, or natural isotopes.
- The calibrated EPM regional model is used for sensitivity analyses of ground water flow paths and transport of solutes.

2.2 Modelling with DarcyTools

DarcyTools is an equivalent porous media (EPM) flow code specifically designed to treat flow and salt transport in sparsely fractured crystalline rock intersected by transmissive fractures. It comprises, among other things, a fracture network generator, upscaling algorithms for the computation of finite-volume (block-size) properties and a multi-rate diffusion model. It is noted that some of the components of DarcyTools are not used in the work reported here as they are still under development or subjected to testing and verification. The work flow of modelling with DarcyTools essentially follows that shown in Figure 2-2.

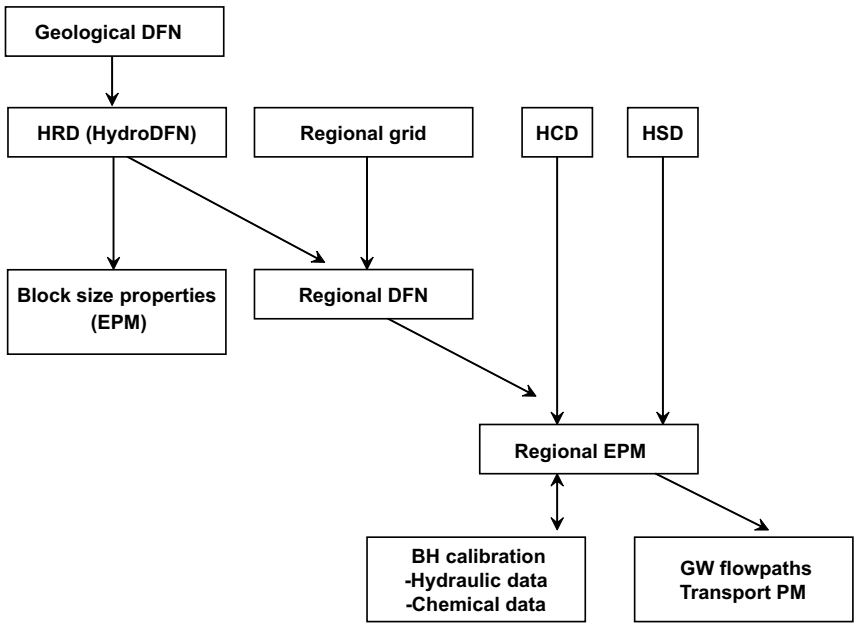

Figure 2-2. *Work flow of hydrogeological modelling. PM = Performance Measures.*

2.3 Discrete Fracture Network (DFN) representation

The built-in discrete fracture network (DFN) generator of DarcyTools is a simple model of reality and based on the following key geometric assumptions/limitations:

- Univariate Fisher distributed fracture orientations.
- Power-law distributed fracture sizes.
- Poisson distributed fracture centres.

These basic assumptions are used to define geometry of the stochastically modelled fracturing. The hydraulic properties are either specified or sampled from probability distribution functions (PDFs) specified for each fracture set. The properties may be sampled independently or correlated. In model version 1.2 the site-specific fracture data available for modelling consist of fracture transmissivities T [m^2/s], whereas general formulae are used for assigning equivalent parameter values of the storativity S [–] and the transport aperture e_t [m]:

$$S = 7 \cdot 10^{-4}\ T^{0.5} \tag{2-1}$$

$$e_t = 0.5\ T^{0.5} \tag{2-2}$$

These formulae are taken from /Rhén et al. 1997, Rhén and Forsmark 2001, Andersson et al. 1998b, 2000, Dershowitz et al. 2003/. It is noted that the storativity and the transport aperture are both modelled as power-law functions of the fracture transmissivity. Chapter 4 focuses on the experimental basis and uncertainties for assuming that fracture transmissivity, in turn, is a power-law function of the fracture size.

Fractures are commonly modelled as circular discs. In DarcyTools, however, fractures are modelled as squares. The equivalent radius r of a square of size L is simply:

$$r = L/\sqrt{\pi} \tag{2-3}$$

The aforementioned geometric assumptions/limitations imply that the number of discrete fractures per unit volume P_{30} in the size interval $[r, r + dr]$ may be written as /Hedin 2005/:

$$P_{30}[r, r+dr] = P_{32}[r > r_0]\, r_0^{(k_r-2)}\, \frac{(k_r-2)}{\pi\ k_r} \left(r^{-k_r} - (r+dr)^{-k_r} \right) \tag{2-4}$$

where k_r is the shape parameter of the power-law size distribution and $P_{32}[r > r_0]$ is the fracture surface area per unit volume of all fractures r greater than the location parameter r_0. In the work presented here we call k_r the scaling exponent and r_0 the reference size. It is noted that the fracture surface area per unit volume of rock depends strongly on the chosen value of $r_{\min}$, whereas the intensity expression in DarcyTools, α_{DT}, is not dependent on $r_{\min}$, see Figure 2-3.

k_r and r_0 may be estimated from in situ fracture trace measurements on outcrops and $P_{32}[r > r_0]$ from a corrected fracture frequency in core-drilled boreholes. k_r may be evaluated from the straight-line slope k_t of the complementary cumulative density function (CCDF) of fracture trace lengths t plotted in a log-log plot. The equation for the trace length CCDF may be written as provided that $t << t_{\max}$:

$$G[t' \geq t] = \left(\frac{t_0}{t} \right)^{k_t} \tag{2-5}$$

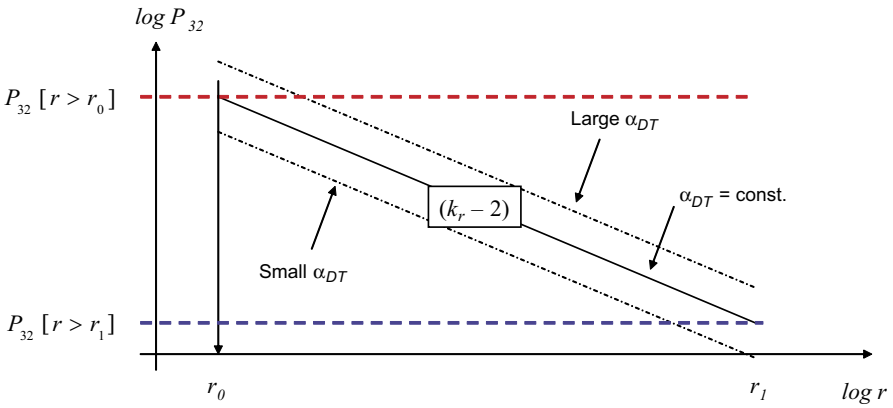

Figure 2-3. *Graph showing the relationship between P_{32} and r for a power-law distributed size distribution with a fixed value of k_r. α_{DT} denotes the intensity parameter used in DarcyTools. Its relation to P_{32} is commented on in the text.*

where t_0 is the trace length value where the fitted straight line intersect at $G[t' \geq t] = 1$. In practice, the fracture mapping is truncated and there is not a perfect fit of the straight line. Notwithstanding, it is common to assume that:

$$t_0 = t_{\min} \tag{2-6}$$

where $t_{\min} = \min[t_i]$, $i = \{1, N\}$. The relationship between the reference fracture size r_0 and t_0 is difficult to determine with certainty simply due to the fact that the minimal trace length is very difficult to assess in the field. The relationship between k_r (the parent fracture size in 3D) and k_t (the trace length in 2D) is /La Pointe et al. 2005/:

$$k_r = k_t + 1 \tag{2-7}$$

Since the fracture size distribution is power-law distributed so is the fracture surface area per unit volume of rock:

$$P_{32}[r > r_1] = P_{32}[r > r_0]\left(\frac{r_0}{r_1}\right)^{(k_r-2)} \tag{2-8}$$

Equation (2-8) renders that $P_{32}[r_1, r_1 + dr]$ may be written as:

$$P_{32}[r_1, r_1 + dr] = P_{32}[r > r_0]\left(\frac{(r_1)^{(2-k_r)} - (r_1 + dr)^{(2-k_r)}}{(r_0)^{(2-k_r)}}\right) \tag{2-9}$$

If the upper bound, $r_{\max}$, is sufficiently large the intensity expression used in DarcyTools may be written as:

$$\alpha_{DT}(r) = P_{32}[r > r_{\min}]\frac{(k_r - 2)}{\pi} r_{\min}^{(k_r-2)} r_{ref}^{k^{-1}} \tag{2-10}$$

Figure 2-4 shows the dependence of P_{32} on $r_{\min}$, k_r and α_{DT} for $r_{ref} = 1$.

In summary, the vital geometric/geological parameters/assumptions in this study are the scaling exponent k_r, the fracture intensity α_{DT}, the assumptions for the reference size r_0 and the inter-connected fracture intensity available for flow $P_{32CON}[r > r_0]$ (explained in

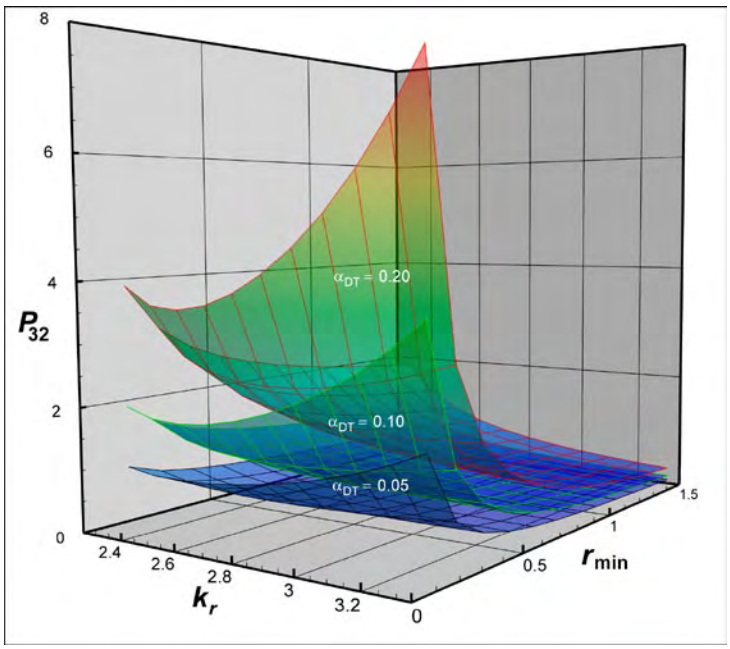

Figure 2-4. *Illustration of the dependence of P_{32} on r_{min}, k_r and α_{DT}. The surfaces show that the value of $P_{32}[r > r_{min}]$ is less sensitive to uncertainties in k_r and r_{min} for $k_r > 2.6$ and $r_{min} > 0.25$ m.*

Chapter 5). A crucial hydraulic assumption in DarcyTools concerns the foundation and derivation of a power-law correlation between fracture transmissivity and fracture size:

$$T = a\, r^{b} \qquad (2\text{-}11)$$

2.4 Fracture representation as equivalent EPM flow properties

In order to assess the implications of the inferred DFN model on flow and transport on the regional-scale, it is necessary for practical reasons to convert the DFN model to an EPM model with appropriate properties. The resulting parameters are a directional hydraulic conductivity tensor, fracture kinematic porosity and other transport properties (such as the fracture surface area per unit volume).

DarcyTools uses a staggered computational grid of cells, which means that scalar entities such as pressure, flow porosity and salinity use a cell-centred mesh, whereas directional entities such as hydraulic conductivity, hydrodynamic diffusivity, mass flux and Darcy velocity use a mesh centred at the cell walls. This grid arrangement was first introduced by /Harlow and Welch 1965/ and is described in textbooks; see e.g. /Patankar 1980/. Each variable is assumed to be representative for a certain control volume, which is the volume the discretised equations are formulated for. In DarcyTools a technique called the GEHYCO-method is used for the upscaling of all fracture properties to equivalent grid cell properties:

A fracture contributes to the grid value of a variable by an amount which is equal to the intersecting fracture volume times the value of the variable in question. Contributions from all elements that intersect the control volume are added and the sum is divided by the volume of the cell.

The basic principle of the GEHYCO-method is obviously very simple but still general enough to handle even complex fracture networks. A few properties of the method are noted:

- All cell wall hydraulic conductivities will be different in the general case. In result, an anisotropic hydraulic conductivity field is obtained.
- A fracture smaller than the cell size can not generally contribute to the anisotropy or the correlation of the hydraulic conductivity field.

/Svensson 2001ab, Svensson et al. 2004/ provide simple calculations that illustrate the GEHYCO method and the accuracy that can be expected.

It may be noted the term "background properties" generally refers to the equivalent cell properties of the stochastic DFN. No extra component for matrix conductivity or micro-fracturing is added. However, the stochastic DFN is necessarily truncated in some way e.g. based on fracture size which consequence means that some cells may not include a connected network of fractures or may only be connected in some directions. To avoid this just being a result of the choice of truncation limit and chance, a minimum grid cell conductivity and porosity is set for any cells that have zero properties. The assignment of appropriate minimum properties is an important output of the block-scale property studies, see Chapter 6.

In conclusion, there is a trade off between using the best fit truncation size and the limit of the simulation that is possible to run computationally. In DarcyTools the smallest fracture considered will often be of the same size as the grid size. Smaller fractures are, however also of importance, in particular for diffusion. These are in DarcyTools represented as storage volumes (immobile zones) and exchange matter with the flowing water by molecular diffusion only, see Section 2.5.

2.5 Variable-density groundwater flow and salt transport

DarcyTools computes fracture network flows using a continuum model in which the mass conservation equation for groundwater is associated to several mass fraction transport equations for the salinity and/or particle mass concentrations, and to a heat transport equation. The mass conservation for groundwater in DarcyTools is written as:

$$\frac{\partial(\rho\,\varepsilon)}{\partial t}+\frac{\partial}{\partial x}(\rho\,u)+\frac{\partial}{\partial y}(\rho\,v)+\frac{\partial}{\partial z}(\rho\,w)=Q \tag{2-12}$$

The mass conservation equation is turned into a pressure equation by means of the Darcy assumption:

$$\begin{aligned}\rho\,u &= -\frac{K_x}{g}\frac{\partial p}{\partial x}\\ \rho\,v &= -\frac{K_y}{g}\frac{\partial p}{\partial y}\\ \rho\,w &= -\frac{K_z}{g}\frac{\partial p}{\partial z}-K_z(\rho-\rho_0)\end{aligned} \tag{2-13}$$

Salt transport is treated by means of two processes in DarcyTools:

- advection-diffusion within the mobile pore volume in the computational grid, and
- diffusive exchange between the immobile and mobile pore volumes on a sub-grid scale.

The mass fraction transport equation (the advection-dispersion equation) for the salinity in DarcyTools is written as /Svensson et al. 2004/:

$$\begin{aligned}\frac{\partial(\rho\,\varepsilon)}{\partial t} &+ \frac{\partial}{\partial x}\left(\rho\,u\,C - \rho\,\gamma\,D_x\frac{\partial C}{\partial x}\right)\\ &+ \frac{\partial}{\partial y}\left(\rho\,v\,C - \rho\,\gamma\,D_y\frac{\partial C}{\partial y}\right)\\ &+ \frac{\partial}{\partial z}\left(\rho\,w\,C - \rho\,\gamma\,D_z\frac{\partial C}{\partial z}\right) = Q\,C + Q_c\end{aligned} \qquad (2\text{-}14)$$

In Equations (2-11) through (2-13) ρ is the fluid density, ε the flow porosity, (u, v, w) the Darcy fluxes, (K_x, K_y, K_z) the hydraulic conductivities, g the acceleration of gravity, ρ_0 a reference fluid density, p the dynamic fluid pressure relative to the reference hydrostatic pressure, C the transported mass fraction of salt and (D_x, D_y, D_z) the hydrodynamic dispersion. Q and Q_c are source/sink terms per unit volume of fluid mass, where Q_c represents the diffusive exchange of salt between the mobile and immobile pore volumes. The concept of diffusion into immobile volumes in DarcyTools ranges from the short time (fast) diffusion into the easily reached stagnant pools of water nearby a flowing fracture to the long time (slow) diffusion into the less porous rock "far" away from the flowing fracture, the depth of which depends on the modelled time scale and the matrix properties. Figure 2-5 shows a conceptual model of the transition zone between flow and immobile pore volumes.

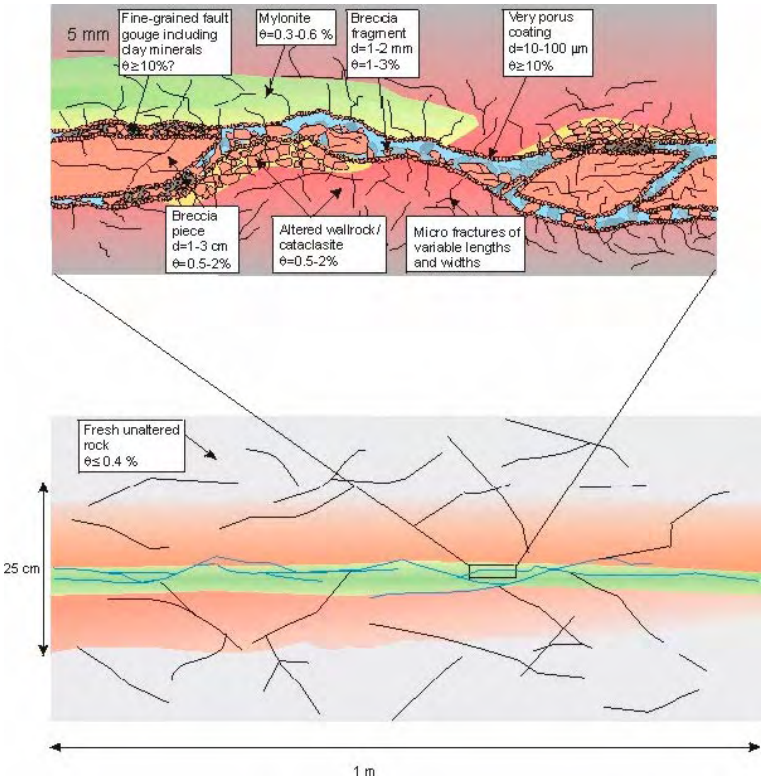

Figure 2-5. *Generalised conceptual model of a typical conductive structure /Winberg et al. 2003/.*

The diffusive exchange of salt between the immobile and mobile pore volumes Q_c is modelled by a multi-rate diffusion process in DarcyTools. The implementation of the multi-rate diffusion process is based on the one-dimensional multi-rate diffusion model by /Haggerty and Gorelick 1995/. One of the key parameters of the multi-rate diffusion model is the capacity ratio between the immobile and mobile pore volumes. The pore volume in the rock matrix accessible for diffusion ε_p is expected to be 10–100 times greater than the pore volume in the water-conducting fractures, ε_f (I Neretnieks, personal communication, September 2004). The current working hypothesis used in DarcyTools is that the capacity ratio ought to be of the same order of magnitude.

The multi-rate parameter values used in the work reported here are presented in Chapter 7. The values used are adopted from the experiences gained in Task 6 /Svensson and Follin 2005/. No particular adaptation is made to the fracture size statistics derived in the DFN analysis presented in Chapter 5. Since a power-law size relationship is assumed, also fractures in the immobile volume are related to the DFN statistics. Below follows a brief summary of how the multi-rate method is implemented in DarcyTools version 2.1.

The grid cell capacity ratio β_c in DarcyTools may be written as:

$$\beta_c = \frac{V_{im,c}}{V_{m,c}} \tag{2-15}$$

where $V_{im,c}$ and $V_{m,c}$ are the grid cell values of the immobile and mobile pore volumes, respectively. By the same token, the total, or global, capacity ratio of the entire model domain β_G may be written as:

$$\beta_G = \frac{\sum_c V_{im,c}}{\sum_c V_{m,c}} \tag{2-16}$$

In DarcyTools it is assumed that the spatial distribution of the immobile pore volume is directly proportional to the spatial distribution of the accumulated flow wetted surface area. If FWS_f denotes the contribution to the flow wetted surface area of a grid cell from fracture f and FWS_c the accumulated flow wetted surface area of all connected fractures that intersect the cell, the assumption made in DarcyTools may be written as:

$$FWS_c = \left(\sum_f FWS_f \right)_c \tag{2-17}$$

$$V_{im,c} = k\ FWS_c \tag{2-18}$$

$$\sum_c V_{im,c} = k \sum_c FWS_c \tag{2-19}$$

The ratio between the immobile pore volume in a grid cell and the total immobile pore volume may be written as:

$$\frac{V_{im,c}}{\sum_c V_{im,c}} = \frac{FWS_c}{\sum_c FWS_c} \tag{2-20}$$

If the value of the total capacity ratio of the bedrock is given, or assumed to be known, the spatial distribution of the capacity ratio on the scale of a computational grid cell can be estimated by combining the definitions in Equations (2-14) and (2-15) with the assumption behind Equation (2-19):

$$\beta_c = \beta_G \left(\frac{FWS_c}{\sum_c FWS_c} \right) \left(\frac{\sum_c V_{m,c}}{V_{m,c}} \right) \tag{2-21}$$

As a consequence, the value of the proportionality constant k in Equations (2-18) and (2-19) may be written as

$$k = \frac{\beta_G}{\left(\frac{\sum_c FWS_c}{\sum_c V_{m,c}} \right)} \tag{2-22}$$

A series of capacity boxes with different mass transfer coefficients α_i are used in the multi-rate model to model the diffusive exchange of matter between the mobile and immobile pore volumes /Haggerty and Gorelick 1995, Svensson et al. 2004/. α_i has the unit [s^{-1}], thus $(\alpha_i)^{-1}$ may be interpreted as the residence time for the diffusive exchange of matter to enter and exit capacity box i.

The exchange of matter by diffusion with the rock mass exposed by the flow wetted surface area can be expected to be related to two parameters; the flow wetted surface area per unit volume of flowing water a_w and the advective travel time t_w. The exchange will increase with both these parameters and a new variable, the F-quotient) /Andersson et al. 1998a/ has been introduced for this product:

$$F = a_w \, t_w \tag{2-23}$$

The discretised form of Equation (2-23) for a flow path through a grid cell may be written as:

$$F_c = \left(\frac{FWS}{V_m} \right)_c \left(t_{exit} - t_{entrance} \right)_w \tag{2-24}$$

Integration along the entire flow path yields:

$$F = \sum_c F_c \tag{2-25}$$

The mobile pore volume of a grid cell c in DarcyTools may be written as:

$$V_{m,c} = \sum \left(\varepsilon_f \, V_f \right)_c \tag{2-26}$$

where ε_f is the flow porosity of an intersecting water-conducting fracture and V_f the volume of the fracture in the grid cell. The fracture flow porosity may be written as:

$$\varepsilon_f = \frac{e_f}{b_{hyd}} \tag{2-27}$$

where e_f is the total thickness of the empty space in the flowing fracture and b_{hyd} the hydraulic thickness of the flowing fracture. It is noted that e_f may be thought of as the transport aperture e_t for which there exists several expressions, among which the cubic law probably is the most well known. Equation (2-2) shows a power-law expression used in the TRUE project at the Äspö HRL. It is noted that Equation (2-2) is derived from tracer experiments in single fractures over short distances and that there are few if any tracer experiments conducted in fractured rocks over longer distances, e.g. 100 m or more. There is also limited experience of using Equation (2-2) in regional flow studies such as the work reported here.

The practical use of the equations listed above for a computational grid cell can best be illustrated by an example:

A grid cell of size $(100\ m)^3$ is intersected by a large horizontal deformation zone, which has a hydraulic thickness of 10 m and a transmissivity of $2 \cdot 10^{-5}\ m^2/s$. Equation (2-2) renders that the transport aperture of the zone is $2.24 \cdot 10^{-3}$ m and Equation (2-27) that its flow porosity is $2.24 \cdot 10^{-4}$. Its contribution to the grid cell's total mobile pore volume is $22.4\ m^3$ according to Equation (2-26) and if no other fractures are intersecting the grid cell, the flow porosity of the grid cell becomes $2.24 \cdot 10^{-5}$.

2.6 Water types

Two primary concepts used in the regional-scale palaeo-hydrogeological groundwater flow modelling are:

- The current hydrogeological and hydrogeochemical situation in Forsmark is the result of natural transient processes (infiltration of glacial water, land-rise, marine transgressions and regressions, dilution/mixing of sea water) that have evolved during the Holocene period.

- The integration with hydrogeochemistry can be evaluated by assuming appropriate initial and boundary condition for the flow, dispersion and diffusion of different types of particles (water types) representing, ideally, the four reference waters treated by hydrogeochemistry – Rain 1960, Marine, Glacial and Brine – see /Laaksoharju et al. 2004, 2005/. That is, groundwater located at any place and time within the model domain is the result (or can be explained as) a mixing between two or more of the aforementioned reference waters.

The use of water types can be considered to be a particular form of particle tracking where concentration is used instead of individual particle traces. In the work reported here we did not try to subject the water types to matrix diffusion, but it is noted that the multi-rate model used for modelling diffusion of salt can be used also for modelling diffusion of water types. Five water types are treated as conservative tracers. These are named in a fashion that resembles the names of the reference waters treated by hydrogeochemistry, Brine, Glacial, Littorina, Meteoric (precipitation before 1960), and Rain 1960 (precipitation after 1960). The boundary and initial conditions associated with the usage of five water types are explained in Section 2.7.

2.7 Boundary and initial condition concepts

Simulating the palaeo-hydrogeology at Forsmark requires modelling of the evolution of groundwater flow and solute transport during the Holocene period up to the present day. A key issue in this task is how to represent the time-varying top boundary conditions for flow, solutes (salt) and reference waters. The general hypothesis of the evolution of surface and sub-surface reference waters in the work presented here is influenced by the geological modelling by /Hedenström and Risberg 2003/ and the hydrogeochemical modelling by /Laaksoharju et al. 2004, 2005/. The simulations begin at c 8,000 BC (10,000 BP) at a time Uppland when was covered by the Ancylus Lake, which was a fresh water lake with a strong glacial melt water signature. The penetration depth of the glacial melt water in the bedrock is uncertain but probably it dominated the groundwater composition in the upper parts then gradually vanished while mixing with old saline groundwater at depth. The Ancylus Lake period is followed by the Littorina Sea period, whose salinity first increase and the gradually decreases, and eventually the land emerges from the sea and so becomes exposed to infiltration of modern meteoric water. Around 1960 the chemical composition of the meteoric water is considerably affected by the high tritium content in the atmosphere.

The boundary conditions used in version 1.2 of the Forsmark site descriptive model represent the transient processes of (i) shoreline displacement due to postglacial rebound sea level changes, and (ii) the variations in the salinity of the Baltic Sea. The uncertainties in the evolution of the shoreline displacement during the considered postglacial period are discussed in /Hedenström and Risberg 2003/. The uncertainties in the variations in the salinity of the Baltic Sea are commented on in /Westman et al. 1999, Gustafsson 2004/. Figure 2-6 and Figure 2-7 show the descriptions used for the regional flow simulations in the work reported here.

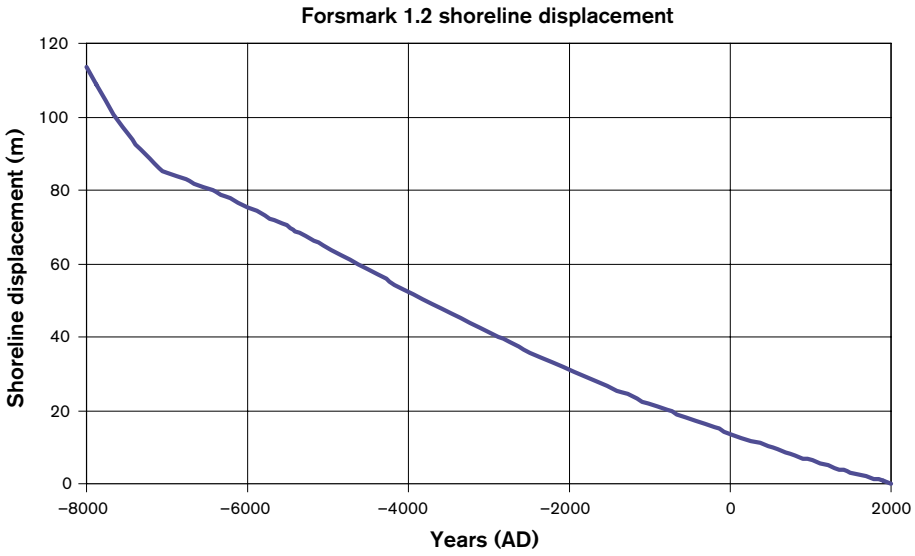

Figure 2-6. *The shoreline displacement at Forsmark relative to the current sea-level for the time period considered in the simulations.*

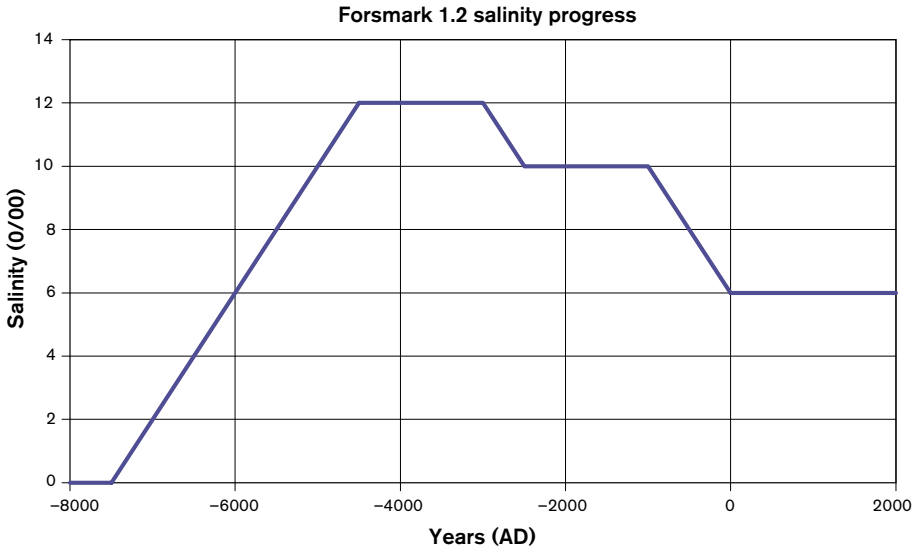

Figure 2-7. *The salinity progress in the Baltic Sea at Forsmark for the time period considered in the simulations.*

The general modelling approach was to hold the model domain fixed (i.e. same x, y and z coordinates), but modify the head and salinity on the top surface in time. The rate of the land rise is fairly constant over the time period considered, although it is initially greater for about the first thousand years until 7,000 BC. The maximum current elevation in the regional-scale model is about 26 m, so the area has only emerged from sea in the last 3,000 years. Salinity rises gradually at the start of the Littorina period about 7,500 BC, reaches a maximum at 4,500 BC, and then gradually starts to reduce toward modern salinity levels from 3,000 BC. It is noted that there is a considerable uncertainty associated with the exact looks of the graph in Figure 2-7. The uncertainty concerns both the timing and the magnitude of the salinities, cf /Hedenström and Risberg 2003, Westman et al. 1999/.

In is noted that the changes in the stresses caused by the melting of the ice cap and the subsequent rebound stress are not considered in the work reported here. However, we recognise that these phenomena may have a significant impact on the near surface fracture frequency and transmissivity field.

For flow, there are two main possibilities onshore, specified head or a flux type boundary condition. Offshore, specified head is the only alternative.

The specified head boundary condition is straightforward to implement numerically by setting the value at nodes on the surface to the required head at each time-step specified head. If the onshore part of the model domain is assumed to be fully saturated, the head is equal to the height of the topographic surface at that time according to the shoreline displacement process. Offshore, the head is equal to the depth of the Baltic Sea multiplied by the relative salinity of the Baltic Sea. It is noted that both the bathymetry and the salinity of the Baltic Sea alter in time.

The flux type boundary condition is more realistic than the fully saturated specified head boundary condition, but it is also a lot more complicated to implement and solve, in particular if the model domain is large and the shoreline retreats. The approach used in this work is to replace the specified flux type boundary condition by a more gently undulating specified head boundary condition. The procedure used consists of two steps:

1. Identification of the main discharge areas; this is accomplished by computing the second derivate of the topographic elevation model.
2. Calibration of the elevation of the water table between the discharge areas; this is accomplished by a generic matching of available head data from the site investigations /Juston and Johansson 2005/.

/Juston and Johansson 2005/ concludes that the topographical positions of the groundwater monitoring wells in soil are fairly representative for the study area, though low areas were somewhat over-represented. The groundwater levels in soil are very shallow with most of the wells showing levels between zero and one metre below ground for most of the year, see Figure 2-8. The annual level amplitudes were between a half and one and a half metre for most of the wells. The maximum depth below ground observed is circa four metres.

The modelled differences in head between a fully saturated flow model and a more gently undulating groundwater used in the work reported here are shown in Figure 2-9.

For salinity, the boundary condition is generally a specified concentration where there is advective flow into the model (recharge area), and a boundary condition where there is advective flow out of the model (discharge). Theoretically, this requires a mixing of a Dirichlet type boundary condition with a Neumann type boundary condition. In the work reported here, however, we consider a relevant simplification where a Dirichlet type boundary condition is used throughout the model domain, but with different specified values depending on if onshore or offshore conditions are treated. The onshore concentrations are set to zero and the offshore concentrations are the same as the salinity of the Baltic Sea at the time of consideration.

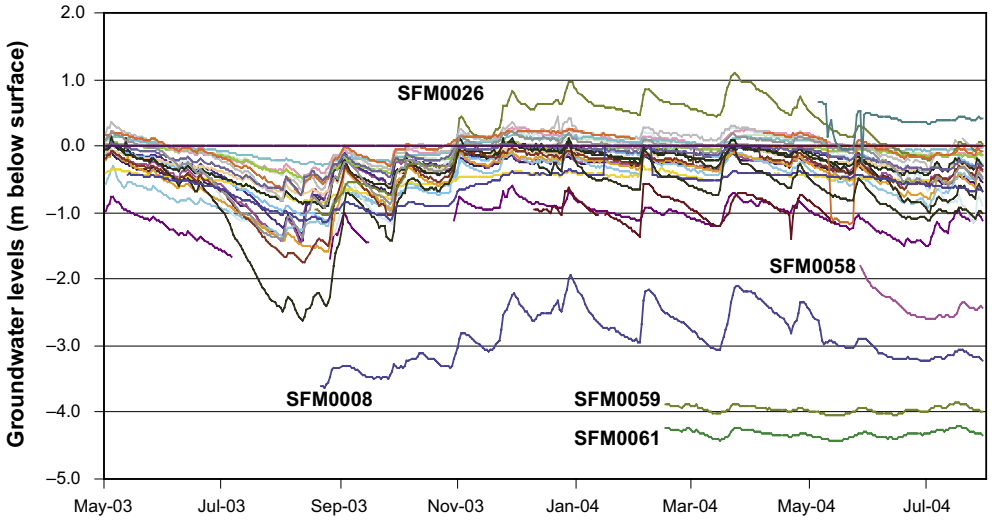

Figur 2-8. *Daily average depth of the hydraulic head below ground surface for groundwater monitoring wells in soil /Juston and Johansson 2005/.*

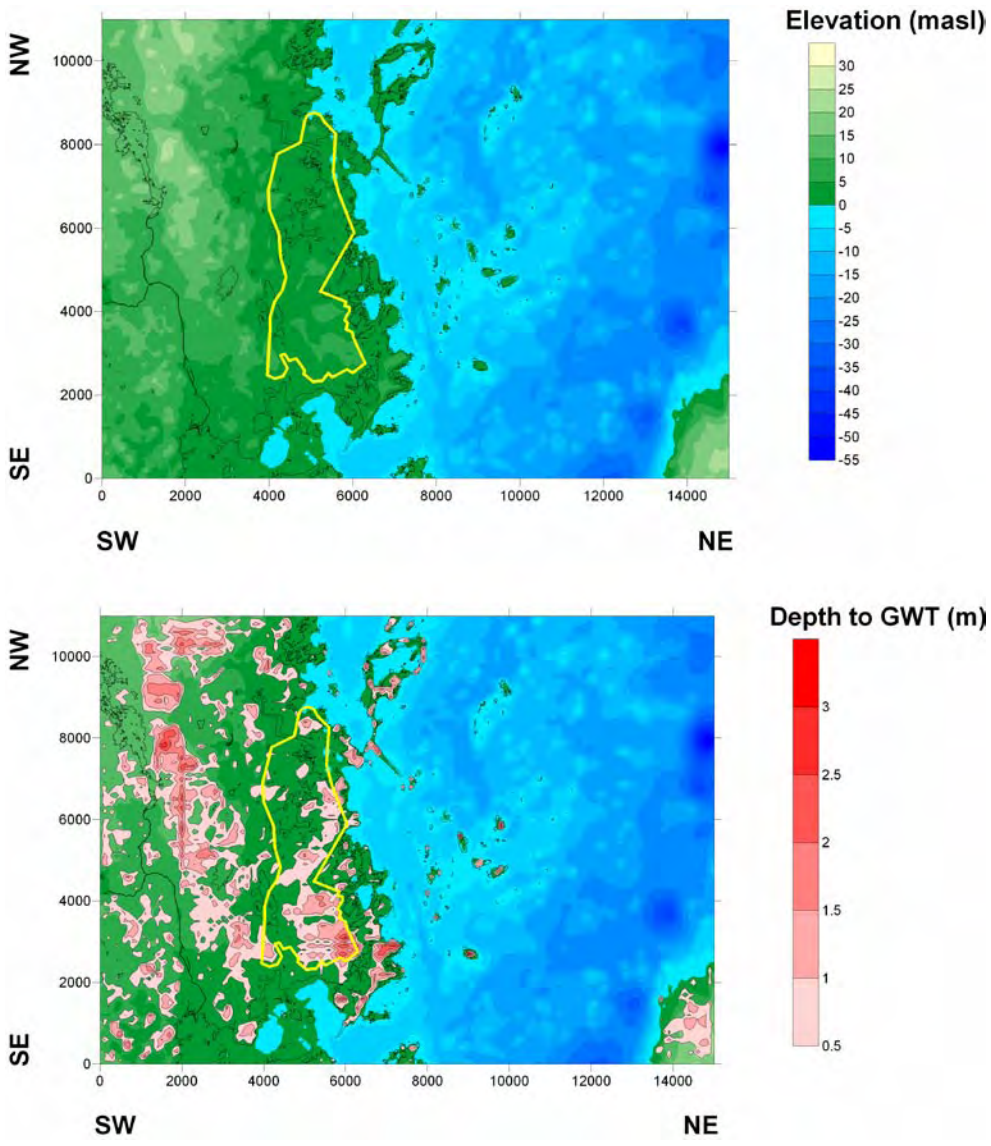

Figure 2-9. *Visualisation of the differences in head between a fully saturated flow model (TOPO; top) and a more gently undulating groundwater table (GWT; below).*

The lateral boundary conditions of the rectangular regional model domain are treated as no-flux boundaries. To assess the sensitivity of the flow within the target area to this simplification a different position of the regional model domain is also studied, see Figure 2-10. The sensitivity is studied by means of particle tracking and expressed in terms of several flow-related transport performance measures, see Section 2.8.

The boundary condition at the bottom of the 2.1 km deep rectangular regional model domain is treated as a no-flux boundary. For the salinity a specified concentration of 100 g Total Dissolved Solids / L (~ 0.1 kg TDS / kg) is used. These settings are tentative and largely based on data from the deep core-drilled borehole KLX02 in Laxemar and the experiences gained from model versions 1.1 and 1.2 of the Simpevarp area /Follin et al. 2004ab, Hartley et al. 2005ab/. The sensitivity to the position of the no-flux boundary and the magnitude of the specified concentrations is not tested by means of an alternative setting in the work reported here. However, the assumption that the body of the groundwater flow in Forsmark is in the upper kilometre or so is considered reasonable given the general impression of available hydraulic and hydrogeochemical information treated by model version 1.2.

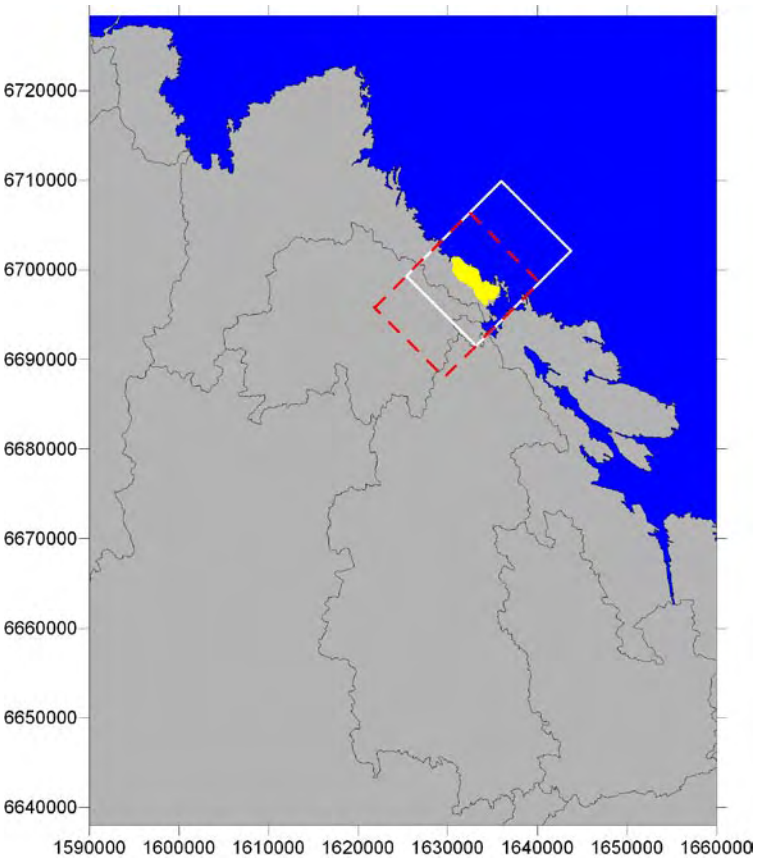

Figure 2-10. *The position of the candidate area (yellow surface) is clearly separated from the regional surface run-off from southwest; grey lines indicate regional water divides. The lateral boundaries of the rectangular regional model domain (white line) are treated as no-flux boundaries. To assess the sensitivity of the flow within the target area (cf the release area in Figure 1-5) to this simplification a different position of the model domain is also studied (red dashes).*

The aforementioned boundary condition for the salinity at the bottom of the 2.1 km deep model domain is accompanied by an assumption for the initial conditions of salinity, pressure and water types. The initial condition for the salinity and the water types used in this study assumes a profile of full Brine at depth and full Glacial at the surface, with a start time of 8,000 BC, see Figure 2-11. That is, in this work full Glacial means zero salinity and Full Brine means a salinity of c 100 g TDS/L. Moreover, the initial conditions of the salinity profile in the kinematic porosity field were assumed to be in equilibrium with the salinity profile in the matrix porosity field. The initial condition for pressure was calculated from the initial salinity profile assuming isothermal conditions:

$$\rho(z, TDS) = \rho_0 \left(1 + 0.078\, TDS(z)\right) \tag{2-28}$$

$$dp = -\, g\, \rho(z, S)\, dz \tag{2-29}$$

where ρ_0 is the reference density for zero salinity, e.g. 1,000 kg/m^3, p is the fluid pressure, and g is the acceleration of gravity. Figure 2-11 shows one of the initial water type conditions used in the models reported here; full Glacial to c 450 m depth, and then Brine rises linearly to full Brine at c 1,900 m depth.

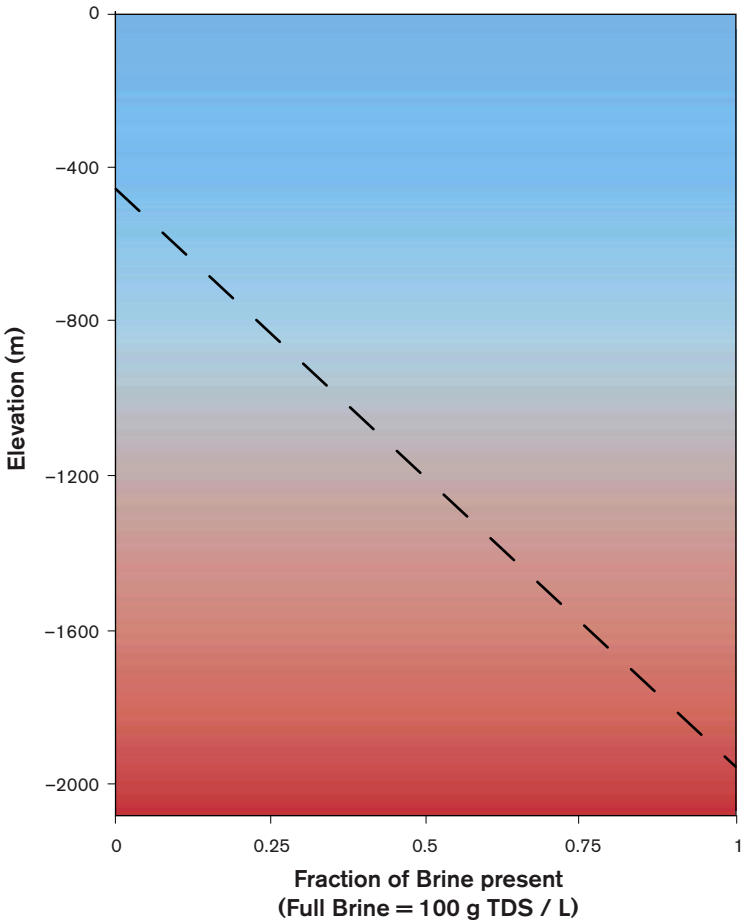

Figure 2-11. *Example of an initial condition for reference water transport at 8,000 BC. Above –450 masl the water is pure Glacial (coloured cyan). There is then a linear transition between Glacial and Brine (coloured pink) toward pure Brine below –1,900 masl. Full Glacial means zero salinity and Full Brine means a salinity of 100 g TDS/L.*

In conclusion, the following boundary and initial conditions are used for the five water types:

- The Brine water type is governed by an initial condition and a stationary boundary condition at the bottom of the model domain (cf Figure 2-11).
- The Glacial water type is governed by an initial condition only (cf Figure 2-11).
- The Littorina, Meteoric and Rain 1960 water types are governed by a consecutive order of time-dependent conditions on the top boundary mimicking the salinity progress (cf Figure 2-7).

The concentration of a particular (conservative) chemical constituent at any point and time in the model then is just the sum of the products of each water type fraction with the concentration of the constituent of the corresponding reference water.

2.8 Flow-related transport performance measures

One objective of the site descriptive modelling is to understand groundwater flow paths from a local-scale area to the surface. The approach taken is to track particles moving with the advective flow velocity from a range of release points until they reach the top surface. Although it would be possible in *DarcyTools* to track particles as they move through a velocity field that evolves in time, it is preferred here to only use the velocity field from the present day. This is mainly because particle tracks released in a transient velocity field would be sensitive to the release time and the kinematic porosity, making it more difficult to interpret the results due to the added uncertainties.

This study treats the sensitivity of flow paths within the target area to various geological and hydraulic simplifications/uncertainties, e.g. deformation zone models, boundary and initial conditions, hydraulic properties, etc. The sensitivity is expressed in terms of three flow-related transport performance measures:

1. the relative difference between medians (*MED*),
2. the distance between mass centres (*DMC*),
3. the mean of all point to point differences (*MPP*).

The definitions of the four performance measures are given in (2-30) through (2-32). In these equations CC denotes a Comparison Case and SC a Sensitivity Case, i.e. a variant or a perturbation of the CC:

$$MED = (X_{50\%,SC} - X_{50\%,CC}) / X_{50\%,CC} \quad (2\text{-}30)$$

$$DMC = (MC_{SC} - MC_{CC}) = mean\ (x, y, z)_{SC} - mean\ (x, y, z)_{CC} \quad (2\text{-}31)$$

$$MPP = \Sigma\ \sqrt{(\Delta x^2 + \Delta y^2 + \Delta z^2)} / N_p \quad (2\text{-}32)$$

where $X_{y\%}$ is the y-th percentile of the variable of concern, MC is the mass centre of the exit locations of the discharging particles, Δx is the difference $(x_{SC} - x_{CC})$ etc, and N_p is the number of discharging particles.

The three performance measures are calculated for the following variables X:

- the advective travel time t_w from the release point to the discharge point:

  $$t_w = \sum\left(\frac{\varepsilon\ \delta}{q}\right) \quad (2\text{-}33)$$

  where ε is the kinematic porosity, δ an increment in distance along the flow path and q the Darcy velocity,

- the length L_w of the flow path from the release point to the discharge point:

  $$L_w = \sum(\delta) \quad (2\text{-}34)$$

- the Darcy velocity at the release point (canister flux) q_0,

- the F-quotient of the flow path from the release point to the discharge point:

  $$F = \sum\left(\frac{2\ P_{32CON}[r > r_0]\delta}{q}\right) \quad (2\text{-}35)$$

where $P_{32CON}[r > r_0]$ is the interconnected fracture surface area per unit volume of rock mass (cf Chapter 5), δ an increment in distance along the flow path and $q$the Darcy velocity. (Equations (2-35) and (2-25) are equivalent since $a_w = 2\ P_{32}[r > r_0] / \varepsilon$ and $t_w = \delta / (q / \varepsilon)$.)

The approach to calculating the performance measures is to release a large number of particles distributed evenly (fixed spacing) over the release area shown in Figure 1-5 and use these to produce ensemble statistics for the performance measures, as well as locating the discharge areas. No attempt is made to avoid starting particles in either deterministic fracture zones or high transmissivity stochastic fractures. In reality such fractures are likely to be avoided during repository construction, and hence the model may tend to see particles start in a wider range of possible fracture transmissivities than might be encountered in reality.

2.9 Modelling strategy

A key philosophy in developing the groundwater models described here is to test the need for far-field realism within a margin appropriate to the quality and availability of the data. To accomplish this a number of sensitivity cases studied have been constructed to demonstrate the role of some of the uncertainties that remain in the model concepts and parameters, and consequent model predictions, due to the lack of constraint by the available data. These variants form the basis for recommending important uncertainties that should be propagated to the Site and the Safety Assessment.

3 Bedrock hydraulic test data available for modelling

3.1 Introduction

A number of hydraulic test methods are used in a more or less standardised fashion for the hydraulic characterisation of the bedrock penetrated by the boreholes drilled during the site investigations. The hydraulic characterisation of the uppermost part of the bedrock down to c 200 m depth is conducted mainly by means of single-hole hydraulic tests in 140 mm diameter percussion-drilled boreholes (HFMxx). The hydraulic characterisation of the interval 100–1,000 m depth is conducted by means of single-hole hydraulic tests in 76 mm diameter cored drilled boreholes (KFMxxx). The locations of the boreholes are shown in Figure 1-1 and Figure 1-5. Table 3-1 shows in which boreholes a particular type of hydraulic test was conducted.

Below follows an overview of the bedrock hydraulic test data available for modelling and a discussion of the rationale for the division of the bedrock into HCDs and HRDs. The latter is based on the nature of the hydraulic data and the aforementioned rock domain model and base deformation zone model (cf Figure A-1 and Figure A-2). The hydraulic properties of the HCDs and HRDs are derived in Chapters 4 and 5. The working hypothesis used in the work reported here is that the key hydraulic entity deduced from the use of traditional interpretation models, the radial transmissivity, is relevant for a forward modelling of the heterogeneity and anisotropy of undisturbed groundwater flow and salt transport in fractured rocks on a regional scale. The assumption implies that the interpretations of the hydraulic tests (and the numerical simulations used to underpin the interpretations) must take the detailed geometrical description of the borehole structures into account.

Table 3-1. Overview of single-hole hydraulic tests conducted in the core-drilled and the percussion-drilled boreholes available for modelling.

Test method	Acronym of method	Type of test performed	Boreholes
Pipe String System	PSS	Injection tests performed as constant pressure tests (100 m, 20 m, 5 m)	KFM01A–KFM03A
Hydraulic Test System	HTHB	Open-hole pumping tests performed as constant rate tests, generally combined with impeller flow logging and, if needed, injection tests above the submersible pump	HFM01–HFM06 HFM08–HFM13 HFM15–HFM19 Percussion-drilled parts of KFM01A and KFM03A
Posiva Flow Log	PFL-s	Flow logging in sequential test sections	KFM01A–KFM04A
	PFL-f	Fracture flow logging in overlapping test sections	KFM01A–KFM05A

3.2 Overview of results from HTHB single-hole tests

Almost all of the 19 percussion-drilled boreholes are tested with the HTHB method in combination with impeller flow logging. The tested boreholes intercept all together 49 fracture inflows or circa three fracture intercepts per borehole. The transmissivity distribution of the intercepted inflows is shown in Figure 3-1. The range in transmissivity of the near-surface inflows varies circa three orders of magnitude. The borehole lengths vary between 14–220 m with a mean value of 134 m.

Figure 3-2 shows a histogram of the apparent hydraulic conductivity of the near-surface rock adjacent to the percussion-drilled boreholes. The apparent hydraulic conductivity values are obtained by dividing the cumulative transmissivity by the borehole length.

In Chapter 4 sixteen of the tested percussion-drilled boreholes are interpreted to intersect deterministically treated deformation zones. If one subtracts the inflows and thicknesses associated with these zones from the data shown in Figure 3-1 the geometric mean of the

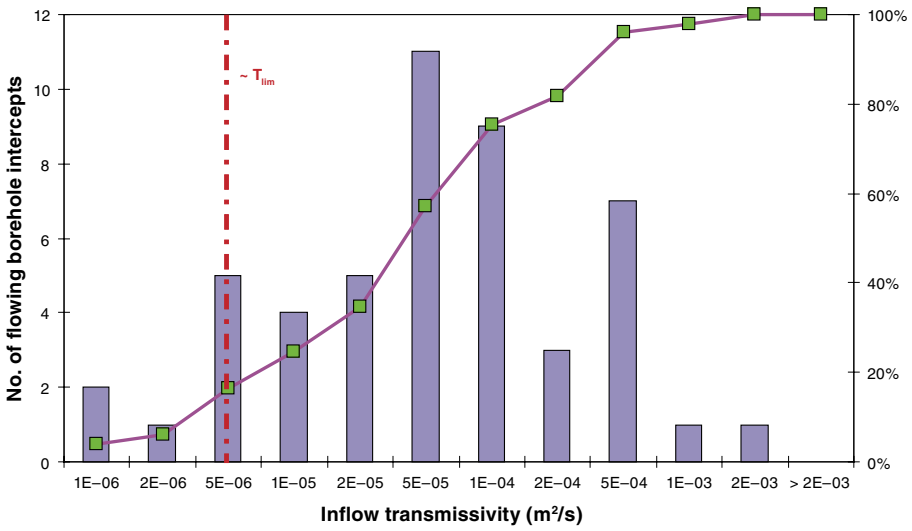

Figure 3-1. *Histogram of inflow transmissivities for all percussion-drilled boreholes available for modelling in version 1.2.*

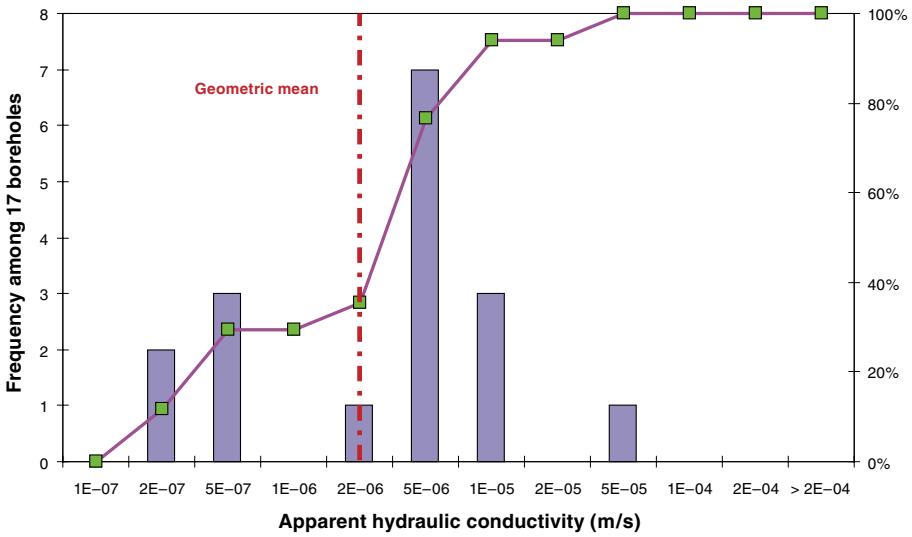

Figure 3-2. *Histogram of the apparent hydraulic conductivity of the near surface rock adjacent to the HTHB tested percussion-drilled boreholes.*

apparent hydraulic conductivity of the upper c 100 m of rock mass shown in Figure 3-2 changes from c $2 \cdot 10^{-6}$ m/s to c $7 \cdot 10^{-7}$ m/s.

3.3 Overview of results from PSS and PFL single-hole tests

The deep core-drilled boreholes are characterised by two kinds of single-hole test methods, difference flow logging during pumping (PFL) and double-packer injection (PSS), see Table 3-1. The main reason for using two test methods is that the pros and cons differ. For instance, the high-resolution PFL tests are run after several days of pumping of the entire borehole, which suggests a pseudo-stationary radial flow regime. In comparison, the high-resolution PSS tests are run for c 20 minutes of injection. In the latter case, various disturbances such as leakage around the packers and a non-stationary and/or a non-radial flow regime cannot be excluded. Moreover, the best resolution of the PFL tests is much better than the best of the PSS tests, 0.1 m versus 5 m. On the other hand, it should be noted that the PSS tests have a somewhat better transmissivity threshold (lower value of the lower measurement limit) than the PFL tests and are much less sensitive to borehole disturbances such as a rough borehole perimeter, gas bubbles, drilling debris, clay particles, high flow rates along the borehole, etc.

The PSS data are given as the transmissivity of contiguous 5 m, 20 m and 100 m intervals (test sections) for boreholes KFM01A–KFM03A. The PFL data are given as the transmissivity of contiguous 5 m intervals (PFL-s) and as the transmissivity of individual fractures (flow anomalies, PFL-f) for boreholes KFM01A–KFM05A. Figure 3-3 shows a compilation of available PSS and PFL-s data for KFM01A–KFM03A. The three boreholes are drilled at different locations along the centre line of the candidate area and RFM029, see Figure 1-5 and Figure A-1. The two types of test data, 5 m PSS and PFL-s, generally show consistent results and reliable values below the practical measurement limit are not uncommon. The practical lower measurement limit of the 5 m PSS tests is circa two to three times lower (better) than the practical lower measurement limit of the PFL-s and PFL-f tests, which is c (1 to 2)$\cdot 10^{-9}$ m^2/s.

The use of different test sections (5 m, 20 m and 100 m), different test methods (PSS and PFL), and different interpretation methods (e.g. transient and steady-state) allows for hydraulic comparisons of various kinds for KFM01A–KFM03A. Such comparisons are made by /Ludvigson et al. 2004, Källgården et al. 2004ab/ and show that there is generally a pretty good agreement between different hydraulic cross-plots but also that there are both practical and conceptual limits when it comes to detailed comparisons and conclusions.

The 5 m PSS data cannot be directly compared to the PFL-s data because the positions of the test sections along the borehole are not identical, and hence it is necessary to transfer the PFL-f data into compatible format. This may be achieved by grouping the PFL-f anomalies according to the same 5 m intervals for which the PSS data are provided. However, while grouping of the PFL-f data into 5 m intervals one loses control of the vital information provided by the individual flow anomalies such as the strike and dip of the associated fractures, low magnitude transmissivities and the frequency of flow anomalies, i.e. the frequency of connected fractures that conduct water above the measurement limit.

Figure 3-3 reveals significant hydraulic differences between KFM01A–KFM03A in terms of the number of PFL-s and 5 m PSS tests above the practical lower measurement limits. In KFM01A there is practically no flow below c 360 m depth. The same situation is at hand in KFM02A below c 520 m depth. In KFM03A, however, there are numerous of conductive test sections along the entire borehole. These differences constitute a major observation of the bedrock hydrogeology at Forsmark.

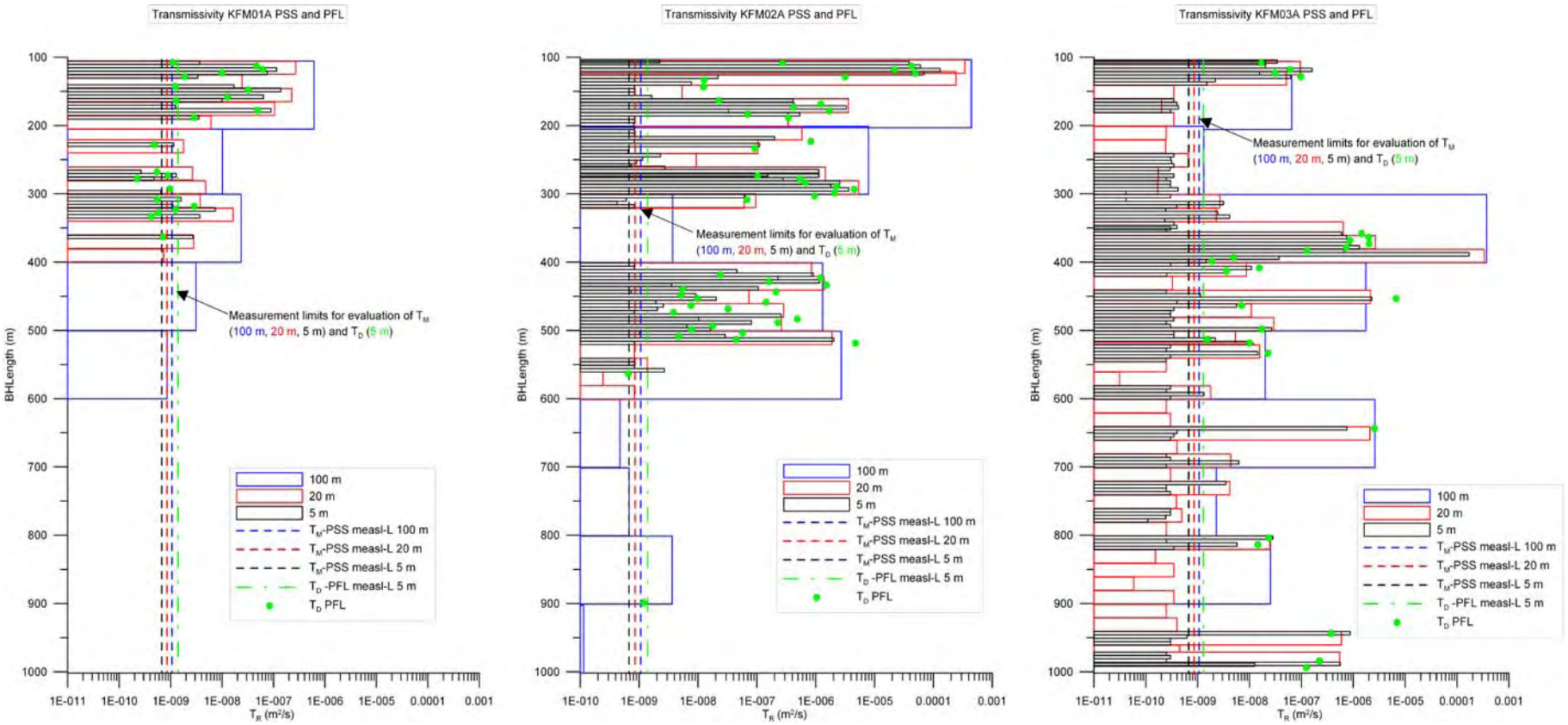

Figure 3-3. *Comparison between PFL-s test results and PSS test results (5 m, 20 m and 100 m) for the three boreholes where both types of hydraulic test data are available, KFM01A–03A. The three boreholes are drilled at different locations along the centre line of the candidate area, see Figure 1-5. The test results reveal significant hydraulic differences between the three boreholes, e.g. in terms of the number tests above the practical lower measurement limit. These differences constitute a major observation of the bedrock hydrogeology at Forsmark. An integrated interpretation between the hydraulic test results and intercepted deformation zones, see Figure 3-4, is presented in Chapter 4. T_M denotes transmissivity determined with Moye's formula /Moye 1967/. T_D denotes transmissivity deteremined with Thiem's equation /Thiem 1906/. Figure 3-4 shows a NW-SE cross-section that passes close to the three boreholes KFM01A–KFM03A shown in Figure 3-3. The cross-section shows the steeply dipping deformation zones that strike north-east and the gently dipping zones that dip to the south-east and south. All these zones transect the candidate volume and are sandwiched between first and second order, vertical and steeply dipping deformation zones that strike WNW-NW (not present in this cross-section), see Figure 1-3.*

From Figure 3-3 and Figure 3-4 it may be foreseen that a large amount of the transmissivity data in borehole KFM03A probably can be coupled to gently dipping deformation zones intersecting this borehole. This observation appears also to be at hand in borehole KFM02A down to c 520 m depth, which is lower limit of the gently dipping deformation zone ZFMNE00A2. Below this depth the rock mass appears to be sparely fractured with few transmissive fractures. This indicates a low hydraulic conductivity. In borehole KFM01A there are few if any gently dipping deformation zones intersecting below c 100 m depth and the intersecting steeply dipping deformation zones, e.g. ZFMNE0061 at c 660 m depth, appears to be of low transmissivity. Also in this borehole the rock mass appears to be of low hydraulic conductivity. From the looks of Figure 3-3 and Figure 3-4 it appears reasonable to characterise the 'tectonic lens' as a sandwiched hydrogeological system consisting of HCDs of different transmissivity depending on dip (cf Figure 1-4). Outside (in between) the deformation zones there are HRDs of low hydraulic conductivity.

Fracture transmissivity data available for modelling determined with the Posiva Flow Log (PFL-f) exist for boreholes KFM01A–KFM05A. Figure 3-5 shows a BIPS image of a flowing fracture detected by the PFL-f tests.

In the core mapping, each fracture is classified as Sealed, Open or Partly Open and with a judgement of how certain the geologist is of this classification – expressed as Certain, Probable and Possible. Partly Open fractures refers to all fractures that do not cut the core entirely but have (1) altered or weathered fracture planes or are (2) associated with a measurable aperture in the borehole wall using BIPS to indicate an edge of a fracture. The number of Partly Open fractures is small but not negligible. Above all they demonstrate that the division of fractures into Open and Sealed is not a clear cut, nor is the definition of fracture frequency.

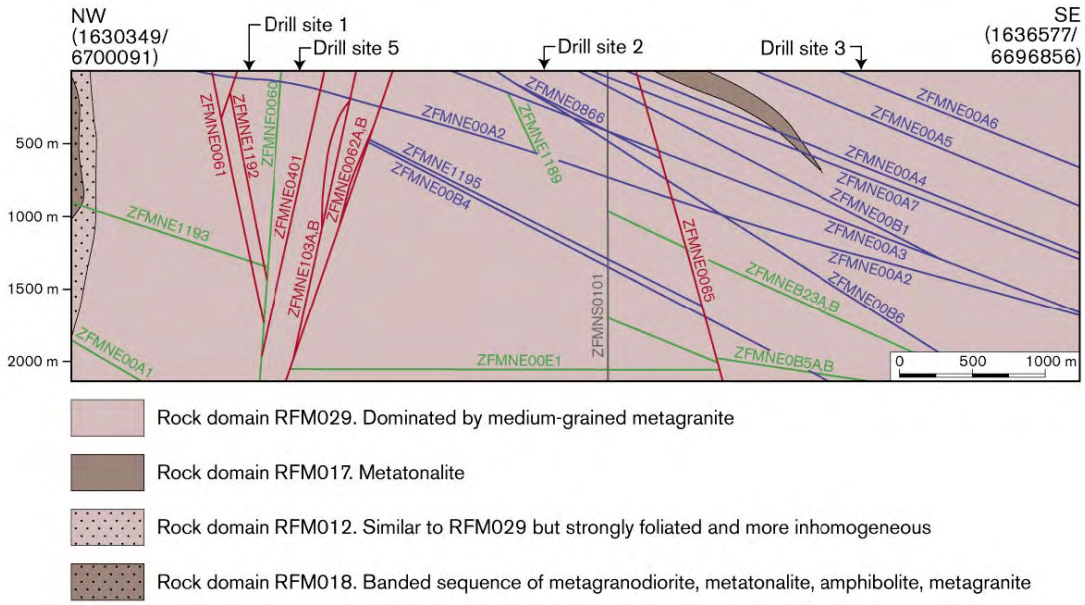

Figure 3-4. *NW-SE cross-section that passes close to the three boreholes KFM01A–KFM03A. The cross-section shows the steeply dipping deformation zones that strike north-east and the gently dipping zones that dip to the south-east and south. All these zones transect the candidate volume and are sandwiched between first and second order, vertical and steeply dipping deformation zones that strike WNW-NW. The zones coloured in red are vertical and steeply dipping zones with high confidence, the zones coloured in blue are gently dipping zones with high confidence, the zones coloured in green are medium confidence zones irrespective of their dip, and the zone coloured in grey is a vertical zone with low confidence /SKB 2005a/.*

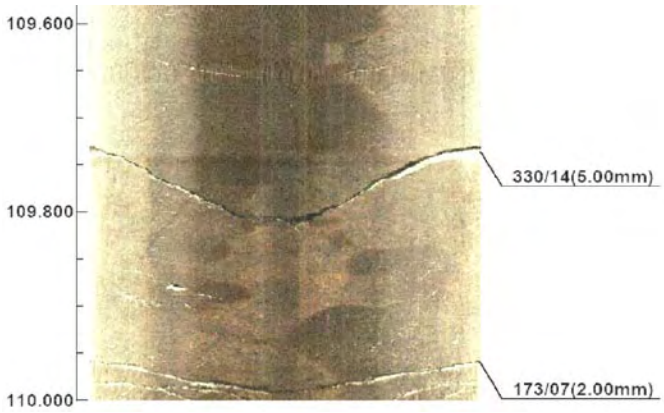

Figure 3-5. *BIPS image showing a borehole section in borehole KFM05A. The fracture in the centre is associated with a flow anomaly determined by the PFL-f tests.*

The identification of a flow anomaly is classified as Certain or Uncertain. Both the core mapped data and the flow anomalies are rigorously length corrected and it is expected that the positions of objects along the boreholes normally can be correlated to within 0.2–0.3 m.

/Forsman et al. 2004/ provide a joint interpretation of the PFL-f tests, the fracture data from the core mapping and the single-hole geological interpretations of rock domains and deformation zones. Figure 3-6 through Figure 3-10 show a compilation of their results. The classification of "flow indication Open fractures", or the PFL confidence, is defined as the distance between the anomaly and the interpreted fracture. That is, if the anomaly has a flow indication in Class 1, the interpreted fracture is within 1 dm from the anomaly. In the same way, the anomaly has the flow indication Class 2, if the interpreted fracture is within 2 dm from the anomaly. Four classes have been defined: Class 1: 0–1 dm; Class 2: 1–2 dm; Class 3: 2–3 dm; and Class 4: 3–4 dm.

As a first assumption all Open and Partly Open fractures as well as Crush Zones are assumed to be potential flowing fractures. In most cases, one or several Open fractures were identified within 0.2 m from a given flow anomaly. Only in a few cases could no Open fractures, Partly Open fractures or Crush Zones be linked to within 0.5 m of a flow anomaly, probably indicating that a fracture mapped as Sealed should have been classified as Open. In such cases one could generally find Sealed fractures classified as Probable or Possible and mapped as broken near the flow anomaly. Table 3-2 shows a compilation of the interpretation by /Forsman et al. 2004/.

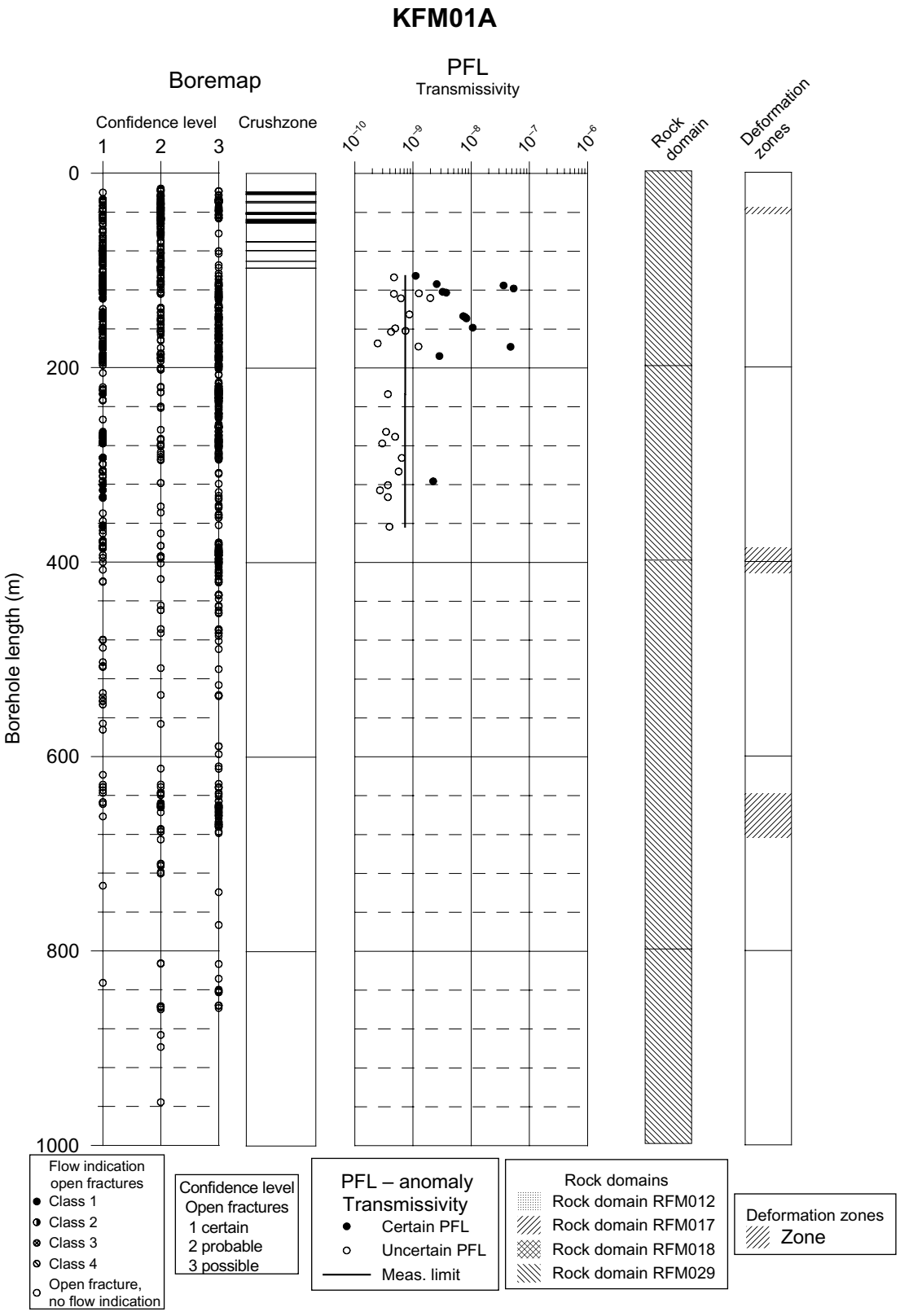

Figure 3-6. *Correlation of hydraulic fractures, based on PFL-f overlapping measurements, to mapped Open/Partly Open fractures (all plotted as Open fractures above) or crush zones. Interpreted deformation zones (mainly brittle or ductile) and rock domains shown to the right. Fractures with PFL confidence (flow indication class) > 4 are not plotted /Forsman et al. 2004/.*

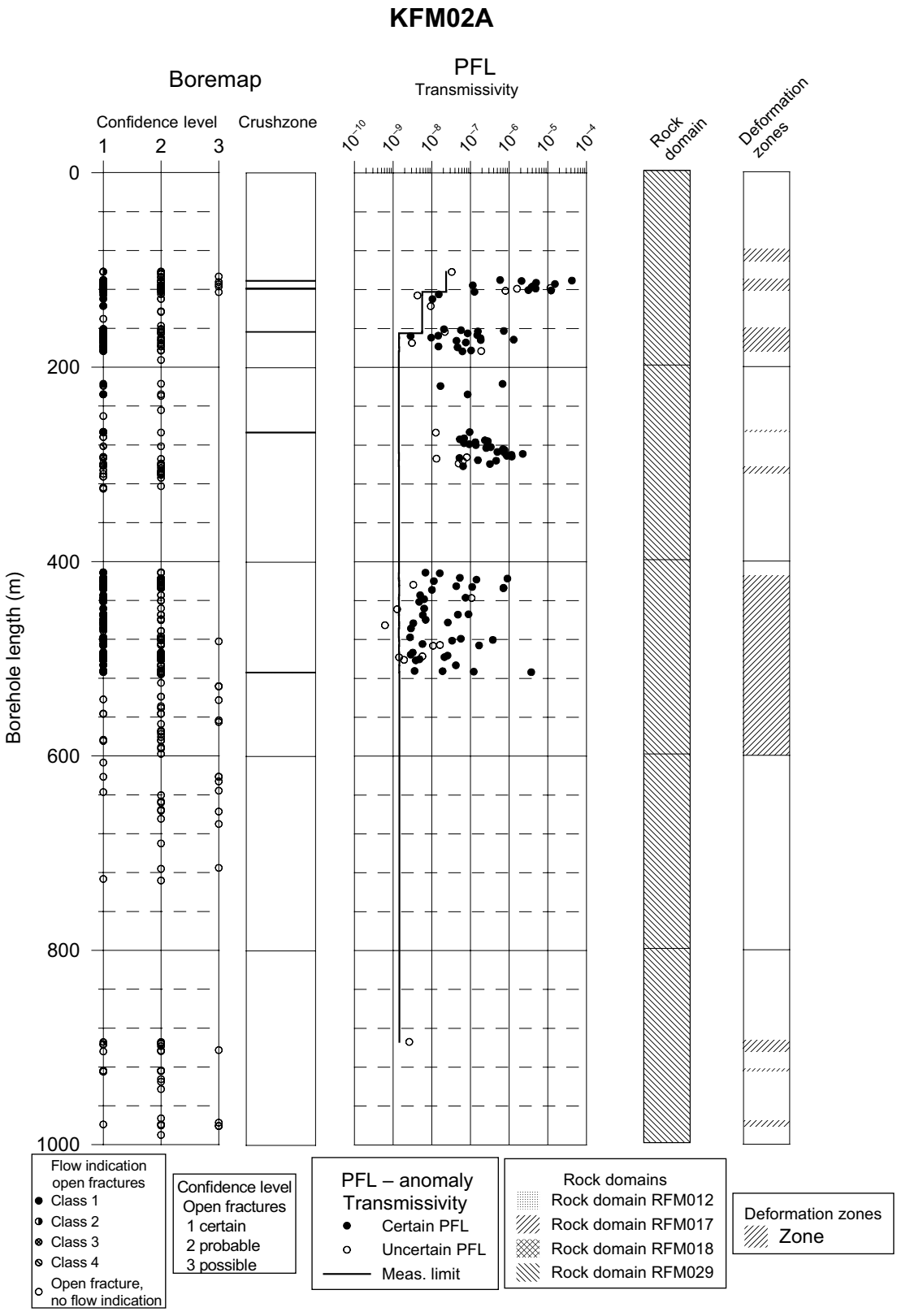

Figure 3-7. *Correlation of hydraulic fractures, based on PFL-f overlapping measurements, to mapped Open/Partly Open fractures (all plotted as Open fractures above) or crush zones. Interpreted deformation zones (mainly brittle or ductile) and rock domains shown to the right. Fractures with PFL confidence (flow indication class) > 4 are not plotted /Forsman et al. 2004/.*

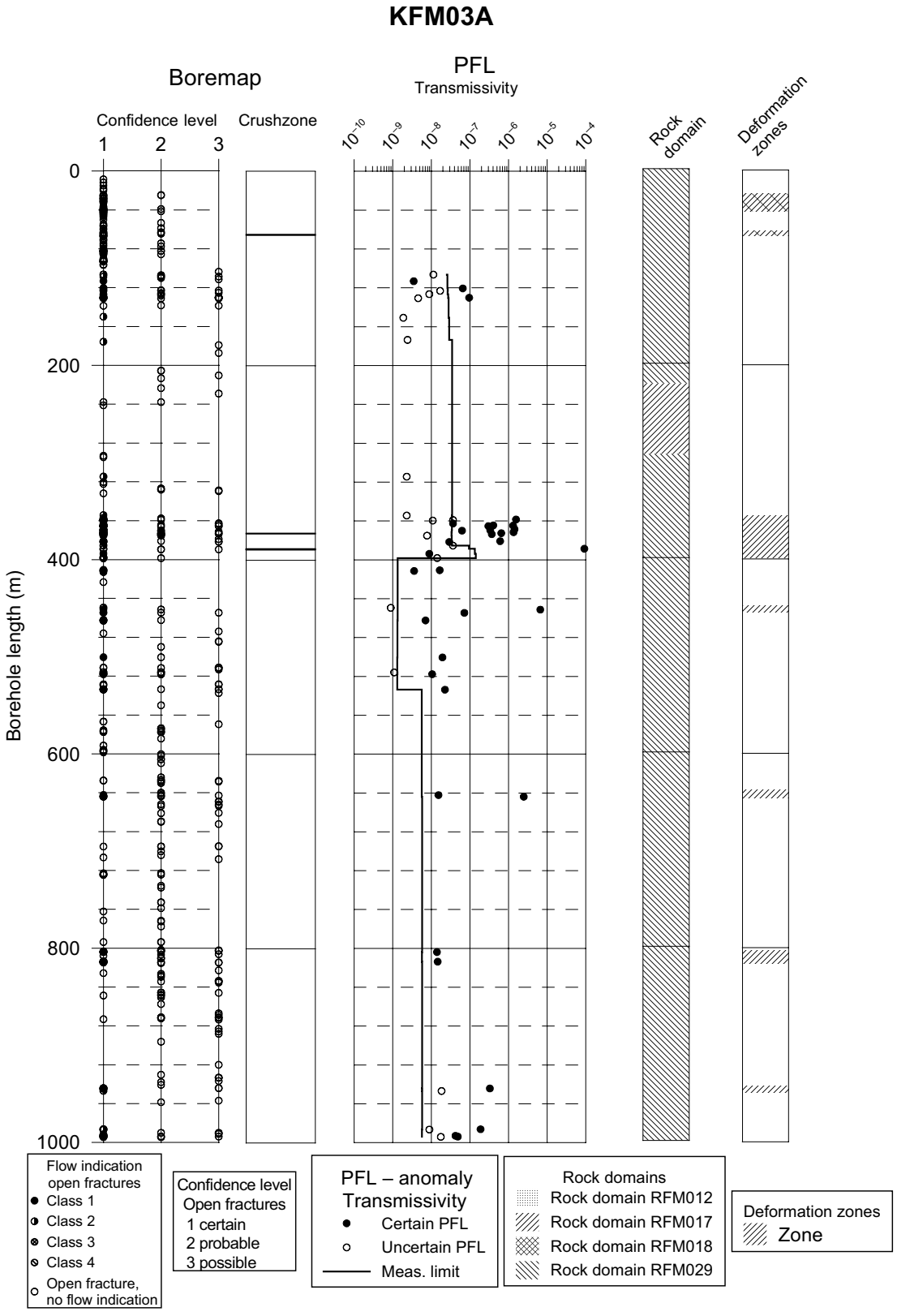

Figure 3-8. *Correlation of hydraulic fractures, based on PFL-f overlapping measurements, to mapped Open/Partly Open fractures (all plotted as Open fractures above) or crush zones. Interpreted deformation zones (mainly brittle or ductile) and rock domains shown to the right. Fractures with PFL confidence (flow indication class) > 4 are not plotted /Forsman et al. 2004/.*

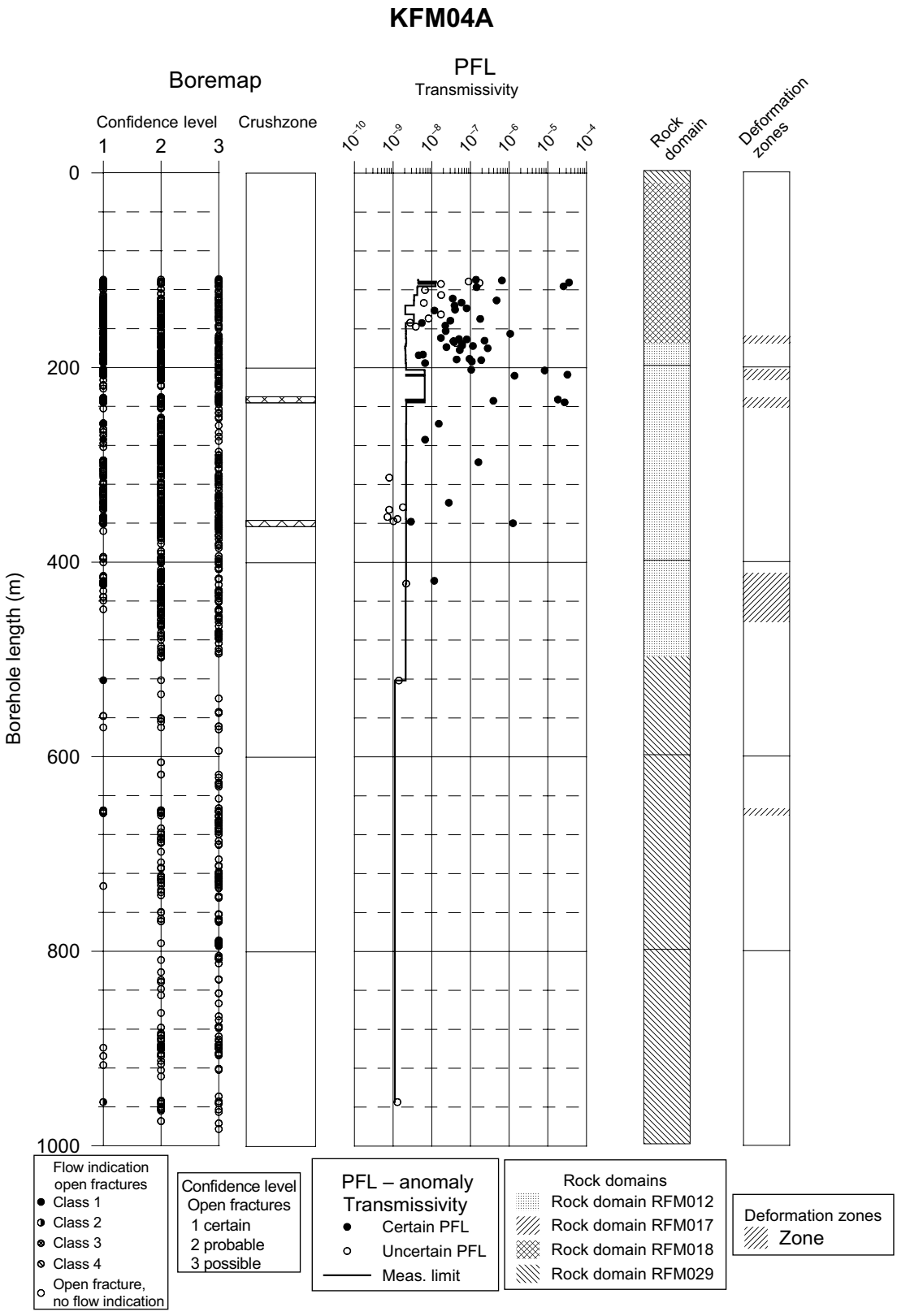

Figure 3-9. *Correlation of hydraulic fractures, based on PFL-f overlapping measurements, to mapped Open/Partly Open fractures (all plotted as Open fractures above) or crush zones. Interpreted deformation zones (mainly brittle or ductile) and rock domains shown to the right. Fractures with PFL confidence (flow indication class) > 4 are not plotted /Forsman et al. 2004/.*

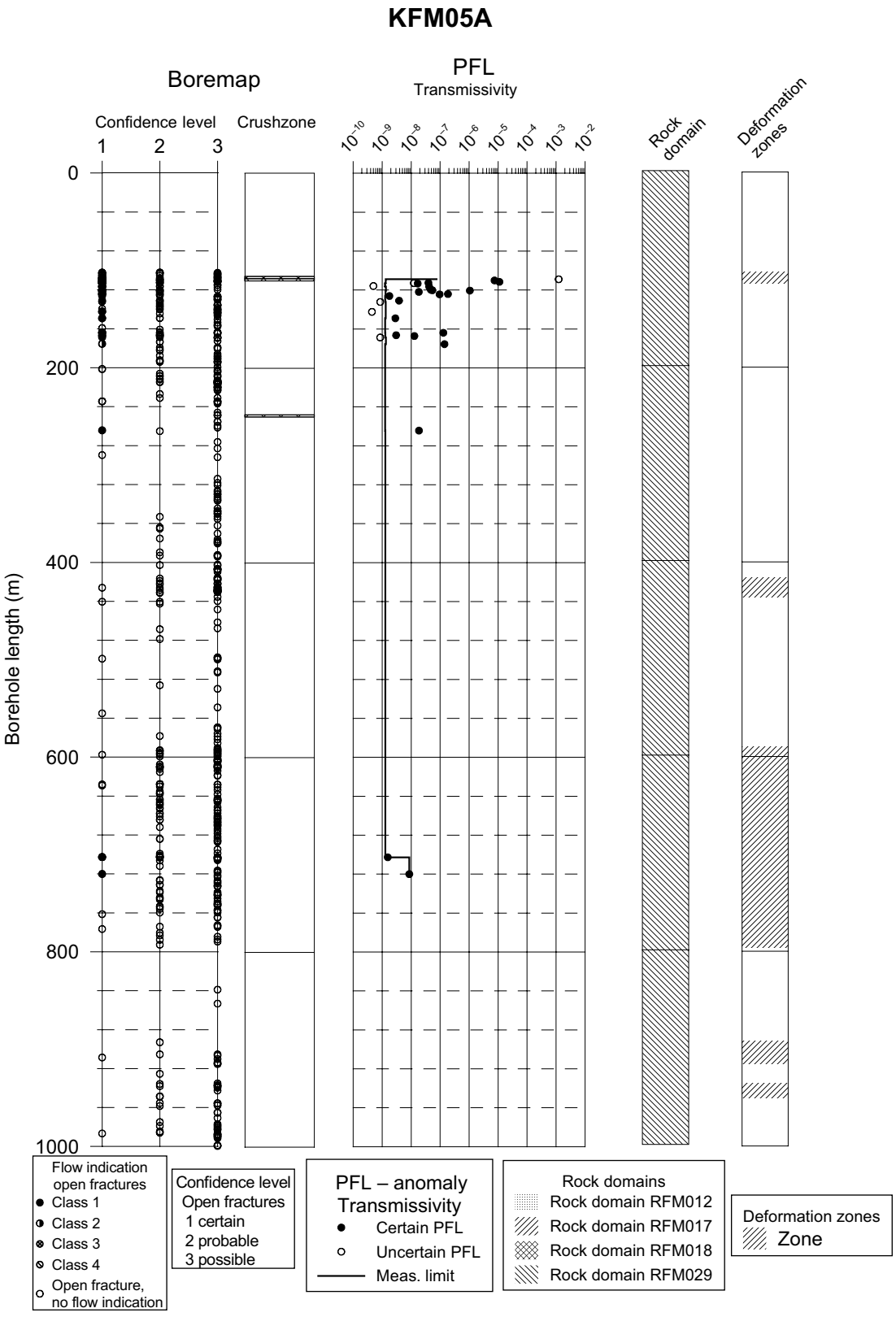

Figure 3-10. *Correlation of hydraulic fractures, based on PFL-f overlapping measurements, to mapped Open/Partly Open fractures (all plotted as Open fractures above) or crush zones. Interpreted deformation zones (mainly brittle or ductile) and rock domains shown to the right. Fractures with PFL confidence (flow indication class) > 4 are not plotted /Forsman et al. 2004/.*

Table 3-2. Compilation of the results obtained from a joint interpretation between PFL-f tests and Boremap data /Forsman et al. 2004/.

Object	KFM01A	KFM02A	KFM03A	KFM04A	KFM05A
Total no of PFL-f anomalies	34	125	52	71	27
No of PFL-f anomalies mapped as "Certain"	13	100	34	50	21
No of fractures identified with distance < 0.2 m from PFL-f anomaly	76	185	110	195	80
No of fractures identified with distance 0.2–0.4 m from PFL anomaly	5	7	2	9	0
No of fractures identified with distance 0.4–0.5 m from PFL-f anomaly	0	3	0	1	0
No of fractures identified with distance > 0.5 m from PFL-f anomaly	0	3	2	1	0
No of PFL-f anomalies not correlated to Open or Partly Open fractures	0	14	8	1	2
No of sealed fractures (broken/ unbroken) within a distance of 0.1 m from PFL-f anomalies not correlated to Open or Partly Open fractures	0/0	29/1	10/2	1/0	4/0

3.4 Joint interpretation between geology and hydrogeology

An integrated interpretation between the *base model* deformation zones and the hydraulic test results from the PFL and PSS tests is presented in Chapter 4. The PFL-f test transmissivity data not associated with the deterministically treated deformation zones have been the main input data for the HydroDFN analysis of the HRDs in the work reported here. The analysis is presented in Chapter 5.

4 Assessment of properties of the Hydraulic Conductor Domains

4.1 Modelling methodology

The approach used for model version 1.2 is to treat the HCDs as macroscopic three-dimensional fractures, the geometries of which are defined by geology and modelled in SKB's Rock Visualisation System , RVS /Curtis et al. 2004/. Complex shaped HCDs are triangulated before they are transferred to DarcyTools.

The hydraulic properties of the HCDs are based on single-hole hydraulic tests mainly. Data from cross-hole (interference) hydraulic tests are still very scarce at this stage. In conclusion, the site-specific data available for modelling consist of transmissivity T and hydraulic thickness b_{hyd} estimates, whereas general formulae are used for assigning equivalent parameter values of the storativity S, the transport aperture e_t and the kinematic porosity ε of the HCDs, cf Equations (2-1), (2-2) and (2-27). These formulae are taken from the findings reported in /Rhén et al. 1997, Rhén and Forsmark 2001, Andersson et al. 1998b, 2000, Dershowitz et al. 2003/. It is noted that the HCD storativity, transport aperture and kinematic porosity are all modelled as power-law functions of the HCD transmissivity.

4.2 Historic data and Data Freeze F1.2

Historic data available at the time of model version 0 provide transmissivities for about seven of the 44 HCDs forming the Base Case (and Variant Case). The corresponding figure for model version 1.1 is twelve, i.e. seven plus five. In comparison, model version 1.2 treats data for all together 28 HCDs. The difference in hydraulic information between model versions 1.1 and 1.2 is illustrated in Figure 4-1 and Figure 4-2. These figures show a perspective view of the regional model domain together with the 44 HCDs that constitute the *base model* of model version 1.2. The deformation zones are visualised as translucent shades. Red shades indicate steeply dipping HCDs that are hydraulically tested, and blue shades indicate gently dipping HCDs that are hydraulically tested. White shades indicate HCDs not tested hydraulically.

Table 4-1 shows a compilation of the transmissivities of intercepted deformation zones deduced from a joint interpretation of the single-hole tests and deformation zones. The reference P-report for each hydraulic test is given together with an indicator about the deformation zone dip, **S** for steeply dipping and **G** for gently dipping. There are 14 of each kind. It is noted that some of the deformation zones have two or more hydraulic test interpretations associated to them. For instance, deformation zone ZFMNE00A2 has 13 hydraulic test interpretations associated to it in model version 1.2.

The interference tests conducted between HFM01 and HFM02 /Ludvigson and Jönsson 2003/ and between HFM11 and HFM12 /Jönsson et al. 2004/ provide hydraulic data of two of the deformation zones ZFMNE00A2 and ZFMNW003A. The transmissivity values deduced from the interference tests are in accordance with the values reported from the single testing of the corresponding boreholes, cf Table 4-1. and the deduced values of the storativity from the interference tests is c $5 \cdot 10^{-5}$ in both cases.

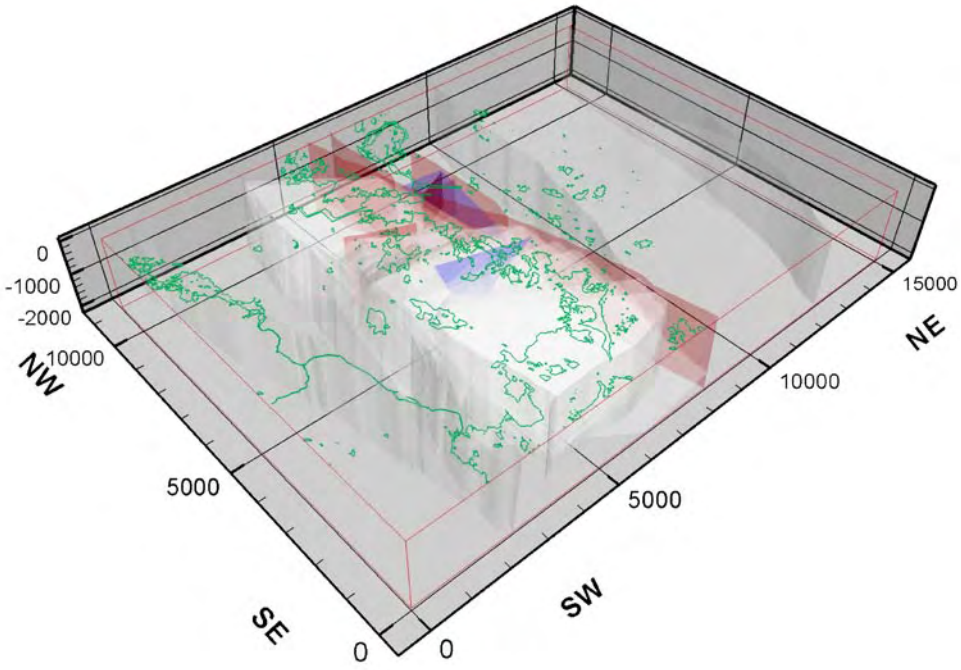

Figure 4-1. *Perspective view of the regional model domain together with the 44 HCDs that form the model version 1.2 Base Case (shown as translucent shades). Red and blue shades represent HCDs hydraulically tested at the time of model version 1.1. Red shades are steeply dipping HCDs and blue shades are gently dipping HCDs. White shades indicate that the HCDs in question were not tested hydraulically.*

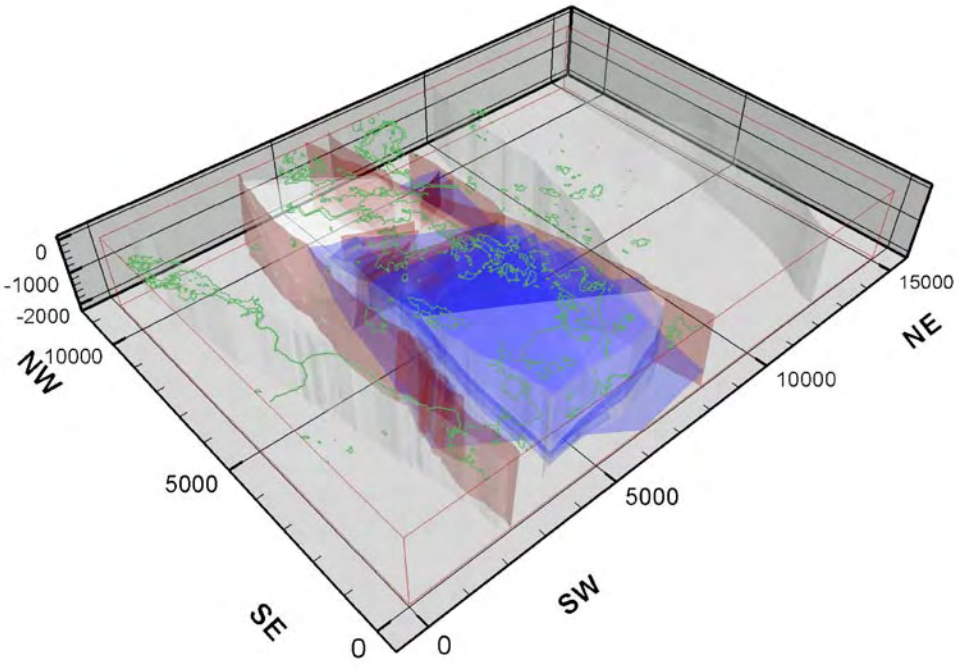

Figure 4-2. *Perspective view of the regional model domain together with the 44 HCDs that form the model version 1.2 Base Case (shown as translucent shades). Red and blue shades represent HCDs hydraulically tested at the time of model version 1.2. Red shades are steeply dipping HCDs and blue shades are gently dipping HCDs. White shades indicate that the HCDs in question were not tested hydraulically.*

Table 4-1. Compilation of the transmissivities and maximum geological thicknesses deduced from a joint interpretation of the single-hole tests and the single-hole deformation zone interpretation. The last column provides information about the deformation zone dip, S for steeply dipping and G for gently dipping. There are 14 deformation zones of each kind. Transmissivity values marked as "< 1.0E–09" indicate that the magnitude is less than the lower practical measurement limit of the PFL method as no flow was measured.

HISTORIC DATA

Borehole	ZFM#####	Elevation of centre (masl)	Maximum thickness (m)	T (m^2/s)	Reference	Category
SFR	ZFMNW0001	< –100	30	2.4E–05	R-02-14	S
SFR	ZFMNW0002	< –100	30	2.4E–05	R-02-14	S
SFR	ZFMNW0805	< –100	10	8.0E–06	R-02-14	G
SFR	ZFMNE0869	< –100	7	2.0E–05	R-02-14	S
SFR	ZFMNE0870	< –100	5	2.0E–07	R-02-14	S
SFR	ZFMNE0871	< –100	10	2.0E–06	R-02-14	S
DBT1	ZFMNE1193	–319	6	> 1.0E–05	R-02-32	G

DATA FROM F1.1 AND F1.2 PERCUSSION-DRILLED BOREHOLES

Borehole	ZFM#####	Elevation of centre (masl)	Maximum thickness (m)	T (m^2/s)	Reference	Category
HFM01	ZFMNE00A2	–36	8	4.5E–05	P-03-33	G
HFM02	ZFMNE00A2	–44	5	5.9E–04	P-03-33	G
HFM04	ZFMNE0866	–62	3	7.9E–05	P-03-34	G
HFM04	ZFMNE00B6	–184	4	2.4E–05	P-03-34	G
HFM05	ZFMNE0866	–153	1	4.0E–04	P-03-34	G
HFM06	ZFMNE00A5	–66	10	1.8E–04	P-03-36	G
HFM08	ZFMNE00A5	–138	5	1.2E–03	P-03-36	G
HFM09	ZFMNE1187	–22	9	3.3E–04	P-04-74	G
HFM10	ZFMNE1187	–104	8	3.1E–04	P-04-74	G
HFM11	ZFMNW003A	–92	58	3.0E–05	P-04-64	S
HFM12	ZFMNW003A	–98	60	7.8E–06	P-04-64	S
HFM13	ZFMNE0401	–145	12	2.9E–04	P-04-71	S
HFM14	ZFMNE00A2	–62	7	1.5E–03	P-04-71	G
HFM15	ZFMNE00A2	–63	7	1.0E–04	P-04-71	G
HFM16	ZFMNE00A2	–41	59	5.0E–04	P-04-72	G
HFM18	ZFMNE00A4	–36	11	1.6E–04	P-04-72	G
HFM18	ZFMNE0065 ZFMNE00A7	–114	25	2.0E–05	P-04-72	G G
HFM19	ZFMNE00A2	–114	23	1.6E–05	P-04-72	G
HFM19	ZFMNE00A2	–150	14	2.8E–04	P-04-72	G

Table 4-1 (contin) Compilation of the transmissivities and maximum geological thicknesses deduced from a joint interpretation of the single-hole tests and the single-hole deformation zone interpretation. The last column provides information about the deformation zone dip, S for steeply dipping and G for gently dipping. There are 14 deformation zones of each kind. Transmissivity values marked as "< 1.0E–09" indicate that the magnitude is less than the lower practical measurement limit of the PFL method as no flow was measured.

F1.1 AND F1.2 CORE-DRILLED BOREHOLES

Borehole	ZFM#####	Elevation of centre (masl)	Maximum thickness (m)	T (m^2/s)	Reference	Dip
KFM01A	ZFMNE00A2	–42	12	2.3E–03	P-03-33	G
KFM01A	ZFMNE1192	–398	26	3.2E–09	P-04-95	S
KFM01A	ZFMNE0061	–660	45	< 1.0E–09	P-04-95	S
KFM02A	ZFMNE0866	–85	12	4.0E–04	P-03-34	G
KFM02A	ZFMNE00B6	–116	12	1.1E–04	P-04-188	G
KFM02A	ZFMNE00A3	–171	24	3.5E–06	P-04-188	G
KFM02A	ZFMNE1189	–306	7	1.3E–06	P-04-100 P-04-188	S
KFM02A	ZFMNE00A2	–466	105	7.8E–06	P-04-100 P-04-188	G
KFM02A	ZFMNE1195	–896	12	2.6E–09	P-04-188	G
KFM02A	ZFMNE00B4	–976	6	< 1.0E–09	P-04-100	G
KFM03A	ZFMNE00A4	–376	43	1.0E–04	P-04-189	G
KFM03A	ZFMNE00A7	–450	7	6.7E–06	P-04-189 P-04-194	G
KFM03A	ZFMNE00B1	–640	8	2.5E–06	P-04-189 P-04-194	G
KFM03A	ZFMNE00A3	–807	13	2.9E–08	P-04-189 P-04-194	G
KFM03B	ZFMNE00A5	–33	18	1.4E–05	P-04-278	G
KFM04A	ZFMNE00A2	–132	5	5.0E–07	P-04-190	G
KFM04A	ZFMNE00A2	–159	8	4.2E–05	P-04-190 P-04-293	G
KFM04A	ZFMNE00A2	–182	8	5.0E–05	P-04-190 P-04-293	G
KFM04A	ZFMNE1188	–335	38	1.4E–08	P-04-190 P-04-293	S
KFM04A	ZFMNE1188	–504	5	1.0E–09	P-04-293	S
KFM05A	ZFMNE00A2	–83	9	1.3E–03	P-04-191	G
KFM05A	ZFMNE0401	–326	15	< 1.0E–09	P-04-191	S
KFM05A	ZFMNE103A ZFMNE103B	–531	158	1.0E–08	P-04-191	S S
KFM05A	ZFMNE062B	–693	24	< 1.0E–09	P-04-191	S
KFM05A	ZFMNE062A	–722	14	< 1.0E–09	P-04-191	S

Figure 1-4 shows a scatter plot of the data in Table 4-1 excluding the historic data. The values are coloured with regards to the general dip of the deformation zones; red squares for steeply dipping and blue for gently dipping. Blue squares with a yellow infilling refer to the hydraulic test interpretations associated to the gently dipping deformation zone ZFMNE00A2. Transmissivity values marked as "< 1.0E–09" in Table 4-1 indicate that the actual value is less than the lower practical measurement limit of the PFL method, i.e. no flow was measured. Thus, the actual values may be lower than indicated in Figure 1-4.

The two data sets – gently and steeply dipping – show different tendencies for a depth trend, where the transmissivities of the steeply dipping set appears to decrease with a higher rate. (Impermeable deformation zones are assigned a transmissivity value of $1 \cdot 10^{-9}$ m²/s in Figure 4-3.) It is noted that the body of the steeply dipping deformation zones are striking NE, which mean that they are orientated perpendicular against the principal horizontal stress. The tentative trends fitted in Figure 4-3 are used as a means to characterise the information and do not prove that the deformation zones become impervious at greater depth. There may be transmissive zones at various depths that deviate from the imprint of Figure 4-3. This is commented on in Chapter 5.

Still, Data Freeze 1.2 leaves a strong impression of a hydraulic contrast in transmissivity between steeply and dipping deformation zones. Close to ground surface the contrast appears to be less than at c 400 m depth, where the contrast is at least an order of magnitude, see Figure 4-3. However, the 13 hydraulic test interpretations associated with deformation zone ZFMNE00A2 in model version 1.2 suggest that the deformation zones may also be heterogeneous, which implies an uncertainty about the exact magnitude of the contrast and the usefulness of simple deterministic regression models.

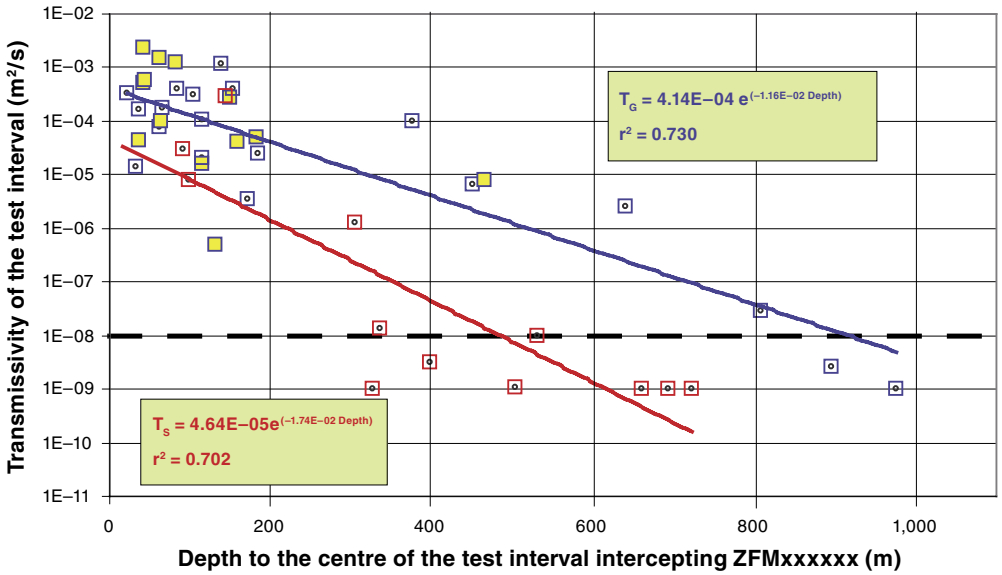

Figure 4-3. *Replicate of Figure 1-4 with the addition of two depth trends. Red squares indicate steeply dipping HCDs and blue gently dipping. Blue squares with a yellow infilling refer to the hydraulic test interpretations associated to the gently dipping deformation zone ZFMNE00A2. Impermeable deformation zones are assigned a transmissivity value of $1 \cdot 10^{-9}$ m²/s in Figure 4-3.*

4.3 Assignment of preliminary hydraulic properties

In order to handle the variability and complexity of the hydraulic information, three different cases, HCD1, HCD2 and HCD3, are treated in the work reported here. In HCD1, the initial approach, different deterministic spatial trends are assumed for the gently and steeply dipping deformation zones, see Figure 4-3:

$$T_G\ (Depth) = \max(4.1 \cdot 10^{-4}\ \exp(-0.0116\ Depth), 1 \cdot 10^{-8}) \qquad (4\text{-}1a)$$

$$T_S\ (Depth) = \max(4.6 \cdot 10^{-5}\ \exp(-0.0174\ Depth), 1 \cdot 10^{-8}) \qquad (4\text{-}1b)$$

Equations (4-1a) and (4-1b) are used for the 44 high confidence deformation zones that form the HCDs of the Base Case. For the additional 171 steeply dipping lineaments of low confidence as HCDs belonging to the Alternative Case the more transmissive Equation (4-1a) is used.

It should be noted that all deformation zones are assumed to be transmissive including the two deformation zones that bound the candidate area, the Eckarfjärden and Singö deformation zones, see Figure 1-3 and Figure 1-5. Moreover, both trends may be halted at $1 \cdot 10^{-8}$ m^2/s. This constraint prevents grid cells intersected by deformation zones at great depth to become less conductive than surrounding grid cells representing the hydraulic conductivity of the HRDs. However, the hydraulic conductivity of the HRDs is not homogeneous and in some cases the use of a lower limit of the deformation zone transmissivity of $1 \cdot 10^{-8}$ m^2/s is not consistent with field data and thus exaggerates the grid cell equivalent hydraulic conductivity.

A semi-homogeneous HCD2 case was applied to the Variant Case. A constant transmissivity value of $1 \cdot 10^{-5}$ m^2/s was assigned to the dominating deformation zones in the area, i.e. the steeply dipping regional deformation zones known as Forsmark (ZFMNE004A), Eckarfjärden (ZFMNE003A) and Singö (ZFMNE0001) deformations zones, plus four of the gently dipping local major deformation zones denoted by ZFMNE00A1, -A2, -C1 and -C2, respectively. (In the Variant Case the four gently dipping local major deformation zones are extended until they terminate against the Forsmark deformation zone, see Figure 1-2.) All other deformation zones were assigned depth trends in accordance to Equations (4-1a) and (4-1b).

Finally, a fully heterogeneous HCD3 case was applied to the Base Case. This case assumed a stochastic component on top of the deterministic trend. The transmissivity models of the fully heterogeneous case were:

$$T_{G,RD}\ (Depth) = \max(10^{\left\{\log\left[4.1 \cdot 10^{-4}\ \exp(-0.0116\ Depth)\right] + N[0,1][1.2(1-Depth/2{,}100)]\right\}}, 1 \cdot 10^{-8}) \qquad (4\text{-}2a)$$

$$T_{S,RD}\ (Depth) = \max(10^{\left\{\log\left[4.6 \cdot 10^{-5}\ \exp(-0.0174\ Depth)\right] + N[0,1][1.2(1-Depth/2{,}100)]\right\}}, 1 \cdot 10^{-8}) \qquad (4\text{-}2b)$$

where N(0,1) is a normally distributed random deviate (RD) with mean zero and standard deviation one. The magnitude of the standard deviation, 1.2, is chosen in consideration to previous results reported from the investigations in the Finnsjön area /Andersson et al. 1991/. This value reproduces the spread around the regression lines quite well.

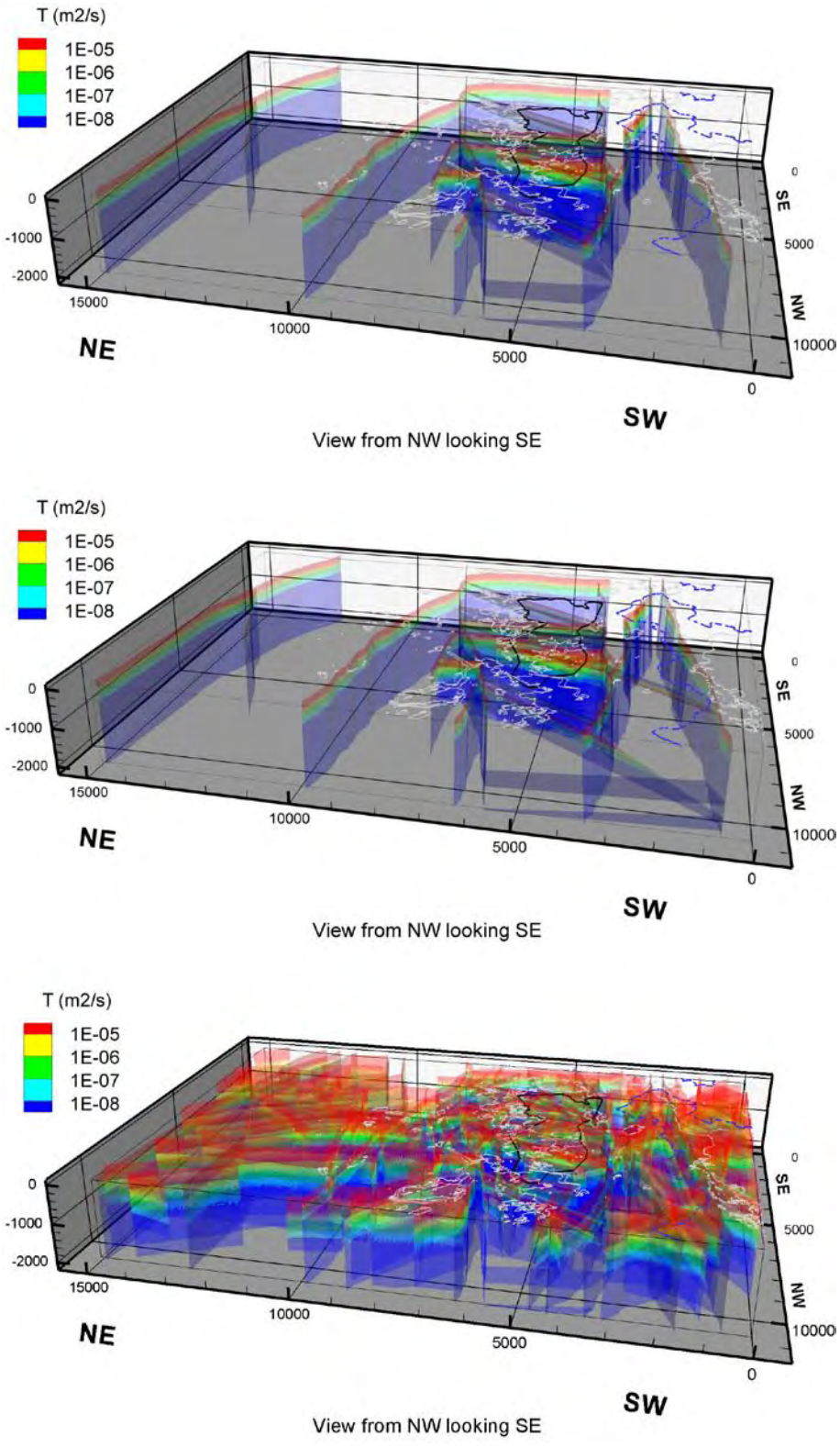

Figure 4-4. *Replicate of Figure 1-2 with the addition of transmissivity trends, see Equations (4-1a) and (4-1b). Top: The base model. Middle: The base variant model. Bottom: The alternative model.*

The thickness values shown in Table 4-1 represent the lengths of the intercepts of the deformation zones as estimated from the geological single-hole interpretations. Hence, the values constitute some kind of upper bound estimates of the geological thicknesses of the HCDs. More realistic geological thickness values are estimated from a correction for the deformation zone orientation and the borehole trend and plunge. Thickness values are of interest as they provide information about the hydraulic nature of the deformation zones (transmissivity divided by thickness yields the homogenised mean value of the hydraulic conductivity).

The deformation zone dip and thickness are important also for the choice of resolution of the computational grid used in the numerical simulations. Table 4-1 suggests that almost all of the gently dipping deformation zones are much less than 50 m thick. However, the thickness of the gently dipping deformation zone ZFMNE00A2 seems to vary a lot, which suggests that deformation zone thicknesses observed may be spatially varying. Based on historic data from the investigations of the SFR facility /Axelsson et al. 2002/ the hydraulic thickness b_{hyd} is generally considerably less than the geological thickness. The general assumption for model version 1.2 is that the mean hydraulic thickness is half the mean geological thickness.

Figure 4-5 shows a scatter plot of the mean geological thickness versus the deformation zone trace lengths. The data represent interpreted surface thicknesses of outcropping *base model* deformation zones. The tentative fit of the power-law regression is inserted to demonstrate the uncertainty of using a statistical model. The regression equation is of interest for the Alternative Case as there is no information available about the thickness of the lineaments modelled as low-confidence deformation zones. The mean value of the thickness to trace length ratio deduced by extrapolating the regression model to the size range 100–1,000 m is estimated to c 0.7%.

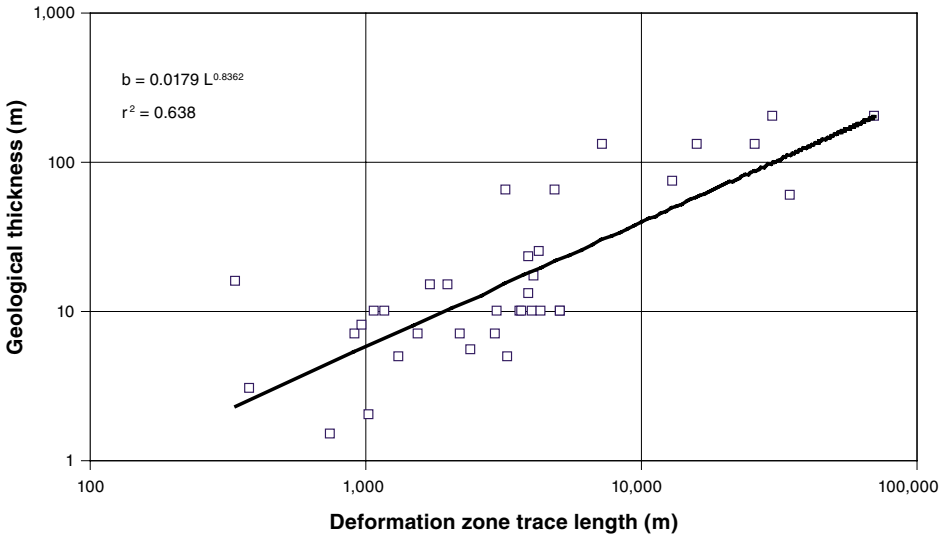

Figure 4-5. *Scatter plot of interpreted geological thicknesses versus interpreted lineament trace lengths for the base model. The mean value of the thickness to trace length ratio deduced by extrapolating the regression model to the size range 100–1,000 m is estimated to c 0.7%.*

5 Assessment of hydraulic properties of the Hydraulic Rock Domains

5.1 Modelling methodology

Hydraulic properties are assigned to the HRDs by hydrogeological DFN analyses. /La Pointe et al. 2005/ have provided a geological DFN (GeoDFN) model for the fracturing of the rock mass within RFM029, see Section 5.3. The model is based on lineament data, outcrop fracture data and cored borehole fracture data. For the hydrogeological modelling it is necessary to integrate the hydraulic borehole data presented in Chapter 3. In doing so, it is necessary to make some practical simplifications to derive a complete hydrogeological DFN (HydroDFN) fit for modelling. Having derived a HydroDFN, block-scale properties are required for regional groundwater flow property assignment, and also for repository design issues, cf Figure 2-2.

The hydrogeological DFN modelling carried out in the work presented here comprises four main steps:

1. Assessment of geological DFN data.
2. Assessment of hydrogeological DFN data.
3. Assessment of interconnected fracture intensity.
4. Assessment of parameter values for a correlated transmissivity model.

Step 1 covers an examination of the geological DFN and the geological single-hole interpretations followed by an analysis of the fracture properties and intensities as well as orientations within each deformation zone and each rock domain in the boreholes.

Step 2 includes an analysis of hydraulic data to obtain a representative value for each uncertain (stochastic) deformation zone treated as a part of the hydrological DFN model. The certain (deterministic) deformation zones are excluded from the analysis. A second component is to define the transmissivity distribution.

Step 3 aims at generating stochastic fracture models (realisations) that compare with the mapped orientations and borehole fracture frequencies of Open and Partly Open fractures in the core-drilled boreholes in RFM029. Once the measured geological intensity of intercepts is matched, the interconnected fracture surface area per unit volume of rock mass is determined by a connectivity analysis.

Step 4 aims at deriving parameter values for the correlated transmissivity model in Equation (2-11).

It is noted that the fourth step is a working hypothesis. Indeed, any transmissivity model can be brought into play, but a correlated model is considered the most intuitive and easiest to adopt without hydraulic simulations. The correlated transmissivity model is invoked by assuming that it is the largest interconnected fractures intercepting the borehole in each stochastic DFN realisation that correspond to the measured fracture transmissivities.

5.2 Assumptions

To derive a complete hydrogeological DFN (HydroDFN) fit for modelling it is necessary to make some practical simplifications. The basic concepts and assumptions used are outlined in this section.

5.2.1 Conductive fractures

All naturally Open and Partially Open fractures, regardless of their geological confidence (Certain, Probable and Possible), are considered to be potential candidates for flow from the onset in the connectivity analysis. Sealed fractures, on the other hand, were considered impervious. This simplification is due to the scale of the flow problem treated in model version 1.2. It is recognised to be incorrect on the scale of the fracture aperture, cf Section 5.2.2.

An Open fracture is by definition associated with a naturally broken core, i.e. the natural fracture is as large as or larger than the core diameter. Consequently, a Partly Open fracture is by definition a fracture that does not break the core, but still have some kind of aperture associated to it. According to the method description for core mapping /SKB 2002/, all Partly Open fractures are mapped to the extent possible. Partly Open and Open fractures are often treated alike as they both contribute to the concept of borehole fracture frequency (borehole fracture intensity) P_{10}.

According to the geological DFN model /La Pointe et al. 2005/, the borehole fracture intensity P_{10} associated with Partly Open fractures in RFM029 is c 8% of the total P_{10} of Open and Partly Open fractures in this rock domain. Recognising the conceptual difficulties associated with the mapping of Partly Open fractures and the relatively large number of Partly Open fractures seen in the cored boreholes it is obvious that the fracture mapping procedures and the techniques used to simulate and condition borehole fracture intercepts have to be consistent. This becomes even more important as c 9% of the PFL flow anomalies may be associated with what are mapped as Partly Open fractures, see /Forsman et al. 2004/.

5.2.2 Flow in conductive fractures

Conductive fractures are assumed to be completely flat surfaces with homogenous macroscopic hydraulic properties, i.e. transmissivity T_f and storativity S_f. In case of heterogeneous fracture properties, equivalent homogeneous (effective) values are considered. In reality, the flow is distributed through channels across the fracture plane. Possibly, also intersections between fractures can be considered as potential channels. The physical channels are formed by the undulating fracture surfaces (spatial distribution of the fracture asperity) that do not exactly match, thus creating channels. The distribution of flow channels is, however, governed by the acting boundary conditions, which may be transient. The flow channels in the fracture plane occupy only a minor part of the fracture volume, and parts of the fracture surface are closed due to its undulating nature.

Exchange of solutes to stagnant pools of water, outside the flow channels, is governed by diffusion in more or less free water, which is faster than the diffusive exchange with the rock matrix. It can also be expected that parts of the fracture are filled with fault gauge material, i.e. fine-grained, clayey material, cf Figure 2-3. All these characteristics cannot, and need not always, be modelled in detail, but must be approximated in some way. For the diffusion processes, DarcyTools uses a multi-rate diffusion model.

5.2.3 Stochastic deformation zones as single conductive fractures

Large fractures of trace lengths on the order of 100 m may exist as single breaks. However, it is more common that discontinuities of trace lengths greater than about 50 m exist as deformation zones or 'fracture swarms'. A number of fracture swarms are observed in the boreholes. Some of the swarms are treated (modelled) as deterministic deformation zones, other as uncertain, i.e. stochastic. Hence, it is useful to characterise these fractures to get some indication of the width and fracture intensities within these zones. However, at this regional modelling stage, fracture swarms interpreted as certain or uncertain deformation zones will be approximated as large fracture planes in a continuous range of fracture sizes, as shown in Figure 5-1. It is important that data, such as fracture intensity and the PFL-f flow anomalies, are handled in a manner consistent with this concept. Also, transport parameters, such as fracture porosity and flow-wetted surface, may have to be enhanced in the larger fractures to reflect their zonal properties.

Figure 5-1 implies that the fracturing within a deformation zone is not studied in terms of its components, but treated as a single object. Both stochastic and deterministic deformation zones are treated in this way.

If N_{TOT} is the total number of Open and Partly Open fractures in a borehole and N_{DZ} is the number of Open and Partly Open fractures in an intercepted stochastic deformation zone, the remaining number of potentially flowing Open and Partly Open fractures in the borehole to be matched in the modelling process N_{CAL} may be written as:

$$N_{CAL} = N_{TOT} - \sum (N_{DZ} - 1) \qquad (5\text{-}1)$$

The summation in Equation (5-1) is made over all intercepted stochastic deformation zones. The subtraction by 1 is made as the zone itself is one fracture to be included in the modelling process. This is found to be important in cases where the rock is sparsely fractured.

In analogy with Equation (5-1) the transmissivity of a potentially flowing stochastic deformation zone is considered equal to its geological thickness-hydraulic conductivity product and the storativity is equal to its geological thickness-specific storativity product. This implies that the transmissivity of a stochastic deformation zone, as determined at its intersection with a borehole, is equal to the sum of the transmissivities of the flowing fractures:

$$T_{DZ} = \sum (T_f) \qquad (5\text{-}2)$$

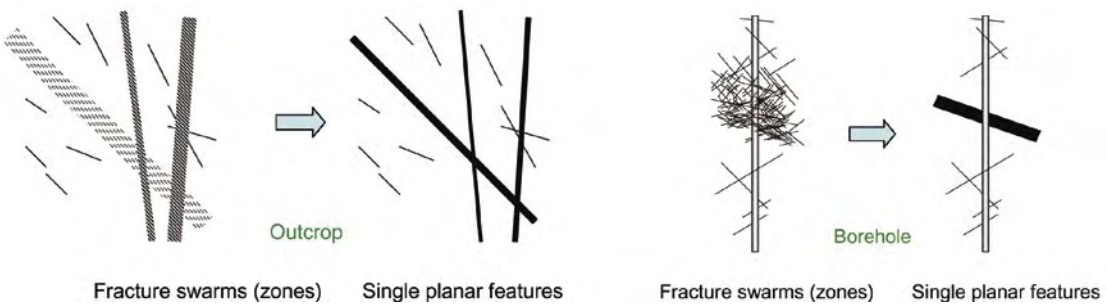

Figure 5-1. *An important assumption in the hydrogeological DFN analysis is the representation of fracture swarms (zones) as single planar fractures.*

The summation in Equation (5-2) is made over all PFL-f anomalies belonging to the intercepted stochastic deformation zone. In case of heterogeneous deformation zone properties, equivalent homogeneous values are considered. It is noted that Equation (5-2) may overestimate the deformation zone transmissivity T_{DZ} if the flowing fractures intersecting the borehole merge at some distance away from the borehole. The similarity in results between the aforementioned test methods, the difference flow logging (PFL) and the double-packer injection tests (PSS), does not suggest that this may be a major problem, however.

5.2.4 Size distribution of conductive fractures

One of the most difficult fracture characteristics to measure directly in the subsurface is fracture size. Fracture trace lengths can be measured on outcrops for fractures on the scale of centimetres to several metres, and data are available for lineaments on the scale of 500 m to several kilometres, but this leaves a gap between the scales. A widely used assumption in geology is one of a continuum of fractures that spans all scales and that can be described by a power-law relationship between fracture intensity and size, see Figure 5-2.

Figure 5-2 illustrates the conceptual relationship between the deterministically treated deformation zones and the stochastic geological DFN. It is noted that fracture shapes are modelled as squares in DarcyTools with a side length L, whereas fracture shapes are modelled as circles of radius r in the geological DFN model. The equivalent radius r of a square of size L is shown in Equation (2-3).

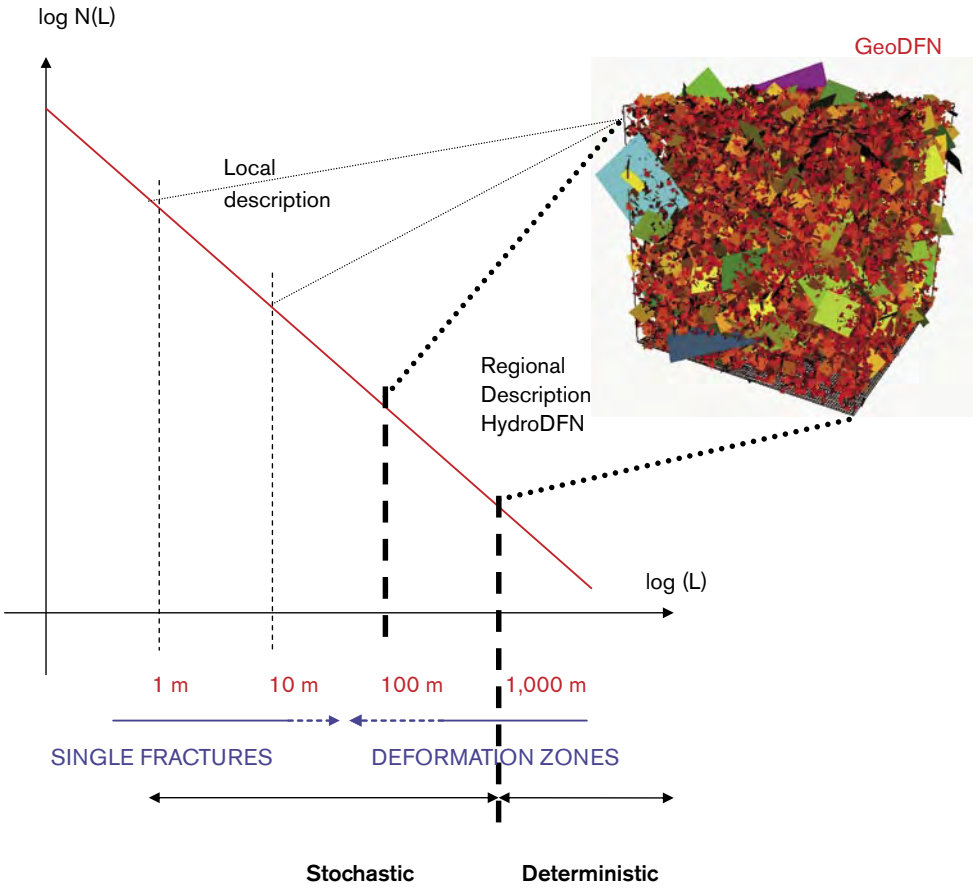

Figure 5-2. *Illustration of the power-law size distribution and the conceptual relationship between deterministically treated deformation zones and the stochastic geological DFN.*

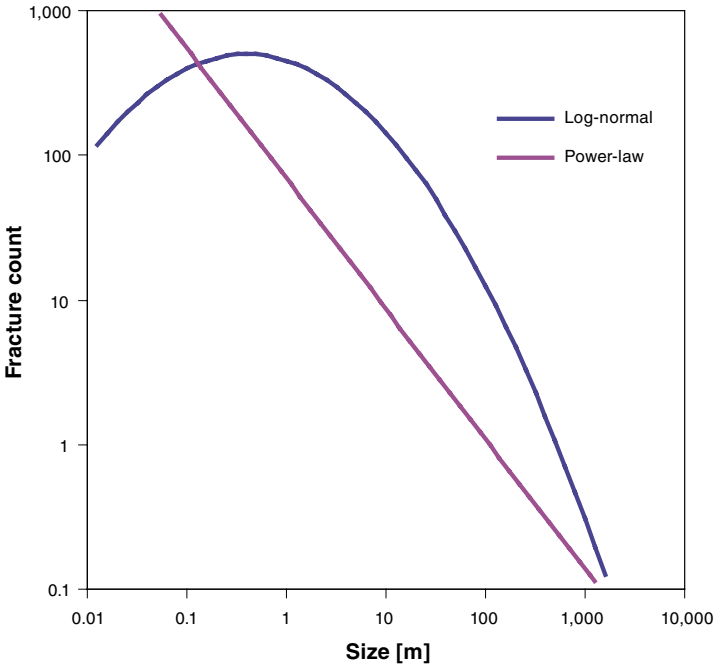

Figure 5-3. *Example of a power-law and a log-normal fracture size distribution. When a fracture network is simulated, it is often necessary for practical reasons to truncate the distributions and use data between a lower and upper limit. Modified after /Hartley et al. 2004/.*

Another commonly used model for fracture size is the log-normal distribution. The two distributions are schematically illustrated in Figure 5-3. One obvious difference between a power-law model and a log-normal model is in the lower end where the log-normal size distribution approaches zero for small sizes. However, fracture trace length data are often biased due by censoring an truncation which in fact may a power-law size distribution look as if it was log-normal.

5.2.5 Reference size of conductive fractures

The key parameters of the power-law relationship providing the number of fractures of different sizes are the slope k_r and the fracture intensity α (cf Equation (2-11)). The slope k_r may be estimated from a complementary cumulative density function plot (CCDF) of fracture trace lengths, see Section 2.3. The estimation of the intensity can theoretically be made from outcrop trace length data after normalisation of the frequencies observed by the outcrop surface area. In practice, however, the determination of intensity is a much more difficult task as the numbers of fractures increase significantly for a power-law distribution when the sizes of fractures get smaller. Observations of fracture trace lengths on outcrops down to 0.5 m can generally be mapped, whereas shorter fractures become quite cumbersome to map. The issue is not trivial as large fracture sizes may also produce small trace lengths. Moreover, 95% of the area in the central part is covered by Quaternary deposits, which means that

It is important to note that the rock mass fracturing at ground surface often differs significantly from that seen in core-drilled boreholes at depth. In general, the fracture intensity decreases towards depth. For this reason we assume in the work reported here that the desired fracture intensity is better represented by the observed variations in the borehole fracture frequency. The working hypothesis tested in the work reported here is:

All Open and Partly Open fractures seen in a cored borehole are assumed to cross-cut the borehole diameter, i.e. P_{10} ($r > r_w$), i.e. frequency of partially intersecting fracture is not included in the fracture frequency. This implies that for $r_0 > r_w$, r_0 needs to be assessed to achieve a statistical matching of simulated versus observed fracture frequency.

The sensitivity of this assumption is explored for the following cases:

1. $r_0 = r_w$: The radius of a cored borehole is 0.038 m. The equivalent size of square is 0.067 m.
2. $r_0 > r_w$: The assumption tested here is a reference radius of 0.282 m, i.e. an equivalent square of 0.5 m.

For a given value of the fracture surface area per unit volume P_{32} it is vital to note that the statistical matching of simulated versus observed borehole fracture frequencies is insensitive to the chosen value of the reference size r_0 provided that the borehole is treated as a scanline, i.e. $r_w = 0$. If the borehole used for the statistical matching is simulated as a cylinder with a finite radius, i.e. $r_w > 0$, a portion of all fractures intersecting the perimeter of the cylinder will not intersect the scanline, i.e. the centre line of the borehole. In effect, it is necessary to reduce the fracture surface area per unit volume to retain the match to the observed borehole fracture frequency. However, this raises pertinent concerns about the procedures used for fracture mapping and simulation of Partly Open fractures, as these may not necessarily intersect the scan line (the centre of the borehole diameter). The sensitivity to the borehole radius in this study is commented on below.

5.2.6 Transmissivity of conductive fractures

An important topic concerns the relationship between the transmissivities of conductive fractures and the transmissivities deduced from hydraulic single-hole tests. The 5 m PFL-s and the PSS tests generally comprise a lot more fractures within each test section than 0.1 m PFL-f tests. This suggests that the latter kind of testing is much more suitable for a discrete statistical analysis.

Transmissivity data from single-hole tests often show a wide range of variability and it is common to use statistical distributions for the fracture transmissivity assignment, e.g. the power-law distribution or the log-normal distribution. Figure 5-4 shows an example where PFL-f transmissivity data outside the deterministically treated deformation zones in borehole KFM03A are plotted in a complementary cumulative density function plot (CCDF) and in a log-normal cumulative density function plot (CDF), respectively. The straight lines fitted indicate the level by which data above the lower measurement limit conform to the tested distributions.

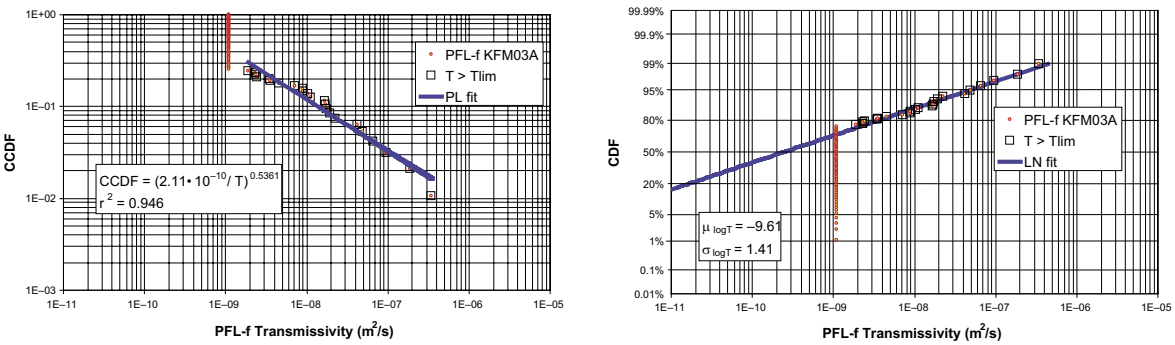

Figure 5-4. *Example of a power-law fit and a log-normal fit of PFL-f transmissivity data. The data in the plot come from the rock between the deformation zones in KFM03A.*

The statistical assignment of transmissivity to discrete fractures can be made in different fashions, e.g.

1. Transmissivity T is uncorrelated to fracture radius r by a specified normal variability of mean $\mu_{\log10(T)}$ and standard deviation $\sigma_{\log10(T)}$:

   $$T = 10^{N(\mu,\sigma)} \qquad (5\text{-}3a)$$

2. Transmissivity is correlated to fracture radius by a factor a and an exponent b,

   $$T = a\, r^{b} \qquad (5\text{-}3b)$$

3. Transmissivity is semi-correlated to fracture radius by a factor a, an exponent b and a standard deviation $\sigma_{\log10(T)}$:

   $$T = 10^{\left[\log_{10}(a\, r^{b}) + \sigma\, N(0,1)\right]} \qquad (5\text{-}3c)$$

The three relationships in Equations (5-3a) through (5-3c) are illustrated in Figure 5-5.

From a hydraulic perspective one can advocate that a correlated model is logical. This comes from the consideration that hydraulic tests have different scales of support, i.e. radius of influence. A hydraulic test in a fracture of high transmissivity implies a large radius of influence and vice versa. If the physical radius (size) of the high transmissive fracture is less than its theoretical hydraulic radius of influence, the hydraulic test will sensor this limitation as a physical boundary and in effect a lower transmissivity may be interpreted if the "boundary" is constraining the flow.

Another argument for it is that, at least for deformation zones, the zone width often increases with size (cf Figure 4-5), and thus generally so does the number of individual conductive fractures associated with a zone (cf Figure 5-1). If the transmissivity distribution for individual fractures is the same, then based on the above assumption it follows that the effective transmissivity for the deformation zone should increase with the size of the fracture zone.

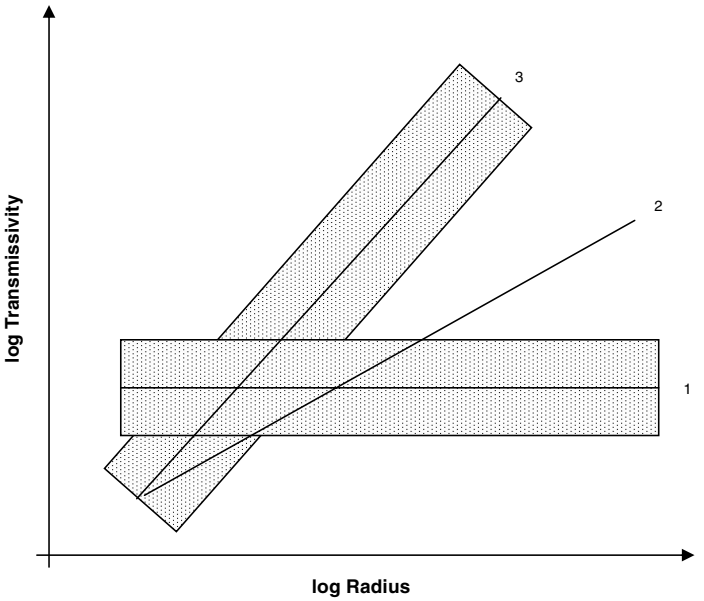

Figure 5-5. *Schematic of three statistical transmissivity models: 1) Uncorrelated with a specified uncertainty; 2) Correlated; 3) Semi-correlated, i.e. correlated with a specified uncertainty.*

These arguments are the primary motives for assuming that is the largest interconnected fractures intercepting the borehole in each stochastic DFN realisation that correspond to the measured fracture transmissivities.

5.2.7 Connectivity of conductive fractures

The behaviour seen in Figure 5-4 is characteristic for flow in sparsely fractured rocks. There is great heterogeneity and it is generally quite difficult to discriminate between a power-law fit versus a log-normal fit because of the substantial amount of data below the lower measurement limit.

The most transmissive of the potentially flowing Open and Partially Open fractures are assumed to be detected by the Posiva Flow Log:

$$N_{PFL} \leq N_{CAL} \tag{5-4}$$

N_{PFL} refers to the number of PFL-f flow anomalies above the lower measurement limit and N_{CAL} is the number of potentially conductive features as defined in Equation (5-1). An important component of the connectivity-based approach used in the work reported here is the determination of N_{CON}, i.e. the geometrically connected feature intensity. N_{CON} is determined by sorting out all isolated features and isolated clusters of features. The intuitive relationship between N_{PFL}, N_{CON}, N_{CAL} and N_{TOT} becomes:

$$N_{PFL} \leq N_{CON} \leq N_{CAL} \leq N_{TOT} \tag{5-5}$$

The probabilistic framework between the simulated connected feature intensity and the interpreted transmissivities is illustrated in Figure 5-6.

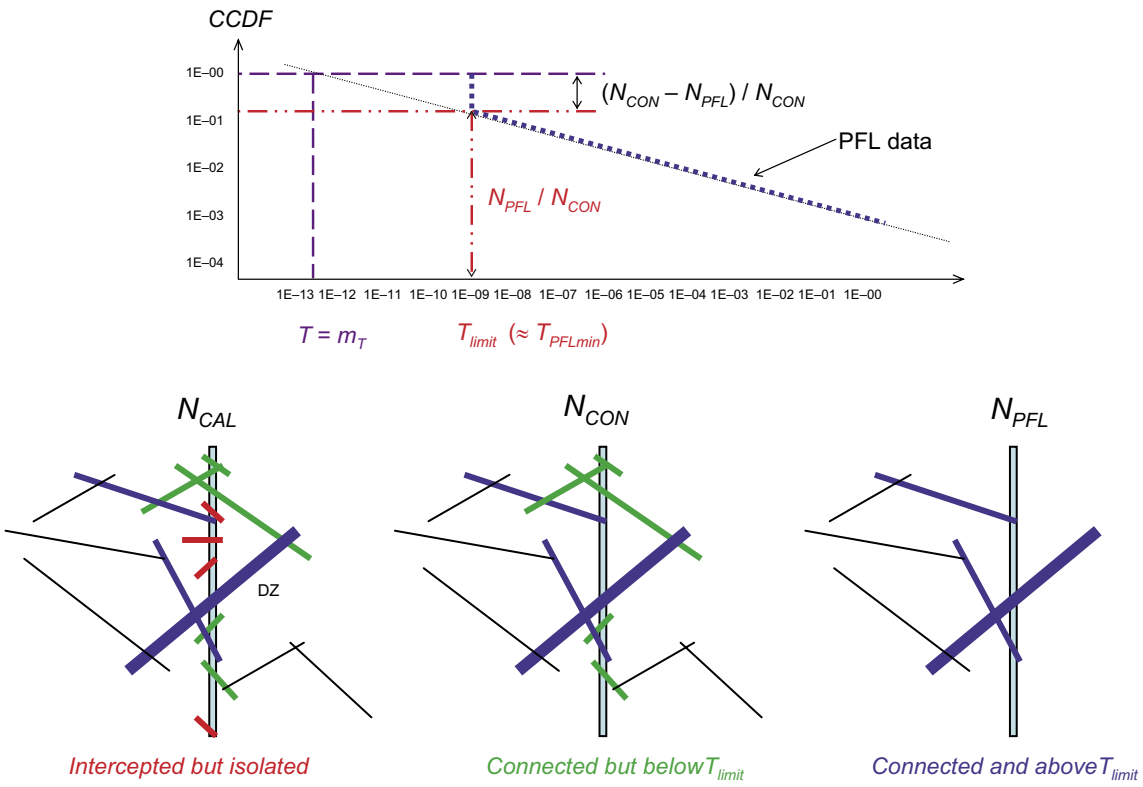

Figure 5-6. *Top: Illustration showing how the CCDF plot of the measured fracture transmissivities is used together with information about $N_{PFL} \leq N_{CON} \leq N_{CAL} \leq N_{TOT}$. Bottom: Illustration showing the definitions of N_{CAL}, N_{CON} and N_{PFL}.*

5.2.8 Spatial distribution of conductive fractures

The spatial pattern of *all* fractures in the rock mass outside the deformation zones is assumed to be Poissonian in the geological DFN, see Section 5.3. The discrimination of isolated features in a Poissonian simulation model leads to a connected network of features that become more and more governed by the positions of the largest features. The resulting spatial pattern of the connected Open and Partly Open fracture network may be different from Poissonian.

5.2.9 Intensity correction of conductive features

To mitigate against under-predicting the intensity of fractures sub-parallel to the borehole trajectories it is common practice to use analytical or numerical correction methods. The Terzaghi correction method /Terzaghi 1965/ is applied in the work reported here as it provides a rapid means for correcting all sets simultaneously. The correction is used as a weighting when calculating the percentage of fractures in each orientation set $P_{10,corr}$. That is, rather than just counting the number of fractures in each set, a weighted percentage is calculated by weighting each fracture by $1/\cos(\vartheta)$, where ϑ is the angle between the pole to the fracture plane and the borehole trajectory. A maximum weight of 7 for $\vartheta \approx 90°$ is used based on previous experiences.

The Terzaghi method is an approximation, e.g. it does not take fracture size into account. The implications of this approximation is discussed by /Davy et al. in press, Darcel et al. 2004/. The general experience, however, is that the computed $P_{10,corr}$ values provide a good first guess of the desired three dimensional fracture intensity P_{32}.

5.2.10 Block size properties

The main modelling assumptions are:

1. The hydraulic conductivity in the rock mass is governed by the connected fracture system and can be modelled by the DFN concept.
2. Flow within fractures can be approximated by Darcy's law.
3. Fracture transmissivity can be described by a correlated model as envisaged by Equations (2-10) and (5-3b).
4. Fracture transport aperture is correlated to fracture transmissivity as envisaged by Equation (2-2).
5. The heterogeneity between grid blocks on a specified scale can be modelled by calculating the hydraulic conductivity of an array of sub-blocks within a much larger domain and use this as an ensemble.

5.3 Assessment of geological DFN data

Figure 5-7 through Figure 5-11 show an overview of Open and Partly Open fractures in the rock mass outside the deterministically treated deformation zones. The left insets show the stereo nets of the fracture poles and the right insets show the cumulative fraction of fractures versus elevation. The two types of plots demonstrate the sparse fracturing of rock domain RFM029 between the deformation zones and three dominating fracture sets; northeast NE, northwest NW and horizontal HZ.

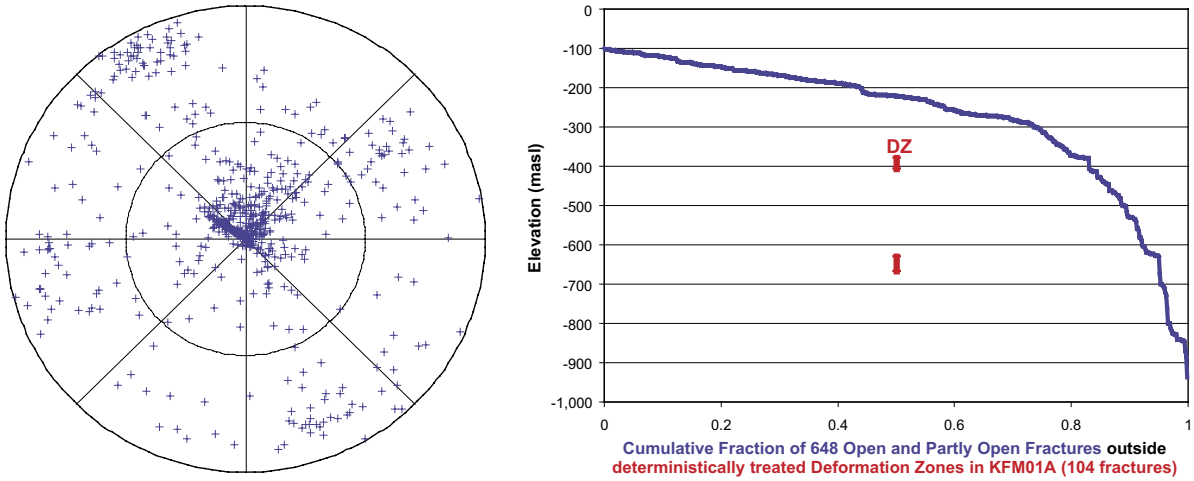

Figure 5-7. *Overview of 648 Open and Partly Open fractures outside the intercepted deformation zones in KFM01A. Left: Stereo net of fracture poles (trend and plunge). Right: Cumulative fraction of Open and Partly Open fractures versus elevation. KFM01A holds two deformation zones below c –100 masl in base model version 1.2.*

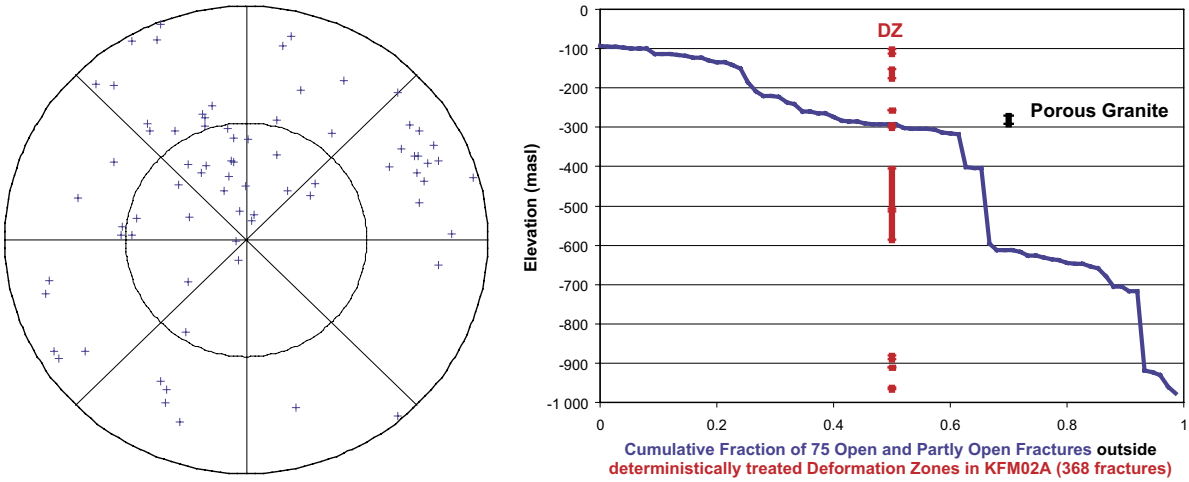

Figure 5-8. *Overview of 75 Open and Partly Open fractures outside the intercepted deformation zones in KFM02A. Left: Stereo net of fracture poles (trend and plunge). Right: Cumulative fraction of Open and Partly Open fractures versus elevation. KFM02A holds nine deformation zones below c –100 masl in base model version 1.2.*

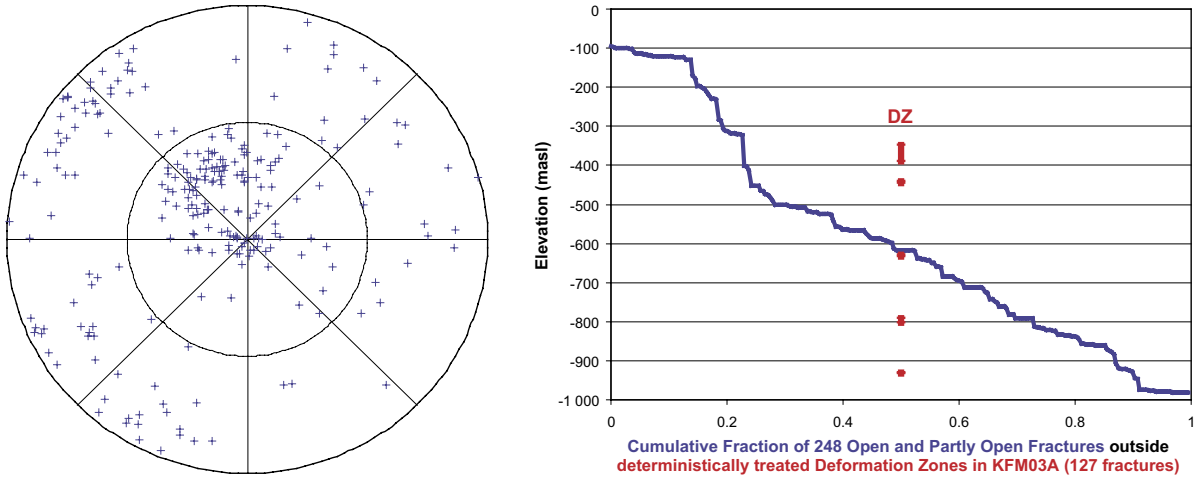

Figure 5-9. *Overview of 248 Open and Partly Open fractures outside the intercepted deformation zones in KFM03A. Left: Stereo net of fracture poles (trend and plunge). Right: Cumulative fraction of Open and Partly Open fractures versus elevation. KFM03A holds five deformation zones below c –100 masl in base model version 1.2.*

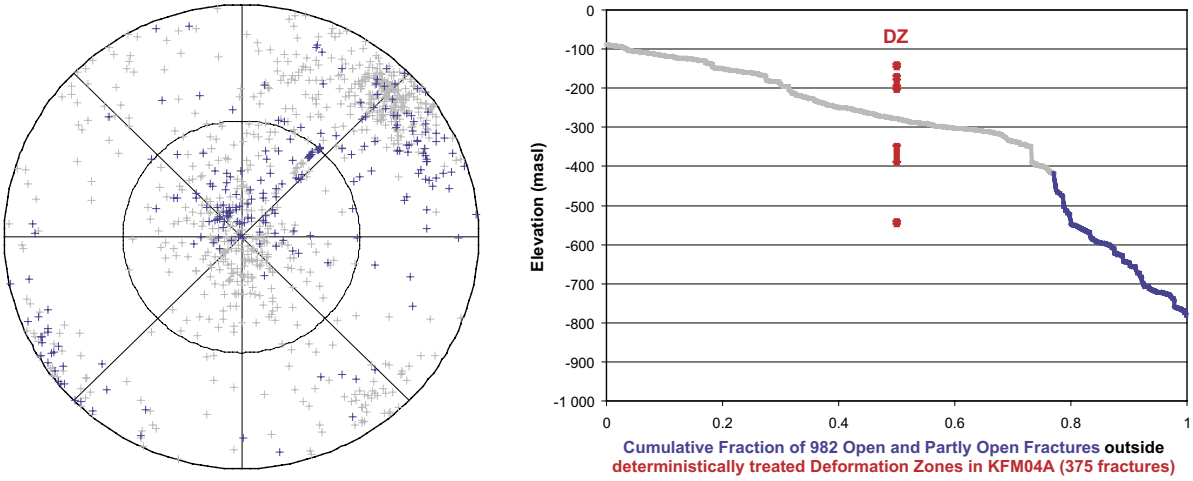

Figure 5-10. *Overview of 982 Open and Partly Open fractures outside the intercepted deformation zones in KFM04A. Left: Stereo net of fracture poles (trend and plunge). Right: Cumulative fraction of Open and Partly Open fractures versus elevation. Fracture data inside the candidate area and RFM029 are in blue colour. KFM04A holds five deformation zones below –90 masl in base model version 1.2, one of which is encountered below c –430 masl in RFM029.*

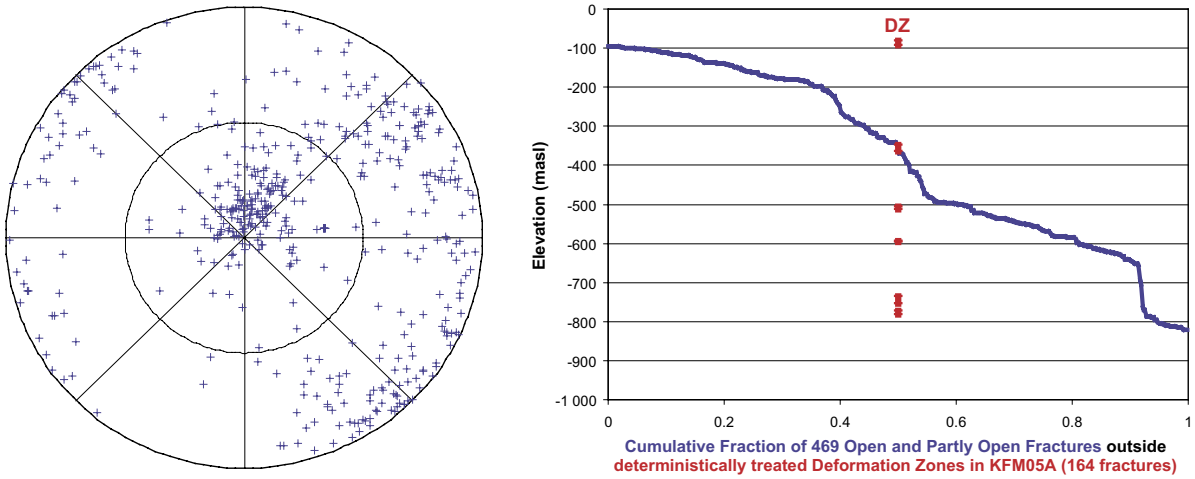

Figure 5-11. *Overview of 469 Open and Partly Open fractures outside the intercepted deformation zones in KFM05A. Left: Stereo net of fracture poles (trend and plunge). Right: Cumulative fraction of Open and Partly Open fractures versus elevation. KFM05A holds six deformation zones below c –90 masl in base model version 1.2.*

Table 5-1 presents the geological DFN for RFM029 provided by /La Pointe et al. 2005/. The motive for using the Univariate Fisher distribution for the orientation of the NS and NE fracture sets in the work reported here instead of the main alternative for these sets – the Bivariate Fisher and the Bivariate Bingham distributions, respectively – is twofold: (i) the practical differences are found to be small, and (ii) the Univariate Fisher distribution is simpler to generate. Vis-à-vis the assumptions of Poisson distributed fracture centres and the assumption of power-law distributed fracture sizes, the uncertainties in the details of the orientation model are of second order significance. The most important component of the orientation model is to get relative proportions between the identified steeply and gently dipping fracture sets fairly correct.

Figure 5-12 displays the borders between the five fracture sets of the geological DFN in an equal angle projection stereo net. The hard sector division between the gently dipping fracture set HZ and the four steeply dipping fracture sets NS, NE, NW and EW is c 50°.

Table 5-1. Compilation of DFN parameter settings for rock domain RFM029. The following probability distributions are applied: Univariate Fisher distribution for fracture orientation (Trend, Plunge, Kappa (concentration)), Poisson distribution for the fracture centre points and Power-law distribution for fracture size and intensity (k_r, r_0, P_{32}) /La Pointe et al. 2005/.

Set	Trend	Plunge	Kappa	k_r	r_0	$P_{32}(r > r_0)$ *	Rel P_{32}
NS	87.2	1.7	21.66	2.88	0.28	0.13	11%
NE	135.2	2.7	21.54	3.02	0.25	0.51	42%
NW	40.6	2.2	23.90	2.81	0.14	0.17	14%
EW	190.4	0.7	30.63	2.95	0.15	0.05	4%
HZ	342.9	80.3	8.18	2.92	0.25	0.35	29%
					Sum	1.21	100%

* The P_{32} values refer to Open and Partly Open fractures for the given values of k_r and r_0.

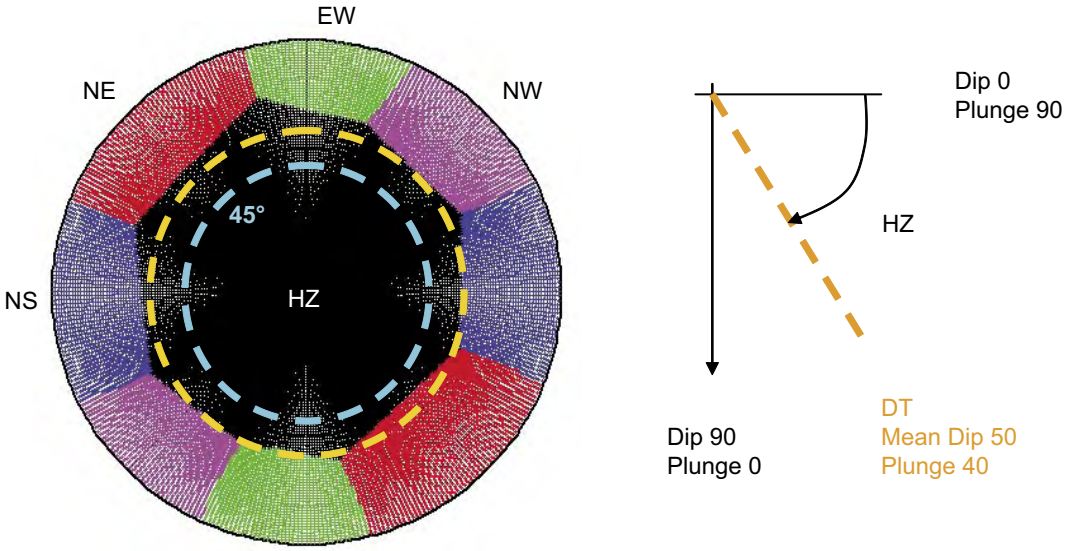

Figure 5-12. *Equal-angle projection of the five fracture sets of the geological DFN. The hard sector division between the gently dipping fracture set and the four steeply dipping fracture sets is c 50° (dashed orange line). The set probability of a randomly chosen fracture is given by the relative proportions between the fracture sets, see Table 5-1.*

The data in Table 5-1 is used to cross-validate the computer code used for generating discrete fracture networks in the work reported here against the computer code used for the derivation of the geological DFN. The two codes are found to yield consistent results for a common setup of model parameters. However, it is observed that the mean borehole fracture intensity P_{10} of the global geological DFN decreases by 30%, from 0.67 m^{-1} to 0.47 m^{-1}, if a scanline is used in the numerical simulations instead of a finite borehole radius. Hence, the statistical matching of simulated intensities against measured is very sensitive to the assumption about the borehole radius. This is due to the steep slopes of the power-law size distributions. In the work reported here we treat all core-drilled boreholes as scanlines in the statistical matching against measured data. In contrast, /La Pointe et al. 2005/ tacitly assumed a finite borehole radius of 0.038 m in their analyses (J Hermanson, personal communication, May 2005).

The geological DFN does not allow for a description of the intra-domain heterogeneity of RFM029. This is because all borehole data and outcrop data outside the deformation zones were pooled to form data sets useful for a description of the inter-domain heterogeneity only.

The consequences of using a global geological DFN model for the hydrogeological DFN analysis are many. A vital example of concern is shown in Figure 5-13. The aforementioned mean borehole fracture intensity P_{10} of the global geological DFN is plotted as a dashed line in Figure 5-13 together with a moving average of all Open and Partly Open fractures between the deformation zones in KFM01A–KFM05A. Figure 5-13 indicates that the geological DFN predicts fairly well the overall borehole fracture intensity between 400–600 m depth, but underestimates the borehole fracture intensity between 0–200 m depth by a factor of 3 and the borehole fracture intensity between 200–400 m depth by a factor of 2.

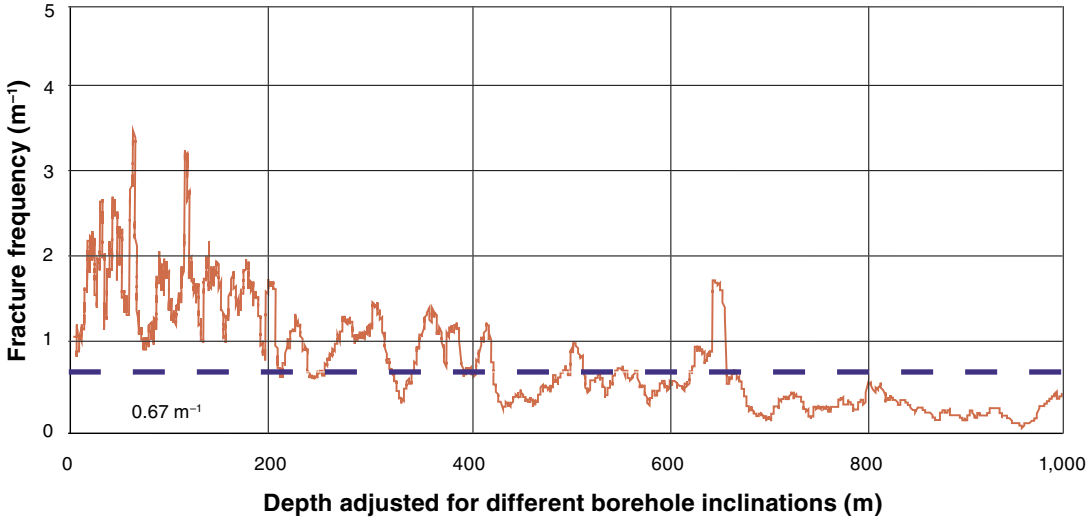

Figure 5-13. *Moving average of all Open and Partly Open fractures between the deformation zones in KFM01A–KFM05A. The blue dashed line indicates the predicted mean borehole fracture intensity of the global geological DFN.*

Another matter of concern is the censoring of the fracture statistics due to the borehole trajectories. To mitigate against under-predicting the intensity of fractures sub-parallel to the borehole trajectories it is common practice to use the Terzaghi correction method, cf Section 5.2.9. Table 5-2 demonstrates the effect for two intervals in KFM01A. The relative proportions between steeply and gently dipping fracture in both intervals are significantly altered as a result of the Terzaghi correction. The Terzaghi corrected relative proportions $P_{10,corr}$ indicate that there are considerably more gently dipping fractures in the uppermost interval, 103–222 m, compared to the relative intensity proportions of the geological DFN, see Table 5-1.

About 85% of the observed PFL-f anomalies in each interval can be associated with gently dipping fractures. Moreover, the mean dip of the flowing gently dipping fractures is c 15° with a coefficient of variation of c 0.6. This suggests that the transmissivity data seen in the upper part of KFM01A, 103–363 m, is to be associated with the horizontal fracturing mainly and that the body of the transmissivities of the steeply dipping fractures probably fall below the lower measurement limit. (A pertinent concern for bias is if the PFL-f method is appropriate for measuring the transmissivity of steeply-dipping fractures. These fractures have a lower probability of intersecting, bur when the intersect they have a larger zone of intercept, which in fact can be larger than the spacing of PFL-f measurements.)

The sum of the P_{10corr} values indicates the three-dimensional fracture intensity (fracture surface area per unit volume) P_{32} needed in numerical simulations in order to reproduce the measured borehole fracture frequencies P_{10}. However, the Terzaghi correction is an approximate correction only, e.g. it does not take differences in the size distributions into account and the scaling exponents k_r of the five fracture sets vary a lot, from 2.81 to 3.02. This variability in k_r means that the relative intensity proportions between the sets at are not fixed but dependent on the fracture size, see Equation (2-8).

Table 5-2. Demonstration of the effect of Terzaghi correction for two length intervals in KFM01A. The Terzaghi correction makes no consideration to the size distribution.

Fracture set	No of intercepts	P_{10} (m^{-1})	Rel P_{10} (%)	No of Terzaghi corr intercepts	P_{10corr} (m^{-1})	Rel P_{10corr} (%)
Interval: 103–222 m						
NS	16	0.13	5.1	55	0.46	11.0
NE	35	0.29	11.4	115	0.97	23.0
NW	13	0.11	4.3	34	0.29	6.8
EW	8	0.07	2.7	28	0.24	5.6
HZ	232	1.95	76.5	267	2.23	53.5
	304	2.55	100.0	499	4.19	100.0
		Steeply dipping:	23%		Steeply dipping:	46%
		Gently dipping:	77%		Gently dipping:	54%
Interval: 222–363 m						
NS	12	0.09	6.0	52	0.37	9.2
NE	50	0.35	23.5	315	2.23	55.8
NW	5	0.04	2.7	15	0.11	2.7
EW	3	0.02	1.3	14	0.10	2.5
HZ	140	0.99	66.4	169	1.20	29.9
	210	1.49	100.0	565	4.01	100.0
		Steeply dipping:	34%		Steeply dipping:	70%
		Gently dipping:	66%		Gently dipping:	30%

A third matter of concern is the values of the scaling exponents k_r. The values shown in Table 5-1 are all greater than the scaling exponent value of 2.70 reported in the recent lineament study of northern Uppland for the SKB project SR 97 by /La Pointe et al. 1999/. A possible explanation to the reported difference in the scaling exponent values is the type of data considered. /La Pointe et al. 1999/ treated predominantly regional lineaments of historic origin in their analysis, whereas /La Pointe et al. 2005/ treat local outcrop data and lineaments derived from the site investigations.

To test the hypothesis if the reported difference in the scaling exponents is due to the size of the area/data analysed the scaling exponent of the *alternative model* is evaluated (cf Section 1.3). Figure 5-14 shows the trace map of the *alternative model* and Figure 5-15 shows a complementary cumulative density plot of the alternative model.

The size of trace lengths used for the power-law fit in Figure 5.15 range from 1.7 to 4.4 km. By choosing an intermediate leg of trace lengths away from the tails tentative disturbances such as censoring and truncation of very short and very large trace lengths, respectively, are avoided. If all trace lengths are incorporated in the slope of the power-law fit decreases significantly.

The fitted slope in Figure 5-15 renders a scaling exponent of 2.75, which is only somewhat smaller than the values reported for the global geological DFN. Still, the hypothesis that the reported difference in the scaling exponents is due to the size of the area/data analysed cannot be rejected. The result indicates that there may be an uncertainty in the scaling exponents of the geological DFN in Table 5-1.

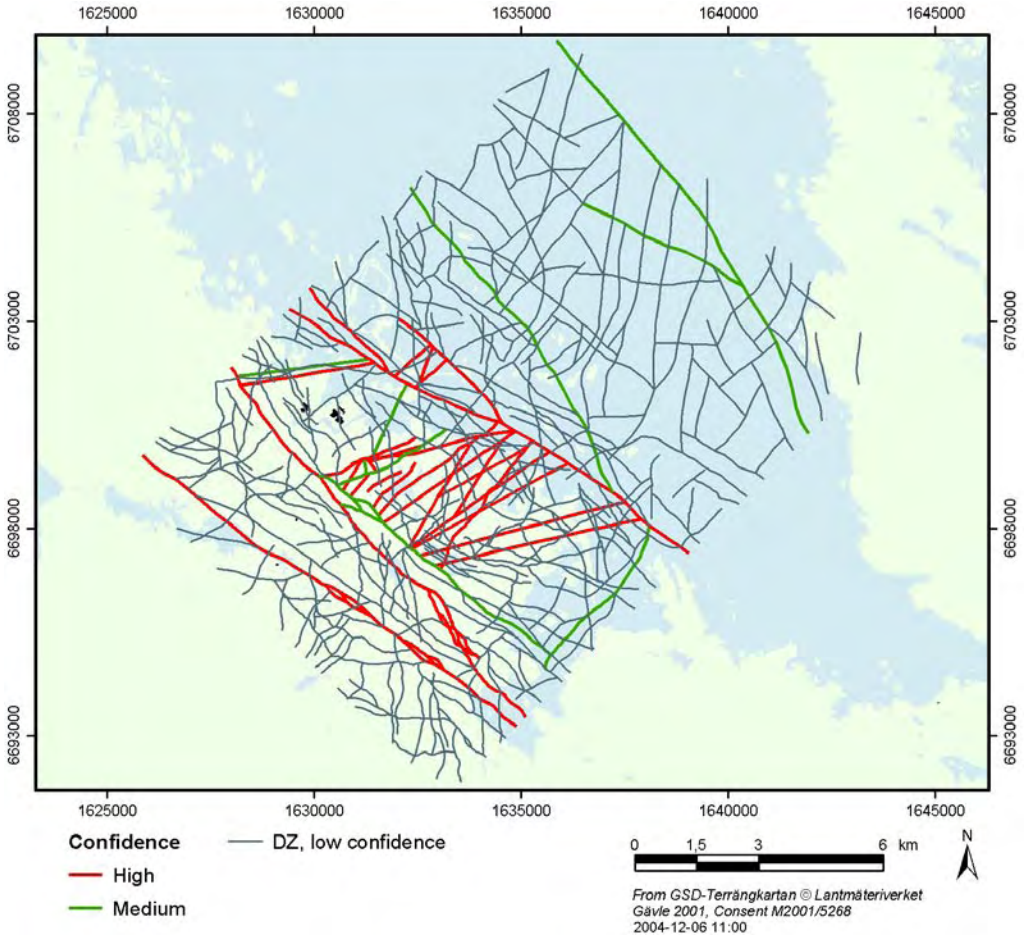

Figure 5-14. *Trace map of the alternative model.*

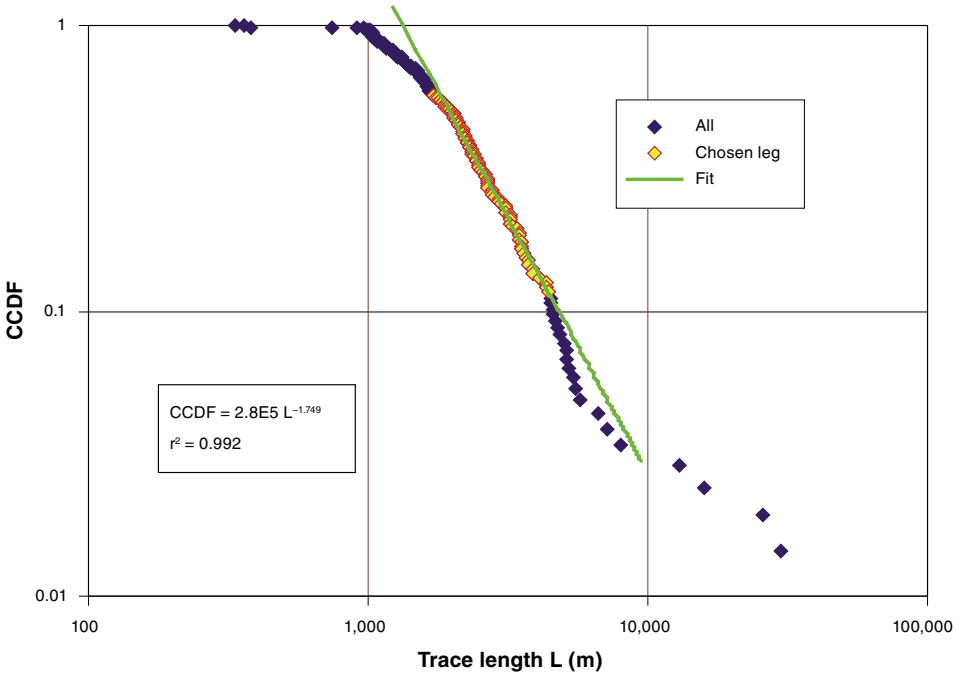

Figure 5-15. *Complementary cumulative density plot of the alternative model. The trace lengths used for the fitting range from 1.7 to 4.4 km. If all trace lengths above one kilometre are incorporated in the slope of the power-law fit decreases to –1.43.*

If the observed difference between the scaling exponents is indicative of a real difference one may wonder if the primary assumption of the geological DFN is correct (cf Section 5.2.4). What about if there is no single, continuous power-law size distribution, but that the slopes and intensities of borehole fractures, outcrop fractures and large deformation zones obey different power-law size distributions.

5.3.1 Divison of RFM029 into sub-volumes

The heterogeneity in the borehole fracture intensity P_{10} versus depth seen in Figure 5-13 suggests that the global geological DFN significantly underestimates the fracture intensity of the uppermost parts of RFM029 between repository depth and ground surface. The uneven occurrence of the PFL-f flow anomalies versus depth shown in Figure 3-6 through Figure 3-10 reinforces the interpretation that there is heterogeneity also in the rock mass hydraulic properties versus depth. It is important to recognise that the sparse, uneven fracturing and few flow anomalies is seen in KFM01A below c 360 m depth also applies to borehole KFM05A below c 200 m depth, to KFM02A below c 510 m depth, and to KFM04A below c 430 m depth.

The demarcation of HRDs generally coincides with that of lithological rock domains defined by geology. However, several rock domains may be merged into one HRD or one rock domain may be divided into several HRDs depending on the structural and hydrogeological complexities. The observed differences regarding:

- the fracture intensity versus depth,
- the relative proportions between the fracture sets between the boreholes, and
- the uneven distribution of flow anomalies above the lower measurement limit

make it difficult to adopt a global geological DFN covering large volumes. A division of RFM029 into several HRDs or sub-volumes seems more rational.

Figure 5-16 shows a schematic cross-section through the tectonic lens from NE to SW illustrating the division of RFM029 into four sub-volumes. The relative locations of the five core-drilled boreholes in relation to the gently dipping deformation zone ZFMNE00A2 ("A2") are also indicated. The sub-volumes have the following approximate fracture intensity characteristics:

Volume A is associated with KFM03A and the upper part of KFM02A above the gently dipping deformation zone ZFMNE00A2 ("A2"). These two boreholes intersect sparsely fractured rock masses with Terzaghi corrected fracture intensities P_{10corr} of 0.4–0.7 m^{-1}.

Volume C is associated with the uppermost parts of KFM01A and KFM05A down to c 220 m depth.

Volume B is associated with KFM01A between 220–360 m depth. Volumes B and C have both a low P_{10corr} of 4–5 m^{-1}, but differ significantly in terms of numbers and magnitudes of PFL-f transmissivities, see Section 5.4.

Volume D is associated with KFM01A below c 360 m depth, with KFM02A below c 510 m depth (below ZFMNE00A2), with KFM05A below c 220 m depth and with KFM04A below c 430 m depth. These three intervals are very sparsely fractured with a P_{10corr} of 0.2–0.5 m^{-1}, and very few or none PFL-f anomalies or 5 m PSS data above the lower measurement limits.

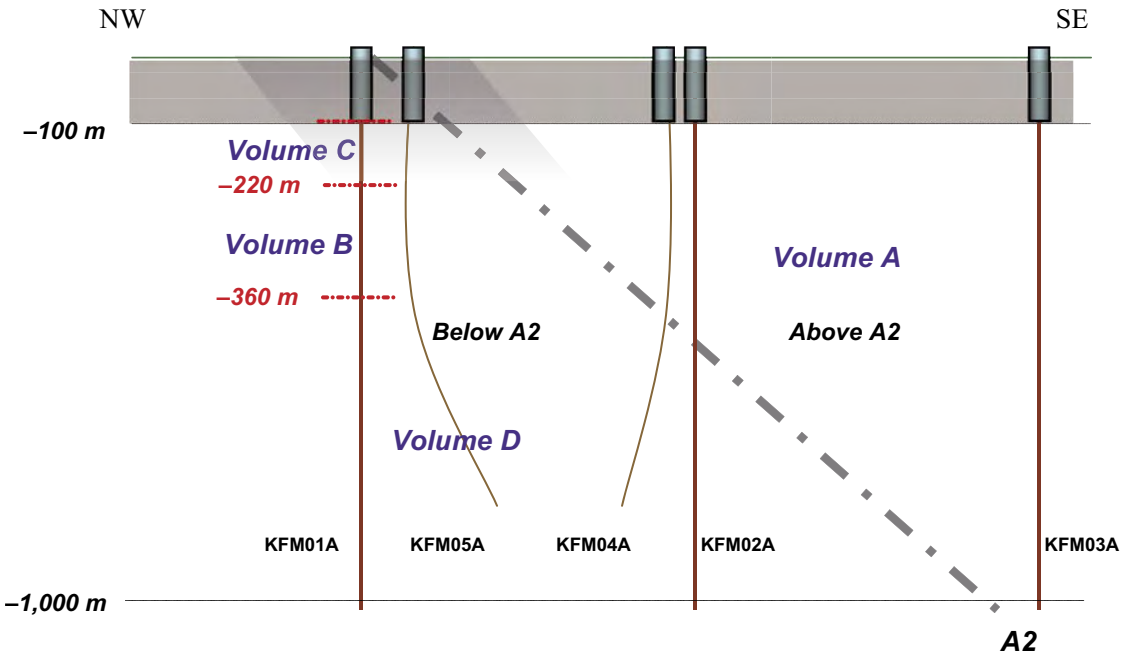

Figure 5-16. *Schematic cross-section through the tectonic lens illustrating the division of RFM029 into smaller volumes A–D. The uppermost 100 m of each borehole KFM01A–KFM05A is percussion drilled. A casing is installed in all boreholes except KFM03A.*

Table 5-3 summaries the relative intensity proportions between the four Volumes A–D.

Table 5-3 indicates that the relative intensity of the global geological DFN is closest to the proportions in Volume A, i.e. above the gently dipping deformation zone ZFMNE00A2 and outside the target volume.

Table 5-3. Relative intensity proportions of Open and Partly Open fractures for the four Volumes A–D and the global geological DFN (GeoDFN).

Fracture set	GeoDFN P_{32} [%]	Vol A P_{10corr} [%]	Vol B P_{10corr} [%]	Vol C P_{10corr} [%]	Vol D P_{10corr} [%]
NS	11	17	9	11	25
NE	42	31	56	23	32
NW	14	16	3	7	3
EW	4	8	2	6	0
HZ	29	28	30	53	40

5.4 Assessment of hydrogeological DFN data

The PFL-f transmissivities not associated with the deterministically treated deformation zones are the main sources of information for the HydroDFN analysis reported here. The PFL-f transmissivities have the best spatial resolution of all hydraulic tests and represent fractures that are flowing after several days of pumping. The latter implies that they belong to a connected fracture network away from the borehole.

Table 5-4 shows an assessment of the numbers of Certain and Uncertain PFL-f anomalies that are coupled to Certain, Probable and Possible Open or Partly Open fractures within RFM029 outside the deterministically treated deformation zones.

Out of a total of 309 PFL-f anomalies, 240 are associated with RFM029 and RFM017 in the candidate area and 69 with other rock domains outside the candidate area. 149 of the 240 flow anomalies are associated with deterministically treated deformation zones and 91 with uncertain (stochastic) discrete fractures and deformation zones in the rock mass.

35 of the 91 flow anomalies occur below c 220 m depth; eleven in KFM01A (Volume B), six in KFM02A, 15 in KFM03A, two in KFM04A and one in KFM05A. At repository depth below the gently dipping deformation zone ZFMNE00A2, there are two flow anomalies all together associated with the rock mass fracturing in boreholes KFM01A, KFM02A, KFM04A and KFM05A. Hence, we may already at this point conclude that the rock mass between the deterministically treated deformation zones is very sparsely fractured by transmissive fractures. The absence of Open fractures in Forsmark is confirmed by the large number of unbroken 3-m drill cores captured.

Figure 5-17 shows the 91 flow anomalies in rock domain RFM029, coloured according to borehole. The left hand plot suggests a depth trend for data below ZFMNE00A2. The centre plot shows the dips and the right hand plot shows the strikes. From these plots it may be noted that the body of the flow anomalies, 77%, coincides with gently dipping fractures and there is weak preference for NW and NE fractures concerning strike.

Table 5-4. Compilation of the results obtained from a joint interpretation between Certain and Uncertain PFL-f anomalies and Certain, Probable and Possible Open or Partly Open fractures in RFM029 outside the deformation zones.

Object	KFM01A	KFM02A	KFM03A	KFM04A	KFM05A
Total no of PFL-f anomalies	34	125	52	71	27
PFL-anomalies outside the deformation zones	34	12	24	2	19
Certain PFL-f mapped as Certain Open or Partly Open	13	3	16	0	15
Certain PFL-f mapped as Probable Open or Partly Open	0	6	1	0	3
Certain PFL-f mapped as Possible Open or Partly Open	0	0	1	0	0
Uncertain PFL-f mapped as Certain Open or Partly Open	14	1	4	0	0
Uncertain PFL-f mapped as Probable Open or Partly Open	4	2	2	2	1
Uncertain PFL-f mapped as Possible Open or Partly Open	3	0	0	0	0

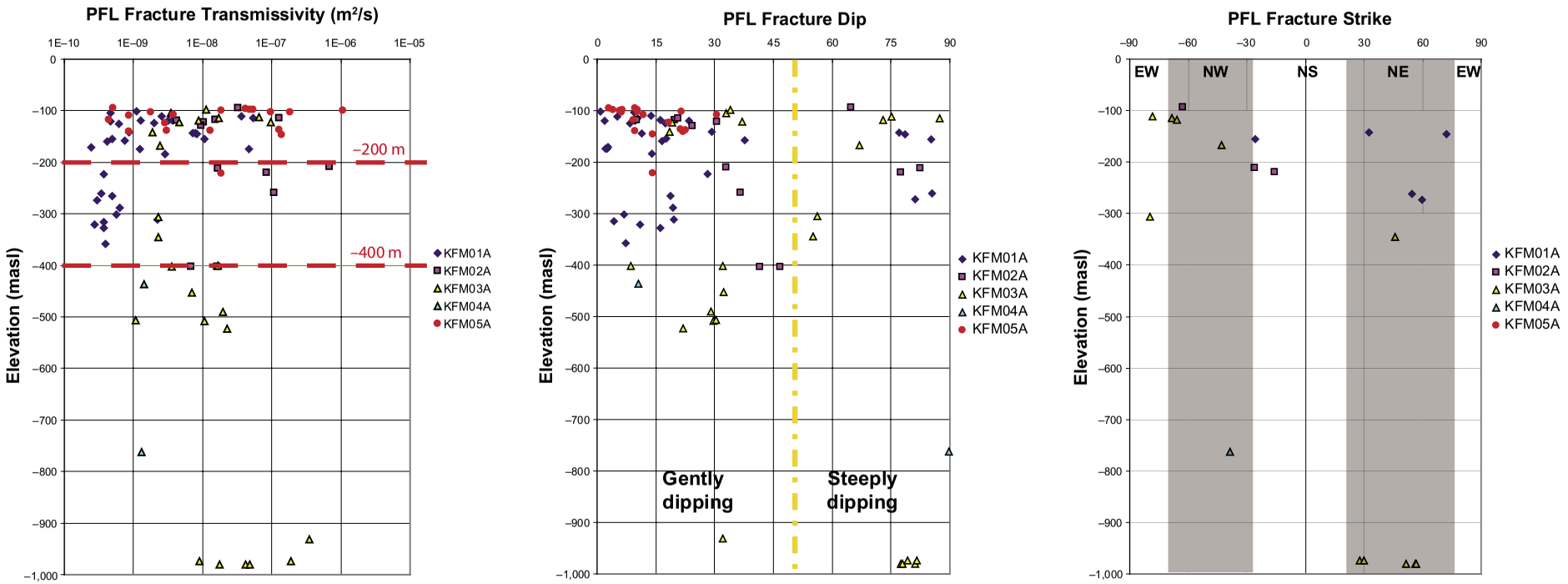

Figure 5-17. *PFL-f flow anomalies in rock domain RFM029 between the deterministically treated deformation zones. The anomalies are coloured according to borehole. The left hand plot shows the elevations, the centre plot shows the dips and the right hand plot shows the strikes. 35 of a total of 91 flow anomalies in RFM029 occur below c 200 m depth; eleven in KFM01A, six in KFM02A, 15 in KFM03A, two in KFM04A and one in KFM05A. At repository depth below the gently dipping deformation zone ZFMNE00A2 there are two flow anomalies. (the whole of KFM03A is above ZFMNE00A2, cf Figure 5-16. The division of the PFL-f anomalies into five sets follows the geological DFN definitions by /La Pointe et al. 2005/, see Table 5-1 and Figure 5-12.*

5.5 Assessment of interconnected fracture intensity

The interconnected fracture intensity is assessed by means of stochastic realisations that match the mapped orientations and borehole fracture frequencies of Open and Partly Open fractures in KFM01A and KFM03A, see Figure 5-7 and Figure 5-9. These boreholes penetrate Volumes A–D at different locations along the centre axis of the tectonic lens, cf Figure 5-16. Once the measured geological intensity of Open and Partly Open fractures is matched, the interconnected fracture intensity is determined by a connectivity analysis. An interconnected fracture is defined as a fracture that directly or indirectly connects to hydraulic boundary, e.g. a deterministically treated deformation zone, the upper surface of the bedrock, a scanline representing a borehole. The methodology used is illustrated in Figure 5-6.

The simulation domain consists of three concentric shells; one large (outer), one intermediate large (middle) and one small (inner). In the centre of the simulation domain there is a scanline mimicking a steeply dipping core-drilled borehole. The model set-up and dimensions of the shells are shown in Figure 5-18. Within the outer shell stochastic fractures in the size range L = 20–1,000 m (r = 11.3–564 m) are generated, within the middle shell L = 1–20 m (r = 0.564–11.3), and within the inner shell $L = L_0$–1 m ($r = r_0$–0.564) m.

The fractures are generated in order beginning with the outer shell. The approximate procedure of generating an interconnected network is done as follows:

- the interconnected stochastic fractures within the outer shell are retained while the stochastic fractures in the middle shell are generated, and
- the interconnected stochastic fractures within the outer and middle shells are retained while the stochastic fractures in the inner shell are generated.

It is noted that suggested approach may be sensitive to high values of the scaling exponent.

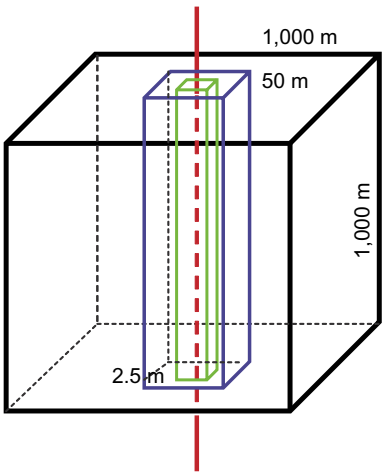

Figure 5-18. *Simulation model set-up and dimensions of the three fracture shells; outer (black), middle (blue) and inner (green).*

The stochastic simulations are done twice for each seed. In the first run there is a scanline in the centre representing the borehole or borehole interval to be matched and in the second run there is no scanline. The scanline (borehole) attracts not only the interconnected fractures but also the isolated fractures. In the second run the latter are discarded and the difference is analysed. This approximate procedure enables a matching against N_{CAL} and a determination of N_{CON} , where N_{CAL} is the total number of potentially flowing Open and Partly Open fractures that intersects the scanline and N_{CON} is the interconnected number of potentially flowing Open and Partly Open fractures that intersects scanline, see Figure 5-6. The relationship between N_{PFL}, which is the number of PFL-f flow anomalies above the lower measurement limit for transmissivity, N_{CON} and N_{CAL} is given by Equation (5-5).

Two different values of r_0 are used, 0.038 m and 0.282 m, as a means to assess the uncertainty in the reference fracture size, cf the discussion in Section 5.2.5. Ten realisations are run (twice) for each value of r_0.

Table 5-5 presents the basic fracture frequency data outside the deformation zones that is used in the connectivity analysis. N_{CAL} is the number of potentially flowing Open and Partly Open fractures in each borehole (Volume) to be matched in the modelling process and N_{PFL} is the number of flow anomalies in the connected network of flowing features above the lower measurement limit of the PFL-f tests. T_{PFLmin} is the smallest transmissivity value measured and may be considered as an estimate of the lower measurement limit T_{lim}. As noted previously, the lower measurement limit of the PFL-f tests is not a threshold with a fixed magnitude, but varies in space dependent on the in situ borehole conditions. For Volume D there are no flow anomalies above the lower measurement limit and in the work reported here we use the bottommost transmissivity value measured in Volume B at elevation –363 masl, $3.94 \cdot 10^{-10}$ m^2/s, as an estimate of T_{PFLmin} in Volume D.

The frequency of potentially flowing Open and Partly Open borehole fractures P_{10CAL} varies an order of magnitude between the Volumes A–D. The aforementioned P_{10} value of the geological DFN, 67 fractures per hundred metres, cf Section 5-3, falls in between the P_{10CAL} values shown in Table 5-5. The value of P_{10PFL} in each Volume is at least one order of magnitude lower than the corresponding value of P_{10CAL}. Between Volume C and Volume D the P_{10PFL} value varies more than two orders of magnitude.

Table 5-6 demonstrates the sensitivity to the reference size for Volume B. A reference size of 0.038 m renders on the average 27 interconnected fractures (12.8% of 210). A reference size of 0.282 m renders on the average 209 fractures (99.6% of 210). In the first case 59% (= (27 – N_{PFL}) / 27) of the interconnected fractures have transmissivities below the minimum value of the PFL-f tests, in the latter case 95% (= (209 – N_{PFL}) / 209). (The value of N_{PFL} is 11 for Volume B according to Table 5-5.)

Table 5-5. Primary fracture frequency and PFL-f data outside the deterministically treated deformation zones.

Borehole	Volume	Interval	N_{CAL} [–]	P_{10CAL} [(100 m)$^{-1}$]	N_{PFL} [–]	P_{10PFL} [(100 m)$^{-1}$]	T_{PFLmin} [m^2/s]	T_{PFLmax} [m^2/s]
KFM03A	A	106–994	248	27.9	24	2.70	1.09E–09	3.46E–07
KFM01A	B	222–363	210	149	11	7.80	2.71E–10	2.22E–09
KFM01A	C	103–222	304	255	23	19.3	2.47E–10	5.35E–08
KFM01A	D	367–956	134	22.8	< 1	< 0.170	3.94E–10	3.94E–10

Table 5-6. Simulated values of N_{CAL} and N_{CON} of the fracturing in KFM01A, Volume B, using two different values of the reference size r_0 , 0.038 m and 0.282 m.

0.038 m	Mean	#1	#2	#3	#4	#5	#6	#7	#8	#9	#10
N_{CAL}	210	222	216	210	209	214	207	206	213	219	184
N_{CON}	27	50	32	28	28	24	15	24	25	31	13
0.282 m	**Mean**	**#1**	**#2**	**#3**	**#4**	**#5**	**#6**	**#7**	**#8**	**#9**	**#10**
N_{CAL}	210	207	223	214	216	191	181	210	244	202	212
N_{CON}	209	206	221	213	216	191	180	210	243	201	211

In summary, a reference size of 0.038 m renders a sparsely connected DFN, where c 13% of all Open and Partly Open fractures are connected. About 41% of these fractures (eleven) are above the lower transmissivity limit of the PFL-f tests in this interval. In comparison, a reference size of 0.282 leads to a "continuum of fractures" where c 100% of all Open and Partly Open fractures are interconnected. However, c 5% of these fractures (eleven) only has a transmissivity above the lower transmissivity limit of the PFL-f tests in this interval.

In conclusion, **the applied methodology** leads to a fork in the conceptual modelling of the rock mass fracture hydrogeology, where the critical assumption to make is the value of the reference size of the power-law size distribution. A reference size of 0.038 m renders 19 interconnected fractures per hundred metres, whereas a reference size of 0.252 m renders 148. From an advective flow point of view these conceptualisations are difficult to separate from one another as the body of the flow occurs in circa eight interconnected fractures per hundred metres that are above the lower transmissivity limit of the PFL-f tests in Volume B. Hence, the important questions to ask concern the flow in the matrix: *What are the implications for Safety Analysis if the interconnected fractures below the lower transmissivity limit of the PFL-f tests in Volume B form a sparsely or well interconnected DFN? Can we decide which reference size of the two that is the most appropriate by analysing the hydrogeochemistry of the matrix water?*

Table 5-7 summaries the simulation results of the connectivity analysis for Volumes A–D and two different values of the reference size, 0.038 m (Model 3a) and 0.282 m (Model 3b). For Volume B we also present the results for the geological DFN reference sizes (Model 1) and for a hypothetical reference size of 0.10 m (Model 2). In Models 1 and 2 the borehole is treated as a cylinder of finite radius, whereas in Models 3a and 3b it is treated as a scanline. By comparing the four cases one can conclude that the assumptions for the borehole radius and the reference size have both a great impact on the calculations. The values shown in Table 5-7 are approximations and represent mean values of ten realisations.

The results for Volumes A and D in Table 5-7 reveal that the rock mass in these volumes are very sparsely fractured and that the higher value of the two reference sizes (0.282 m) needs to be considered in order to form interconnected networks. Table 5-5 suggests that some kind of interconnected network must exist in Volume A, whereas it is an open question if a flowing interconnected network exists in Volume D. A tentative interpretation of the results shown in Table 5-7 is that the vertical spacing between interconnected fractures is c 9 m in Volume A (Model 3b), c 5 m in Volume B (Model 3a), c 1.5 m in Volume C (Model 3a) and c 33 m in Volume D (Model 3b).

Table 5-7. Results of the connectivity analysis for Volumes A–D. N_{CON} is the interconnected number of fractures after calibration against N_{CAL}. P_{10CON} is the interval frequency of N_{CON}. P_{32} is the Terzaghi corrected P_{10corr} based on N_{CAL} after correction for the variability in k_r between the five fractures sets. P_{32CON} [%] is N_{CON}/N_{CAL}. The values shown are approximations and represent mean values of ten realisations.

Model	r_0 [m]	r_w [m]	N_{CON} [–]	P_{10CON} [100m]	P_{32} [m²/m³]	P_{32CON} [%]	P_{32CON} [m²/m³]	$P_{32CON} < T_{min}$ [% of P_{32CON}]	$P_{32CON} > T_{min}$ [% of P_{32CON}]
Volume B									
1	0.14–0.28	0.038	190	135	2.70	90	2.44	94	6
2	0.10	0.038	103	73.0	2.76	49	1.35	89	11
3a	0.038	0	27	19.1	3.98	13	0.512	59	41
3b	0.28	0	209	148	3.97	100	3.95	95	5
Volume C									
3a	0.038	0	80	67.2	4.70	26	1.238	71	29
3b	0.282	0	303	255	4.66	100	4.66	92	8
Volume A									
3a	0.038	0	0	0.00	0.786	0	0.000	N/A	N/A
3b	0.282	0	95	10.7	0.786	38	0.301	75	25
Volume D									
3a	0.038	0	0	0.00	0.523	0	0.000	N/A	N/A
3b	0.282	0	19	3.23	0.523	14	0.0741	100	0

5.6 Assessment of parameter values for a correlated transmissivity model

Figure 5-19 is a composite of selected parts of Figure 5-4 and Figure 5-6. The upper inset shows a simulation of the complementary cumulative density function (CCDF) plot of the ordered fracture transmissivity data in borehole KFM03A (Volume A). The lower inset shows the probabilities associated with the different parts of the CCDF plot. The CCDF equation for the fracture transmissivity may be written as:

$$G\left[T' \geq T\right] = \left(\frac{m_T}{T}\right)^{k_T} \tag{5-6}$$

where m_T is the transmissivity value where the power-law regression intersects $G[T' \geq T]$. In order to compute the value of the transmissivity m_T we make use of T_{PFLmin} and N_{PFL} in Table 5-5 and the previous simulated values of N_{CON} in Table 5-7:

$$m_T = T \sqrt[\{1/k_T\}]{G\left[T' \geq T\right]} = T_{PFL\,\min}\left(\frac{N_{PFL}}{N_{CON}}\right)^{(k_T)^{-1}} \tag{5-7}$$

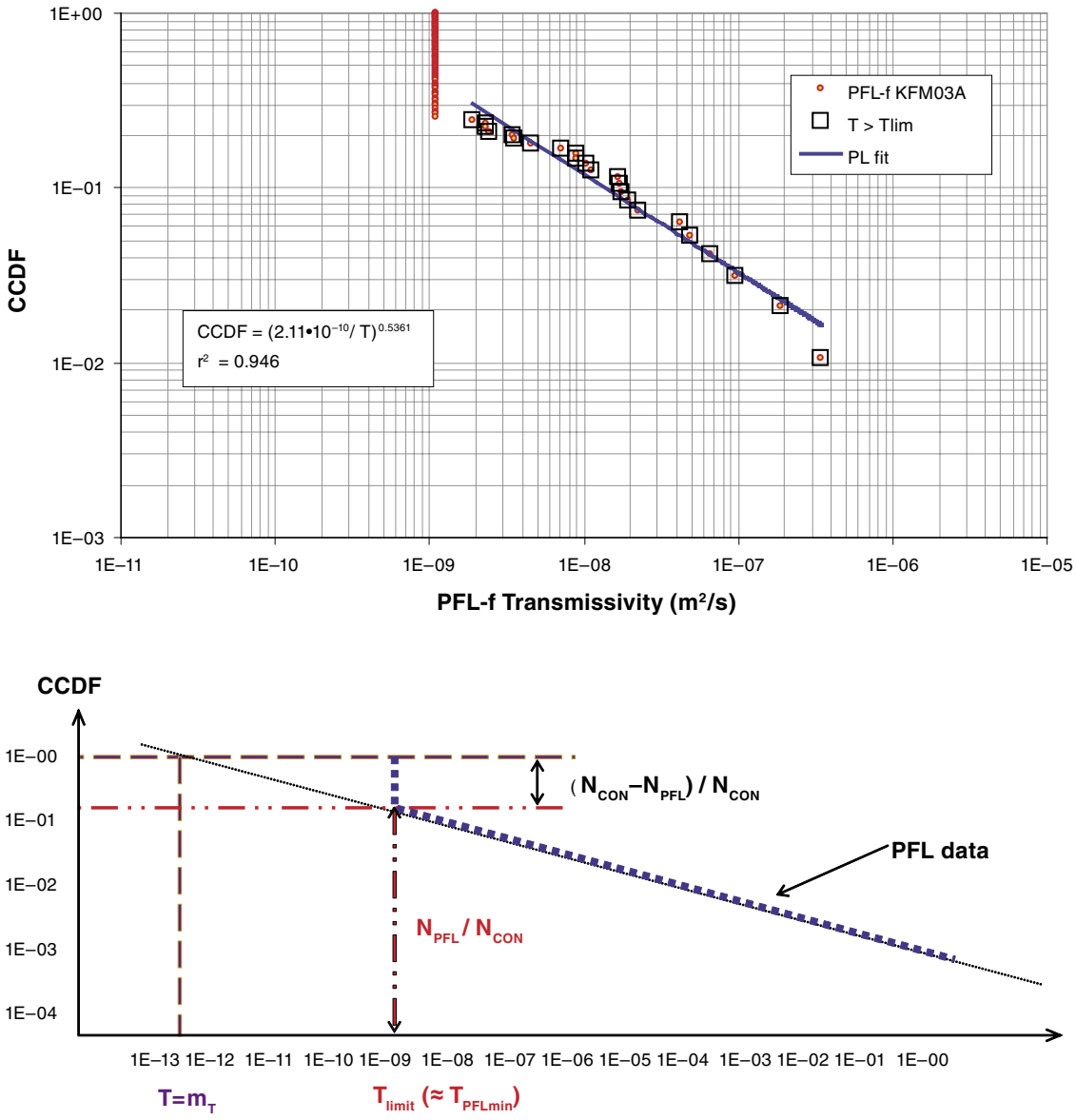

Figure 5-19. *Composite of selected parts of Figure 5-4 and Figure 5-6. The upper inset shows a simulation of the complementary cumulative density function (CCDF) plot of the ordered fracture transmissivity data in borehole KFM03A (Volume A). The lower inset shows the probabilities associated with the different parts of the CCDF plot.*

Figure 5-20 shows the inferred scaling exponents k_T of the fracture transmissivity data observed in Volumes A–C. For Volume D there are no fracture transmissivity data above the measurement limit. In the work reported here it is assumed that the scaling exponent of Volume D is similar to that of Volume B.

Table 5-8 presents the simulated values of m_T in Volumes A–D using Equation (5-7). The input values of T_{PFLmin} and N_{PFL} are shown in Table 5-5 and the input values of N_{CON} in Table 5-7.

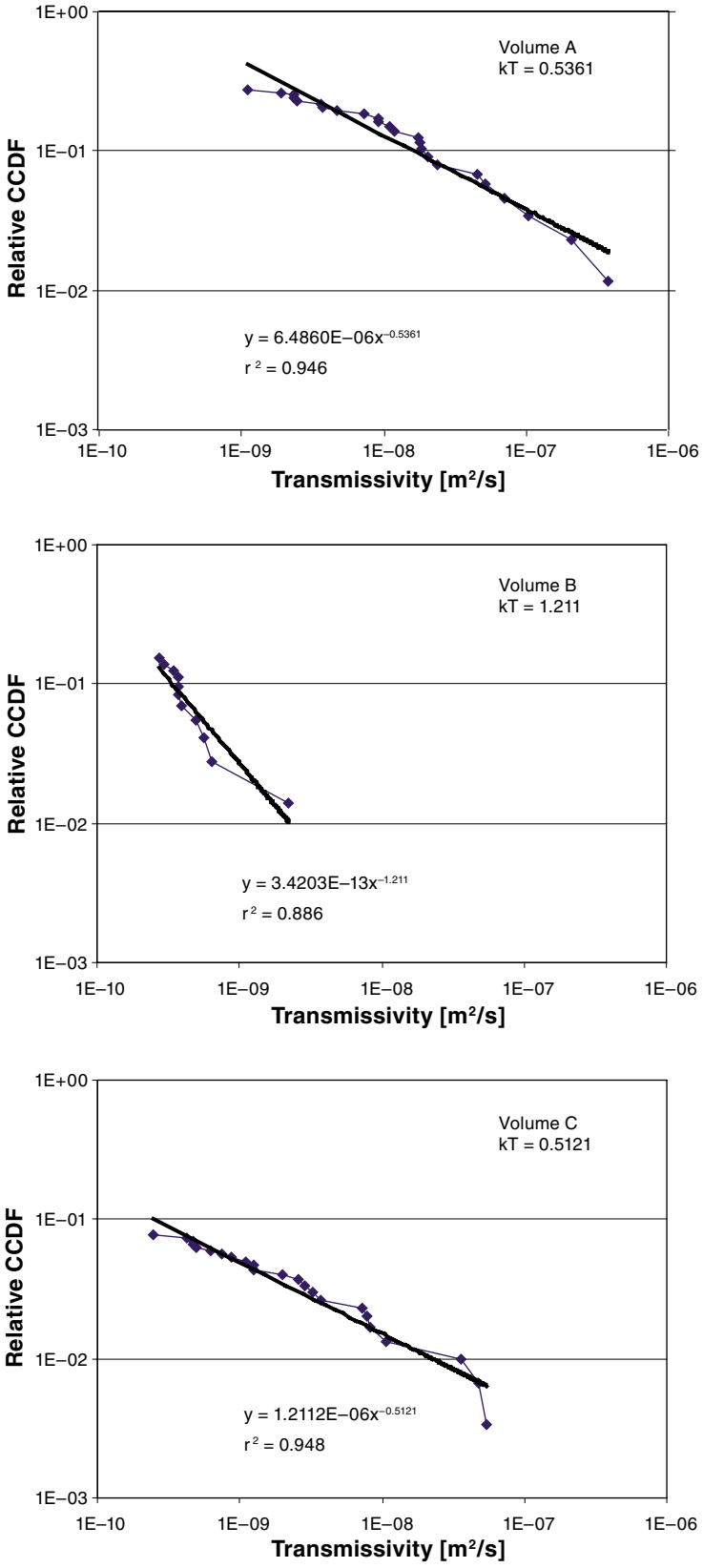

Figure 5-20. *Inferred scaling exponents of the fracture transmissivity data observed in Volumes A–C. For Volume D it is assumed that the scaling exponent of the tentative fracture transmissivities in Volume D is similar to that in Volume B.*

Table 5-8. Estimated values of m_T [m²/s] in Volumes A–D using Equation (5-7). The reference size r_0 is 0.038 m in Volumes B and C (Model 3a) and 0.282 m in Volumes A and D (Model 3b). *N* denotes the figure in each field, i.e. $m_T = N \cdot 10^{-10}$.

Volume ; m_T	#1	#2	#3	#4	#5	#6	#7	#8	#9	#10
A ; $N \cdot 10^{-10}$	2.11	1.97	1.42	2.20	1.78	2.02	1.65	1.75	1.68	1.62
B ; $N \cdot 10^{-10}$	0.69	1.00	1.11	1.11	1.26	1.82	1.26	1.22	1.03	2.03
C ; $N \cdot 10^{-10}$	0.47	0.33	0.47	0.56	0.47	0.37	0.40	0.17	0.41	0.34
D ; $N \cdot 10^{-10}$	0.31	0.64	0.19	0.35	0.59	0.45	0.40	0.36	0.27	0.54

In the work presented here it is assumed that the largest fractures among the N_{CON} interconnected fractures that intersect the borehole in the simulation model, see Figure 5-18, correspond to the flow in the N_{PFL} flow anomalies. Since the borehole (scanline) is a one dimensional object the slope of the power-law regression $k_{r,1D}$ of the in the CCDF plots is:

$$k_{r,1D} = k_r - 2 \tag{5-8}$$

where k_r is the three-dimensional scaling exponent of the parent fracture size distribution. The magnitude of $m_{r,1D}$, i.e. the fracture size where the power-law regression intersects $G[r \geq m_{r,1D}] = 1$ is evaluated as:

$$m_{r,1D} = r^{(1/k_{r,1D})}\sqrt{G\left[r' \geq r_{1D}\right]} = r_{N_{PFL}} \left(\frac{N_{PFL}}{N_{CON}} \right)^{(k_{r,1D})^{-1}} \tag{5-9}$$

where $r_{N_{PFL}}$ denotes the size of the smallest fracture among the N_{PFL} largest interconnected fractures.

Ten realisations are run for each volume. Table 5-9 presents the minimum (i.e. $r_{N_{PFL}}$) and maximum values of the N_{PFL} largest fracture sizes of each realisation in Volumes A–C. For Volume D there are no flow anomalies above the measurement limit, but N_{CAL} is 134 and the average value of N_{CON} is estimated to 18, cf Table 5-5 and Table 5-7, respectively. The values shown for Volume D in Table 5-9 refer to the minimum and maximum of the N_{CON} fracture sizes of each of the ten realisations. The largest of these fractures in each realisation is used as a tentative estimate for $r_{N_{PFL}}$ in Volume D. Figure 5-21 demonstrates the looks of the first realisation in each volume.

Table 5-10 and Table 5-11 present the deduced values of $k_{r,1D}$ and $m_{r,1D}$ of Volumes A–D, respectively. The inferred values of the four variables $\{m_T, k_T\}$ and $\{m_{r,1D}, k_{r,1D}\}$ make it possible to derive the values of the coefficient *a* and the exponent *b* in Equation (2-11) by assuming that the complementary cumulative density functions are correlated:

$$G\left[T' \geq T\right] = G\left[r' \geq r\right] \tag{5-10}$$

Table 5-9. Minimum and maximum fracture sizes of each realisation and volume. The reference size r_0 is 0.038 m in Volumes B and C (Model 3a) and 0.282 m in Volumes A and D (Model 3b).

Volume	#1	#2	#3	#4	#5	#6	#7	#8	#9	#10
A min *r*	1.93	1.88	1.79	1.68	1.71	2.39	2.94	1.97	3.49	4.23
A max *r*	184	424	191	340	101	260	26.0	62.8	83.3	83.8
B min *r*	0.378	0.140	0.362	0.276	0.197	0.155	0.291	0.254	0.293	0.090
B max *r*	30.9	0.476	95.3	1.73	6.37	4.88	0.939	7.86	10.2	8.30
C min *r*	0.321	0.306	0.249	0.301	0.269	0.350	0.272	0.482	0.207	0.311
C max *r*	98.6	25.2	10.3	101	8.82	10.2	66.1	9.78	6.94	10.0
D min *r*	0.287	0.363	0.299	0.312	0.283	0.283	0.383	0.296	0.355	0.357
D max *r*	84.5	48.6	261	262	10.3	7.82	314	42.3	81.1	67.1

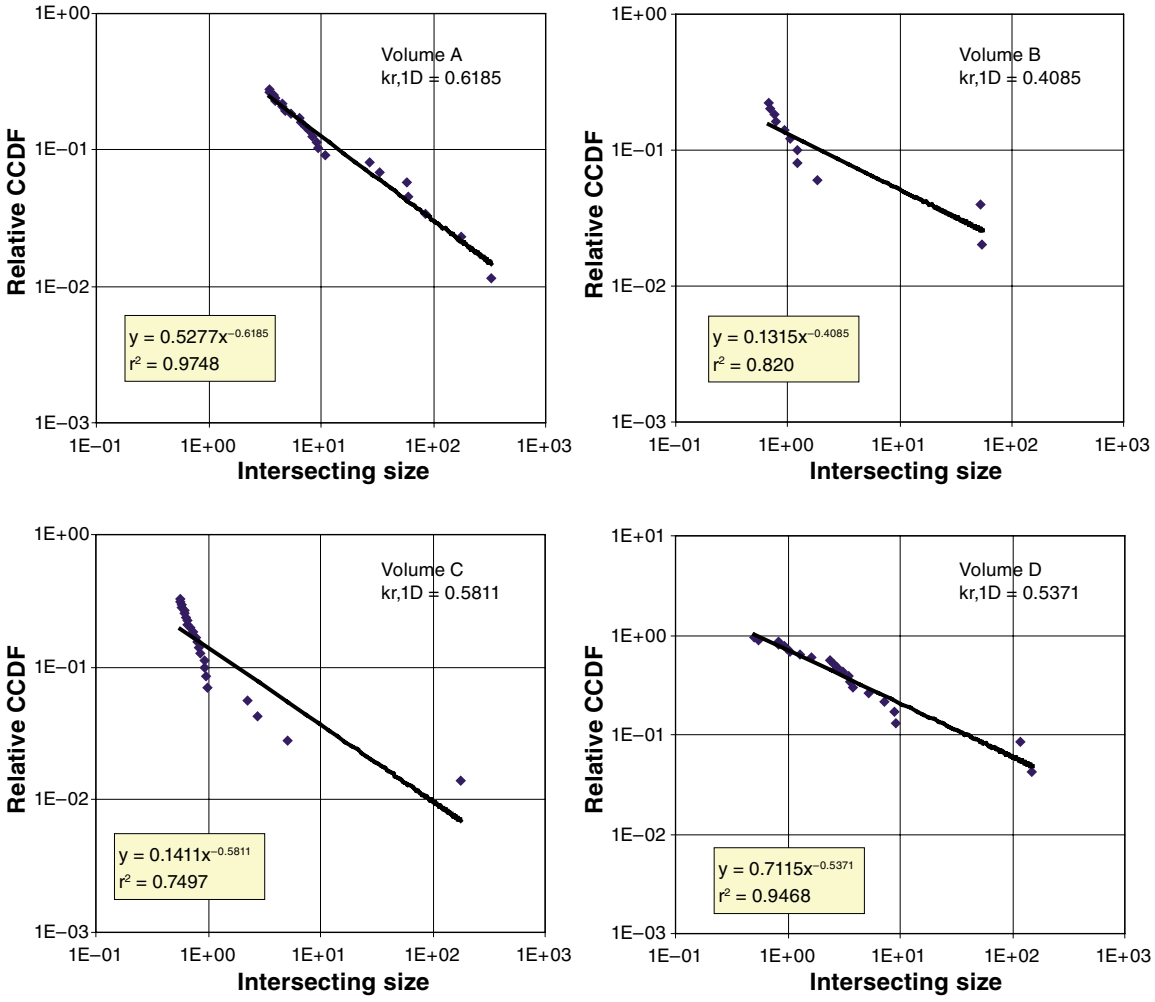

Figure 5-21. *Looks of the first realisation of the N_{PFL} greatest fractures among the N_{CON} interconnected fractures that intersect the borehole in the simulation domain. The values shown for Volume D refer to the interconnected fractures N_{CON}.*

Table 5-10. Simulated power-law regression slopes $k_{r,1D}$ [–] of the N_{PFL} greatest fractures in Volumes A–C. The values shown for Volume D refer to the slope of the N_{CON} simulated fracture sizes. The reference size r_0 is 0.038 m in Volumes B and C (Model 3a) and 0.282 m in Volumes A and D (Model 3b).

Volume	#1	#2	#3	#4	#5	#6	#7	#8	#9	#10
A	0.619	0.609	0.692	0.666	0.924	0.646	1.286	0.895	0.832	0.868
B	0.408	1.803	0.388	1.168	0.682	0.763	2.164	0.707	0.569	0.556
C	0.581	0.672	0.966	0.510	0.969	0.944	0.461	1.023	0.793	0.781
D	0.537	0.328	0.479	0.459	0.599	0.609	0.445	0.565	0.563	0.439

Table 5-11. Estimated values of $m_{r,1D}$ [m²/s] in Volumes A–D using Equation (5-8). The reference size r_0 is 0.038 m in Volumes B and C (Model 3a) and 0.282 m in Volumes A and D (Model 3b).

Volume	#1	#2	#3	#4	#5	#6	#7	#8	#9	#10
A	0.201	0.154	0.181	0.184	0.359	0.327	0.996	0.450	0.634	0.821
B	0.004	0.104	0.016	0.129	0.039	0.102	0.190	0.054	0.039	0.055
C	0.019	0.029	0.069	0.020	0.082	0.080	0.012	0.121	0.040	0.046
D	0.267	0.060	0.124	0.428	0.221	0.102	0.619	0.253	0.250	0.285

By substituting both sides of Equation (5-10) by their corresponding power-law expressions we get the desired variables into play:

$$\left(\frac{m_T}{T}\right)^{k_T} = \left(\frac{m_{r,1D}}{r}\right)^{k_{r,1D}} \tag{5-11}$$

and

$$T = m_T \left(\left\{ m_{r,1D} \right\}^{-1} r \right)^{\left(\frac{k_{r,1D}}{k_T}\right)} \tag{5-12}$$

Thus, the coefficient a and the exponent b in Equation (2-11) can be computed from:

$$b = \frac{k_{r,1D}}{k_T} \tag{5-13}$$

$$a = \frac{m_T}{\left(m_{r,1D}\right)^b} \tag{5-14}$$

The variability between the realisations means that there is an uncertainty in the exact looks of the correlation between the fracture transmissivity and the fracture size. Table 5-12 and Table 5-13 show the deduced values of a and b for ten realisations in each of the four volumes, respectively. Table 5-14 provides the geometric means of a and b for all simulations and Models 1, 2, 3a and 3b, cf Table 5-7.

Table 5-12. Estimated values of a [m²/s] in Volumes A–D using Equation (5-14). The reference size r_0 is 0.038 m in Volumes B and C (Model 3a) and 0.282 m in Volumes A and D (Model 3b). N denotes the figure in each field, i.e. $a = N \cdot 10^{-10}$.

Volume ; a	#1	#2	#3	#4	#5	#6	#7	#8	#9	#10
A ; $N \cdot 10^{-10}$	13.4	16.6	12.9	18.1	10.4	7.75	1.66	6.61	3.40	2.22
B ; $N \cdot 10^{-10}$	4.46	29.0	4.22	8.02	7.87	7.67	24.5	6.68	4.69	7.68
C ; $N \cdot 10^{-10}$	40.9	34.1	72.8	27.7	53.3	38.8	21.5	11.7	60.1	37.2
D ; $N \cdot 10^{-10}$	0.55	1.37	0.44	0.48	1.24	1.40	0.48	0.69	0.51	0.86

Table 5-13. Estimated values of b [–] in Volumes A–D using Equation (5-13). The reference size r_0 is 0.038 m in Volumes B and C (Model 3a) and 0.282 m in Volumes A and D (Model 3b).

Volume	#1	#2	#3	#4	#5	#6	#7	#8	#9	#10
A	1.15	1.14	1.29	1.24	1.72	1.20	2.40	1.67	1.55	1.62
B	0.34	1.49	0.32	0.96	0.56	0.63	1.79	0.58	0.47	0.46
C	1.13	1.31	1.89	1.00	1.89	1.84	0.90	2.00	1.55	1.53
D	0.44	0.27	0.40	0.38	0.49	0.50	0.37	0.47	0.47	0.36

Table 5-14. Geometric means of a [m²/s] and b [–] for all realisations in Volumes A–D.

Parameter		r_0 [m]	r_w [m]	Volume A	Volume B	Volume C	Volume D
Model 1:	a	0.14–0.28	0.038	–	$9.04 \cdot 10^{-11}$	–	–
Model 1:	b	0.14–0.28	0.038	–	0.669	–	–
Model 2:	a	0.10	0.038	–	$2.27 \cdot 10^{-10}$	–	–
Model 2:	b	0.10	0.038	–	0.737	–	–
Model 3a:	a	0.038	0	N/A	$8.30 \cdot 10^{-10}$	$3.56 \cdot 10^{-9}$	N/A
Model 3a:	b	0.038	0	N/A	0.645	1.451	N/A
Model 3b:	a	0.282	0	$7.14 \cdot 10^{-10}$	$5.12 \cdot 10^{-11}$	$4.17 \cdot 10^{-11}$	$7.23 \cdot 10^{-11}$
Model 3b:	b	0.282	0	1.459	0.767	1.618	0.408

Figure 5-22 and Figure 5-23 display the looks of the ten realisations for Volumes A–D. The outcome of applying Models 1, 2 and 3a in Volume B and to Model 3a in Volume C is shown in Figure 5-22. The outcome of applying Model 3b in Volumes A–D is shown in Figure 5-23. The geometric mean of the realisations is denoted by T_{gm}.

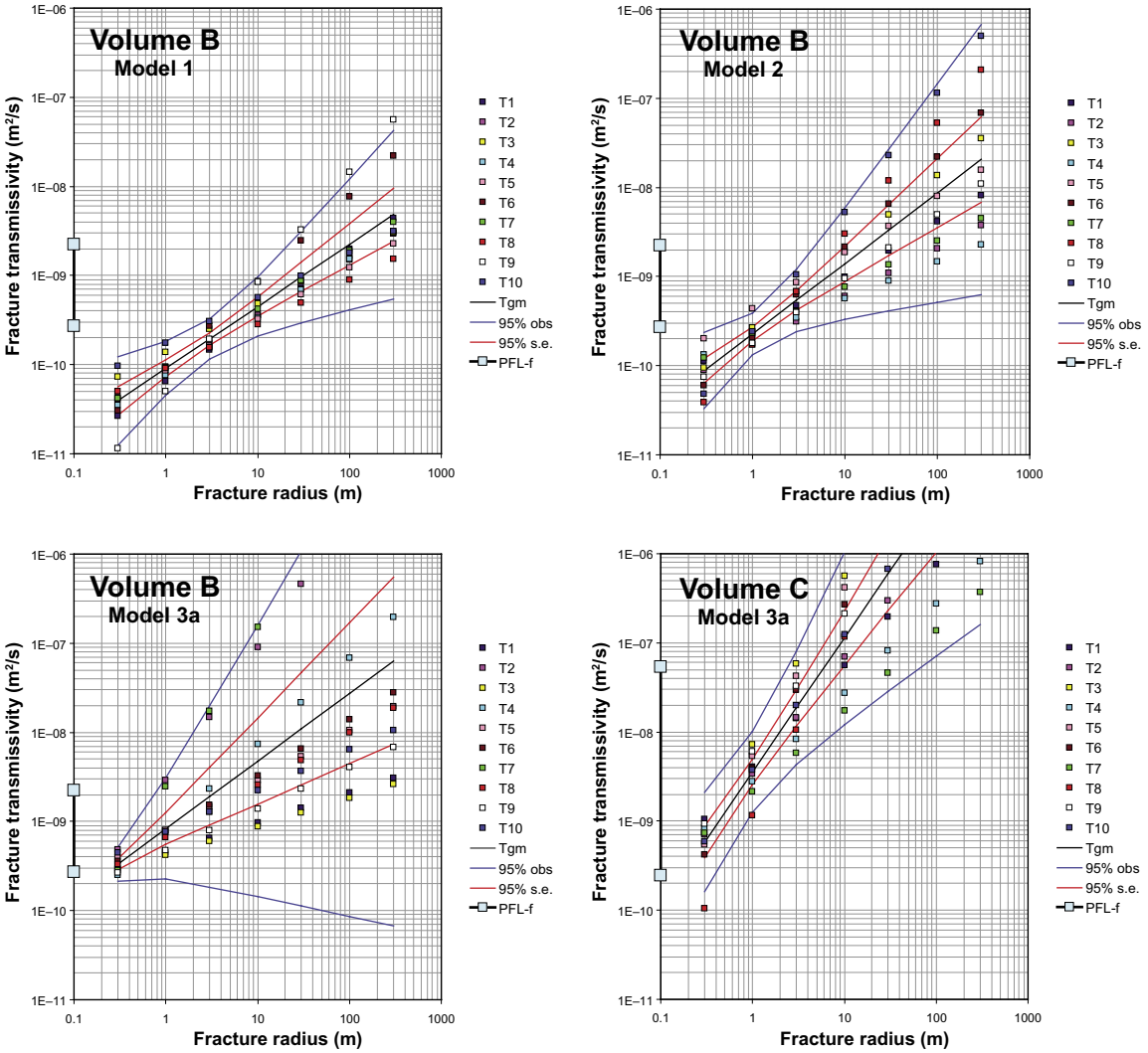

Figure 5-22. *Simulation results for Models 1, 2 and 3a in Volume B and Model 3a in Volume C.*

The difference in mean slope (exponent *b*) reflects mainly the differences in fracture transmissivity as observed in the associated volumes (boreholes). The variability in the offset (coefficient *a*) and between the stochastic realisations demonstrate the sensitivity of the connectivity analysis to the assumptions concerning the borehole radius and the reference size. Although the final model in each case has unique values of *a* and *b* a semi-correlated model could in fact be produced as an alternative.

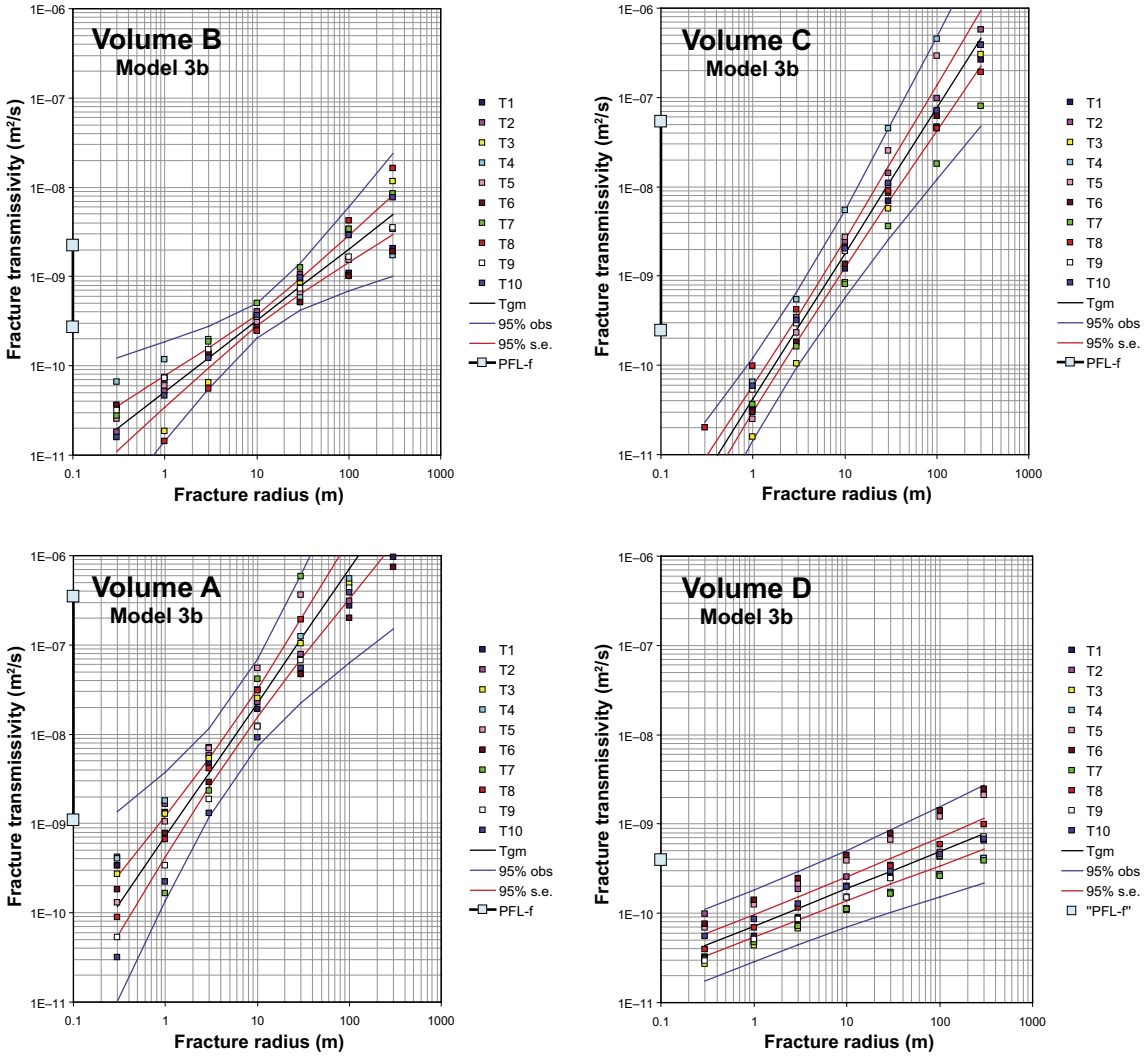

Figure 5-23. *Simulation results for Model 3b in Volumes A–D.*

5.7 A validity test

Up till now the use of single-hole hydraulic test data from the core-drilled boreholes have been purposely limited to treat PFL-f. The reason for this is twofold. First, the methodology developed in the work presented here requires the detailed information about fracture transmissivities provided by PFL-f measurements. Secondly, we need a second data set to test the validity of the hydrogeological DFN models derived, i.e. Models 3a and 3b. In the work reported here the only geometrical difference between these two models is in the reference size:

Model 3a

The geological fracture intensity of Open and Partly Open fractures seen in a cored borehole is assumed to be in proportion to the size of the borehole diameter, 0.038 m. The equivalent size of square is 0.067 m.

Model 3b

The geological fracture intensity of Open and Partly Open fractures seen in a cored borehole is assumed to reflect intercepts with fractures larger than the borehole diameter only. The

assumption tested here is a reference radius of 0.282 m, i.e. an equivalent square of 0.5 m. The motive for this assumption is the applied trace length threshold on outcrops.

The validity test proposed here is to produce cross plots of simulated T_{5m}, using Models 3a and 3b, versus measured T_{5m} of the PSS injection tests. The simulated T_{5m} are calculated by using an equation in analogy to Equation (5-2), i.e.

$$T_{5m} = \sum_{\sec up}^{\sec low} (T_f) \qquad (5\text{-}15)$$

where T_f is estimated from Equation (2-11) using the values of a and b shown in Table 5-14. The summation in Equation (5-14) is made over all simulated fractures belonging to the given the positions of the 5 m PSS test sections as provided by the section bounds [secup, seclow].

The validity test is conducted for Volume C where there are more than twenty 5 m PSS tests out of which c 43% are at or below the lower measurement limit of the PSS equipment for 5 m injection tests, i.e. $6.88 \cdot 10^{-10}$ m²/s. Each model is run ten times and the results are shown in Figure 5-24 and Figure 5-25.

The results in these figures indicate that Model 3a is only slightly better than Model 3b in terms of explaining the variability seen the 5 m PSS injection tests for Volume C. Still, the number of 5 m test sections at or below the PSS transmissivity threshold as well as the variability of around the unit slope both suggests that Model 3a is slightly better.

Figure 5-26 shows the looks of the single "best" realisation for Model 3a. Despite the apparently good match of this cross plot, however, it is important to point at the variability between the realisations, see Figure 5-24. The spread between the realisations is circa one and half order of magnitude and reflects the sparse connectivity of the fracture network and the resulting variability in the transmissivity model, see Figure 5-22 and Figure 5-23.

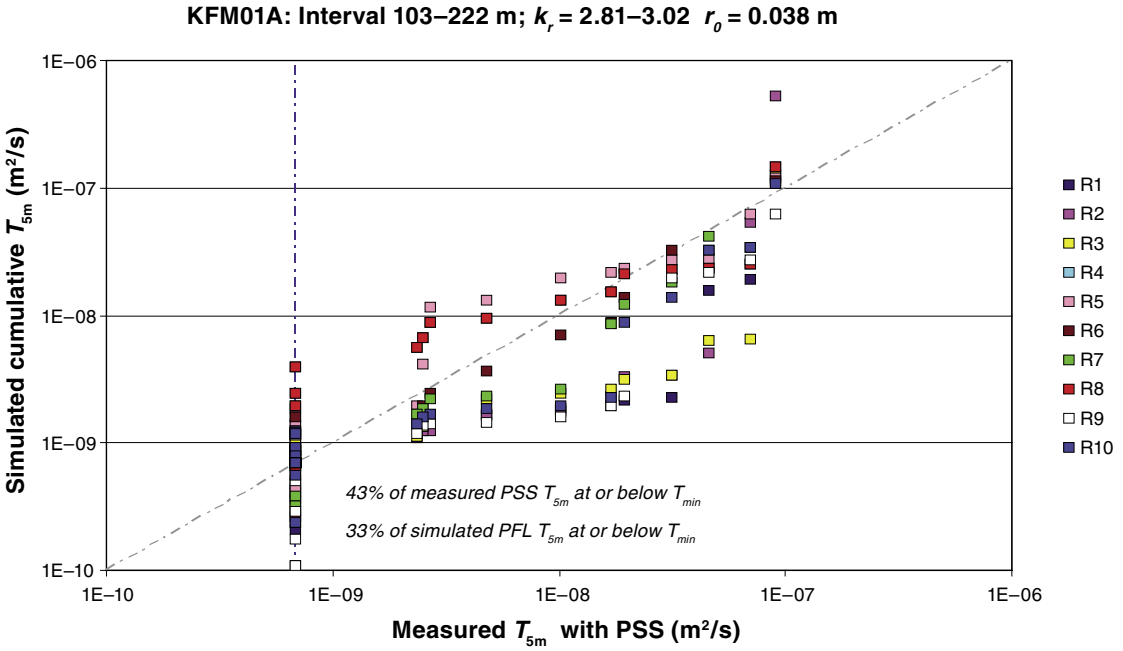

Figure 5-24. *Cross plot of simulated T_{5m} using Model 3a versus measured T_{5m} of the PSS injection tests conducted in Volume C. The dashed line indicates the measurement limit.*

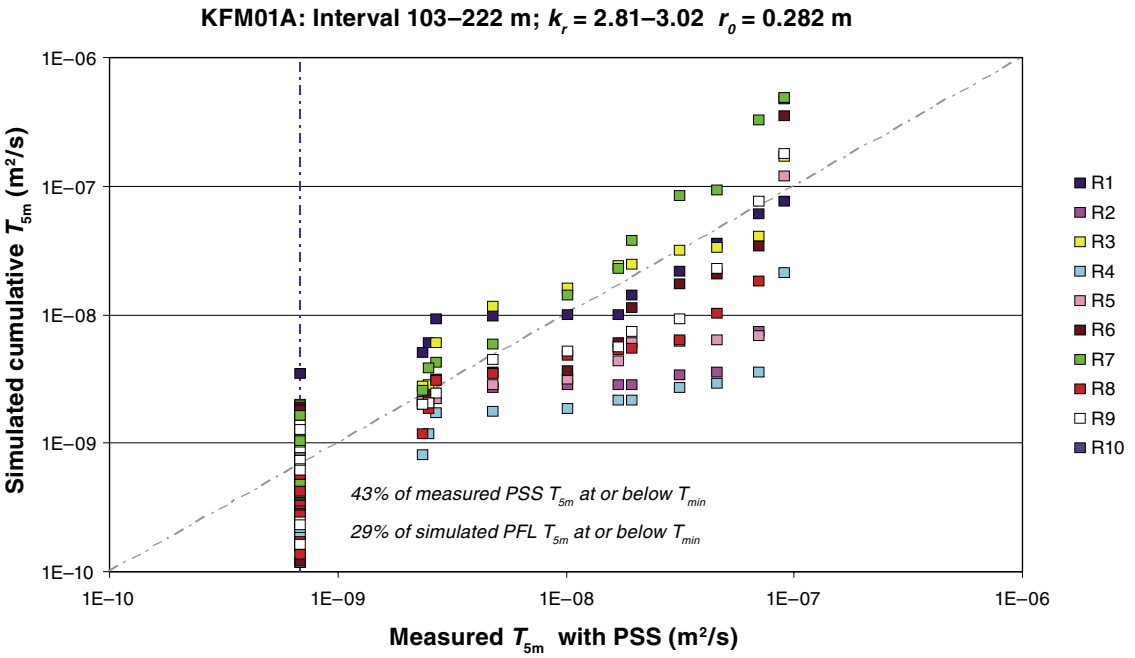

Figure 5-25. *Cross plot of simulated T_{5m} using Model 3b versus measured T_{5m} of the PSS injection tests conducted in Volume C. The dashed line indicates the measurement limit.*

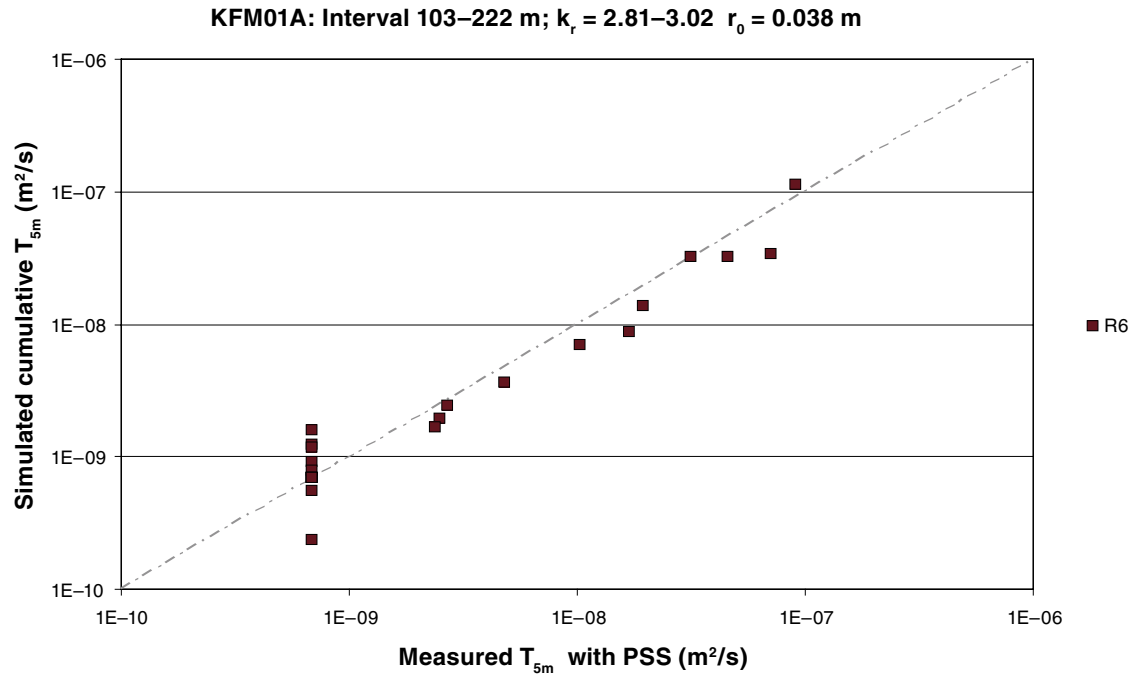

Figure 5-26. *Cross plot of the single best realisation in Figure 5-25 (Model 3a).*

5.8 Discussion of geological-hydrogeological DFN findings

The significant differences between the five core-drilled boreholes demonstrate that the geological and hydrogeological conditions within RFM029 do not lend themselves to a single (global) fracture network model covering large volumes as suggested by the geological DFN model by /La Pointe et al. 2005/.

The pragmatic approach taken in the work reported here is to divide the rock mass between the deterministically treated deformation zones into four sub-volumes based on the heterogeneities observed in the structural (orientation and intensity) and hydraulic (transmissivity) information. However, the key assumptions of the geological DFN model have been taken for granted in the work reported here, i.e. the Poisson process and the power-law size distribution. The profit of assuming a simple model is in the mathematics providing powerful analytical equations useful for both general and detailed design and safety assessment calculations. The weak point is in the adaptation to local heterogeneities. This is particularly true in RFM029, where large volumes of rock between the deterministically treated deformation zones are at or below the practical measurement limits of the test equipments, thus difficult to characterise by traditional hydraulic test methods.

The main findings of the presented connectivity analysis are:

- Depending on the assumptions made for the reference size and the borehole radius different geological-hydrogeological DFN solutions are obtained. This shows that both the reference size and the borehole radius are important for the calibration against the borehole fracture frequency, which is a fundamental component of the DFN analysis. The concept of borehole fracture frequency implies that core-drilled boreholes are treated as scanlines in the geological mapping of intersecting fractures. In the core mapping, each fracture is classified as Sealed, Open or Partly Open and with a judgement of how certain the geologist is of this classification – expressed as Certain, Probable and Possible. Partly Open fractures refers to all fractures that do not cut the core entirely but have (1) altered or weathered fracture planes or are (2) associated with a measurable aperture in the borehole wall using BIPS to indicate an edge of a fracture. The number of Partly Open fractures is small but not negligible. Above all they demonstrate that the division of fractures into Open and Sealed is not a clear cut, nor is the definition of fracture frequency.

- The choice of reference size is a geological uncertainty that needs to be treated with concern. In order to make progress in the uncertainty assessment in this matter during the remaining part of the site investigations, it is necessary to compare fracture data from outcrop measurements with fracture data from a number of shallow core-drilled boreholes. If there is little or no consistency on this scale of comparison there is probably even less consistency at depth. In model version 1.2 this information is absent due to the telescoping drilling technique used for the deep core drilling of KFM01A–KFM05A. Fracture data near-surface core drilling and from underground measurements in shafts, drifts and tunnels will be a very valuable piece of information in due time.

- Volumes A–D may be modelled as percolating networks of discrete features, but with quite different hydrogeological DFN properties depending on the assumption of the reference size. This is an important observation that demonstrates the significance of using a connectivity-based analysis in combination with flow simulations.

If a small value of the reference size is assumed (Model 3a) the body of N_{CAL} in Volumes B and C represents isolated features rendering, relatively speaking, smaller values of P_{32CON}, 13% and 26%, respectively. This means that the rock masses between the deformation zones in Volumes B and C consist of very sparsely interconnected hydrogeological DFNs, with c 30–40% of the connectivity above T_{PFLmin}. For Volumes A and D, a small value of the reference size results in no connectivity at all, suggesting a low hydraulic conductivity rock matrix of these HRDs.

If a large value of the reference size is assumed (Model 3b), the hydrogeological DFNs of Volumes B and C become, relatively speaking, well interconnected, but with less than 10% of the connectivity above T_{PFLmin}. Moreover, Volumes A and D now become sparsely connected. In Volume A, c 25% of the connectivity is above T_{PFLmin}, whereas in Volume D zero percent is above T_{PFLmin}. The mean spacing between the flowing features above T_{PFLmin} in Volume D is c 600 m, see Table 5-5, whereas the mean spacing between the connected features below T_{PFLmin} becomes c 33 m, see Table 5-7.

In conclusion, a small or a large value of the reference size lead to different DFN approaches regarding the fracture connectivity, but where the body of the interconnected fractures have transmissivities below T_{PFLmin} in all volumes regardless of the reference size studied. In comparison with a well interconnected DFN the major hydraulic implication of a sparsely interconnected DFN is a much greater uncertainty concerning the relationship between fracture transmissivity and fracture size, cf Figure 5-22 and Figure 5-23.

The validity tests conducted for Volume C in Section 5.7 indicates that Model 3a is only slightly better than Model 3b in terms of explaining the variability seen the 5 m PSS injection tests. Still, the number of 5 m test sections at or below the PSS transmissivity threshold as well as the variability of around the unit slope both suggests that Model 3a is slightly better. The variability between the realisations is great though.

The reason why Model 3b m is chosen for Volume A is because Model 3a cannot provide an interconnected network for this rock mass, see Table 5-7. Possibly one or more of the key assumptions are invalid. For instance, the alternative geological DFN presented in Section 5.3 suggests that the slopes of the power-law size distributions used in the work reported here may be too high thus rendering too many short fractures. For instance, a scaling exponent of 2.75 and a reference size of 0.038 m may produce an equally good fit as the one derived here using k_r = 2.81–3.02 and r_0 = 0.282 m.

Another vital assumption that may be invalid in Volume A is the assumption of a Poisson process for the spatial distribution of the fracture centres in the rock mass. The exceptional pattern and frequency of high-transmissive gently dipping deformation zones above ZFMNE00A2 may be an indicator of unusual stresses. There are currently no data gathered to support a working hypothesis for the hydrogeology, however.

A summary of the hydrogeological DFN findings is given in Table 5-15. The results refer to the orientation data and the scaling exponents provided by the global geological DFN model in Table 5-1. The combination of information in these two tables constitutes the resulting hydrogeological DFN model for RFM029 in the work reported here. This model is likely to be revisited and altered during the coming modelling stages.

Table 5-15. Summary of the hydrogeological DFN results.

Parameter	Volume A	B	C	D
r_w [m]	0	0	0	0
P_{32} [m²/m³]	0.786	3.98	4.70	0.523
r_0 [m]	0.282	0.038	0.038	0.282
P_{32CON} [m²/m³]	0.301	0.512	1.238	0.0741
Rel P_{32}: NS [–]	0.173	0.920	0.111	0.251
Rel P_{32}: NE [–]	0.312	0.558	0.230	0.315
Rel P_{32}: NW [–]	0.164	0.027	0.068	0.034
Rel P_{32}: EW [–]	0.075	0.025	0.056	0.000
Rel P_{32}: HZ [–]	0.276	0.299	0.535	0.400
Correlated T model: a [–]	$7.14 \cdot 10^{-10}$	$8.30 \cdot 10^{-10}$	$3.56 \cdot 10^{-9}$	$7.23 \cdot 10^{-11}$
Correlated T model: b [–]	1.459	0.645	1.451	0.408
T_{100m}[m²/s]	$5.91 \cdot 10^{-7}$	$1.61 \cdot 10^{-8}$	$2.84 \cdot 10^{-6}$	$4.73 \cdot 10^{-10}$
Ratio T_{100m} / T_{10m} [–]	28	4	28	2

5.9 Assessment of block-size properties

The remit for this study, as specified by Repository Engineering, is to calculate Equivalent Porous Media (EPM) statistics of the hydraulic conductivity tensor of 20 m and 100 m blocks using the results from the hydrogeological DFN. The block-size simulations are useful also for the implementation of the DFN findings into a regional scale groundwater flow model. In the latter case, Equivalent Porous Media (EPM) parameters are calculated on the scale of the computational grid resolution, which is c 100 m cf Figure 1-5.

The north-westernmost part of the candidate area has been selected as the target area for continued site investigations /SKB 2005b/. This means that the rock mass properties of Volumes B–D below the gently dipping deformation zone ZFMNE00A2 are of key interest. Figure 5-27 illustrates the north-westernmost part of the candidate area and the simulation domain used in the work reported here to calculate EPM statistics of the hydraulic conductivity tensor. The computational grid of the 1,400 m square domain is parallel with the horizontal principal stresses, with the y-axis pointing NW and the x-axis pointing NE.

The calculations reported here are restricted to treat the rock mass properties of 20 m blocks in the proximity of repository depth, i.e. c 400 m depth, which implies that the focus is put on Volume D (> 363 m depth), cf Figure 5-16. However, the absence of hydraulic information for Volume D imposes imperative constraints, which in practice forces the analysis to treat the more permeable Volume B (222–363 m depth). Figure 5-28 shows the simulation domain in perspective view together with an example of a DFN realisation using the parameter values representative for Volume B, see Table 5-15. Two 1,400 m long horizontal scanlines are inserted at 400 m depth striking NW and NE, respectively. The calculations of the components of the hydraulic conductivity tensor is based on the GEHYCO-method, see Section 2.4.

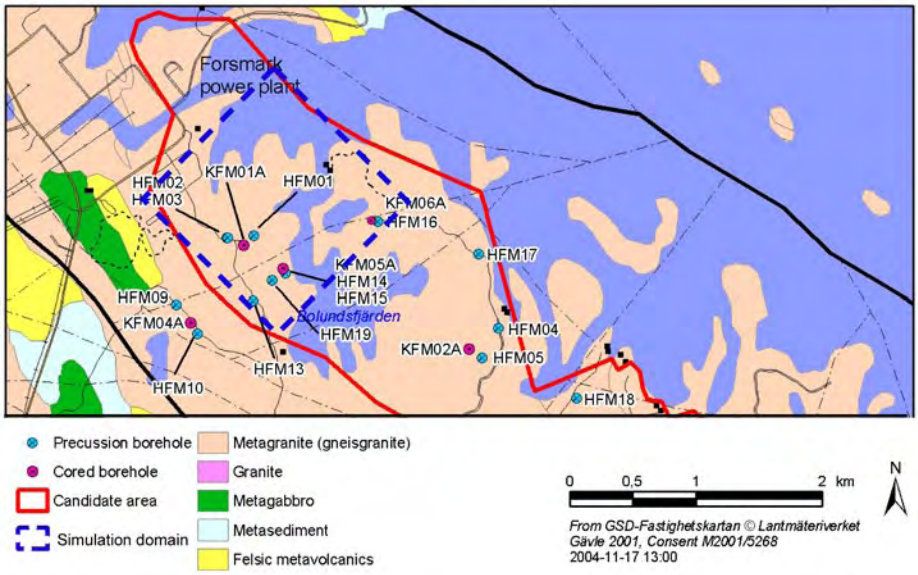

Figure 5-27. *Schematic of the north-westernmost part of the candidate area and the simulation domain used in the work reported here to calculate EPM statistics of the hydraulic conductivity tensor.*

The simulation model used assumes a Poisson process for the distribution of fracture centres and scaling exponents of the five fracture sets as specified in Table 5-1. The results shown in Table 5-16 reveal that the interconnectivity is sensitive to the absolute number of features generated, which in turn is dependent on the truncation size used.

The importance of aiming at a perfect representation of the sparsely connected DFN in Volumes B and D is an open question due to the low transmissivities. It may be advocated that moderately large fractures of low to moderately high transmissivities may not necessarily have much flow in them. This is because the flow rate through a sparsely connected network can be seen as a serial flow system, e.g. a one dimensional pipe-network, and thus governed by the minimum transmissivity value (cf the harmonic mean). It is the probability of occurrence of very large single fractures that do not need other fractures to form connectivity to the nearest deterministically treated deformation zone that constitute the key uncertainty. Such fractures apparently exist in Forsmark even at great depth, see Figure 3-3, and Figure 3-7 through Figure 3-9. Some of these deep flow anomalies are not possible to explain deterministically, whereas others have been possible to tie to lineaments, geophysical anomalies, seismic reflectors, etc. The point made here is that it is vital for hydrogeological DFN that the geological description can delineate the nature of such fractures and incorporate as many of them as possible into the deterministic deformation zone model and thereby reduce the number of unexplained (stochastic) features. If not, the hydraulic behaviour of the rock mass at Forsmark may be characterised as a "hydrogeological DFN of low mean but a high standard deviation".

From a pragmatic point of view there is a trade off between using the best fit truncation size and the limit of the simulation that is possible to run computationally. Hence, a vital issue is how sensitive the calculated EPM block properties are to the truncation size r_{min}. As shown in Table 5-16 the percentage of isolated 20 m blocks decreases as the fracture truncation size decreases; a truncation size of 5.64 m renders that 50% of the 20 m blocks positioned along the two scanlines are isolated (no crossing interconnected fractures), whereas a truncation size of 4.23 m renders 45%. It is noted that the additional interconnectivity associated with a truncation size of 4.23 m provides also an increased survival of larger features.

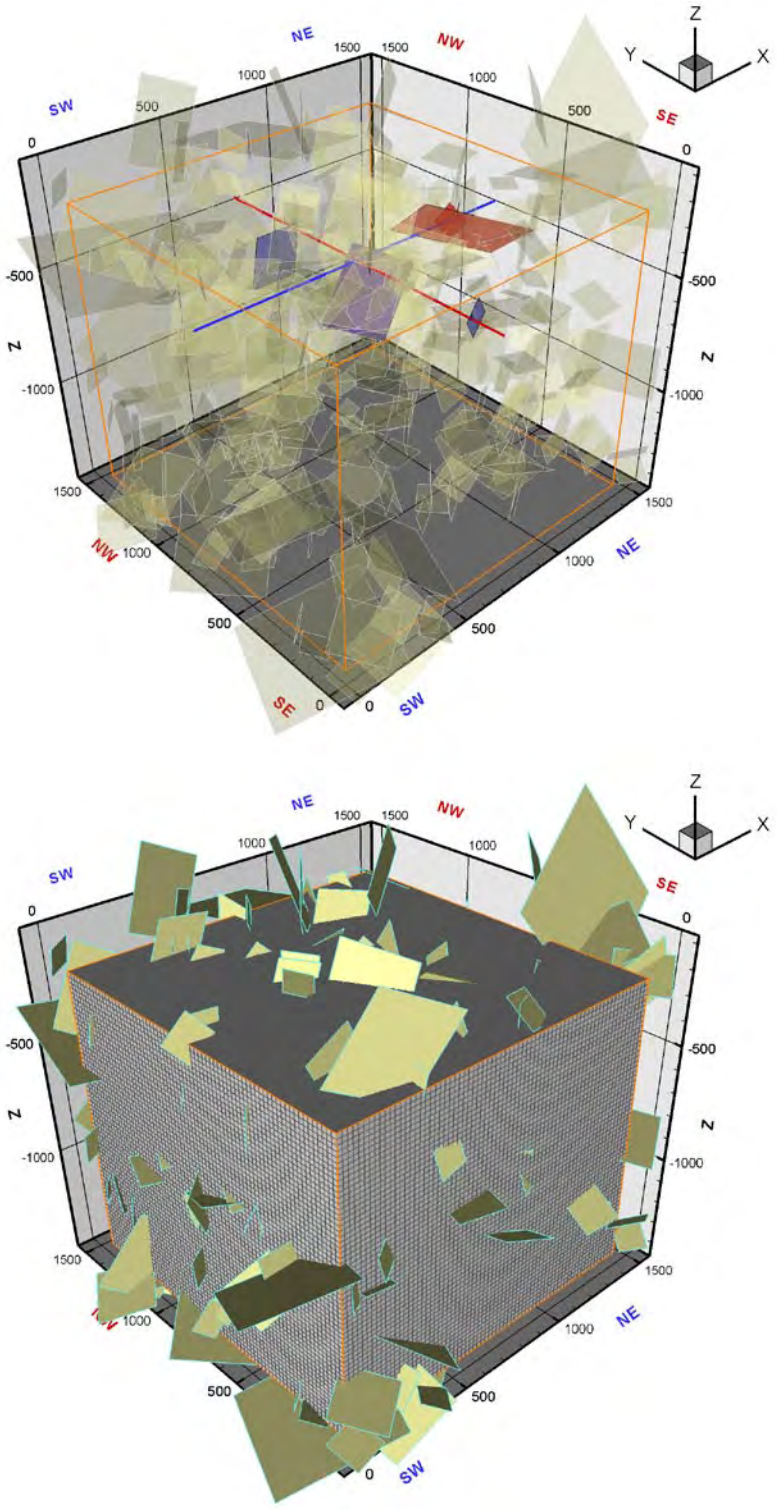

Figure 5-28. *Perspective view of the simulation domain together with a DFN realisation using parameter values representative for Volume B. Two 1,400 m long scanlines were inserted positioned at 400 m depth striking NW and NE, respectively. Interconnected fractures with an equivalent radii greater than 56.4 m (L = 100 m) are shown only. Fractures intersecting the scanlines are coloured in red or blue depending on their strike. In the case shown there are more intersecting features striking NE (blue) but the intersecting features striking NW (red) are longer. This difference follows from the relatively speaking higher intensity of slightly shorter fractures of the NE set in Volume B, cf Table 5-1 and Table 5-15*

Table 5-16. Influence of the truncation size r_{min} on the interconnectivity of a Poissonian simulation model. The truncation size affects the number of intersecting interconnected fractures, hence also the percentage of isolated (non-interconnected) 20 m blocks. ***NIF*** **= number of intersecting interconnected fractures.**

Parameter	Truncation size r_{min} [m]			
	11.3 (*L* = 20)	8.48 (*L* = 15)	5.64 (*L* = 10)	4.23 (*L* = 7.5)
Total no of fractures	40,000	89,000	280,000	648,000
NIF > r_{min}	6	12	14	26
NIF > 28 m [*L* = 50 m]	3	6	8	11
NIF > 56 m [*L* = 100 m]	3	5	4	6
NIF > 113 m [*L* = 200 m]	1	3	4	4
Isolated 20 m blocks	62%	55%	50%	45%

Table 5-17 shows the results of a bracketing calculation with the objective to grasp the range of uncertainty in the log geometric mean of the effective hydraulic conductivity K_{eff}, i.e. the logarithm of $(K_x K_y K_z)^{1/3}$, of the 20 m blocks along the two scanlines in Figure 5-28. The calculations are made for a truncation size of 5.64 m (L = 10 m). An estimate of the upper bound is made by discarding all 20 m blocks that are impermeable in at least one of the directions x, y or z. An estimate of the lower bound is made by assigning a low hydraulic conductivity to these 20 m blocks/directions. (The lowest directional hydraulic conductivity value next to zero encountered in the simulations was used, $1.6 \cdot 10^{-13}$ m/s.) Table 5-17 shows the percentiles of the log effective hydraulic conductivity for the two bounds. The percentiles of the lower bound are estimated from the log-normal probability plot shown in Figure 5-29.

The difference between the medians of the two bounds is huge, almost three orders of magnitude. A fair guess is that the "true median" is somewhere in between, e.g. the geometric mean of the two medians is –11.00. One way to check this is to look at the 20 m PSS data from Volume B in KFM01A. Figure 3-3 reveals that about three to four out of seven 20 m PSS tests are below the measurement limit of the test equipment in Volume B, thus there is some empirical support for the depicted number of c "50% isolated 20 m blocks", cf Table 5-16. Further, the frequency of PFL-f flow anomalies in Volume B is 0.078 m^{-1}, see Table 5-5, which implies a low average of c 1.56 flow anomalies per 20 m block assuming a uniform spacing between the flowing fractures. The product of this frequency times the geometric mean of the PFL-f transmissivities ($4.65 \cdot 10^{-10}$ m^2/s) suggests an average 20 m block log conductivity of –10.44 ($3.63 \cdot 10^{-11}$ m/s), which is pretty close to the aforementioned geometric mean of the two medians obtained from the bracketing calculations.

Table 5-17. Results of a bracketing calculation with the objective to grasp the range of uncertainty in the log geometric mean of the effective hydraulic conductivity K_{eff}, i.e. the logarithm of $(K_x K_y K_z)^{1/3}$, of the 20 m blocks along the two scanlines in Figure 5-28.

Correlated *T* model	Scale	$X_{r,min}$	$Log_{10}(K_{eff})$ [m/s]					
			10%	25%	50%	75%	90%	1σ
Upper bound	20	5.64	–10.17	–9.89	–9.65	–9.14	–9.03	0.60
Lower bound	20	5.64	–15.58	–14.15	–12.55	–10.94	–9.52	2.42

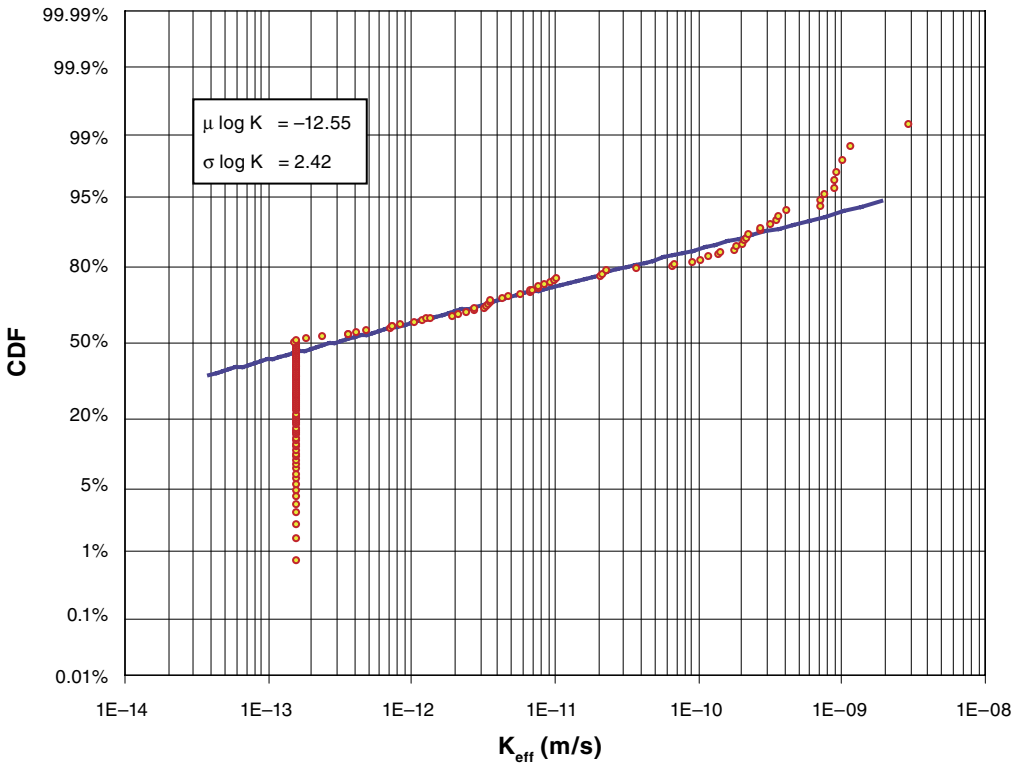

Figure 5-29. *Log-normal probability plot of the effective hydraulic conductivity of 20 m blocks along the two scanlines in Figure 5-25.*

In conclusion, exploration simulations together with field data indicate a low median value and a wide variability of the 20 m log effective hydraulic conductivity in the rock mass immediately above repository depth in the target volume. Concerning hydraulic anisotropy it is noted that Table 5-16 suggest that c 70–80% of the total rock mass fracture intensity in the target volume is associated with two of the five fracture sets, HZ and NE. As already mentioned in Section 5.3 about 85% of the PFL-f anomalies observed in Volumes B and C can be associated with gently dipping fractures.

6 Assessment of hydraulic properties of the Hydraulic Soil Domains

6.1 Background

The regolith, also referred to as the overburden, includes all unconsolidated Quaternary deposits, both glacial deposits such as till, glaciofluvial sediment and clay, as well as postglacial deposits such as marine and lacustrine sediment and peat. The upper part of the overburden, affected by soil-forming processes, is referred to as *the soil*.

All known Quaternary deposits in the Forsmark area were formed during or after the latest glaciation. The oldest deposits are of glacial origin, deposited directly from the inland ice, or by water from the melting ice. The whole area is located far below the highest coastline (more than 120 m), thus the area has been located under the sea during the major part of the Holocene, cf Figure 2-6. Fine-grained sediment has been deposited in local depressions such as the bottom of the lakes and on the present sea floor. Wave action and currents have partly eroded the upper surface of the overburden. Isostatic uplift at Forsmark is still ongoing (6 mm/year) resulting in new land areas emerging from the Baltic (shoreline displacement). The most notable change in the areas uplifted from the Baltic is the development of organic soils, for example the sedimentation of gyttja in the lakes and the formation of peat in the wetlands. The minerogenic Quaternary deposits are affected by coastal and soil-forming processes at the surface, but no major redistribution of these deposits has occurred after the area has been isolated from the Baltic. For a complete description of the present knowledge of the Quaternary deposits in the Forsmark area, see /Lindborg 2005/.

6.2 The surface and stratigraphy of Quaternary deposits

The ground surface of the Forsmark area is flat, dominated by glacial till. Unconsolidated Quaternary deposits cover c 85% of the land area in the regional model area and manmade fill, c 3%. Exposed bedrock (outcrops) occupies c 13% of the land area in the regional model area and only 5% in the central part of the model area.

Glacial till is the oldest known Quaternary deposit in the Forsmark area, deposited directly from the inland ice. The distribution of till in Forsmark is characterised by heterogeneity, in textural composition as well as spatial distribution. The complex composition of the till types makes some generalisations necessary. Based on the composition of the surface layer, three till areas have been distinguished /Sohlenius et al. 2004/. The major part, especially in the west and south, of the model area is dominated by sandy till with medium bolder frequency. At Storskäret and on the island of Gräsö, clayey till with low boulder frequency dominates, see Figure 6-1. At Storskäret, the clayey till is used as arable land and the frequency of bedrock outcrops is generally low. In the area close to the Börstilåsen esker, the till is characterised by a high frequency of large boulders.

The stratigraphical investigations confirm the general pattern of the distribution of the different till types. However, the stratigraphic relations between the different units are complex and have not been fully understood. One example of a complex till stratigraphy is located north of Lake Gällsboträsket. A dark clayey till was revealed under a 1.9 m deep layer of sandy-silty till /Sundh et al. 2004/. The most striking feature about the dark clayey till is the extreme degree of consolidation. Pollen analysis gives the maximum age of deposition

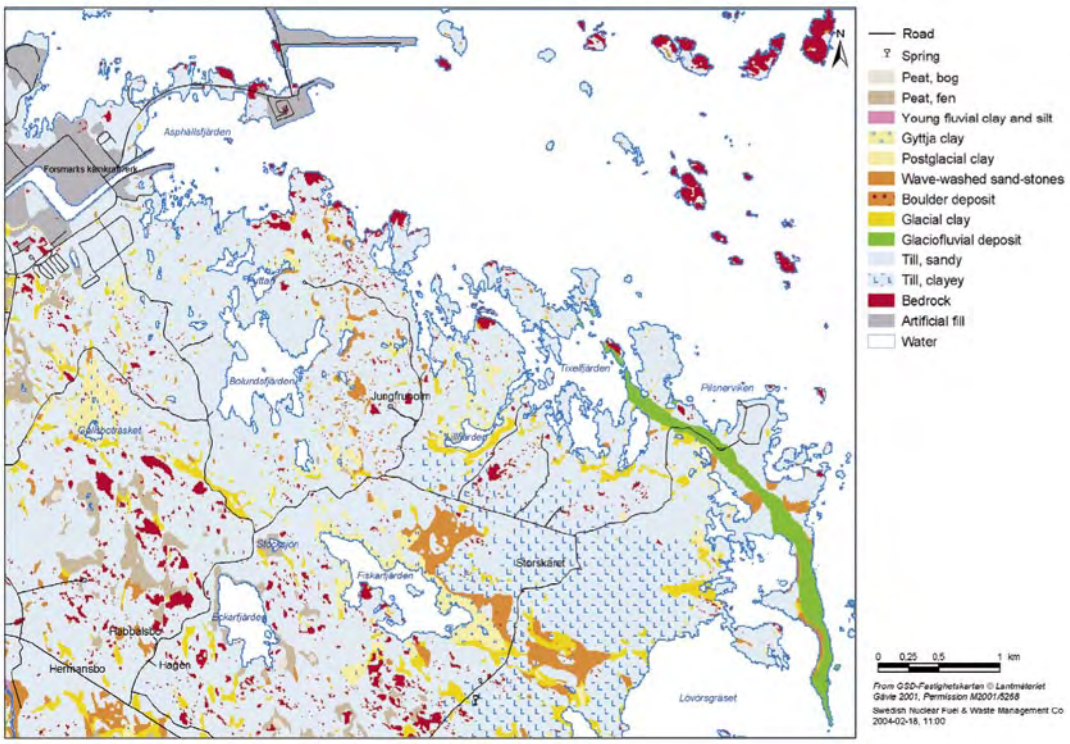

Figure 6-1. *Map showing the spatial distribution of Quaternary deposits in the central part of the Forsmark regional model area /Sohlenius et al. 2004/.*

of the unit to be post Eemian, i.e. some time during the Weichselian glaciation /Robertsson 2004/.

The thickness of the Quaternary deposits, as observed in corings, varies between 0 and 17 m within the investigated area /Johansson 2003/. The depth to bedrock is generally greater in the area covered by clayey till. In the north-western part of the investigated area, the depth to bedrock is generally between 4 and 8 m in the corings performed /Johansson 2003/. Close to drill site 1, the thickness of the till varies between 12 and 4 m although the upper surface of the overburden is quite flat. These variations in depth to bedrock support the concept of a small-scale undulating upper surface of the bedrock, and Quaternary cover that fills out the depressions. Another example of this was observed at the nearby located drill site 5, where a small-scale undulating, fractured bedrock was revealed at excavation.

Glaciofluvial sediments are deposited in a small esker, the Börstilåsen esker, with a flat crest reaching c 5 m above the present sea level. Drilling at the crest showed c 7 m of glaciofluvial sediments (gravel) that rested directly on the bedrock /Werner et al. 2004/. Open sections from abandoned small gravel pits also contain coarse, well-sorted sediment consisting of gravel and stones.

After the deglaciation, c 10,800 years ago, the water level was c 150 m higher than at present, cf Figure 2-6. The distal glaciofluvial sediments, which consist of glacial clay, deposited in stagnant water at some distance from the retreating inland ice, are concentrated in local depressions such as the bottom of lakes and small ponds. Small areas with glacial clay were frequently found during the geological mapping. These deposits are often only a few dm thick and are probably remnants after erosion. Large areas of glacial clay associated with lakes or wetland are situated e.g. south east of Lake Fiskarfjärden and south of Lillfjärden, see Figure 6-1. At these localities, the uppermost surface is often covered by organic sediment.

Postglacial sediments were eroded and re-deposited by waves and streams during the last c 10,000 years. Clay, gyttja clay, sand and peat occur frequently as the superficial Quaternary deposits and cover many small (less than 50 m times 50 m) areas, see Figure 6-1. These small deposits are frequent, but cover only a small part of the total area under investigation. Larger areas of postglacial sediment are e.g. gyttja clay along the shore of Lake Fiskarfjärden and Lake Gällsboträsket.

Figure 6-2 shows the catchment area for Lake Bolundsfjärden together with the calculated depth to bedrock using the program Geo Editor. In areas of low data density, the average modelled soil depth in areas of high density was used (1.9 m).

Compared with the map of Quaternary deposits on land areas, the sea floor is to a larger extent covered by sediments, see Figure 6-3. Offshore Quaternary deposits are dominated by glacial and post-glacial clay, together covering c 55% of the sea floor. The clay in this area occurs most conspicuously in a narrow belt, which trends in NNW and N-S directions. /Carlsson et al. 1985/ have speculated that the occurrence of clay may be linked, in some cases, to deformation zones in the bedrock. The thickness of the offshore Quaternary deposits varies considerably. In the area above SFR, till varies in thickness between 4 and 14 m and clay between 0 and 4 m /Carlsson et al. 1985/. The area covered by glacial till on land is c 75% but only c 30% on the bottom of the Sea. The discrepancy is partly the result of erosion and re-deposition of fine-grained material, e.g. postglacial clay, in the deeper parts still situated below sea level. The discrepancy may also, to some extent, be caused by the different methods used in the mapping.

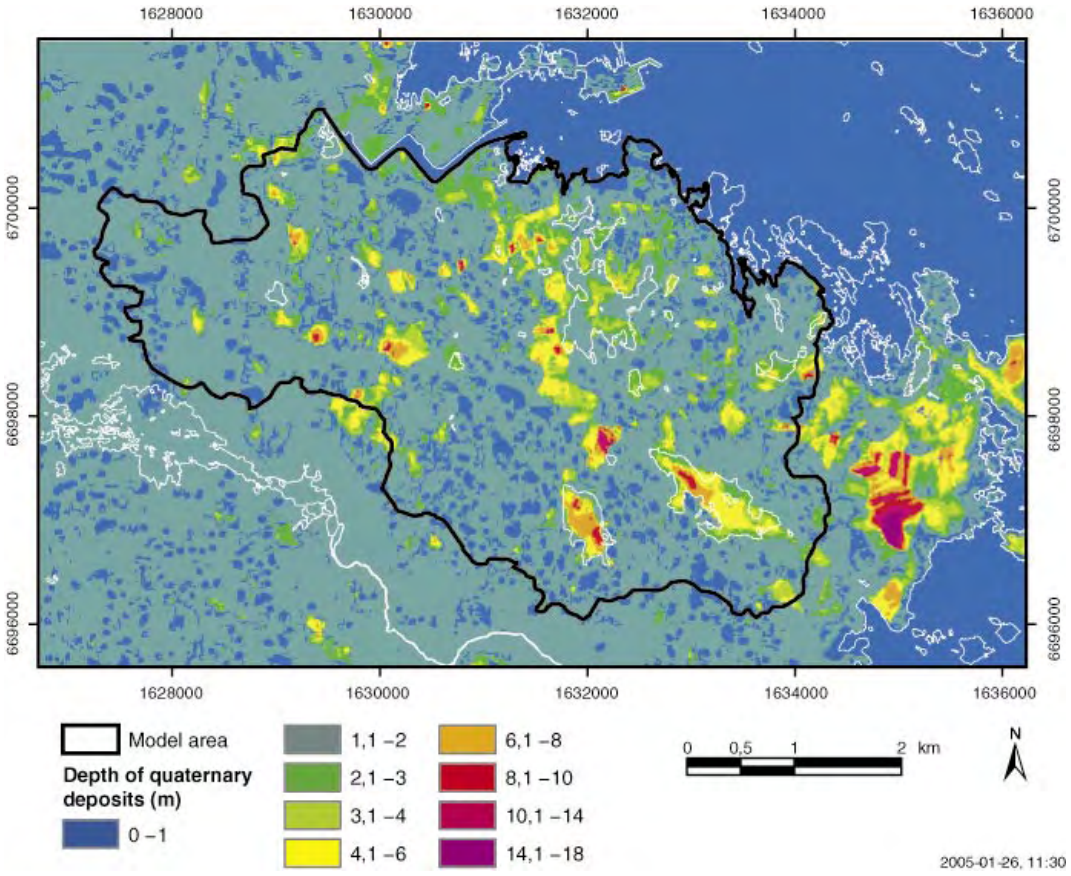

Figure 6-2. *Map showing the depth to bedrock, based on the soil depth modelling in Geo Editor. A near-surface hydrogeological model (Mike-SHE) is developed to study the water balance within the black solid line /Vikström 2005/.*

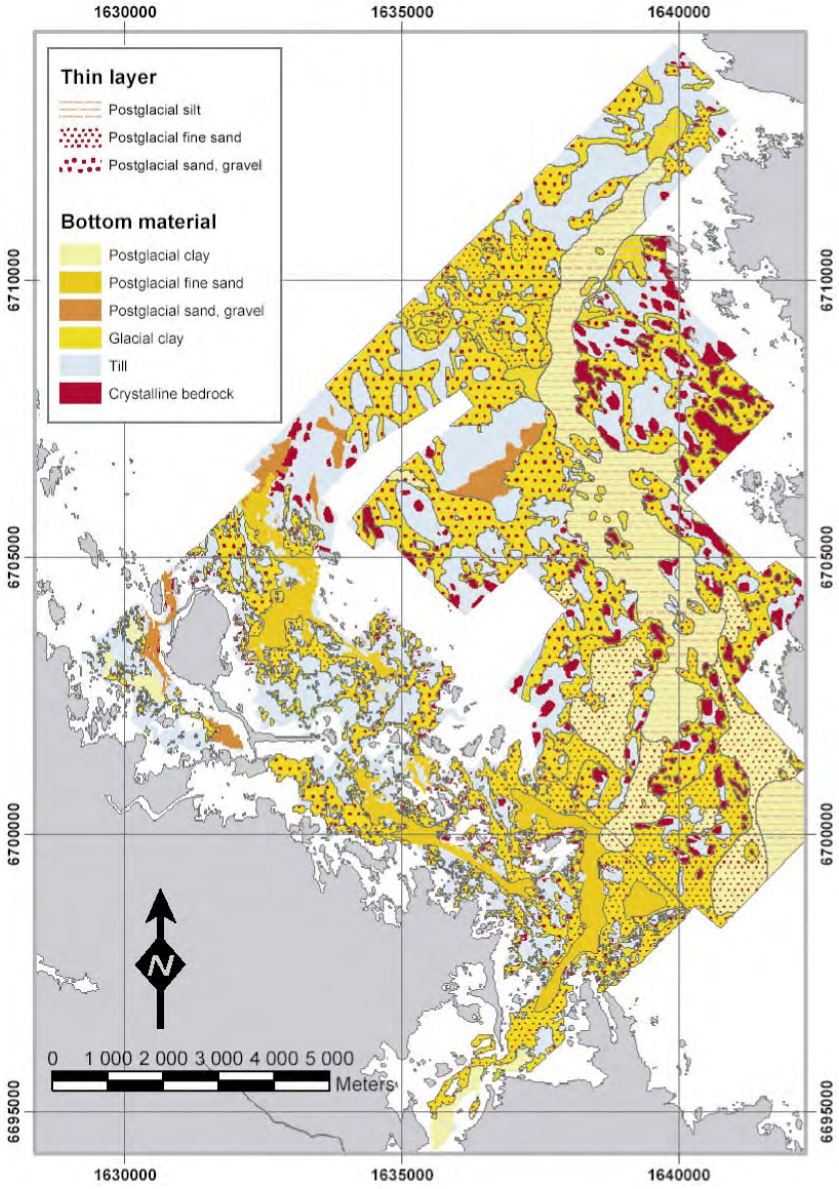

Figure 6-3. *Map showing the distribution of Quaternary deposits on the sea floor /Elhammer and Sandkvist 2005/.*

6.3 Conceptual and descriptive near-surface modelling

The conceptual and descriptive modelling of the meteorological, surface hydrological and near-surface hydrogeological conditions in the Forsmark area is presented in /Johansson et al. 2005/. The model area is characterised by a low relief and a small-scale topography; almost the whole area is located below 20 metres above sea level. The corrected mean annual precipitation is 600–650 mm and the mean annual evapotranspiration can be estimated to a little more than 400 mm, leaving approximatley 200 mm/year for runoff. In total, 25 "lake-centred" catchments, ranging in size from 0.03 to 8.67 km^2 have been delineated and described within the model area. The 25 mapped lakes range in size from 0.006 to 0.752 km^2. The lakes are very shallow with maximum depths ranging from 0.4 to 2.0 m. No major watercourses flow through the model area. Wetlands are frequent and cover 10–20% of the areas of the three major catchments, and up to 25–35% of some sub-catchments. The conceptual model of the near-surface hydrogeological conditions is illustrated in Figure 6-4.

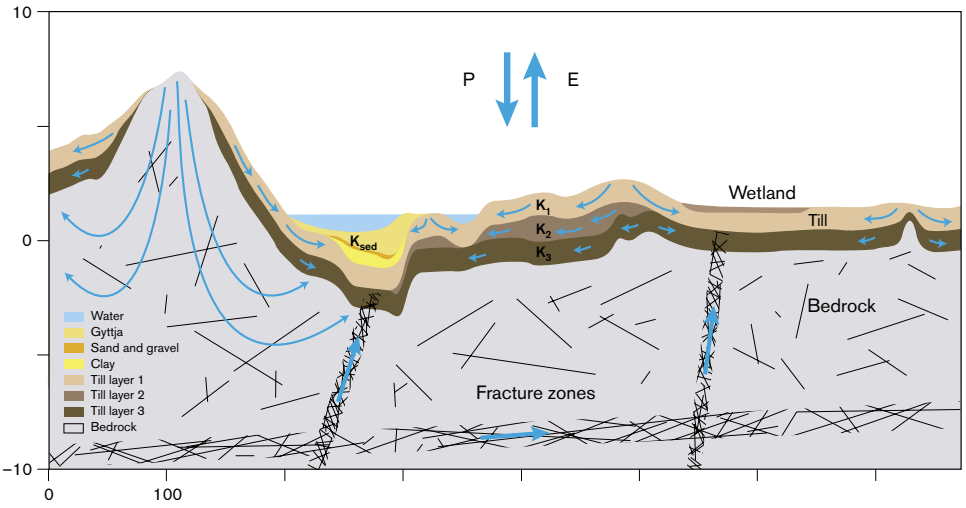

Figure 6-4. *Schematic profile illustrating a conceptual model of the near-surface hydrogeological conditions (note that horizontal and vertical scales are different).*

Table 6-1 shows the proposed geometric mean hydraulic properties of the Quaternary deposits for model version 1.2.

The locations of the groundwater monitoring wells are shown in Figure 6-5. The body of the wells are located in coarse (sandy) and fine-grained (clayey) till and the average thickness of the overburden at these locations of the wells is circa four metres. Figure 2-8 shows the daily average depth of the hydraulic head below ground surface in the monitoring wells.

Figure 6-5 suggests that the detailed hydrogeological conditions in large parts of the regional model domain are essentially unknown. According to /Werner and Johansson 2003, Werner 2004/ the existing hydraulic data show a considerable heterogeneity. For the bedrock hydrogeological modelling reported here it was decided to use a simplistic description of the near surface hydrogeological conditions. The trade off was further motivated by the need of a sufficient detailed description of the bedrock conditions at depth, which put constraints on the numerical modelling.

Table 6-1. Proposed approximate geometric mean hydraulic properties of the Quaternary deposits for a simplified three-layer till profile. The values of the hydraulic conductivity data were based on the slug test results reported by /Werner and Johansson 2003, Werner 2004/. The values for the total porosity, the flow and the specific storativity are generic and estimated from /Knutsson and Morfeldt 2003/.

Layer	Hydraulic conductivity K [m/s]	Total porosity ε_t [–]	Flow Porosity ε [–]	Specific Storativity S_s [m^{-1}]
0 to 1 m below ground	$1.5 \cdot 10^{-5}$	0.35	0.10	$1 \cdot 10^{-4}$
Middle layer				
Coarse till	$1.5 \cdot 10^{-6}$	0.25	0.05	$1 \cdot 10^{-4}$
Clayey till	$1.5 \cdot 10^{-7}$	0.25	0.03	$1 \cdot 10^{-4}$
0 to 1 m above bedrock	$1.5 \cdot 10^{-5}$	0.25	0.05	$1 \cdot 10^{-4}$

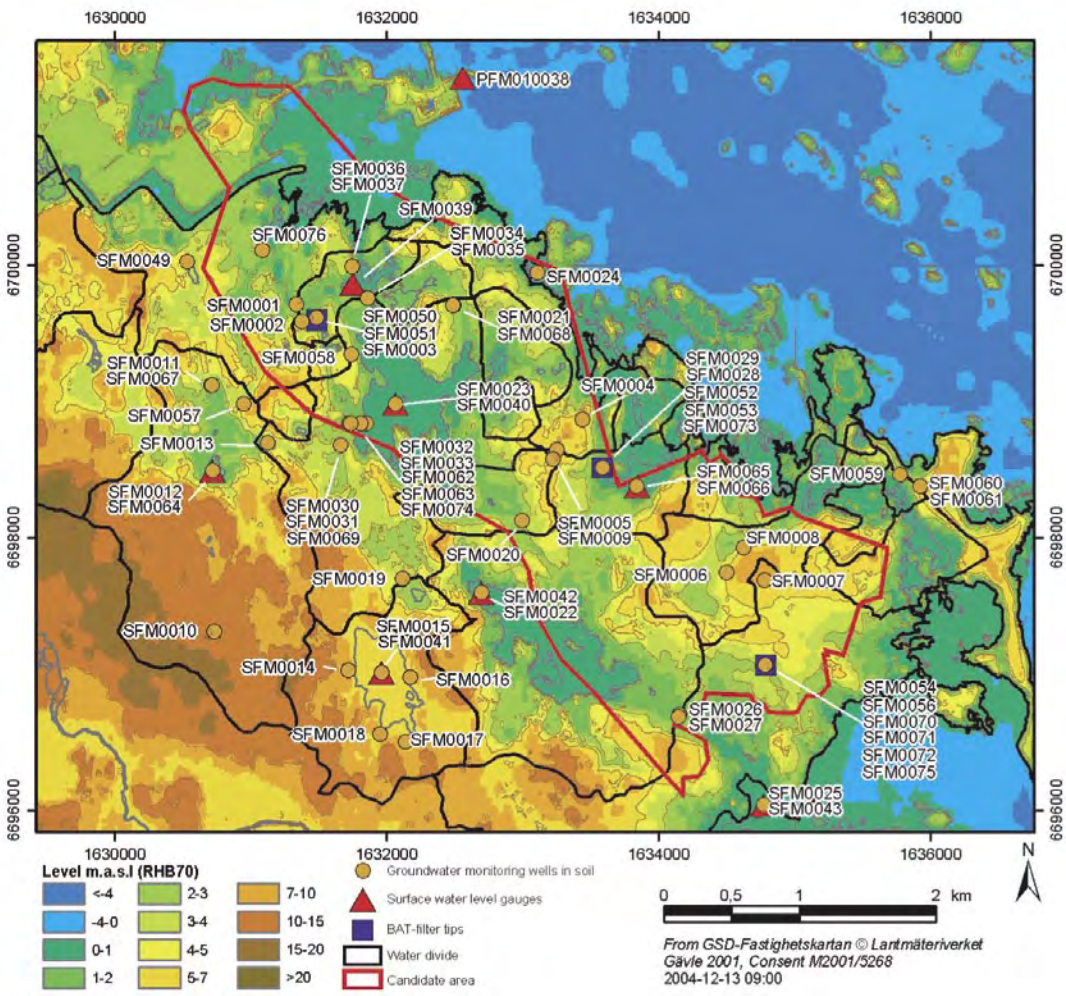

Figure 6-5. *Location of groundwater monitoring wells, abstraction wells, BAT-type filter tips and surface water level gauges (SKB-GIS).*

The chosen HSD model consists of a single layer of sandy till except in small discrete areas where the bedrock is outcropping. The surface properties are represented explicitly in the model and properties are assigned to each grid cell according to whether the cell is predominantly covered by till or exposed rock. Homogeneous and isotropic properties over the entire model domain are used away from the outcrops. The properties used are: a four metres thick layer of sandy till with a hydraulic conductivity of $7.5 \cdot 10^{-6}$ m/s, a flow porosity of 0.05, and a specific storativity of $1 \cdot 10^{-4}$ m^{-1} (P O Johansson, personal communication, December 2004).

It is noted that the near-surface hydrogeological conditions illustrated in Figure 6-4 indicate a much more complex hydrogeology between ground surface and the near-surface deformation zones. This suggests that the simple description chosen may cause difficulties in the matching against measured data in the regional flow simulations.

7 Regional groundwater simulations

The final two steps of the workflow shown in Figure 2-2 involve calibration of the regional flow model against hydraulic and hydrogeochemical measurements and palaeo-hydrogeological simulations, respectively. The latter task comprises flow path simulations and sensitivity tests. In practice, there are not clear distinctions between these steps. For instance, calibration becomes meaningful only if the flow model is free from uncertainties in respect of the size of model domain, choice of boundary conditions and the resolution of the computational grid. Simulations with a non-calibrated model can also be of importance provided that the questions asked are correct vis-à-vis the hydrogeological simplifications (uncertainties). For example, if regional hydrogeological uncertainties can be shown to have little effect on the flow paths within the target volume, although the model domain is simulated to be much more conductive than suggested by the hydraulic field tests, the conclusions drawn from the simulations still ought to be of significance.

7.1 Conceptual models for groundwater flow

The results shown in Table 5-5 and Table 5-7 are schematically illustrated in Figure 7-1. The mean vertical spacing between the interconnected fractures (*c/c CON*) is c 9 m in Volume A (Model 3b), c 5 m in Volume B (Model 3a), c 1.5 m in Volume C (Model 3a) and c 33 m in Volume D (Model 3b). The mean vertical spacing between the flow anomalies (*c/c PFL-f*) is c 37 m in Volume A, c 13 m in Volume B, c 5 m in Volume C and c 600 m in Volume D. The majority of the fracture transmissivities are below T_{PFLmin}, see Table 5-7.

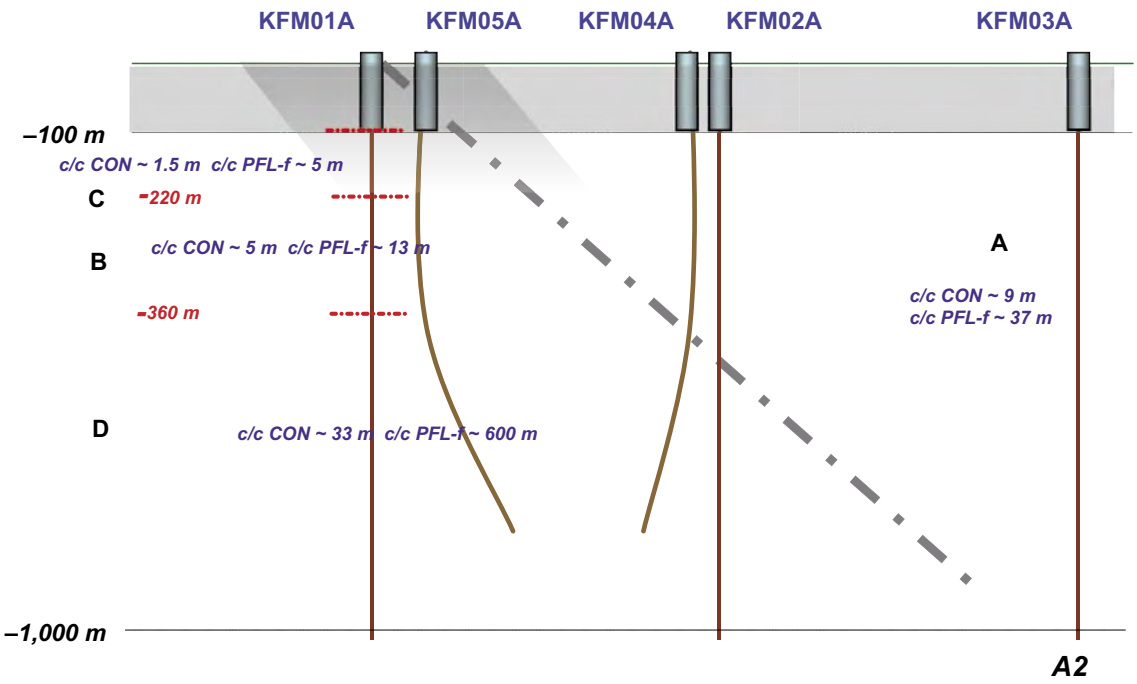

Figure 7-1. *Schematic visualisation of RFM029 and the deduced hydrogeological DFN results. c/c CON and c/c PFL-f denote the mean vertical spacing between the interconnected fractures and between the flow anomalies greater than T_{PFLmin}, respectively.*

Different hydrogeological DFN models may be discussed for the rock mass RFM029 in Forsmark ranging from a quite low conductive rock mass characterised by a very sparsely interconnected and low-transmissive DFN (Volume D) to a moderately conductive rock mass characterised by a well interconnected and moderately-transmissive DFN (Volume C). The existence of interconnected fractures below the lower measurement of the PFL-f tests is an open question, but the findings of the hydrogeological DFN analysis reported here suggest that such networks exist in all Volumes A–D, cf Figure 7-1.

The hydraulic contrast between the high-transmissive deformation zones and the low-transmissive rock mass fractures suggest that the hydrogeological system in RFM029 is not at steady state. This picture is reinforced by the ongoing shoreline displacement and the associated variable-density flow periods. Although the DFN approach appears to be the most obvious flow approach for the rock mass in Forsmark the use of a continuum approach in parallel may provide a means for fruitful discussions about the differences observed when the simulations are compared with measurements. If the differences are small regardless of the approach used, the measured data are probably not sufficient to constrain the conceptual modelling. If the differences are great regardless of the approach used, both approaches probably need to be revised unless there are errors or great uncertainties in the measured data. If one of the approaches is much better than the other, the reason for the differences needs to be understood.

The choice of approach is also related to the spatial and temporal scales of the flow problem, the computational resources and the capabilities of the computer code. By scales we mean the size of the model domain and the time frame of the processes considered as well as the resolution of the computational grid and the chosen time step. On a regional scale it is generally necessary to use a more or less coarse grid resolution if a continuum approach is used and a truncated power-law size distribution if a fully discrete approach is used. The time frame of the palaeo-hydrogeological problem is set to 10,000 years, cf Figure 2-6, which constrains the size of the minimum time step in order to keep the execution time at a minimum. Moreover, in the continuum approach is necessary to assign hydraulic properties to those grid cells not intersected by fractures if a structured grid is used, which implies that some kind of background rock (matrix) needs to be considered. By the same token, it is necessary to define a dual porosity system in the fully discrete approach in order to account for matrix diffusion.

The version of the DarcyTools code used in the work reported here is based on a structured grid. The capabilities of the code are originally developed to model flow and transport through fractured rocks with the EPM approach as we know them at the Äspö HRL, e.g. /Svensson 1997ab, 1999/. For sparsely interconnected and low-transmissive DFNs as suggested by the hydrogeological DFN analysis reported here large volumes of the flow domain need to be assigned background rock properties. Due to the uncertainties associated with the upscaling of a DFN to an EPM given the conditions at Forsmark it was decided to carry out the intended regional variable-density flow simulations and advective particle tracking with DarcyTools using a simple multicomponent continuous porous media (CPM) model. The main objectives of this approach are to provide: (i) a bounding check on the more complex EPM model treated by the *ConnectFlow Team* /Hartley et al. 2005/, (ii) a comprehensible assessment in which the effects of specific assumptions are easily traced, and (iii) identification of key sources of uncertainty. The comparison of the results produced by the two modelling teams will be carried out by SKB's Site Analysis Team for Forsmark.

The multicomponent CPM model represents the rock masses between the Eckarfjärden and Singö deformation zones by a few low-conductive CPMs, based on the hydrogeological DFN analysis of Volumes A–D. The rest of the regional model domain is characterised as a single CPM because there are very little data from outside the 'tectonic lens' with which to parameterise a more sophisticated model. The multicomponent CPM honours the observation in the core-drilled boreholes that there is little flow through the deeper parts of the rock mass of RFM029, in particular below the gently dipping deformation zone ZFMNE00A2. Hence, the bulk of the groundwater flow through the multicomponent CPM is governed by the connectivity and hydraulic properties of the deterministically treated deformation zones.

Figure 7-2 illustrates the multicomponent CPM. The conductivity values in Table 7-1 mimics the 100 m PSS tests shown in Figure 3-3. The other values are deduced in the hydrogeological DFN analysis by applying Equations (2-1), (2-2) and (2-26).

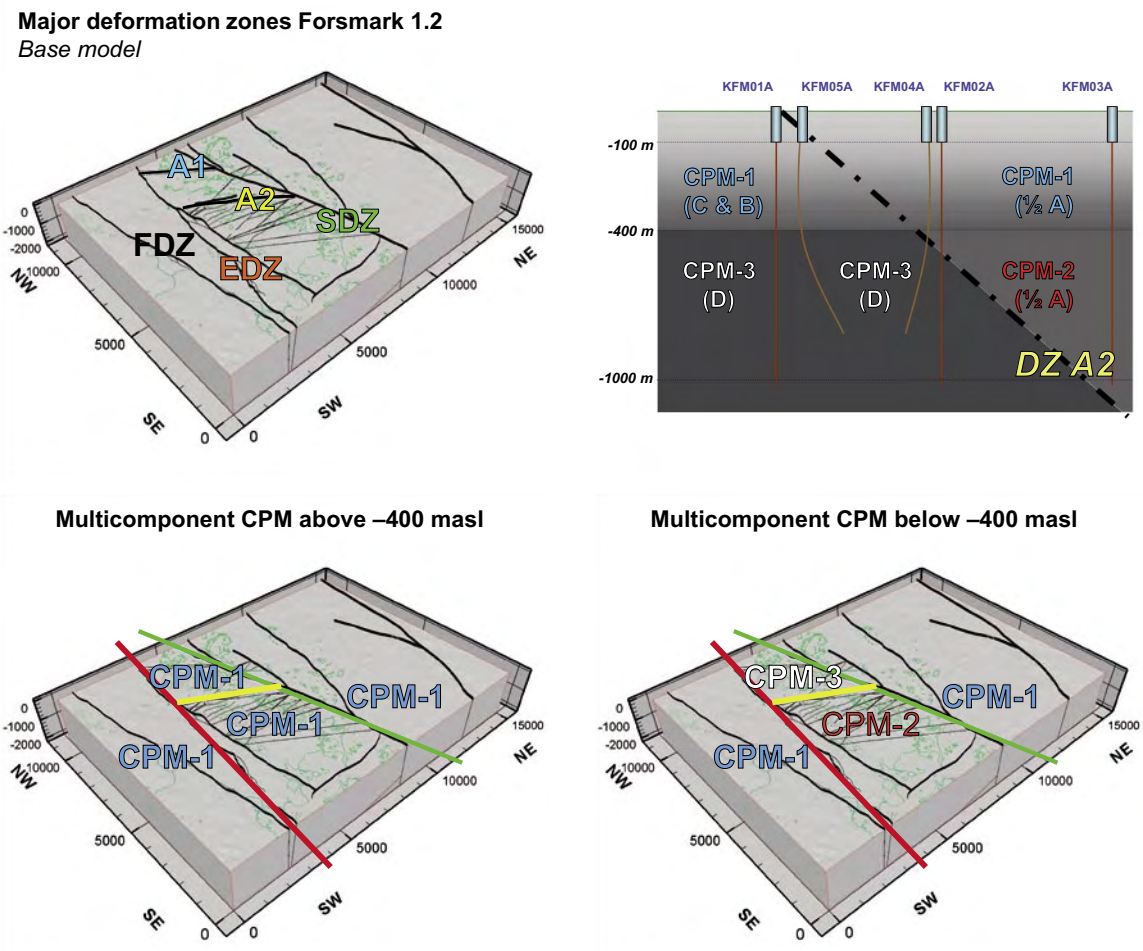

Figure 7-2. *Upper left: Base model: FDZ = Forsmark DZ, EDZ = Eckarfärden DZ, SDZ = Singö DZ, A1 = ZFMNE00A1 and A2 = ZFMNE00A2. Upper right: Suggested division of RFM029 into a multicomponent CPM model. Lower left and right: Lateral distribution of the multicomponent CPM above and below –400 masl: Red line = EDZ, Green line = SDZ, and Yellow line = ZFMNE00A2.*

Table 7-1. Reference parameter values selected for the multicomponent CPM model.

Property	CPM-1 (½ A, B, C) Above –400 masl Above/Below A2	CPM-2 (½ A) Below –400 masl Above A2	CPM-3 (D) Below –400 masl Below A2
Hydraulic conductivity K [m/s]	$1 \cdot 10^{-6} – 5 \cdot 10^{-10}$	$5 \cdot 10^{-10}$	$5 \cdot 10^{-11}$
Flow porosity ε [–]	$1 \cdot 10^{-4} – 2 \cdot 10^{-5}$	$2 \cdot 10^{-5}$	$5 \cdot 10^{-6}$
Specific storativity S_s [m^{-1}]	$7 \cdot 10^{-6} – 2 \cdot 10^{-8}$	$2 \cdot 10^{-8}$	$2 \cdot 10^{-9}$

It is recognised that the multicomponent CPM model is not an evident simplification given the conditions at Forsmark. The low-conductive rock masses in Volume D, the target volume, are in some areas closer to ground surface than to the nearest transmissive deformation zones. Given the better interconnected and more transmissive fracturing associated with Volumes B and C the demarcation of rock mass properties for Volume D is foreseen to be a vital issue for Safety Assessment in future model versions. More boreholes of different orientations need to be drilled during coming stages.

Discrete pathways in terms of gently or steeply dipping large fractures of moderate transmissivity may reach into Volume D from above and, if so, will create flow paths in between the outcropping and more regionally interconnected deformation zones i.e. flow cells of local recharge and discharge. Factors that determine this behaviour are among others (i) the interconnectivity, orientation and transmissivity of the rock mass fracturing in Volumes B–D, and (ii) the relative strength of the local versus the regional boundary conditions. In contrast, the multicomponent CPM model is at every point a part of a continuous flow field (cf Figure 2-1), which suggests that the qualitative and quantitative success of the using the multicomponent CPM model at Forsmark is highly sensitive to the assumption of a low magnitude of the rock mass hydraulic diffusivity and the properties of the deterministically treated deformation zones.

Another important implication of using a multicomponent CPM using DarcyTools concerns the computation of grid cell flow wetted surface. With this approach the occurrence of grid cell flow wetted surface is restricted to those grid cells intersected by deterministically treated deformation zones. For the remaining grid cells there are no intersecting discrete objects and consequently no flow wetted surface that can be used to distribute the global capacity ratio, see Section 2.5. In order to circumvent this problem a uniform and low value of the flow wetted surface is assigned to all grid cells not intersected by deterministically treated deformation zones. This allows the grid cell capacity ratio to be calculated throughout the model domain as described in Section 2.5 and, hence, matrix diffusion to be modelled.

It is noted that the incorporation of matrix diffusion of salt in a low-conductive rock mass surrounded by high-transmissive deformation zones is a matter of great conceptual interest as it raises questions concerning the role of the assumed initial condition of the salinity profile at 8,000 BC. Moreover, concerning the transport performance measure known as the F-quotient it is noted that the calculations become quite arbitrary using a uniform and low value of the flow wetted surface in all grid cells not intersected by deterministically treated deformation zones. For this reason it was decided to not consider the F-quotient calculations in the work presented here as the calculations are not based on an underpinning DFN.

7.2 Objectives

The main objectives of the regional flow modelling are to achieve the following:

I. *Palaeo-hydrogeological understanding*: An improved understanding of the palaeo-hydrogeological conditions is necessary in order to gain credibility for the site descriptive model in general and the hydrogeological description in particular. This requires modelling of the groundwater flow from the last glaciation up to present-day with comparisons against measured TDS and other hydro-geochemical measures.

II. *Simulation of flow paths*: The simulation and visualisation of flow paths from a tentative repository area is a means for describing the role of the current understanding of the modelled hydrogeological conditions in the target volume, i.e. the conditions of primary interest for Safety Assessment. Of particular interest here is demonstration of the need for detailed far-field realism in the numerical simulations. The motivation for a particular model size (and resolution) and set of boundary conditions for a realistic description of the recharge and discharge connected to the flow at repository depth is an essential part of the groundwater flow path simulations.

With regard to the aforementioned objectives of the multicomponent CPM model the regional flow simulations conducted started out with the second objective in mind. That is, a series of sensitivity cases are treated by means of particle tracking to study the need for detailed far-field realism. This to gain an understanding of how the uncertainty of different primary model parameter assumptions interplay with the low-conductive target volume, and ultimately to what extent these parameters contribute to a reasonable match to the field data (palaeo-hydrogeological understanding).

Eventually, an attempt is made to achieve a reasonable matched flow model (first objective) despite the simplification associated with a multicomponent CPM flow model.

7.3 Sensitivity analysis

The sensitivity cases encompass analyses of:

A. Model domain (boundary conditions) and deformation zones.

B. Undulation of groundwater table.

C. Initial conditions for salinity.

D. Deformation zone heterogeneity.

E. Hydraulic anisotropy of near surface rock.

F. Low-confidence deformation zones.

G. Gently dipping deformation zones.

H. A multifactor sensitivity case.

I. Shoreline displacement and particle traces at 5,000 AD.

Each sensitivity case is run for 10,000 years (except Case I, which is run for 13,000 years). Particles are released at the end of the simulation period in the target area shown in Figure 1-5. The particle tracking is made for 2,814 particles during 30,000 years to ensure a sufficient sampling statistics. Apart from that, the 30,000 years is useless information, since the hydrogeological conditions are fixed to represent the state of the system as modelled at

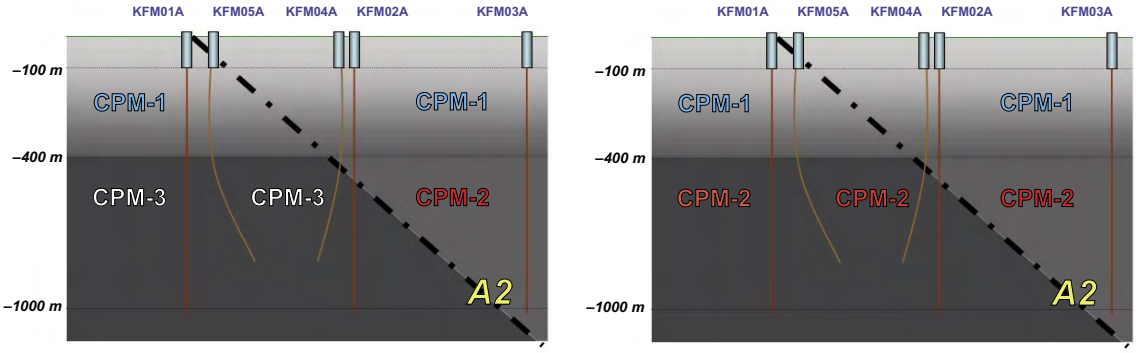

Figure 7-3. *Left: The CPM Reference Case used in palaeo-hydrogeological simulations (cf Table 7-1). Right: The CPM Modified Case used in the sensitivity analysis.*

2,000 AD (5,000 AD for Case J), i.e. there is no shoreline displacement during the particle tracking. The particles are released just below 400 m depth in a regular grid using a spacing of 50 m, regardless if they coincide with a deterministically treated deformation zone.

In order to make the particle tracking workable it was found necessary to modify the hydraulic conductivity within the target volume, i.e. CPM-3, by a factor of 50, from $1 \cdot 10^{-11}$ m/s to $5 \cdot 10^{-10}$ m/s, see Figure 7-3. If the CPM Reference Case value of $1 \cdot 10^{-11}$ m/s is used for CPM-3, cf Figure 7-2 and Table 7-1, c 80% of the particles do not discharge within 30,000 years, thus implying a median travel time of at least 30,000 years. In the CPM Modified Case all particles discharge within 30,000 years with a median travel time of 183 years. Hence, a much greater hydraulic conductivity value is treated for the target volume in the sensitivity cases reported here than suggested by the 100 m PSS tests conducted in KFM01A and KFM02A, see Figure 3-3.

Table 7-2 summarises the hydrogeological properties and conditions of the CPM Reference Case used in the palaeo-hydrogeological simulations and the CPM Modified Case used in the sensitivity analysis. For the modelling of multi-rate diffusion of salt parameter values reported by /Svensson 2004b/ for the modelling of Task 6C in the Äspö Task Force are used. The reason for not including multi-rated diffusion in the CPM Reference Case is explained below.

Figure 7-4 and Figure 7-5 illustrate flow paths of the particle tracking for the CPM Modified Case together with the major deformation zones, the present-day shoreline and lakes, the regional water divide and the steeply inclined boreholes KFM01A–KFM03A. Note the resolution of the computational grid indicated by the three columns of cells encompassing KFM01A–KFM03A.

Figure 7-4 and Figure 7-5 suggest essentially two locations of major discharge. The majority of the released particles are at first moving downwards and thereafter towards the coast. On their way they are either captured by the gently dipping deformation zones ZFMNE00A1 and ZFMNE1193 or the steeply dipping Singö deformation zone (ZFMNE0001). The other major discharge location is governed by the steeply dipping deformation zones intersecting the gently dipping deformation zone ZFMNE00A2, e.g. ZFMNE0060–62. These flow paths occur in the southwest corner of the target volume and are essentially vertical, some of which are discharging into Lake Bolundsfjärden.

Table 7-2. Summary of the hydrogeological properties and conditions for the CPM Reference Case used in the palaeo-hydrogeological simulations and the CPM Modified Case used in the sensitivity analysis.

Parameter	CPM Reference Case	CPM Modified Case
Model domain and grid resolution	15×11×2.1 km with a 100 m cell size except in the vertical between ground surface and 400 m depth where the mean cell size is c 30 m.	15×11×2.1 km with a 100 m cell size except in the vertical between ground surface and 400 m depth where the mean cell size is c 30 m.
Initial conditions	Full Glacial / fresh between 0 and 450 m depth; then linear gradient to no Glacial / full Brine / salinity at 1,950 m depth.	Full Glacial / fresh between 0 and 450 m depth; then linear gradient to no Glacial / full Brine / salinity at 1,450 m depth.
Top boundary condition (BC)	Head equals topography.	Head equals topography.
Lateral BC	No-flux.	No-flux.
Bottom boundary BC	No-flux.	No-flux.
Top surface waters types	Before 7,500 BC – Baltic Ice Ancylus Ice Lake (Glacial). 4,500 BC – Littorina Sea reaches its maximum salinity then successively changing to present-day condition. After 2,500 BC – Meteoric precipitation with land rise.	Before 7,500 BC – Baltic Ice Ancylus Ice Lake (Glacial). 4,500 BC – Littorina Sea reaches its maximum salinity then successively changing to present-day condition. After 2,500 BC – Meteoric precipitation with land rise.
HCD transmissivity T	Equations (4-1a,b), i.e. HCD1 with slightly modified depth dependence for a few DZ.	Equations (4-1a,b), i.e. HCD1.
HCD storativity S	Equation (2-1).	Equation (2-1).
HCD aperture e_t	Equation (2-2).	Equation (2-2).
HRD hydraulic conductivity K, flow porosity ε and specific storativity S_s	Multicomponent CPM with properties CPM-1, CPM-2 and CPM-3 according to Table 7-1 and Figure 7-3 (left).	Multicomponent CPM with properties CPM-1 and CPM-2 according to Table 7-1 and Figure 7-3 (right).
Ratio of immobile volume to mobile β_G	No matrix diffusion.	10
Multi-rate coefficients $[\alpha_{min}, \alpha_{max}]$	No matrix diffusion.	$[1\cdot10^{-10}, 1\cdot10^{-3}]$
Flow wetted surface area per unit area	No matrix diffusion.	2 m^2 per m^2 fracture.

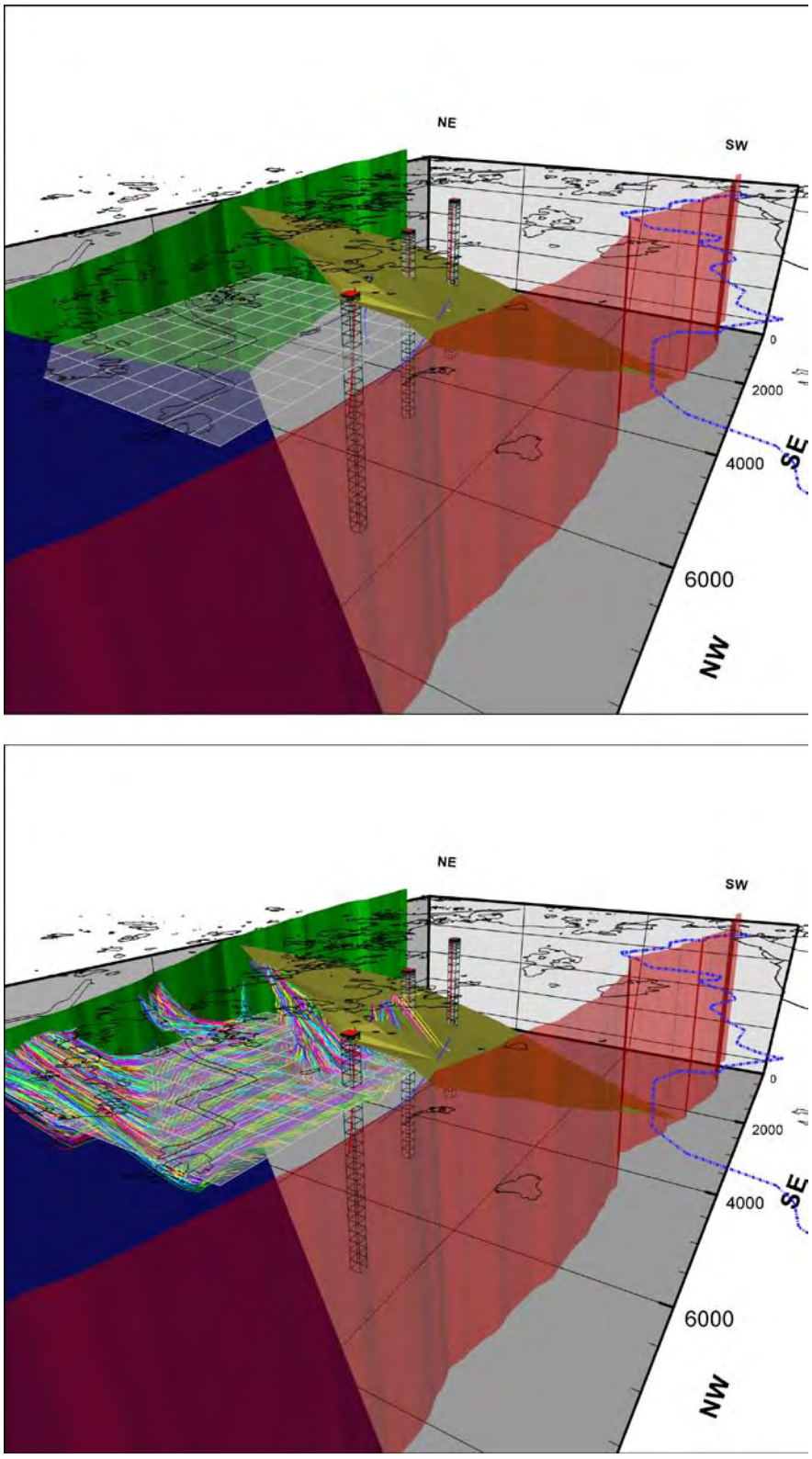

Figure 7-4. *Perspective views towards E of the release area within the target volume and the flow paths of 2,184 particles for the CPM Modified Case. The deformation zones are Singö (green), Eckarfjärden (Red), ZFMNE00A1 (blue) and ZFMNE00A2 (yellow). The present-day shoreline and lakes, boreholes KFM01A–KFM03A and the regional surface water divide are also indicated as well as the resolution of the computational grid. The interpretation of flow paths is commented on in the text.*

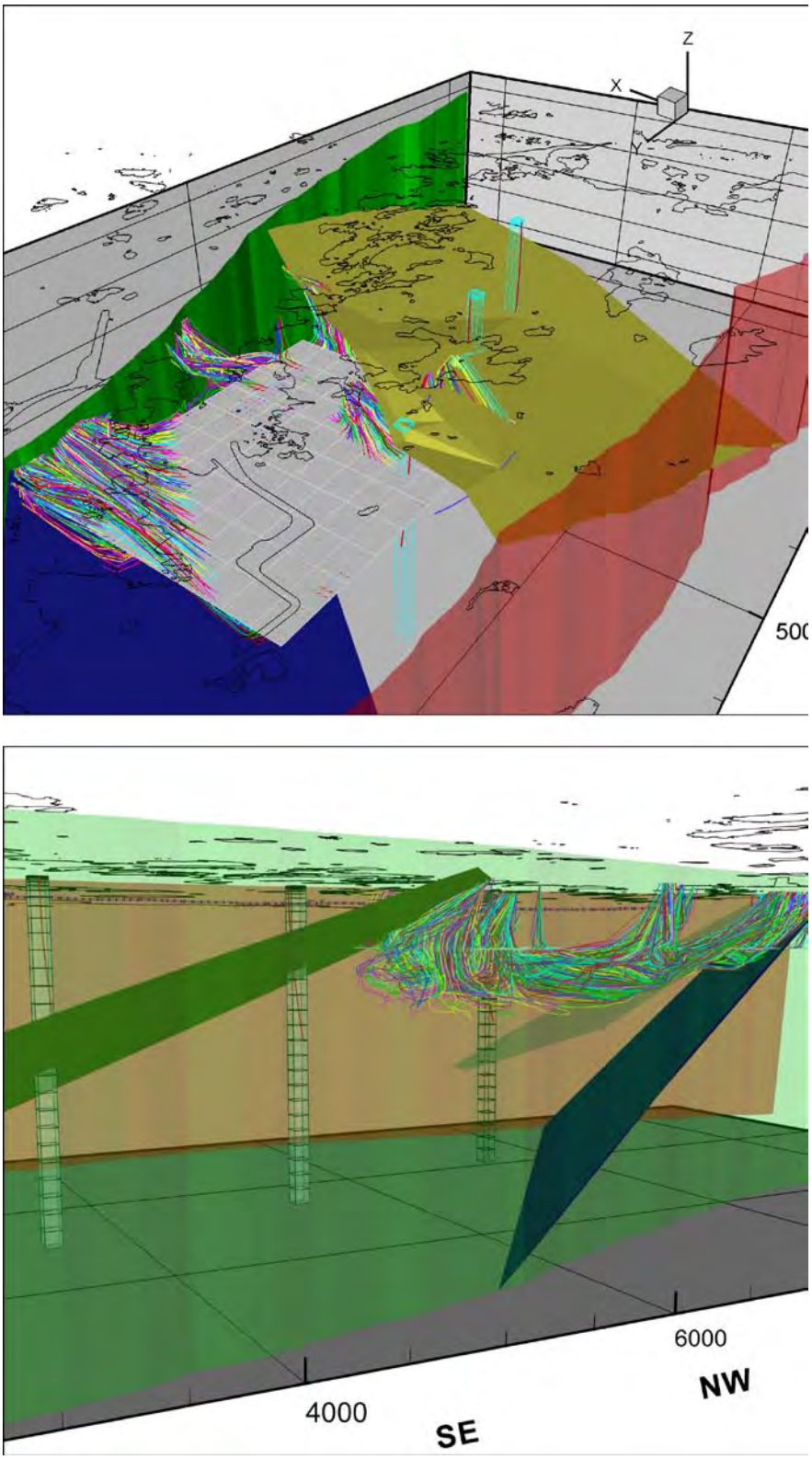

Figure 7-5. *Perspective views towards E (top) and W (bottom) of the release area within the target volume and the flow paths of 2,184 particles for the CPM Modified Case. The deformation zones are Singö (green), Eckarfjärden (Red), ZFMNE00A1 (blue) and ZFMNE00A2 (yellow). The present-day shoreline and lakes, boreholes KFM01A–KFM03A and the resolution of the computational grid are also indicated. The interpretation of flow paths is commented on in the text.*

7.3.1 Model domain (boundary conditions) and deformation zones

Figure 2-10 shows the regional model domain of model version 1.2 together with the regional water divides in northeast Uppland. There is a regional surface water divide between the candidate area and the southwest boundary of the regional model domain. A close up of the local water divides in the vicinity of the Forsmark area is shown in Figure 7-6. The regional water divide is coloured red. The objective of sensitivity case A is to investigate if the location of an upstream artificial no-flux boundary to the southwest is sufficiently far away from the target volume. The simulations are conducted for two deformation zone models, the *base model* and the *alternative model*, and three different model domains denoted by MD1, MD2 and MD4. The size and positions of the model domains are shown in Figure 7-7. The bottom boundary and all later boundaries are assumed no-flux. The top boundary is specified head (topography).

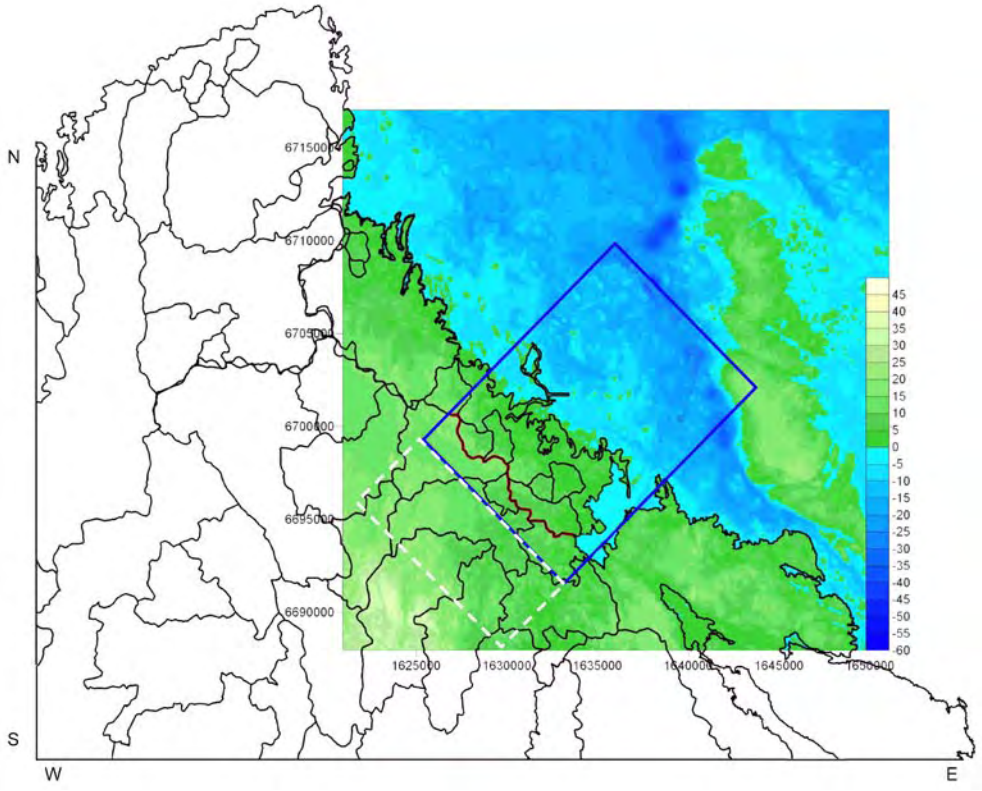

Figure 7-6. *Topography and surface water divides (black lines). The regional water divide southwest of the candidate shown in Figure 2-10 is in red. The regional model domain of model version 1.2 is in blue. The white dashes indicate the extended area considered by MD4, see Figure 7-7.*

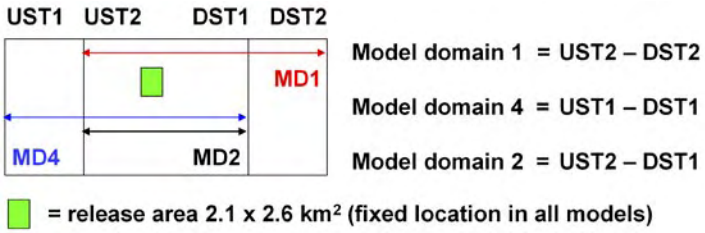

Figure 7-7. *Illustration showing the approach used to test the sensitivity to the size of the model domain. UST and DST mean 'upstream boundary' and 'downstream boundary', respectively. There are two of each corresponding to the different model domains, MD1, MD2 and MD4. MD1 represents the regional model domain of version 1.2. MD2 represents a diminished model domain with a different downstream boundary than MD1. MD4 is as large as MD1 but shifted 5 km to the southwest. The green area in the centre has the same location in all model domains. Within this area 2,184 particles are released at the time slice 2,000 AD. All lateral boundaries are assumed no-flux.*

Table 7-3 shows the outcome in terms of the relative difference between the medians (*MED*), the distance between mass centres (*DMC*) and the mean of all particle to particle differences (*MPP*) for the kinematic travel time t_w, the length of the flow path L_w, and the Darcy velocities at the start positions, q_0, see Section 2-8. Besides showing the results for the model domains MD1, MD2 and MD4, Table 7-3 also provides performance measures for a comparison between the *base model* and the *alternative model*. The specified head on the top boundary follows the elevation, cf Figure 2-9. The conclusions drawn from Table 7-3 are:

- The first four rows of data suggest that the relative differences in the median values for the travel time, path length and start velocity are small when the positions of the no-flux boundaries are changed for both deformation zone models. Also the distances between mass centres and the mean of all particle to particle differences are about the same regardless of the deformation zone model and model domain, which suggests that the regional model area is sufficiently large.

- The last three rows of data suggest that choice of deformation zone model is more important for the performance measures than the choice of model domain. The *alternative model* renders c 25% shorter travel times and almost 20% shorter travel lengths due to the great number of steeply dipping (low confidence) deformation zones. In addition, the distance between the mass centres and the move about 400 m and the mean of all particle to particle differences are also much greater. A closer look at the data reveals, however, that the differences between the two deformation zone models in the last three rows are mainly due to the occurrence of low-confidence zones inside the candidate area in the proximity of the target volume.

Table 7-3. Performance measures for a comparison between model domains MD1, MD2 and MD4, and between the *base model* (BM) and the *alternative model* (AM). *MED* L_w, *MED* q_0 and *MED* t_w denote relative differences between the sensitivity case (SC) and the comparison case (CC) in median path length, Darcy velocity at the starting positions and kinematic travel time, respectively. *DMC* and *MPP* denote "distance between SC and CC mass centres" and "mean of all SC particle to CC particle differences". The specified head on the top boundary follows the topography, cf Figure 2-9. (The definitions of MED, DMC and MPP are found in Section 2.8.)

Object	SC	CC	*MED* L_w [%]	*MED* q_0 [%]	*MED* t_w [%]	*DMC* [m]	*MPP* [m]
BM	MD4	MD1	–1	1.2	–1.8	14	65
BM	MD2	MD1	1	1.7	–2.9	14	123
AM	MD4	MD1	–4.2	–10.4	4.4	44	173
AM	MD2	MD1	3.4	–1.2	4.4	14	102
MD1	AM	BM	–27.6	42.6	–26.5	419	649
MD4	AM	BM	–29.9	26.2	–21.8	372	582
MD2	AM	BM	–25.8	38.4	–21.0	438	661

7.3.2 Undulation of groundwater table

Figure 7-8 shows the differences in head between a fully saturated flow domain TOPO (left) and a more gently undulating groundwater table GWT (right). The top row shows MD1 and the bottom row MD4. Table 7-4 shows the outcome of the particle tracking.

Table 7-4 shows that the position/undulation of the groundwater table, TOPO versus GWT, has little impact on the median travel time for the CPM Modified Case set-up. Figure 7-9 suggests that it is the low-confidence zones in the proximity of the target volume that governs.

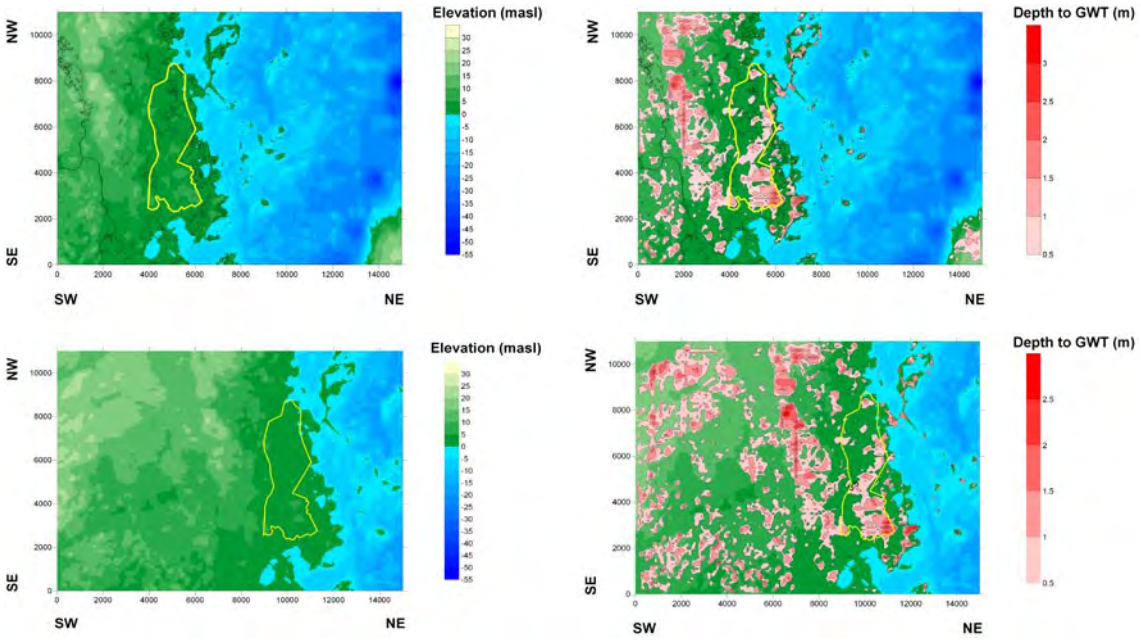

Figure 7-8. *Visualisation of the differences in head between a fully saturated flow model (TOPO; left) and a more gently undulating groundwater table (GWT; right). The top row shows MD1 and the bottom row MD4.*

Table 7-4. Performance measures for a comparison between a fully saturated flow model TOPO and a more gently undulating groundwater table GWT, and between the *base model* (BM) and the *alternative model* (AM). *MED* L_w, *MED* q_0 and *MED* t_w denote relative differences between the sensitivity case (SC) and the comparison case (CC) in median path length, Darcy velocity at the starting positions and kinematic travel time, respectively. *DMC* and *MPP* denote "distance between SC and CC mass centres" and "mean of all SC particle to CC particle differences".

Object	SC	CC	*MED* L_w [%]	*MED* q_0 [%]	*MED* t_w [%]	*DMC* [m]	*MPP* [m]
MD4+BM	GWT	TOPO	–2.2	–1.7	3.1	36	165
MD4+AM	GWT	TOPO	–7.4	–4.6	–1.7	39	174
MD4+GWT	AM	BM	–29.9	26.2	–21.8	378	582

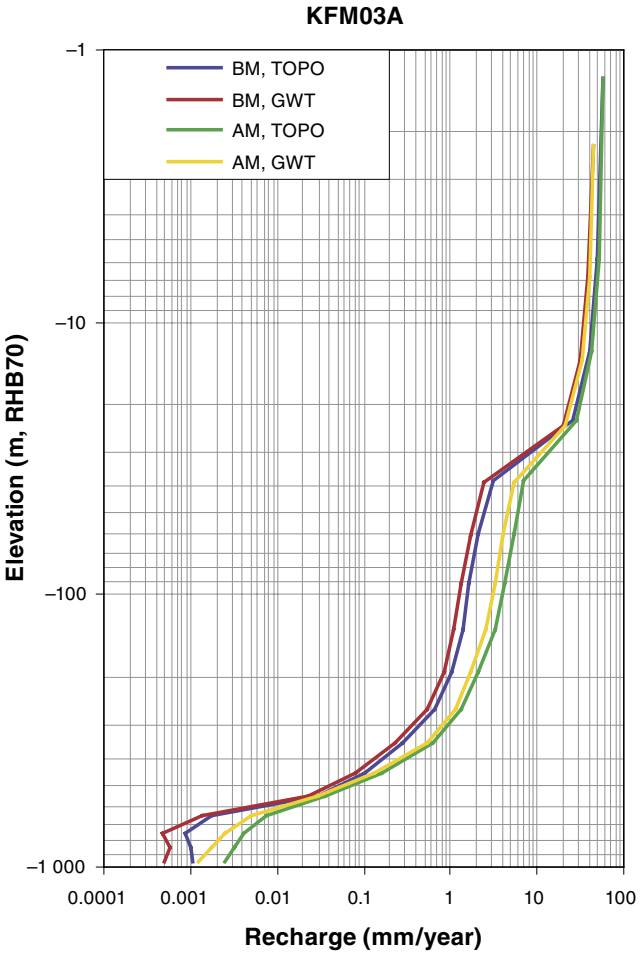

Figure 7-9. *Simulated recharge profile in the vicinity of KFM03A (drill site 3). The integrated value of the vertical component of the Darcy flux across one square kilometre is shown for two deformation zone models, the base model, BM, and the alternative model, AM, and for two specified-head top boundary conditions, TOPO and GWT. The recharge profile of the CPM Modified Case is more sensitive to the deformation zone model than to the position/undulation of the water table.*

7.3.3 Initial conditions for salinity

Figure 7-10 shows two initial conditions for the salinity, GRAD 1 and GRAD 2. Both profiles begin at –450 masl but GRAD 1 reaches the maximum value of 100 g TDS / L at –1,450 masl, whereas GRAD 1 does not reach the maximum value of 100 g TDS / L until –1,950 masl. Hence, GRAD 1 implies sharper interface and possibly also shallower flow cells than GRAD 2. The sensitivity case aims at reinforce this difference by treating MD4, whereas the comparison case considers MD1. Both cases consider the *alternative model*. Table 7-5 shows the outcome of the particle tracking.

Table 7-5 indicates that the initial condition for the salinity has a complex impact although the median travel time in the sensitivity case treated here is practically unchanged. The uncertainties need to be looked at in greater detail and quantified.

Table 7-5. Performance measures between a weaker salinity profile GRAD 2 (sensitivity case) and a sharper GRAD 1 (comparison case). GRAD 1 is used together with MD1 and GRAD 2 with MD4 in order to maximise the potential difference in density effects. Both cases consider the *alternative model* (AM). *MED* L_w, *MED* q_0 and *MED* t_w denote relative differences between the sensitivity case (SC) and the comparison case (CC) in median path length, Darcy velocity at the starting positions and kinematic travel time, respectively. *DMC* and *MPP* denote "distance between SC and CC mass centres" and "mean of all SC particle to CC particle differences".

Object	SC	CC	*MED* L_w [%]	*MED* q_0 [%]	*MED* t_w [%]	*DMC* [m]	*MPP* [m]
AM	GRAD 2 + MD4	GRAD 1 + MD1	–5.7	–8.3	–1.3	37	173

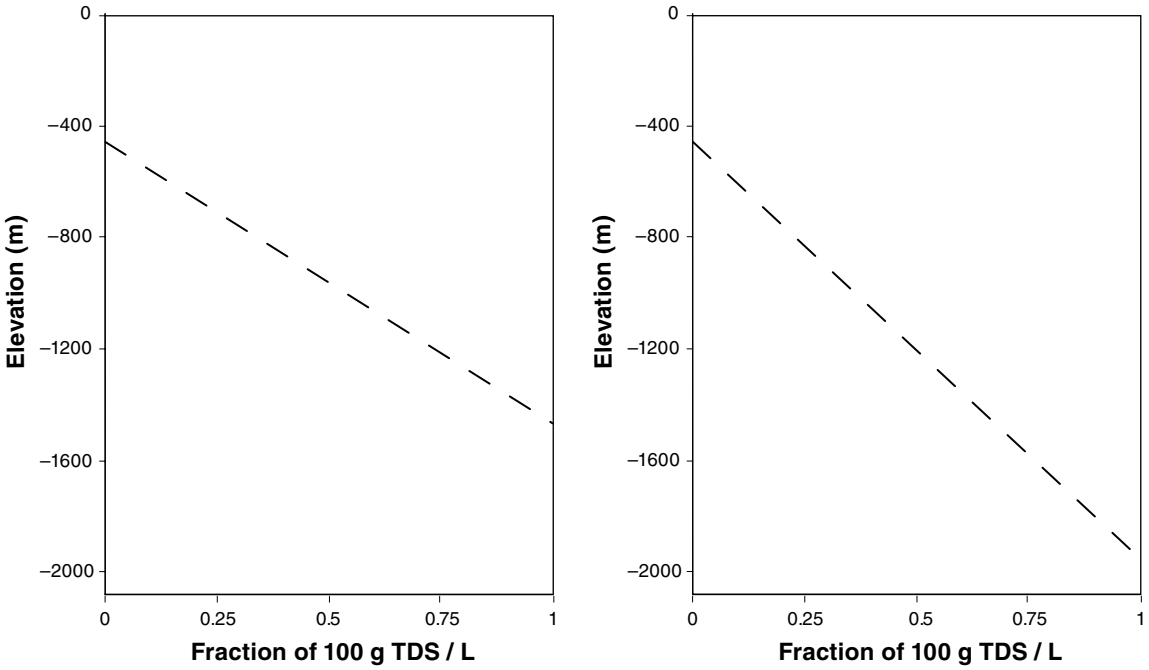

Figure 7-10. *The salinity profile to the left (GRAD 1) is sharper and suggests shallower flow cells than the salinity profile to the right (GRAD 2).*

7.3.4 Deformation zone heterogeneity

Sensitivity case D accounts for the possibility of a random heterogeneity in the deformation zone transmissivity besides the anticipated depth trend (cf case HCD3 in Section 4.3). The discretisation of the deformation zones consists of a large number of small triangles and each triangle is assigned a random deviate from the mean trend, see Equations (4-2a) and (4-2b). The result is visualised in Figure 7-11 and Figure 7-12.

Figure 7-12 shows that the procedure used causes new and faster flow paths (channels) to open up. The median travel length does not change much though and the exit positions differ a little only. The main differences are in Darcy flux field, which affect the overall median travel time, see Table 7-6. In conclusion, the deformation zone heterogeneity has a large impact on the travel times for the CPM Modified Case set-up.

Table 7-6. Performance measures between a heterogeneous transmissivity trend HET DZ (sensitivity case) and a homogeneous trend HOM DZ (comparison case). Both cases are used together with the *base model* (BM) and MD1. *MED* L_w, *MED* q_0 and *MED* t_w denote relative differences between the sensitivity case (SC) and the comparison case (CC) in median path length, Darcy velocity at the starting positions and kinematic travel time, respectively. *DMC* and *MPP* denote "distance between SC and CC mass centres" and "mean of all SC particle to CC particle differences".

Object	SC	CC	*MED* L_w [%]	*MED* q_0 [%]	*MED* t_w [%]	*DMC* [m]	*MPP* [m]
BM+MD1	HET DZ	HOM DZ	4.2	57.9	–50.5	41	327

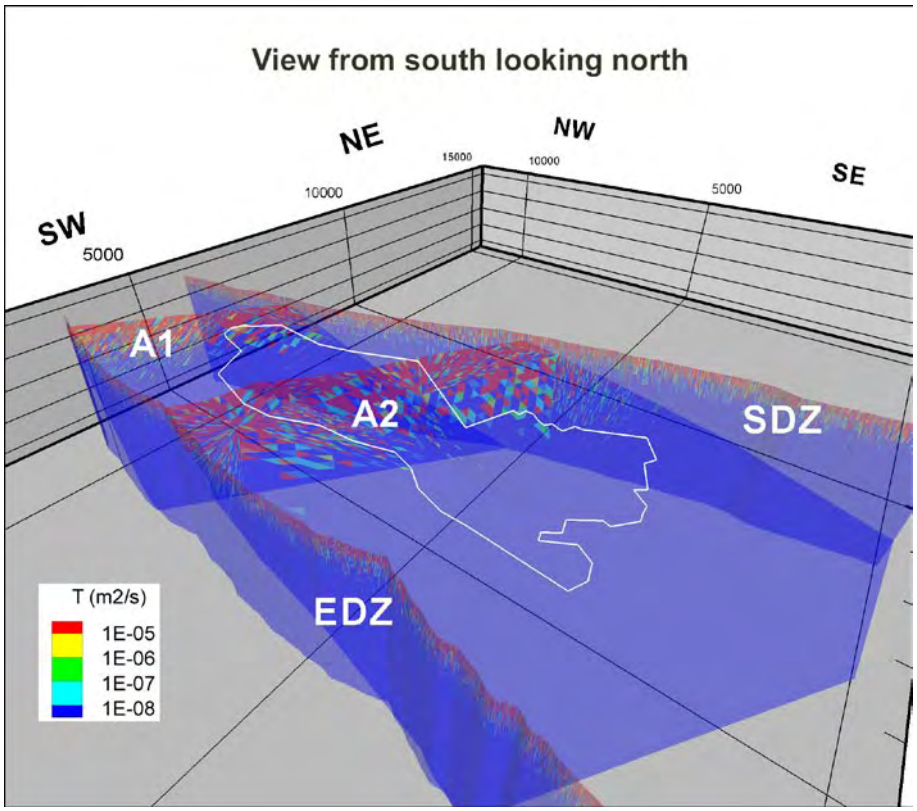

Figure 7-11. *Sensitivity case D; All HCDs of the base model are assigned non-correlated random deviate transmissivities as provided by Equations (4-2a) and (4-2b).*

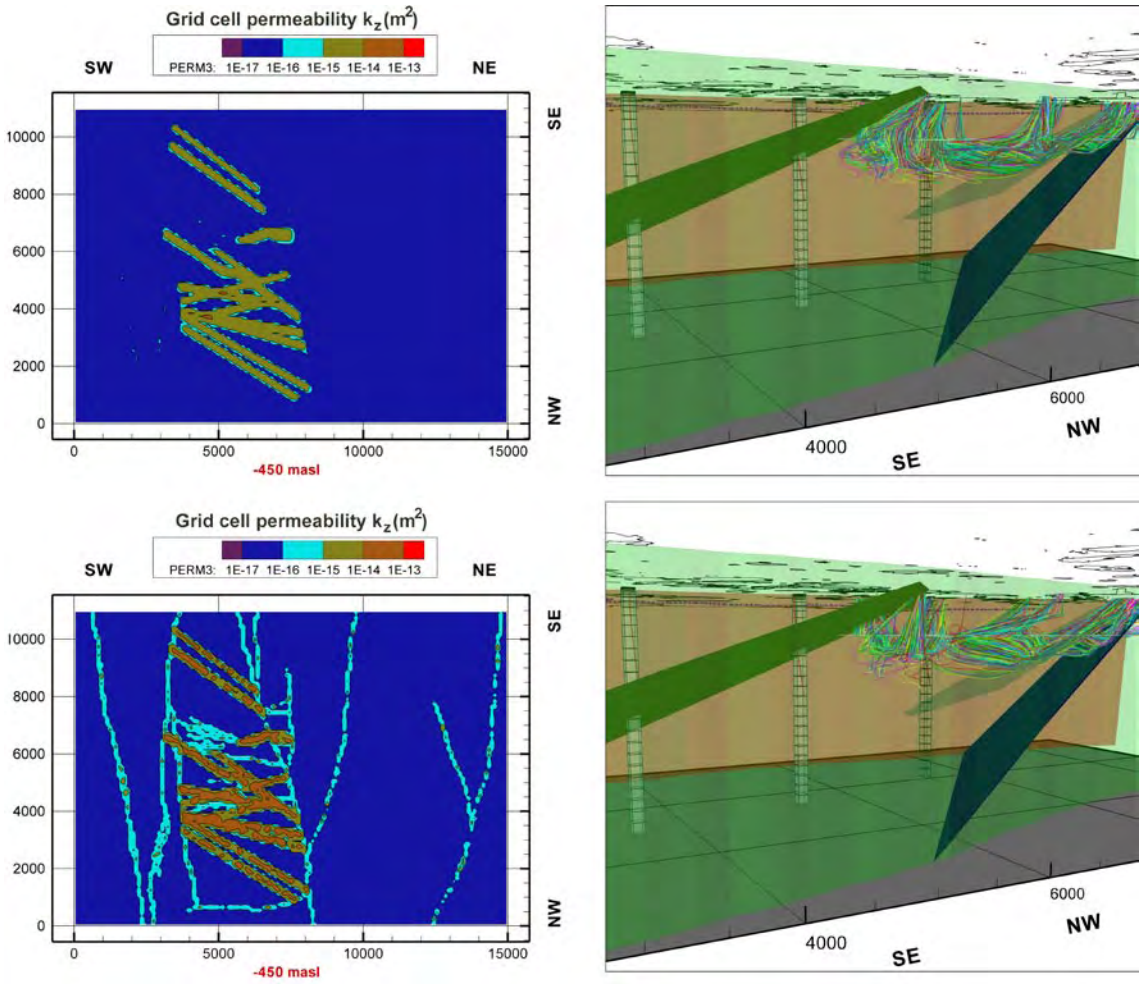

Figure 7-12. *Left: Visualisation of the grid cell permeability in the vertical direction for the comparison case (top) and the sensitivity case (bottom). Right: Visualisation of particle pathways for the comparison case (top) and the sensitivity case (bottom).*

7.3.5 Hydraulic anisotropy of near surface rock

Sensitivity case F investigates the effect of a possible hydraulic anisotropy in the superficial parts of the bedrock. Historic data reported by /Carlsson 1979/ as well as several drilling reports from the site investigation demonstrate that the estimated hydraulic conductivity from the percussion-drilled borehole (cf Figure 3-2) is primarily associated to sub-horizontal fractures ("sheet joints"), some of which carried huge amounts of water whereas others are filled with fine-grained and consolidated sediments. In practical terms this means that the horizontal hydraulic conductivity is probably much greater than the vertical.

The comparison case assumes an isotropic grid cell hydraulic conductivity tensor of $1 \cdot 10^{-6}$ m/s for the superficial rock masses. The sensitivity case assumes a hydraulic conductivity tensor where the magnitude of the tensor is one order of magnitude smaller, i.e. $1 \cdot 10^{-7}$ m/s, in the vertical direction. These values are applied throughout the model domain for the superficial rock masses below the overburden down to c 20 m depth, which has hydraulic conductivity of $7.5 \cdot 10^{-6}$ m/s and a thickness of four meters. No changes are made where the deterministically treated deformation zones are outcropping. Figure 7-13 illustrates the set-up. Both cases assume the *base model*.

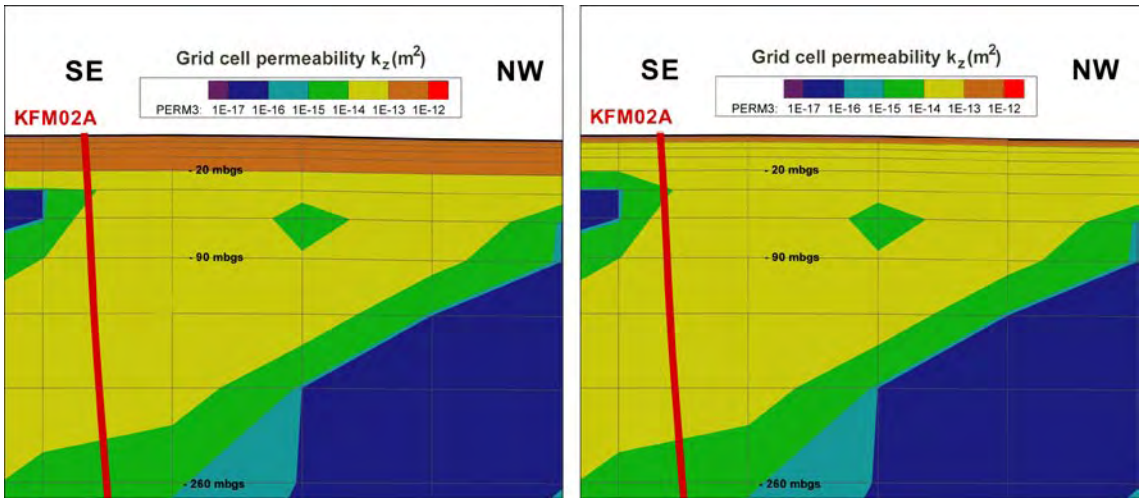

Figure 7-13. *The comparison case (left) assumes an isotropic grid cell hydraulic conductivity tensor of $1 \cdot 10^{-6}$ m/s for the superficial rock masses. The sensitivity case (right) assumes a hydraulic conductivity tensor where the magnitude of the tensor is one order of magnitude smaller, i.e. $1 \cdot 10^{-7}$ m/s, in the vertical direction. The two cases are applied throughout the model domain for the superficial rock masses below the overburden down to c 20 m depth, which has an isotropic hydraulic conductivity of $7.5 \cdot 10^{-6}$ m/s and a thickness of four metres (the thin uppermost layer in the right hand inset).*

The isotropic tensor suggests a relatively speaking larger recharge rate and greater impact of local flow cells than the anisotropic tensor. The recharge profiles shown in Figure 7-14 are positioned at the three drill sites (KFM01A–KFM03A) and represent average values across one square kilometre. Figure 7-14 suggests that the effect on the recharge rate is small (2–3 times) but visible. The greatest differences are for drill site 1 where there are few deterministically treated deformation zones. Table 7-7 shows the outcome of the particle tracking.

Table 7-7 reveals that the median travel length becomes slightly longer, the Darcy flux slightly smaller and, hence, the median travel time slightly longer for the sensitivity case ANISO. The exit locations are more or less unchanged though. In conclusion, the assumed anisotropy of the superficial rock masses has a moderate impact on the calculated travel times for the CPM Modified Case model set-up. The assumption of isotropy renders a greater flushing and does not produce longer travel times.

Table 7-7. Performance measures between a heterogeneous transmissivity trend HET DZ (sensitivity case) and a homogeneous trend HOM DZ (comparison case). Both cases are used together with the *base model* (BM) and MD1. *MED* L_w, *MED* q_0 and *MED* t_w denote relative differences between the sensitivity case (SC) and the comparison case (CC) in median path length, Darcy velocity at the starting positions and kinematic travel time, respectively. *DMC* and *MPP* denote "distance between SC and CC mass centres" and "mean of all SC particle to CC particle differences".

Object	SC	CC	*MED* L_w [%]	*MED* q_0 [%]	*MED* t_w [%]	*DMC* [m]	*MPP* [m]
BM+MD1	ANISO	ISO	1.7	–0.8	9.0	31	130

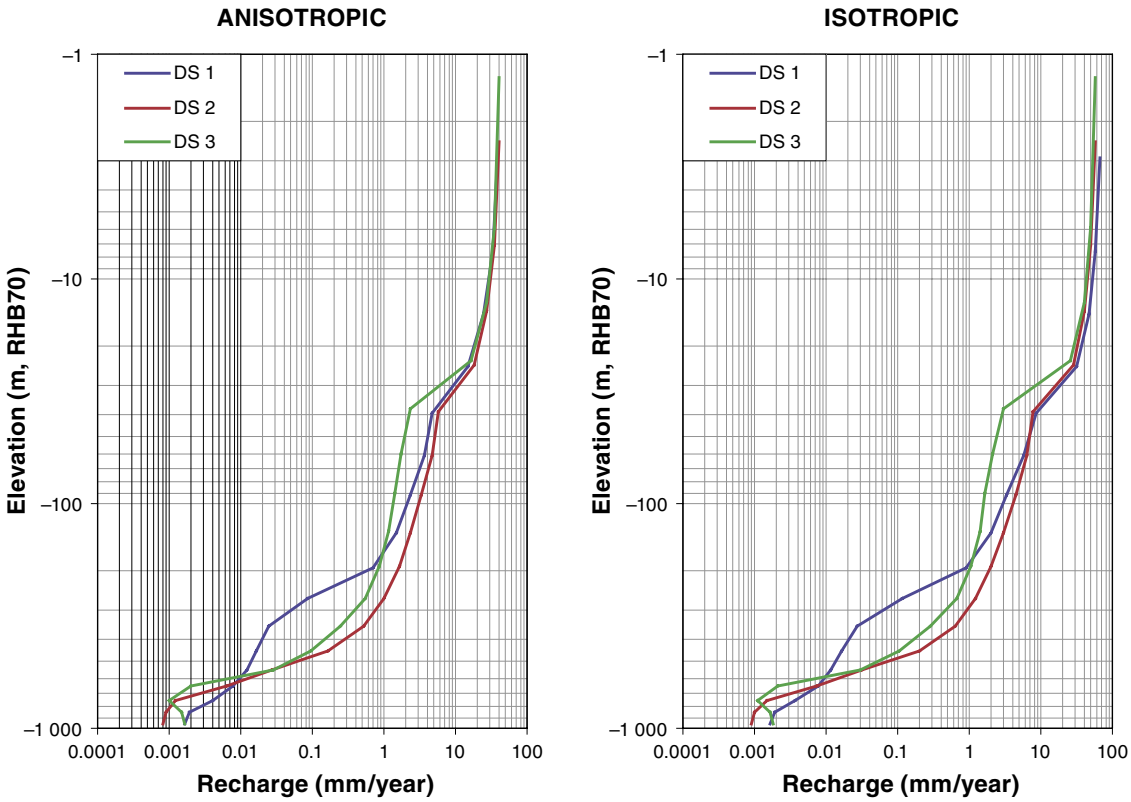

Figure 7-14. *Recharge profiles close to the three drill sites. Left: The sensitivity case ANISO (left). Right: T comparison case ISO (right). DS1 = drillsite 1, etc.*

7.3.6 Low-confidence deformation zones

The *alternative model* consists of high- or medium-confidence *base model* deformation zones plus low-confidence lineaments derived from interpretations of geophysical (magnetic mainly) and topographic anomalies. One part of the low confidence concerns the physical meaning of the anomalies, i.e. is every anomaly a deformation zone. Yet another part of the low confidence concerns the lateral position of the lineaments in space. /Johansson 2005/ provides a compilation of the differences observed in Forsmark regarding the interpretations of geophysical and topographic anomalies as reported by /Isaksson 2003, Isaksson et al. 2004, Isaksson and Keisu 2005, Korhonen et al. 2004/. It is concluded that different modellers may come to different interpretations.

The left inset in Figure 7-15 shows the low-confidence lineaments as modelled in the *alternative model*, cf Figure A-2. The right inset in Figure 7-15 shows a random perturbation of the positions to the left. That is, every lineament is uniformly displaced in the x,y-directions by a maximum amount of +/– 500 m. In a final step the base model high- and medium confidence zones are merged and a flow solution is derived for the two cases, the *alternative model* and a *random variant of the alternative model*. Table 7-8 shows the outcome of the particle tracking.

Table 7-8 suggests that the uncertainty in the positions of the low-confidence zones is important for the median travel time of the CPM Comparison Case set-up. Also, the exit locations are affected. It is important to note, however, that it is the displaced positions of the low-confidence zones within the target volume that cause the changes in the statistics. This is further demonstrated in the following sensitivity case.

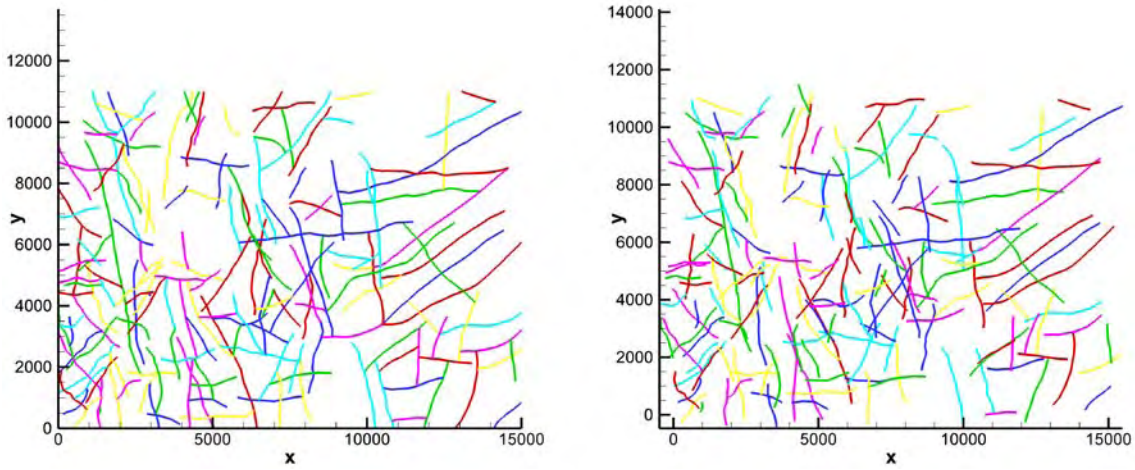

Figure 7-15. *Left: The comparison case (AM); low-confidence lineaments as modelled in the alternative model. Right: The sensitivity case (RVAM); a random perturbation of the lineament positions in the left inset. Each lineament is randomly displaced in the x,y-directions by a maximum amount of +/– 500 m.*

Table 7-8. Performance measures between a random variant of the alternative model RVAM (sensitivity case) and the alternative model AM (comparison case). Both cases are used together with MD1. *MED L_w*, *MED q_0* and *MED t_w* denote relative differences between the sensitivity case (SC) and the comparison case (CC) in median path length, Darcy velocity at the starting positions and kinematic travel time, respectively. *DMC* and *MPP* denote "distance between SC and CC mass centres" and "mean of all SC particle to CC particle differences".

Object	SC	CC	*MED L_w* [%]	*MED q_0* [%]	*MED t_w* [%]	*DMC* [m]	*MPP* [m]
MD1	RVAM	AM	3.6	5.9	–18.9	119	415

7.3.7 Gently dipping deformation zones

Gently dipping deformation zones are frequent within the tectonic lens. Gently dipping deformation zones probably occur also outside the lens, although there is no information to support their identification in Data Freeze 1.2. For instance, there is a gently dipping deformation zone observed below the bottom of the SFR facility, which is located outside the tectonic lens, see Figure 1-3.

Sensitivity case H investigates the role of the uncertainty regarding the occurrence of gently dipping deformation zones outside the tectonic lens. Figure 7-16 shows the *alternative model* split into base model deformation zones (yellow) and low-confidence deformation zones (green) together with stochastic realisations of gently dipping deformation zones on both sides of the tectonic lens. The frequency, strike and dip of the latter mimics the conditions inside the tectonic lens.

Table 7-9 shows the outcome of the particle tracking. The *alternative model* denoted by AM and constitutes the comparison case. The superposition of gently dipping deformation zones is denoted by GDZAM and constitutes the sensitivity case.

Table 7-9 shows that the occurrence of gently dipping deformation zones outside the lens has a very little impact of median travel time of the CPM Modified Case set-up. The exit locations are also fairly similar. In fact, the assumption causes local flow cells also outside the target are thus less impact of regional flow within the target volume.

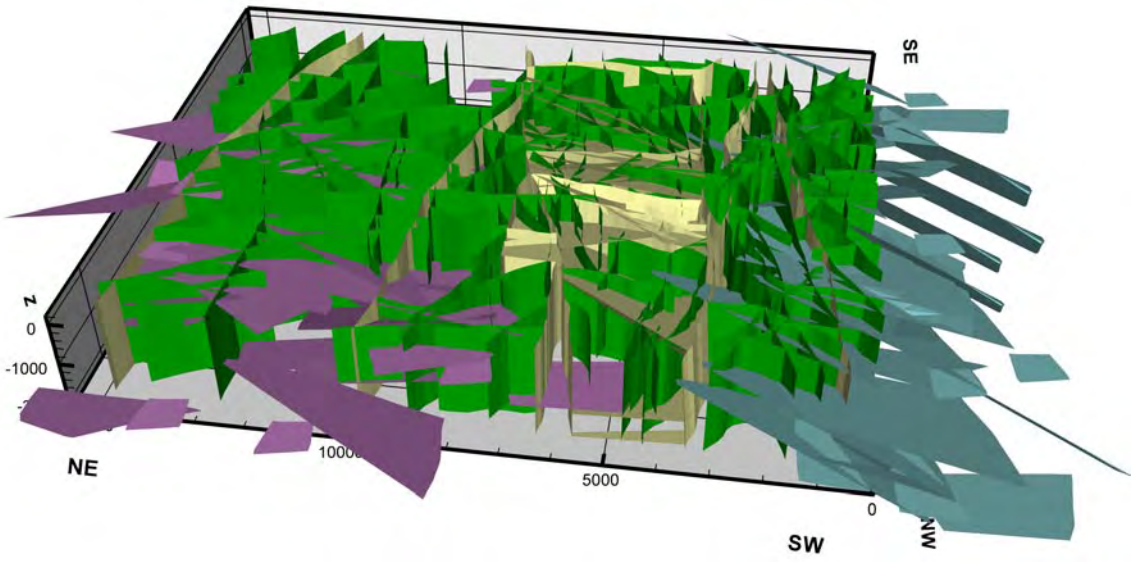

Figure 7-16. *The alternative model split into base model deformation zones (yellow) and low-confidence deformation zones (green) together with stochastic realisations of gently dipping deformation zones on both sides of the tectonic lens.*

Table 7-9. Performance measures between a *variant of the alternative model* with gently dipping deformation zones outside the tectonic lens GDZAM (sensitivity case) and the *alternative model* AM (comparison case). Both cases are used together with MD1. *MED* L_w, *MED* q_0 and *MED* t_w denote relative differences between the sensitivity case (SC) and the comparison case (CC) in median path length, Darcy velocity at the starting positions and kinematic travel time, respectively. *DMC* and *MPP* denote "distance between SC and CC mass centres" and "mean of all SC particle to CC particle differences".

Object	SC	CC	*MED* L_w [%]	*MED* q_0 [%]	*MED* t_w [%]	*DMC* [m]	*MPP* [m]
MD1	GDZAM	AM	5.0	–7.0	4.9	26	135

7.3.8 A multifactor sensitivity case

Sensitivity case I combines a number of interesting settings into a single case, namely:

- The base variant model. This model differs from the base model with regard to the size of four gently dipping deformation zones, see Figure 1-2 and Figure 4-4. The four zones are extended upstream until they intercept the Forsmark deformation zone outside the tectonic lens. The four zones of concern are ZFMNE00A1, -A2, C1 and C2.
- All major deformation zones in the area, i.e. the steeply dipping Singö, Eckarfjärden and Forsmark deformation zones as well as the previously mentioned gently dipping deformation zones ZFMNE00A1, -A2, C1 and C2, are assigned a constant deformation zone transmissivity of $1 \cdot 10^{-5}$ m^2/s regardless of depth, i.e. from ground surface to the bottom of the model domain at –2,100 masl. All other deformation zones were assigned a transmissivity depth trend in accordance to Equations (4-1a) and (4-1b). This setting is previously described in Section 4.3 and named HCD2.
- A greater rock mass hydraulic conductivity outside the tectonic lens. The contrast in hydraulic conductivity varies between 10–100 times depending on depth. The basis for these vales is reported from the investigations in the Finnsjön area /Andersson et al. 1991/.

- The shifted model domain MD4.
- A weaker undulation of the local groundwater table.

The first four settings aim at increasing the upstream regional flow through the model volume. The fifth setting aims to further pronounce this effect at depth by reducing the impact of local recharge and flow cells. Figure 7-17 shows a perspective view of the described set-up of sensitivity case I.

Table 7-10 shows the outcome of the particle tracking. The sensitivity case is denoted by BVM+. The *base model* BM constitutes the comparison case.

Table 7-10 shows that the many uncertainties combined have a quite moderate impact of median travel time of the CPM Modified Case set-up. A major effect seen is in the statistics of the exit positions. Figure 7-18 visualises the particle tracking. The light-blue shade demarcates the isosurface of $K = 5 \cdot 10^{-10}$ m/s. The exit positions resemble the results shown in Figure 7-4 and Figure 7-5 except that the discharge now is more distinct with one area located northwest of the target volume and another straight above the southeast corner around Lake Bolundsfjärden.

Table 7-10. Performance measures between a multiple sensitivity case denoted by BVM+ and the *base variant model* BVM (comparison case). Both cases are used together with MD4. *MED* L_w, *MED* q_0 and *MED* t_w denote relative differences between the sensitivity case (SC) and the comparison case (CC) in median path length, Darcy velocity at the starting positions and kinematic travel time, respectively. *DMC* and *MPP* denote "distance between SC and CC mass centres" and "mean of all SC particle to CC particle differences".

Object	SC	CC	*MED* L_w [%]	*MED* q_0 [%]	*MED* t_w [%]	*DMC* [m]	*MPP* [m]
MD4	BVM+	BM	–5.4	–1.1	–9.7	262	594

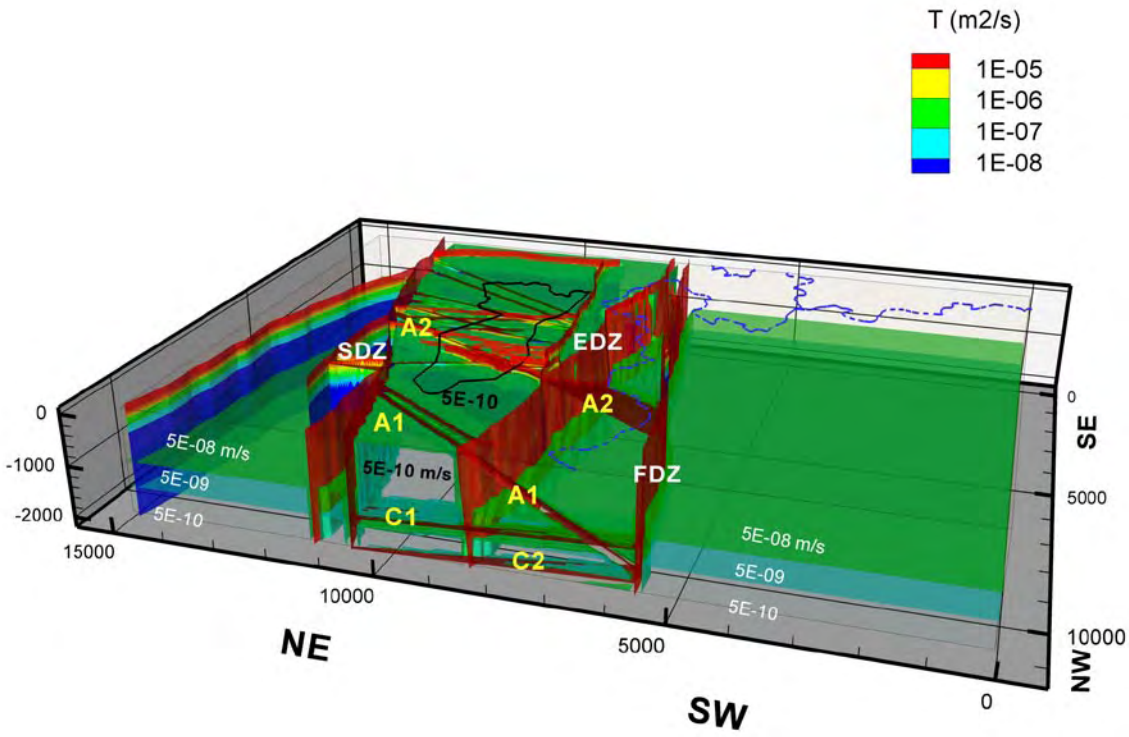

Figure 7-17. *Visualisation of the parameter set-up of sensitivity case I.*

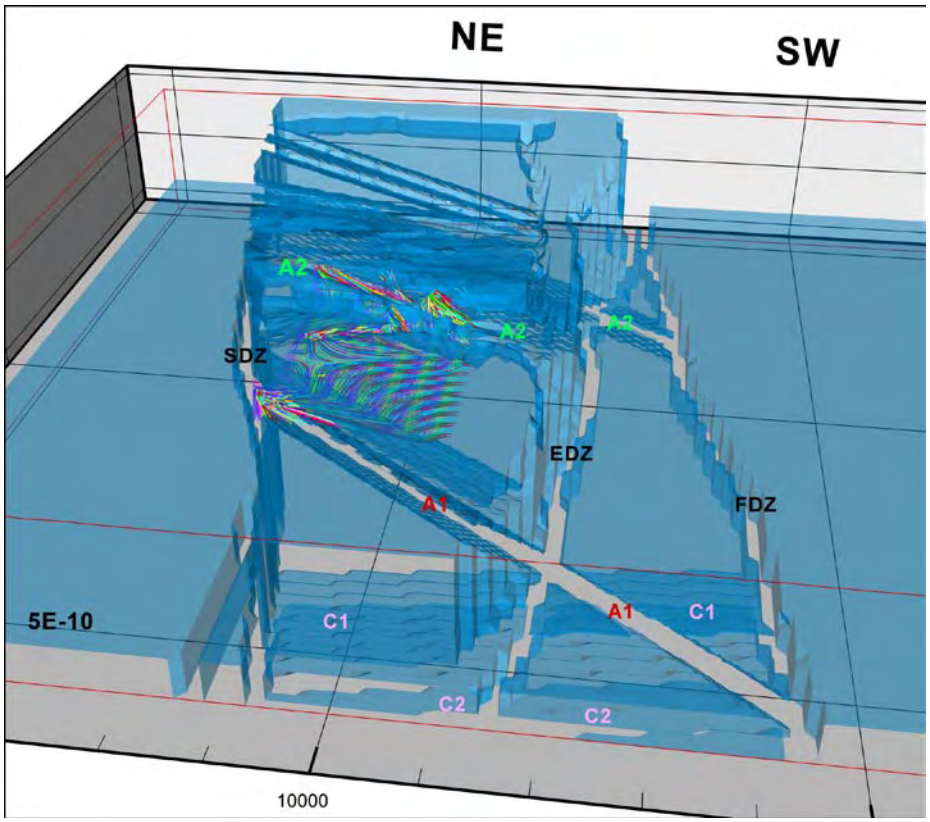

Figure 7-18. *Visualisation of exit positions for the particles released in sensitivity case I. The light-blue shade demarcates the isosurface of $K = 5 \cdot 10^{-10}$ m/s.*

7.3.9 Shoreline displacement and particle traces at 5,000 AD

Although not a part of the objectives of model version 1.2 a simulation is conducted where the shoreline displacement process is not halted at 2,000 AD but extended until 5,000 AD. Particles are then released in a similar fashion as above. The parameter setting follows the original CPM Modified Case described in Table 7-2. The particle flow paths for fixed boundary conditions representing 2,000 AD are visualised in Figure 7-4 and Figure 7-5. Figure 7-19 shows the results for 5,000 AD.

Figure 7-19 suggests that the body of the released particles at 5,000 AD exit close to the new shoreline and possibly some of the new lakes. The reasons for this behaviour are among other things:

- The change of state of the candidate area from being a primarily a discharge area (present-day) to a recharge area (future).
- The assumption of multicomponent continuum, i.e. no discrete path ways.
- The increased rock mass conductivity of CPM-3 in the CPM Modified Case.
- The assumed isotropic transmissivity of the Singö deformation zone, which is known be anisotropic in reality /cf Axelsson et al. 2002/. This means that there is no resistance for transverse flow in the current flow model.

A closer look at the flow paths within the target area shows that there is still a substantial amount of local discharge at 5,000 AD, e.g. around Lake Bolundsfjärden and in the Singö deformation zone, see Figure 7-20, despite the continuum approximation, and a distant sink (shoreline).

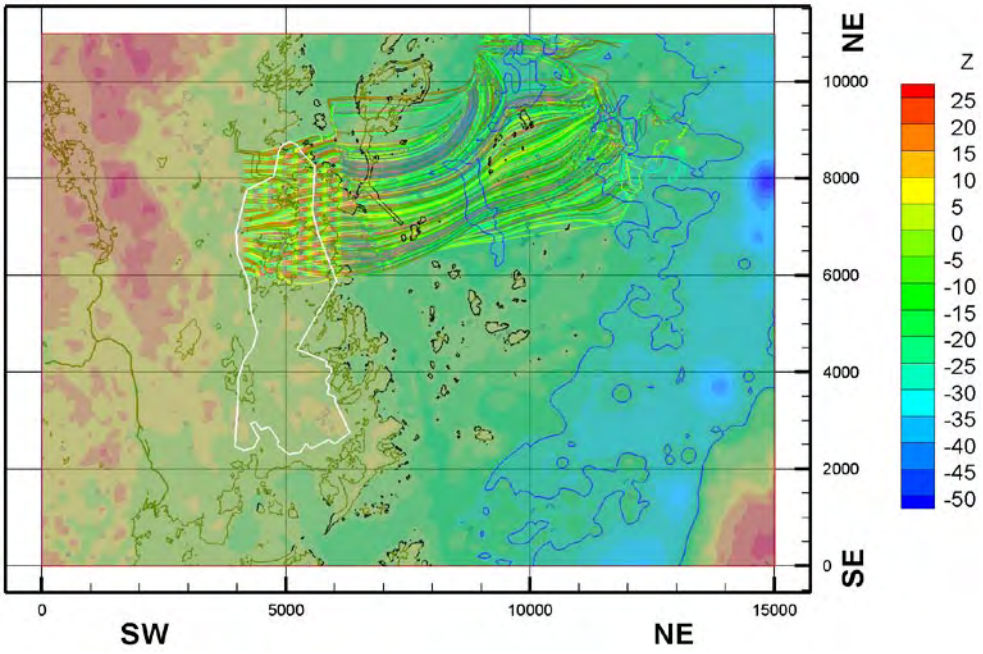

Figure 7-19. *Particle flow paths at 5,000 AD.*

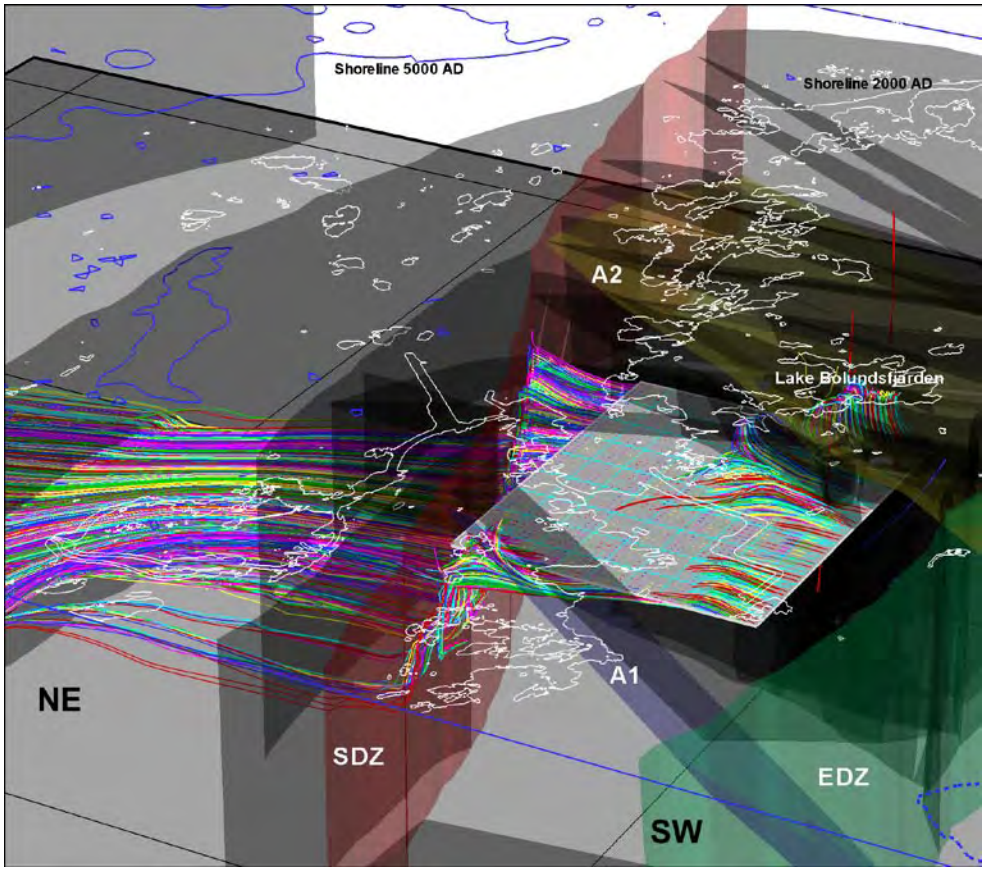

Figure 7-20. *Close up showing particle flow paths in the vicinity of the release area at 5,000 AD. Note the exit positions (discharge area) close to Lake Bolundsfjärden.*

7.3.10 Summary of findings for the sensitivity cases

Table 7-11 provides an overview of the main particle tracking results obtained from the different sensitivity cases treated using the CPM Modified Case properties. The general impression of the sensitivity cases is that the uncertainties about the details of many far-field hydrogeological parameters most likely do not need to be constrained in order to describe the flow paths within the target volume with greater confidence. That is, the relative impact of many far-field hydrogeological parameters is much smaller than the relative impact of most local hydrogeological parameters. For example, the size of the regional

Table 7-11. Compilation of findings for the sensitivity cases.

Uncertainty (sensitivity case)	Observations
Model domain, boundary conditions and deformation zones	The regional model area of version 1.2 is probably sufficiently large. The results observed for the *base model* an the *alternative model* reveal that the differences between the two models are mainly due to the occurrence of low-confidence deformation zones inside the candidate area in the proximity of the target volume for the alternative model.
Undulation of groundwater table	The recharge profile is more sensitive to the deformation zone model than to the position/undulation of the water table.
Initial conditions for salinity	The initial condition for the salinity is judged to have a complex impact although the median travel time in the sensitivity case treated here is practically unchanged. The uncertainties need to be looked at in greater detail and quantified.
Deformation zone heterogeneity	The procedure used to generate deformation zone heterogeneity causes new and faster flow paths (channels) to open up. The median travel length does not change much though and the exit positions differ a little only. The main differences are in Darcy flux field, which affect the overall median travel time. In conclusion, the deformation zone heterogeneity has a large impact on the travel times within the target volume of the CPM Modified Case.
Hydraulic anisotropy of near surface rock.	The assumed anisotropy of the superficial rock masses has a moderate impact on the calculated travel times for the CPM Modified Case set-up. In fact, the assumption of isotropy renders a greater flushing and does not produce longer travel times.
Low-confidence deformation zones.	The uncertainty in the positions of the low-confidence zones is important for the median travel time of the CPM Comparison Case set-up. It is important to note, however, that it is the displaced positions of the low-confidence zones within the target volume that cause the sensitivity.
Gently dipping deformation zones.	The occurrence of gently dipping deformation zones outside the lens has a very little impact of median travel time of the CPM Modified Case set-up. In fact, the assumption causes local flow cells also outside the target area thus less impact of regional flow within the target volume.
Shoreline displacement and particle flow paths at 5,000 AD.	A look at the flow paths within the target area shows that despite the continuum approximation, homogenous properties and a distant shoreline there is still a substantial amount of local exit positions at 5,000 AD, e.g. in the Singö deformation zone and around Lake Bolundsfjärden.

model domain (boundary condition) and existence of deformation zones outside the target volume are found to have little impact on the CPM Modified Case Among the important local hydrogeological parameter uncertainties for the flow path calculations we note in particular (i) transmissivity heterogeneity among the deterministically treated deformation zones, and (ii) uncertainties about the positions of low-confidence zones.

Finally, since many of the regional hydrogeological uncertainties can be shown to have little effect on the flow paths within the target volume, although the model domain is simulated to be much more conductive than suggested by the hydraulic field tests, the conclusions drawn from the simulations still ought to be of significance.

7.4 Comparisons with measured data

An improved understanding of the palaeo-hydrogeological conditions is necessary in order to gain credibility for the site descriptive model in general and the hydrogeological description in particular (cf the first of the two objectives listed in Section 7.2). This requires modelling of the groundwater flow from the last glaciation up to present-day with comparisons against measured hydro-geochemical data.

7.4.1 Premises for comparisons

Hydraulic properties are generally estimated from the evaluation of hydraulic test results related to the geological domains as shown in Chapters 4, 5 and 6. The next phase is to set up a numerical groundwater flow model by combining the geometric information associated with the geological domains with the preliminary hydraulic properties and evaluate the flow model results versus relevant data sets, e.g. natural heads, interference tests, tracer tests, and hydrogeochemical profiles. Some of these data sets come into play as calibration targets during the course of the development of the hydrogeological model. However, at this point the matching of simulations against detailed measurements is above all indicative as a regional model domain is treated with a significant imperfection in terms of detailed discretisation. For instance, the bedrock hydrogeological model treats a flow system that is 2.1 km deep, 15 km long and 11 km wide, hence much of the attention of the flow model by definition prioritises what is going on at repository depth in the regional perspective. In order to cope with this huge volume, a coarse a grid resolution of 100 m is used in the numerical simulations. Additionally, the multicomponent CPM flow model is associated with significant imperfections in terms of detailed hydraulic heterogeneity and anisotropy of the rock mass properties. It is important to recall these shortcomings when comparing simulation results with detailed measurements.

Among the different implications associated with using a coarse grid resolution of 100 m and a multicomponent CPM model the following ones are of particular concern for the integration with near-surface hydrogeology, geology and hydrogeochemistry:

- The deterministically treated deformation zones in Forsmark are significantly more conductive than the sparsely fractured rock mass in between. The deformation zones' thicknesses are generally not thicker than the grid resolution, which means that an implicit representation is used more or less frequently. A few deformations zones only are as thick or thicker.
- Most likely the body of the percolating groundwater circulates fairly high up in the rock due to the aforementioned significant depth trend in the hydraulic conductivity.

- The hydrogeochemical sampling at depth is currently restricted to deal with fractures with a transmissivity of at least $1 \cdot 10^{-8}$ m^2/s, a magnitude which is rarely found in individual fractures outside the deterministically treated deformation zones.
- The hydrogeochemical sampling represents water samples gathered by pumping with small flow rates from individual fractures intersecting very slim boreholes, whereas the simulated flow model concentrations represent data of a numerical continuum with flowing grid cell pore volumes of the order of 10–100 m^3.
- The uppermost parts of the hydrogeochemical profiles are probably governed by the local recharge and the near-surface hydrogeological conditions as the regional topographic relief is low and the body of the model area is covered by Quaternary deposits of a different chemical composition and much greater porosities than the bedrock at depth. The mean thickness of the Quaternary deposits is of the order of a few metres, which means that the vertical to horizontal aspect ratio of the uppermost grid cells is poor, 0.02–0.08. More importantly, however, is the poor representation of the heterogeneity of the hydraulic conductivity of the Quaternary deposits. In the current model there is co consideration to the existence of clayey till, glacial clay, post-glacial clay or gyttja.

The classic definition of a calibration target for groundwater flow simulations, i.e. the difference between simulated and measured hydraulic heads, is difficult to apply in sparsely fracture rocks as it requires a superior geometric control of the positions of the flowing fractures/zones and their intercepts with the boreholes. Moreover, as most boreholes in Forsmark, from which data are available for version 1.2, are fairly new they have so far been subjected to water sampling and single-hole hydraulic tests mainly implying short time series and very few interference tests. The aforementioned drilling induced responses are useful in a qualitative sense but provide no means for a quantitative analysis unfortunately.

The primary data used for comparisons with the regional groundwater flow simulations of version 1.2 are the hydraulic and hydrogeochemical data that were available from boreholes within the candidate area. More precisely, these include the sequential single-hole hydraulic tests and hydrogeochemical samples at discrete positions along the trend and plunge of KFM01A–5A, under present-day conditions. The hydrogeochemical samples are analysed for various concentrations among which the concentration of Cl (chloride) and ratios of the environmental isotopes $\delta^{18}O$ (oxygen 18) and δD (deuterium) are used in the work reported here. Comparisons are also made with the mixing proportions calculated with the M3 method /Laaksoharju et al. 2005/.

It should be noted that only few hydrogeochemical samples are available from the deep core-drilled boreholes, whereas the data from the shallower percussion-drilled boreholes are more frequent. Figure 7-21 shows available data for the salinity of the groundwater in the bedrock. The salinity is here expressed in terms of total dissolved solids TDS.

Unlike most sampling sections in the core-drilled boreholes samples taken in the percussion-drilled boreholes shown in Figure 2-2 are not “point observations” but represent more or less long sampling sections, thus intersecting a number of near-surface fractures and/or deformation zones, see Table 7-12.

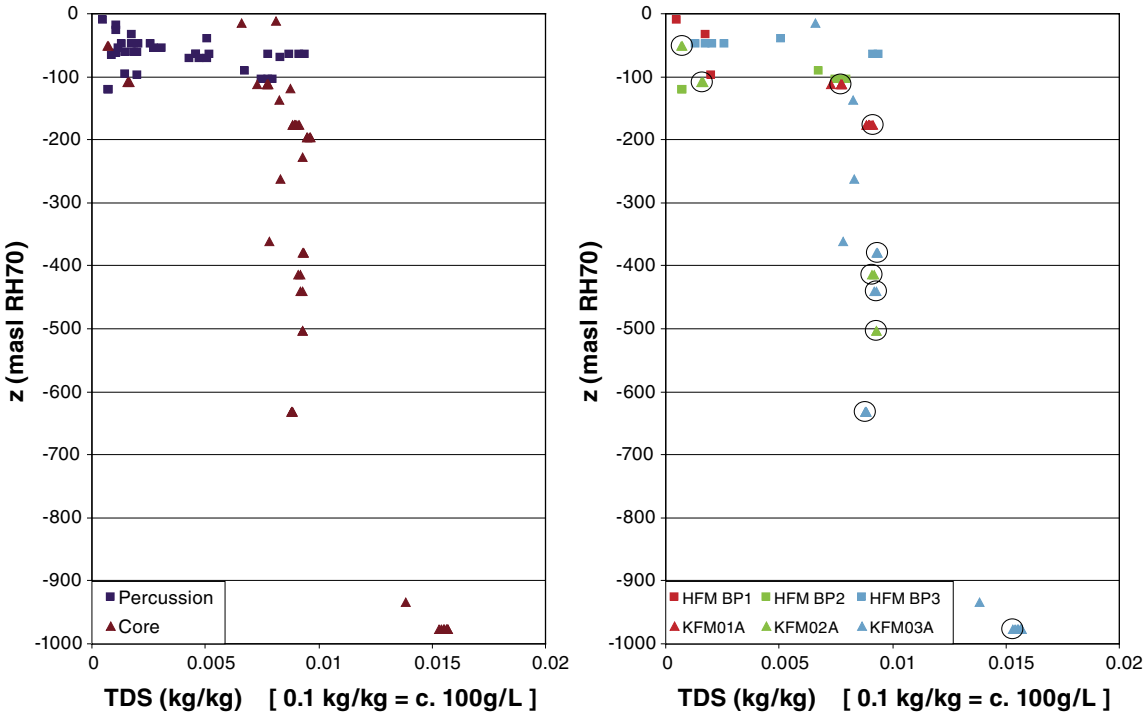

Figure 7-21. Left: Available data for the salinity (TDS) from percussion-drilled and core-drilled boreholes. Right: Data gathered near the three drill sites 1A–3A along the centre line of candidate area. The data points are coloured with regard to the drill site they represent. Squares denote data from percussion-drilled boreholes and triangles denote data from core-drilled boreholes. Data points surrounded by circles are considered the best for chemical modelling purposes, see /Laaksoharju et al. 2005/.

Table 7-12. Length of water sampling sections for the percussion-drilled borehole data shown in Figure 7-21. On the average there are circa three fracture intercepts per borehole, cf Section 3.2.

Percussion-drilled borehole	Length of sampling section [m]	Percussion-drilled borehole	Length of sampling section [m]	Percussion-drilled borehole	Length of sampling section [m]
HFM01	0–71	HFM08	0–144	HFM14	0–151
HFM03	0–26	HFM09	17–50	HFM15	0–200
HFM04	30–222	HFM10	0–150	HFM16	0–133
HFM05	0–200	HFM11	0–182	HFM17	0–203
HFM06	0–111	HFM12	0–210	HFM19	0–173
HFM08	0–93	HFM13	0–176		

Furthermore, some samples are regarded as more representative than others. The representative samples are indicated by circles in Figure 7-21. Unrepresentative samples are not necessarily 'bad' samples. It simply means that some samples are considered more representative and have been picked as the best for chemical modelling purposes, see /Laaksoharju et al. 2005/. In the work reported here data classified as representative are used only, i.e. that data points surrounded by circles in Figure 7-21. This means that data from the percussion-drilled boreholes are not included. The reason for this is two-fold. First, there is an uncertainty regarding their geometrical "point of representation". Secondly, water samples from percussion-drilled holes are taken from water extracted at relatively high pumped flow-rates compared with the cored boreholes.

Concerning the samples from the core-drilled boreholes it is vital to recall that the hydrogeochemical sampling at depth currently is restricted to deal with fractures with a transmissivity of at least $1 \cdot 10^{-8}$ m^2/s, a magnitude which is rarely found in individual fractures outside the deterministically treated deformation zones. This means that the hydrogeochemical data gathered below c 100 m depth by and large represents the water composition in the deformation zones intersected. There are no hydrogeochemical data available for version 1.2 that clearly represents hydrogeochemical conditions in the rock mass fracturing or in the rock matrix pore water.

Figure 7-22 through Figure 7-24 show profiles of the representative hydrogeochemical data, the single-hole geological interpretations and the interpreted hydraulic conductivities of 100 m intervals in KFM01A–KFM03A. The latter data are based 100 m PSS tests except for the uppermost 100 m of rock where the hydraulic testing is conducted by means an open-hole pumping using the HTHB method, see Table 3-1. The profiles demonstrate the impact of the gently-dipping deformation zones on the hydraulic and hydrogeochemical data and the strong correlation to the seismic reflectors. A2 denotes deformation zone ZFMNE00A2 etc. It is important to realise that although the 100 m PSS tests are as long as the vertical resolution of the computational grid of the simulation model below –400 masl many of the intersected deformation zones are much thinner, see Figure 3-3 and Table 4-1. To mitigate the numerical imperfections of the simulation model the vertical resolution of the computational grid above –400 masl is improved. The mean vertical spacing between two adjacent grid nodes in the upper 400 m of the simulation model is c 30 m.

In conclusion, the salinity data available for modelling in version 1.2 are still quite limited in quantity and few are from larger depth. For instance, there are samples from near one kilometre depth only in KFM03A, where presumably a significant amount of Brine has been encountered. The next deepest sample location is at 512 m depth in KFM02A, where data suggest a small proportion of Brine at the base. Hence, data on the dense saline water are quite sparse. From a regional perspective there is a risk of bias if the comparison of salinity is made with data from just one or two deep boreholes. In addition, most of the boreholes are located near to the coast in very low topographic areas. So, there is an additional risk of bias due to sampling essentially in a single hydrogeological environment.

Due to the uncertainties associated with the limited quantity of representative hydrogeochemical data as well as the coarse grid resolution of the multicomponent CPM model the simulations conducted aimed at matching salinity mainly, while checking the effects for Cl, $\delta^{18}O$ and δD. Comparisons with fractions in the M3 mixing approach are also included where the ± 10% error margin is less significant.

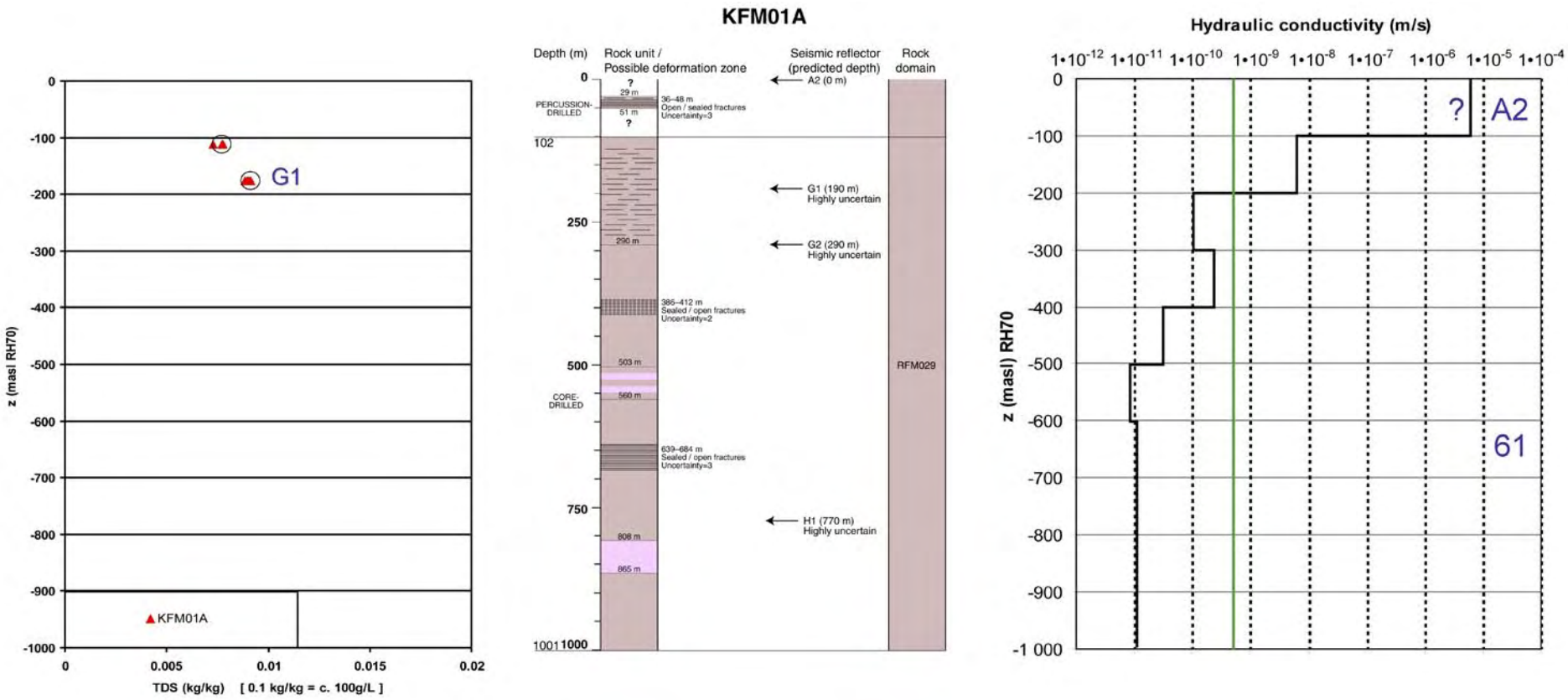

Figure 7-22. *Profiles of the representative hydrogeochemical data, the single-hole geological interpretation and the interpreted hydraulic conductivities of 100 m intervals in the core-drilled borehole KFM01A. The latter data are based 100 m PSS tests except for the uppermost 100 m of rock where the hydraulic testing is conducted by means an open-hole pumping using the HTHB method, see Table 3-1. The profiles demonstrate the impact of the gently-dipping deformation zones on the hydraulic and hydrogeochemical data and the strong correlation to the seismic reflectors. A2 corresponds to deformation zone ZFMNE00A2 in the base model etc. It is important to realise that although the 100 m PSS tests are as long as the vertical resolution of the computational grid of the simulation model below –400 masl many of the intersected deformation zones are much thinner, see Figure 3-3 and Table 4-1. To mitigate the numerical imperfections of the simulation model the vertical resolution of the computational grid above –400 masl is improved. The mean vertical spacing between two adjacent grid nodes in the upper 400 m of the simulation model is c 30 m.*

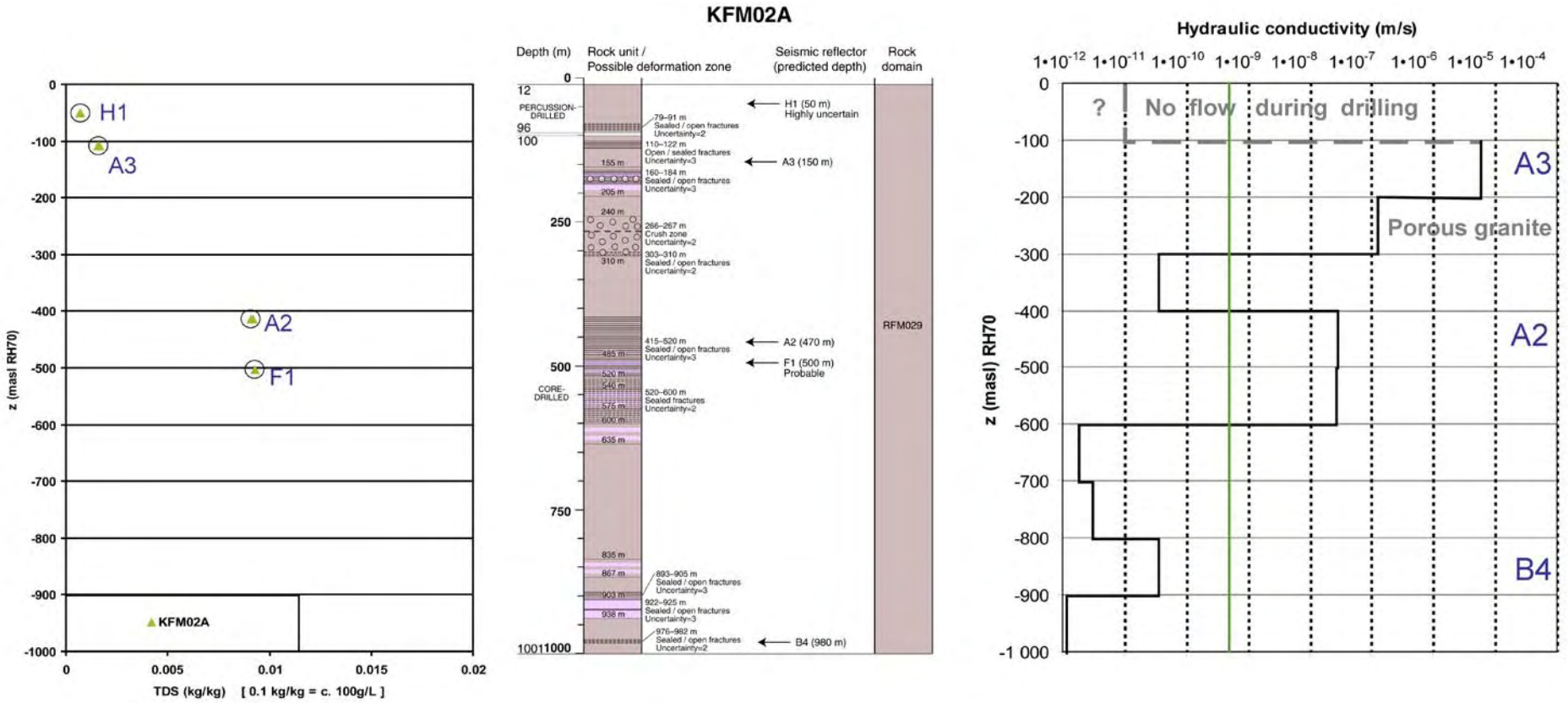

Figure 7-23. *Profiles of the representative hydrogeochemical data, the single-hole geological interpretation and the interpreted hydraulic conductivities of 100 m intervals in the core-drilled borehole KFM02A. The latter data are based 100 m PSS tests except for the uppermost 100 m of rock where no hydraulic testing was conducted, see Table 3-1. The profiles demonstrate the impact of the gently-dipping deformation zones on the hydraulic and hydrogeochemical data and the strong correlation to the seismic reflectors. Reflector A2 corresponds to deformation zone ZFMNE00A2 in the base model etc. It is important to realise that although the 100 m PSS tests are as long as the vertical resolution of the computational grid of the simulation model below –400 masl many of the intersected deformation zones are much thinner, see Figure 3-3 and Table 4-1. To mitigate the numerical imperfections of the simulation model the vertical resolution of the computational grid above –400 masl is improved. The mean vertical spacing between two adjacent grid nodes in the upper 400 m of the simulation model is c 30 m.*

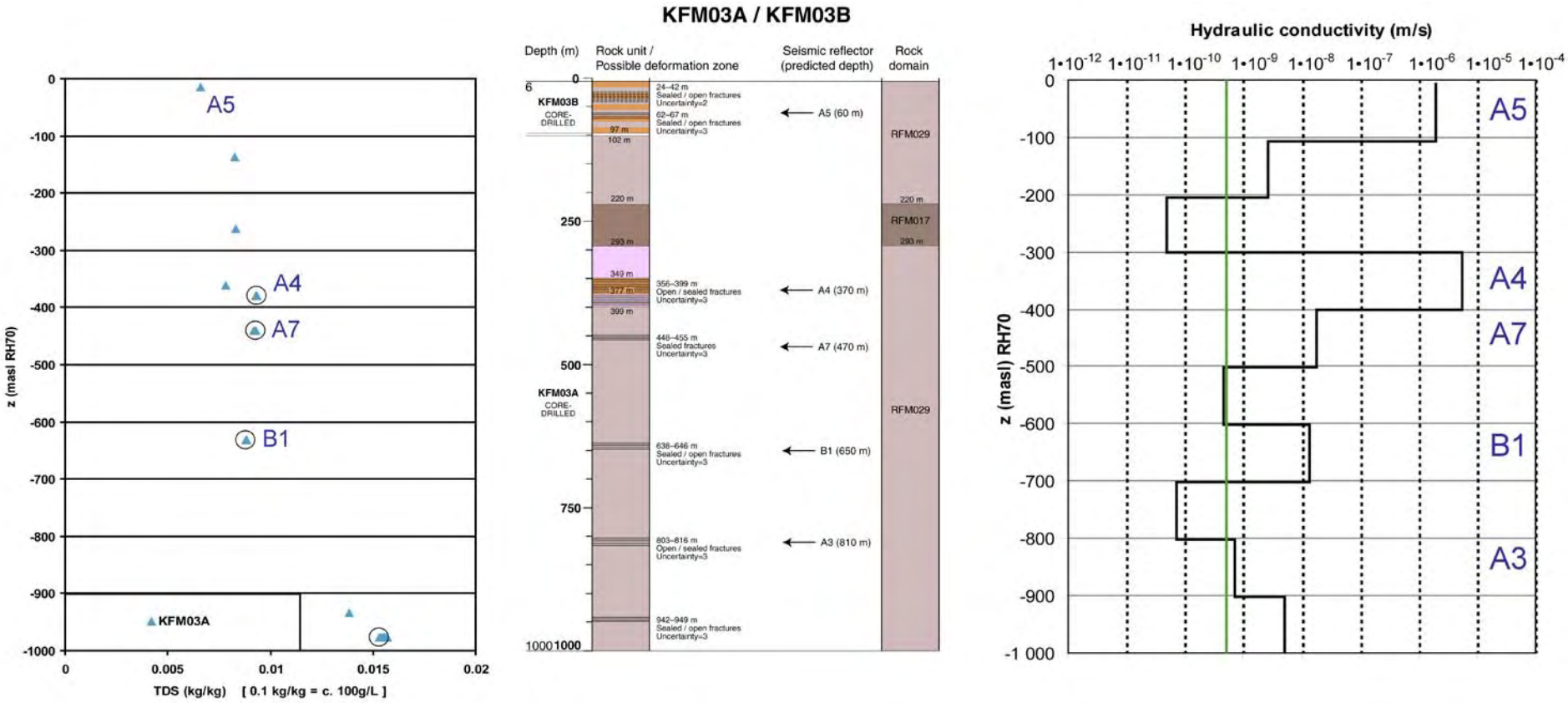

Figure 7-24. *Profiles of the representative hydrogeochemical data, the single-hole geological interpretation and the interpreted hydraulic conductivities of 100 m intervals in the core-drilled borehole KFM02A. The latter data are based 100 m PSS tests except for the uppermost 100 m of rock where the hydraulic testing is conducted by means an open-hole pumping using the HTHB method, see Table 3-1. The profiles demonstrate the impact of the gently-dipping deformation zones on the hydraulic and hydrogeochemical data and the strong correlation to the seismic reflectors. Reflector A4 corresponds to deformation zone ZFMNE00A4 in the base model etc. It is important to realise that although the 100 m PSS tests are as long as the vertical resolution of the computational grid of the simulation model below –400 masl many of the intersected deformation zones are much thinner, see Figure 3-3. To mitigate the numerical imperfections of the simulation model the vertical resolution of the computational grid above –400 masl is improved. The mean vertical spacing between two adjacent grid nodes in the upper 400 m of the simulation model is c 30 m.*

7.4.2 Comparisons with measured hydraulic conductivities

The hydrogeological DFN is matched in a statistical sense against the relatively small-scale 5 m test section transmissivity data from the PSS tests, see Figure 5-24 and Figure 5-25 in Section 5-7. The unconditional statistical matching implies that a distribution of parameter values is fitted, but no specific attention is paid to the location of the individual measurements. This is in accordance with assuming a Poisson process for the position of the fracture centres in space.

During the simulations with the multicomponent CPM Reference Case model it was found that the trend models for the deformation zone transmissivities suggested by Equations (4-1a) and (4-1b) were a problem, as it was difficult to match both the hydraulic conductivity and hydrogeochemistry measurements without adjusting a few particular borehole-deformation zones intercepts in the simulation model to the measured transmissivity values of the sections where the hydrogeochemical data were sampled, see Table 4-1. This observation suggests that the spatial variability around the trend line as suggested by Figure 4-3 is important, and that the hydrogeochemistry data, as we currently know them, by and large are governed by the hydrodynamic properties of the deterministically treated deformation zones. The encountered sensitivity of the hydrogeochemical data to the deformation zone heterogeneity is consistent with the sensitivity of the particle tracking, see sensitivity case D in Section 7.3.4.

Figure 7-25 through Figure 7-27 show comparisons between simulated grid cell hydraulic conductivities and PSS data on contiguous 100 m intervals. Such data are available for KFM01A (above c 600 m depth), KFM02A and KFM03A. Below c 600 m in KFM01A there are no flow anomalies detected, cf Figure 3-3. The good match at depth is unsurprising since a low-conductive multicomponent CPM was used. However, the matches near surface are quite poor, i.e. in KFM01A above c 500 m depth, in KFM02A above c 300 m depth and in KFM03A above c 100 m depth.

7.4.3 Comparisons with measured salinities

Figure 7-25 through Figure 7-27 show comparisons between simulated grid cell salinities and the measured data where available. The purpose of drawing of a line for the simulated data is to emphasise that the underpinning flow and salt transport model is based on a low-conductive CPM rather than a discrete flow system.

The model simulations predict similar profiles down the boreholes. Above c 400 m depth, the CPM Reference Case model strongly under-predicts salinity. This creates a conceptual problem since it is hard to reconcile having sufficient hydraulic conductivity to allow infiltration of a Littorina pulse without a following infiltration of freshwater once the site was exposed to precipitation about 1,000 years ago. This may just be a question of having to fine-tune surface hydraulic, transport properties and boundary conditions to obtain a good match. A possible explanation is that the thickness of low-conductive sediments such as postglacial clay and gyttja increased after the Littorina pulse. Another possible explanation is the near-surface high-transmissive horizontal fractures are very extensive and shortcut the meteoric flushing during the land rise. In contrast, the salinity at 1,000 m depth is over-predicted despite the very gradual rise in Brine specified in the initial condition that gives about 30% Brine at one kilometres depth, see Figure 2-11. It would suggest that the Brine is located even deeper. The interpretation of a deep saltwater interface is supported by the findings reported by /Ludvigson et al. 2004, Ludvigson and Levén 2005/, who looked at the salinity issue in KFM03A in detail. Figure 7-28 shows the differences mentioned above in a single plot.

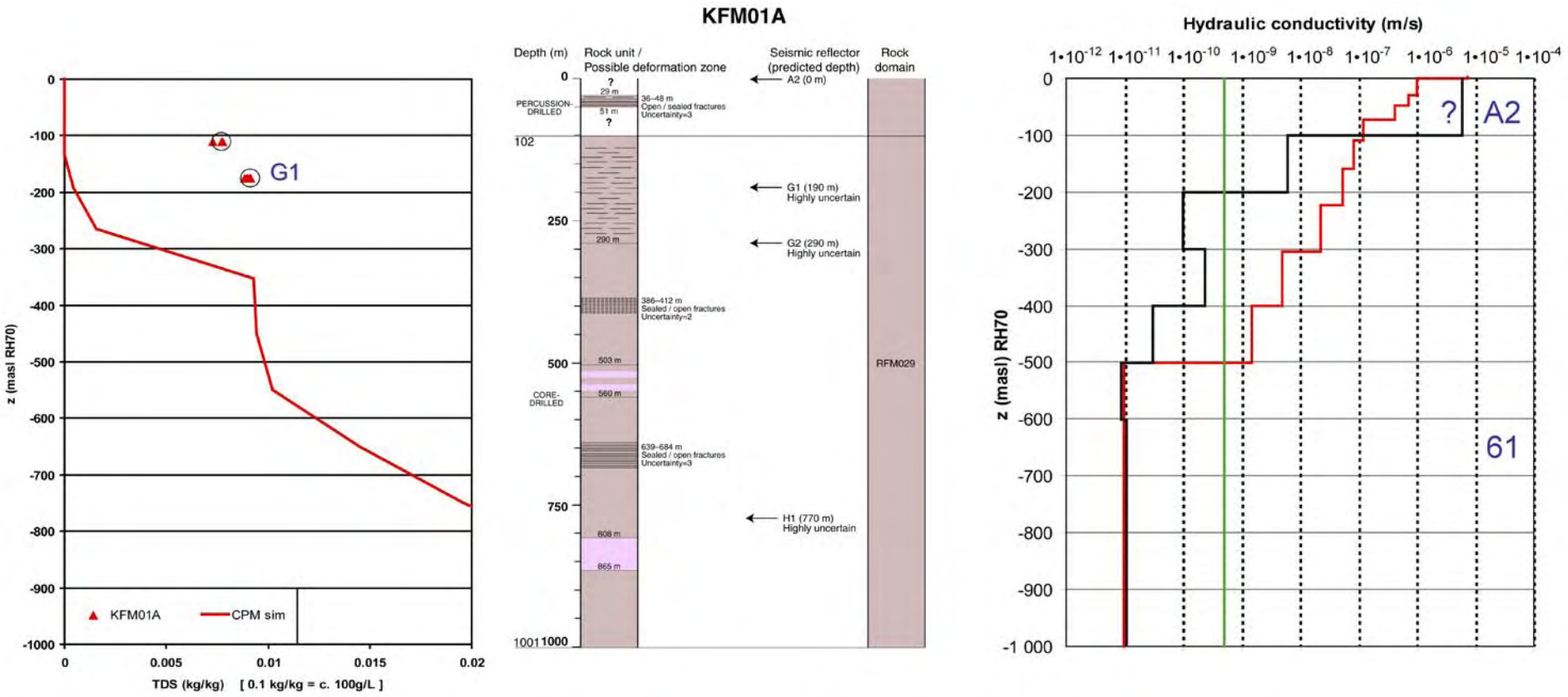

Figure 7-25. *Left: Comparison between simulated grid cell salinities and the high-quality measured data in KFM01A. The purpose of drawing of a line for the simulated data is to emphasise that the underpinning flow and salt transport model is based on a low-conductive CPM rather than a discrete flow system. Right: comparisons between simulated grid cell hydraulic conductivities and PSS data on contiguous 100 m intervals in KFM01A.*

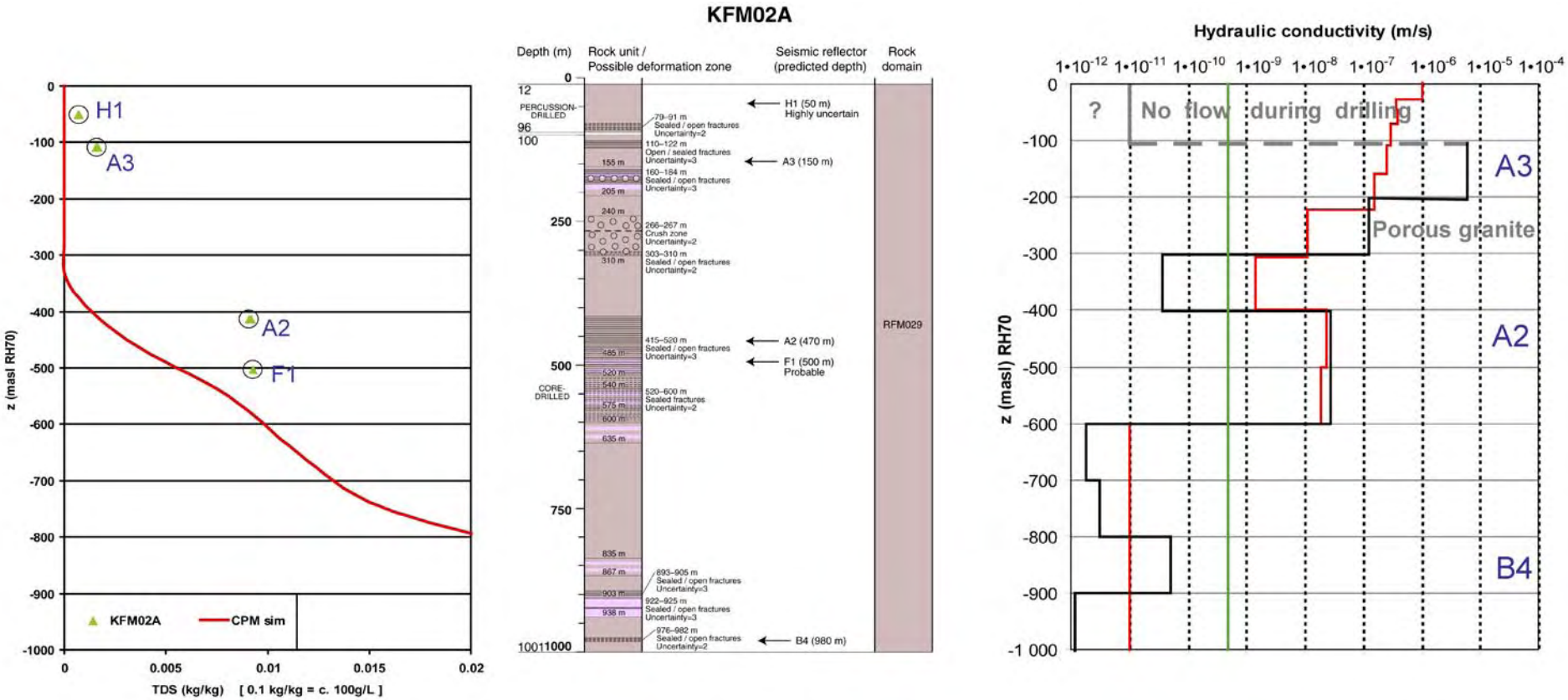

Figure 7-26. *Left: Comparison between simulated grid cell salinities and the high-quality measured data in KFM02A. The purpose of drawing of a line for the simulated data is to emphasise that the underpinning flow and salt transport model is based on a low-conductive CPM rather than a discrete flow system. Right: comparisons between simulated grid cell hydraulic conductivities and PSS data on contiguous 100 m intervals in KFM02A.*

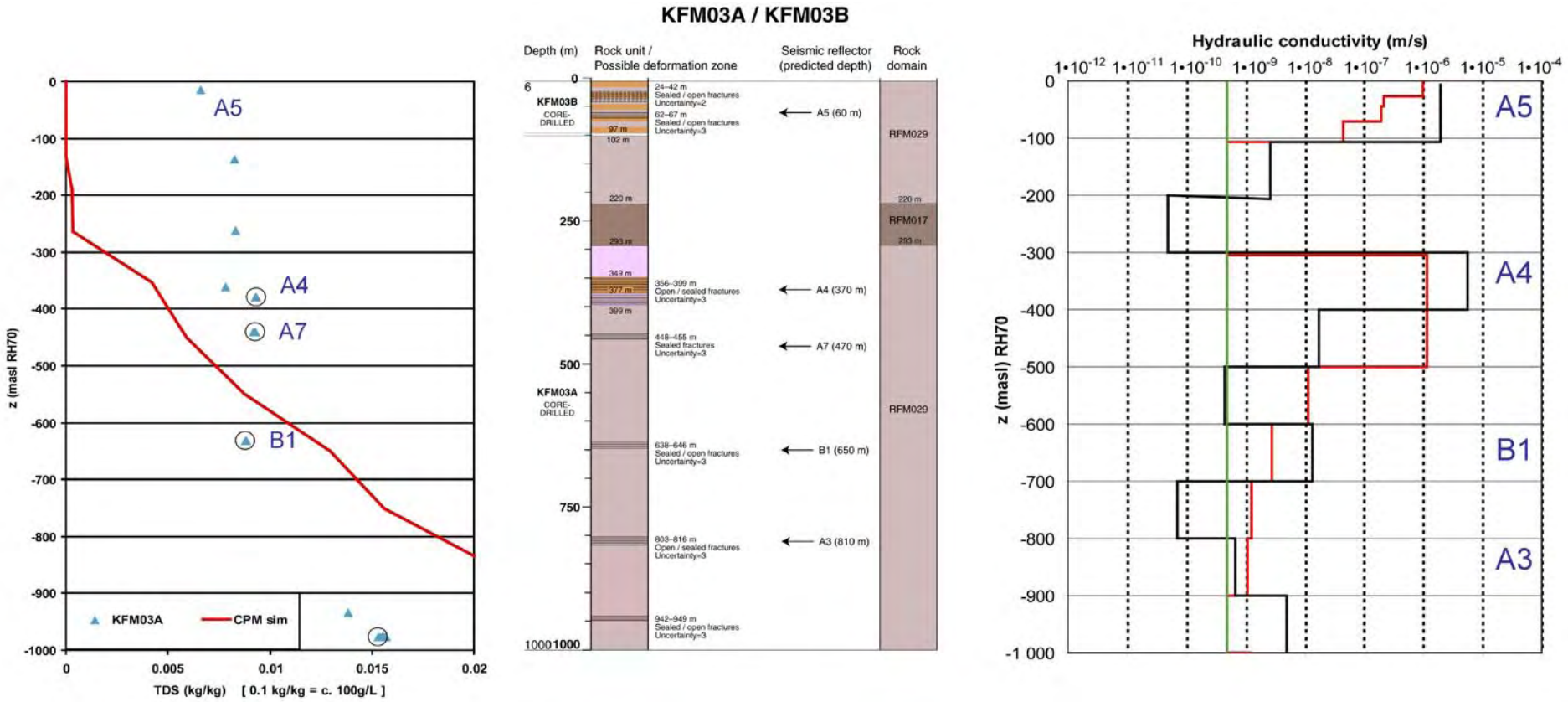

Figure 7-27. *Left: Comparison between simulated grid cell salinities and the high-quality measured data in KFM03A. The purpose of drawing of a line for the simulated data is to emphasise that the underpinning flow and salt transport model is based on a low-conductive CPM rather than a discrete flow system. Right: comparisons between simulated grid cell hydraulic conductivities and PSS data on contiguous 100 m intervals in KFM03A.*

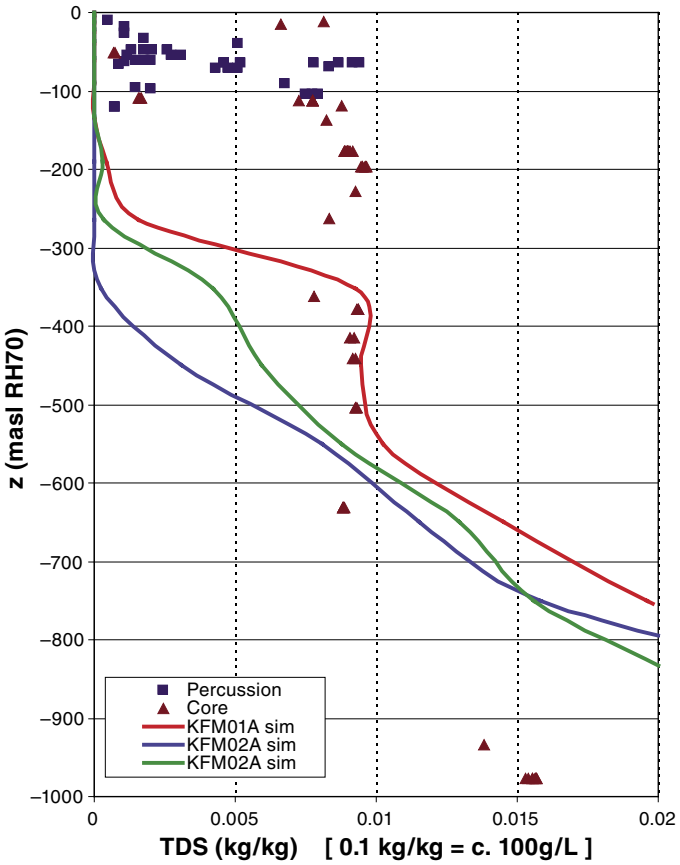

Figure 7-28. *Comparisons between simulated grid cell salinities and the measured data where available. The purpose of drawing of a line for the simulated data is to emphasise that the underpinning flow and salt transport model is based on a low-conductive CPM rather than a discrete flow system.*

Figure 7-29 shows the comparison with measured salinities in boreholes KFM01A–03A for the CPM Reference Case model all the way to 2,100 m depth. The few number of data points in Figure 7-29 reflects the decision to use only the most representative hydrogeochemical data in the CPM Reference Case model. The CPM Reference Case model simulations do not use any matrix diffusion, whereas the CPM Modified Case model simulations in Section 7.3 do. The reason for this is commented on below.

7.4.4 Comparisons with calculated mixing proportions

The groundwater composition may be described using a simplified system of four reference (or end-member) waters; Brine, Glacial, Marine and Rain 1960, see /Laaksoharju et al. 2004, 2005/. The end-member mixing fractions give several different tracers that have entered the groundwater system at different times and with different densities. As such, they give the possibility to quantify sensitivities of transient simulations to initial conditions, boundary conditions and hydraulic properties, which are not possible with salinity data alone. Salinity gives an indication of the balance in driving forces between hydraulic gradients at the surface and buoyancy effects of the dense brine, and how this balance has changed over time due to land rise. Hence, it acts as a natural tracer for transient variable-density flow.

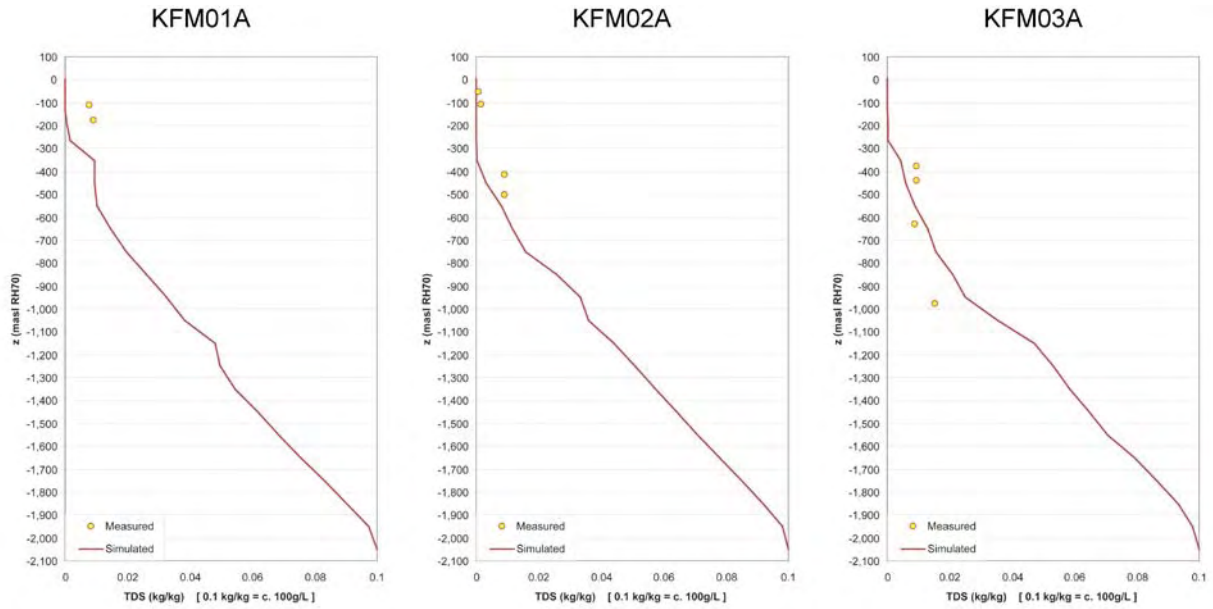

Figure 7-29. *Comparison with measured salinities (TDS) in KFM01A–KFM03A for the CPM Reference Case mode. The simulated salinities are shown by solid lines and the measured data by points. The data represent sampling intervals located in deformation zones. The simulations do not include matrix diffusion.*

A single density driven advection-dispersion equation is solved, where the variable-density flow was governed by specified boundary and initial conditions for the salinity, see Figure 2-6 and Figure 2-11, respectively. The transport of water parcels representing different water types (note the difference in the wording) is made by solving several independent non-reactive advection-dispersion equations in parallel, one for each water type. The concentration of a particular constituent at any point and time in the model was the sum of the products of each water type fraction with the concentration of the constituent of the corresponding reference water.

Figure 7-30 shows the water type profiles for the CPM Reference Case model together with the calculated M3 mixing proportions for boreholes KFM01A–03A. Five water types are simulated: Brine, Glacial, Littorina, Meteoric (precipitation before 1960) and Rain 1960 (precipitation after 1960), cf Section 2.6. The simulations do not include matrix diffusion. The data points in Figure 7-30 represent positions where high quality hydrogeochemical data were sampled, but it is noted that the M3 calculations were based on all data available.

7.4.5 Comparisons with measured environmental isotopes

Due to the interpretation uncertainty associated with the M3 calculations, the simulations were also compared with some basic conservative constituents such as the $\delta^{18}O$ and δD isotope ratios. These isotopes allows for a differentiation between Meteoric/Rain 1960 and Glacial freshwaters by larger negative ratio for the latter water type. However, the interpretation is not definitive as a large negative ratio is also observed for marine waters. Figure 7-31 shows the profiles of $\delta^{18}O$ and δD in KFM01A–3A for the CPM Reference Case model. The data points represent positions where high quality hydrogeochemical data were sampled. The flow simulations behind Figure 7-31 do not include a diffusion (matrix) component.

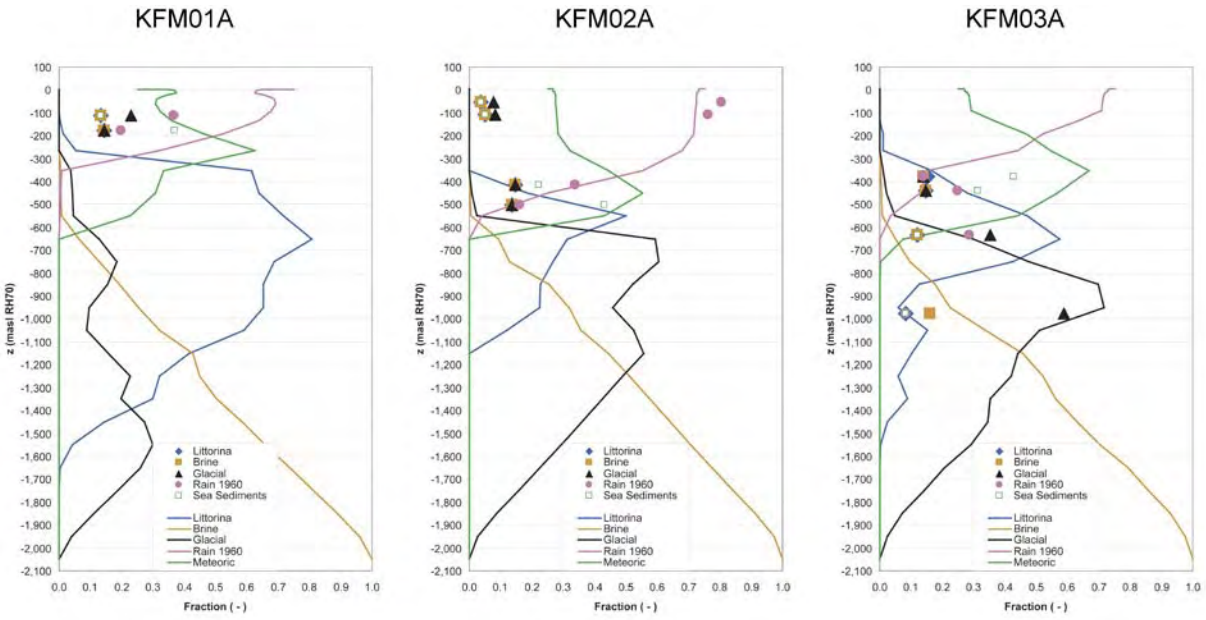

Figure 7-30. *Comparison with 4+1 water types (the meteoric flushing is divided into two events, before and after 1960) in KFM01A–3A for the CPM Reference Case model. The water type fractions in the flow model are shown by solid lines and the mixing proportions calculated by M3 by points. The simulations do not include matrix diffusion.*

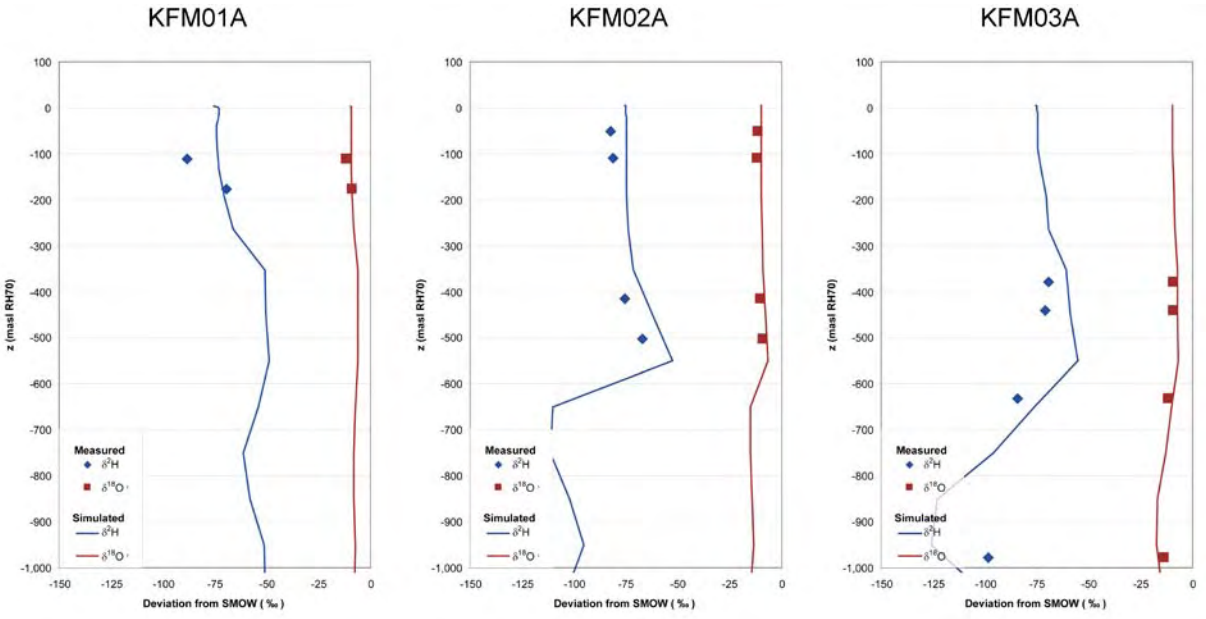

Figure 7-31. *Comparison with $\delta^{18}O$ and δD in KFM01A–3A for the CPM Reference Case model. The simulated values are shown by solid lines and the measured data by points. The simulations do not include matrix diffusion.*

7.4.6 Comparison of simulated flow paths

This section presents results from flow paths simulations using the Reference Case parameter settings. The set-up of the particle tracking is the same as for the CPM Modified Case model, cf Section 7-3 and Figure 7-4. Simulated flow paths and exit locations are shown in Figure 7-32. The upper inset shows the CPM Reference Case model and the lower inset the CPM Modified Case model. It is recalled that the motive for using the CPM Modified Case model in the sensitivity analysis is that the body of the particles of the CPM Reference Case model get stuck due to the low-hydraulic conductivity of the rock mass denoted by Volume D. In the CPM Modified Case model the hydraulic conductivity of the CPM Reference Case model within the target volume is increased by a factor of 50, from $1 \cdot 10^{-10}$ m/s to $5 \cdot 10^{-10}$ m/s.

In the CPM Modified Case, almost all particles arrive at the surface exit locations within 10,000 years. The median travel time is 183 years. The CPM Modified Case assumed a matrix diffusion component and a relatively high salinity gradient (full brine at 1,450 m depth). In the CPM Reference Case model, less than 20% of the particles exit within 30,000 years, thus implying a median travel time of at least 30,000 years. No matrix diffusion was assumed and full brine was specified at 1,950 m depth in this latter case. The exit locations are in both models governed the *base model* deformation zones.

The motive for not activating a matrix diffusion component in the CPM Reference Case flow model does not mean that there is no matrix diffusion. Matrix diffusion is excluded in CPM Reference Case flow model in order to achieve a better performance of the particle tracking. If matrix diffusion is included the velocity field, which governs the particle tracking, is significantly affected by the initial condition for the salinity, the assigned hydraulic diffusivity, and the magnitude of salinity stored in the matrix and available for diffusion.

The absence of pore water hydrogeochemistry data for model version 1.2 means that it is not possible to make conclusive judgements regarding the role of matrix diffusion for the migration of salinity. If one assumes, as it has been done in version 1.2, that the initial salinity profile in the fracture system is in equilibrium with the initial salinity profile throughout the entire low-conductive matrix, there will be diffusion of salt out from the matrix into the transmissive zones as the latter gets flushed out by the meteoric water during the shoreline displacement. This flux of salt is subjected to gravitation once it reaches the deformation zones. The point made here is that variable-density effects seen in the particle-tracking are caused by the initial condition used, i.e. too much salt in the matrix.

For the same reason it was necessary to include matrix diffusion and even use a steeper gradient (sharper interface) in order to prohibit a total washout for the CPM Modified Case, since the hydraulic conductivity was much greater.

For the sake of comparison, a median travel time of 475 years was obtained with 76% of the particles exiting within 30,000 years for a variant where matrix diffusion was included in the CPM Reference Case.

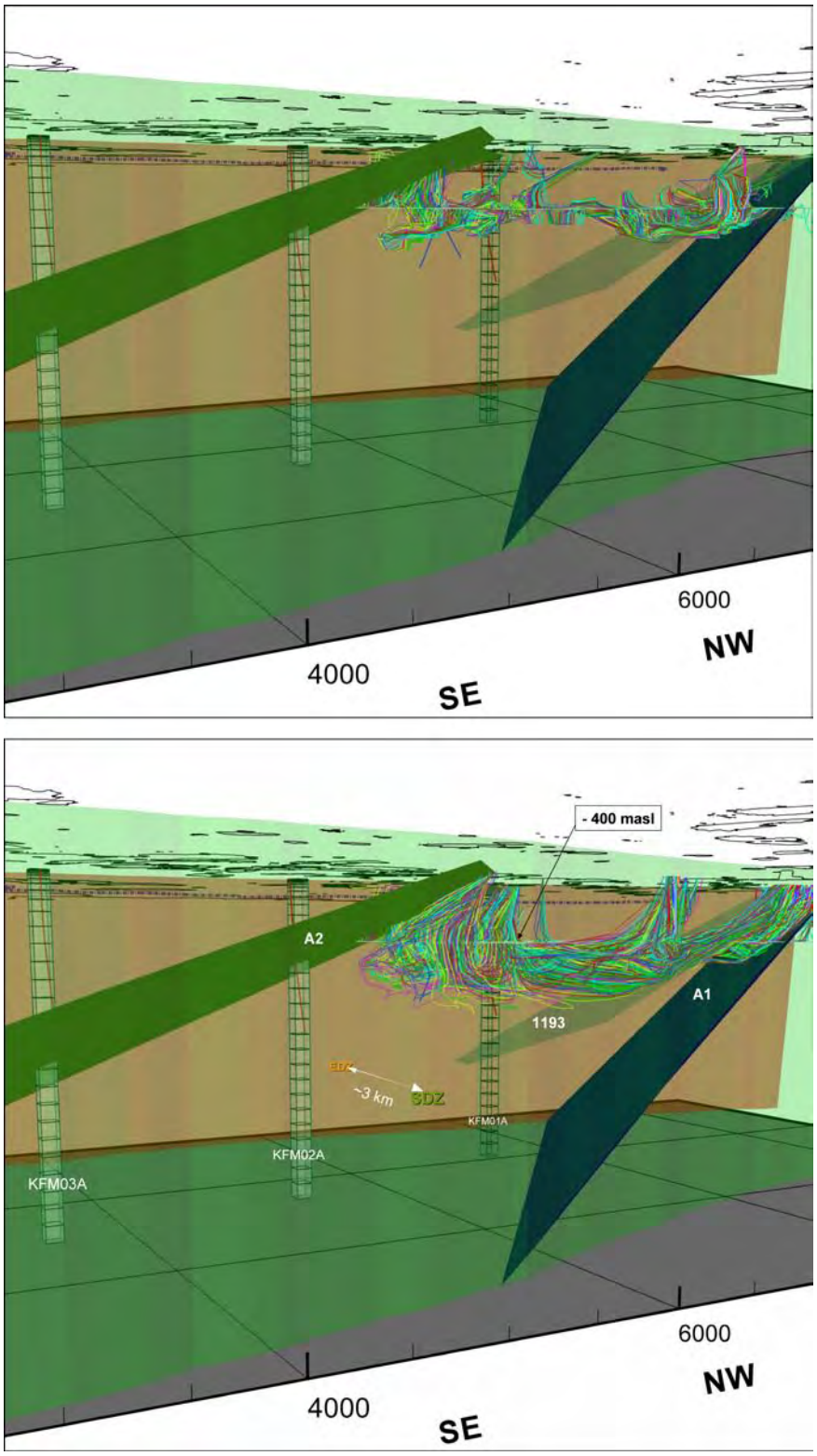

Figure 7-32. *Top: Flow paths for the CPM Reference Case model. Bottom: Flow paths for the CPM Modified Case model. The exit locations are in both models governed the base model deformation zones. Besides the gently dipping deformations ZFMNE00A1, -A2 and -1193 there is a also a significant discharge around Lake Bolundsfjärden.*

7.4.7 Summary of findings using the CPM Reference Case model

Despite the significant imperfections of using a multicomponent CPM model the simulations conducted demonstrate that some features seen in the hydrogeochemical data can be reproduced reasonably well. This is interpreted to be indicative of a low-conductive rock mass where the available hydrogeochemical data are gathered in the deformation zones. The hydraulic heterogeneity of the deformation zones is found to be vital for the hydrogeochemical comparisons as well as for the particle tracking.

Given the objectives of the CPM modelling, the key sources of uncertainty identified in the work reported here are:

- The interplay between the rock mass hydraulic conductivity, the initial condition for salinity and matrix diffusion is shown to be complex and decisive for the simulation results. The simulations conducted lead to a pertinent question concerning the initial salinity profile in a low-conductive rock mass. The tacit assumption that the salinity profile in the fracture system is in equilibrium with the initial salinity profile throughout the entire low-conductive matrix from the onset of the palaeo-hydrogeological simulations starting at 8,000 BC is put in question. If equilibrium is at hand the initial elevation of the salinity interface must be deeper than –450 masl, which was the value used in the work reported here. To improve the understanding of the initial conditions it is desirable to learn more about the salinity profile in the matrix and in the rock mass fracturing both within and outside RFM029.

- The model simulations predict similar profiles down the three boreholes KFM01A–KFM03A. Above c 400 m depth, the CPM Reference Case model strongly underpredicts salinity. If correct, this creates a conceptual problem since it is hard to reconcile having sufficient hydraulic conductivity to allow infiltration of a Littorina pulse without a following infiltration of freshwater once the site was exposed to precipitation about 1,000 years ago. This may just be a question of having to fine-tune surface hydraulic, transport properties and boundary conditions to obtain a good match. For instance, a tentative explanation is that the thickness of low-conductive sediments such as postglacial clay and gyttja increased after the Littorina pulse thereby reducing the flushing of the superficial rock. Another possible explanation is that the high-transmissive horizontal fractures encountered a few metres below the bedrock surface are very extensive and thereby reducing the flushing of the superficial rock beneath.

- In contrast, the salinity at 1,000 m depth is over-predicted despite the very gradual rise in Brine specified in the initial condition that gives about 30% Brine at one kilometres depth. This suggests that the Brine is located even deeper. The interpretation of a deep saltwater interface is supported by the findings reported by /Ludvigson et al. 2004, Ludvigson and Levén 2005/.

8 Discussion and conclusions

A numerical model is developed on a regional-scale (hundreds of square kilometres) to study the zone of influence for variable-density groundwater flow that affects the Forsmark area. Transport calculations are performed by particle tracking from a local-scale release area (a few square kilometres) to test the sensitivity to different hydrogeological uncertainties and the need for far-field realism.

A number of new aspects to the scope of modelling have been included for model version 1.2 (Forsmark 1.2). One of the most important is the representation and treatment of uncertainty of the deformation zones. Three alternative geological models for the deterministically treated deformation zones were produced for Forsmark 1.2 based on different levels of confidence in the interpretation. A *base model* was provided based on high confidence structures local to the site between the Singö and Eckarfjärden deformation zones. One of the key features of this model is the presence of several extensive gently dipping deformation zones within the candidate area. A *base variant model* was developed that considers an extension of some gently dipping deformation zones beyond the candidate area. Finally, an *alternative model* case was proposed with the inclusion of many low confidence steeply dipping lineaments outside the candidate area (mainly). Each of these models are implemented in a numerical flow model and scrutinised hydraulically in the work reported here.

In addition to these considerations of the sensitivity to various structural models, the concept that hydraulic properties for the deformation zones should vary with depth and according to the dip of structures was introduced. The foundation for this concept in terms of field data from the site investigations is thoroughly described and different hydraulic interpretations are tested numerically. A good figure to look at is Figure 1-4.

We suggest that the observed dependence of deformation zone transmissivity on orientation may be due to the present-day stress field. If the observations made so far are correct the transmissivity in the gently dipping deformation zones is on the average greater than the transmissivity of steeply-dipping deformation zones striking NW and much greater than steeply-dipping deformation zones striking NE.

Another difference from model version 1.1 (Forsmark 1.1) is the significant increase in information concerning rock mass fractures and hydraulic tests. Posiva flow log (PFL-f) data were available from five one-kilometre long core drilled boreholes, KFM01A–KFM05A. Considerable spatial variations in fracture frequency and flow were observed within and between boreholes and it was believed important to differentiate rock mass properties inside rock domain RFM029 (the dominating rock domain within the so-called ‘tectonic lens’ that spans the candidate area) from one another by means of sub-volumes as well from those outside. Four subvolumes are suggested in the work reported here based on the available information, see Figure 5-16.

In summary, we suggest that a very sparsely fractured and low-permeable rock mass is located below c –400, NW of the NE-striking, gently-dipping deformation zone ZFMNE00A2. There are four boreholes that support this interpretation, KFM01A, -2A, -4A and -5A. In contrast, borehole KFM03A is located in an entirely different sub-volume.

Above the sparsely fractured and low-permeable rock mass the rock gets more fractured and the fractures more transmissive. The fractures in uppermost 100 m are exceptionally transmissive. The report contains many figures that give a good overview of the hydraulic data

observed in the five deep and 19 shallow boreholes. Table 5-5 provides a brief summary of what rock mass data that underpin the demarcation of the four sub-volumes. Figure 7-1 presents the outcome of the hydrogeological DFN connectivity analysis developed and applied by the DarcyTools modelling team.

Based on the structural and hydraulic data available at Data Freeze 1.2 and the hydrogeological DFN modelling conducted in the work reported here regional groundwater flow simulations were conducted. Figure 2-1 provides an overview of the modelling approaches available for modelling stage 1.2. We conclude in Chapter 5 that different DFN models may be discussed for the rock mass in Forsmark ranging from a quite low conductive rock mass characterised by a very sparsely interconnected and low-transmissive DFN to a moderately conductive rock mass characterised by a well interconnected and moderately-transmissive DFN. The existence and meaning of interconnected fractures below the lower measurement of the PFL-f tests remains an unresolved uncertainty, however. The findings of the hydrogeological DFN analysis reported here suggest that such networks exist in all sub-volumes given the assumed power-law size distributions.

Although the DFN approach appears to be the most obvious flow approach for the rock mass in Forsmark, the use of a low-conductive continuum approach in parallel may provide a means for fruitful discussions about the differences observed when the simulations are compared with measurements. If the differences are small regardless of the approach used, the measured data are probably not sufficient to constrain the conceptual modelling, or, alternatively, the rock mass DFN properties do not play an important role on a regional scale. If the differences are great regardless of the approach used, both approaches probably need to be revised unless there are errors or great uncertainties in the measured data. If one of the approaches is much better than the other, the reason for the differences needs to be understood.

The objectives of the multicomponent continuous porous media (CPM) model used for the regional-scale simulations in the work reported here were to provide: (i) a bounding check on the more complex equivalent porous media (EPM) model treated by the *ConnectFlow Team*, (ii) a comprehensible assessment in which the effects of specific assumptions are easily traced, and (iii) identification of key sources of uncertainty.

Numerical simulations were run with the intention to achieve an improved palaeo-hydrogeological understanding. With regard to the aforementioned objectives of the multicomponent CPM model the numerical simulations started out with a series of sensitivity cases were the need for detailed far-field realism was tested treated by means of particle tracking. This to gain an understanding of how the uncertainty of different primary model parameter assumptions interplay with the low-permeable target volume, and ultimately to what extent these parameters contribute to a reasonable match to the field data (palaeo-hydrogeological understanding). Eventually, an attempt was made to achieve a reasonable matched flow model (first objective) despite the simplification associated with a multicomponent CPM flow model.

Table 7-11 provides a compilation of findings for the sensitivity cases studied. Section 7.4.7 summarises the results from the attempt to achieve a reasonable matched flow model. In spite of the significant imperfections of using a multicomponent CPM model the simulations conducted demonstrate that some features seen in the hydrogeochemical data can be reproduced reasonably well. This is interpreted to be indicative of a low-conductive rock mass where the available hydrogeochemical data to be matched are gathered in the deformation zones. The hydraulic heterogeneity of the deformation zones is found to be vital for the hydrogeochemical comparisons as well as for the particle tracking.

Given the objectives of the CPM modelling, the key sources of uncertainty identified in the work reported here are:

- The interplay between the rock mass hydraulic conductivity, the initial condition for salinity and matrix diffusion is shown to be complex and decisive for the simulation results. The simulations conducted lead to a pertinent question concerning the initial salinity profile in a low-conductive rock mass. The tacit assumption that the salinity profile in the fracture system is in equilibrium with the initial salinity profile throughout the entire low-conductive matrix from the onset of the palaeo-hydrogeological simulations starting at 8,000 BC is put in question. If equilibrium is at hand the initial elevation of the salinity interface must be deeper than –450, which was the value used in the work reported here. To improve the understanding of the initial conditions it is desirable to learn more about the salinity profile in the matrix and in the rock mass fracturing both within and outside rock domain RFM029.

- The model simulations predict similar profiles down the three boreholes KFM01A–KFM03A. Above c –400, the multicomponent CPM (Reference Case) model strongly under-predicts salinity. If correct, this creates a conceptual problem since it is hard to reconcile having sufficient hydraulic conductivity to allow infiltration of a Littorina pulse without a following infiltration of freshwater once the site was exposed to precipitation about 1,000 years ago. This may just be a question of having to fine-tune surface hydraulic properties, transport properties and boundary conditions to obtain a good match. A tentative explanation is that the thickness of low-conductive sediments such as postglacial clay and gyttja increased after the Littorina pulse thereby reducing the meteoric flushing of the superficial rock. Another tentative explanation is the near-surface high-transmissive horizontal fractures are very extensive and shortcut the meteoric flushing during the land rise. In contrast, the salinity at 1,000 m depth is over-predicted despite the very gradual rise in Brine specified in the initial condition that gives about 30% Brine at one kilometres depth. This suggests that the Brine interface is located even deeper.

9 References

Andersson J-E, Nordqvist R, Nyberg G, Smellie J, Tirén S, 1991. Hydrogeological conditions in the Finnsjön area. Compilation of data and conceptual model, SKB TR-91-24, Svensk Kärnbränslehantering AB.

Andersson J, Elert M, Gylling B, Moreno L, Selroos J-O, 1998a. Derivation and treatment of the flow wetted surface and other geosphere parameters in the transport models FARF31 and COMP23 for use in safety assessment, SKB R-98-60, Svensk Kärnbränslehantering AB.

Andersson P, Ludvigsson J-E, Wass E, 1998b. Äspö Hard Rock Laboratory, True Block Scale Project, Preliminary characterisation – Combined interference tests and tracer tests, SKB IPR-01-44, Svensk Kärnbränslehantering AB.

Andersson P, Ludvigsson J-E, Wass E, Holmqvist M, 2000. Äspö Hard Rock Laboratory, True Block Scale Project, Tracer test stage – Interference tests, dilution tests and tracer tests, SKB IPR-00-28, Svensk Kärnbränslehantering AB.

Axelsson C-A, Ekstav A, Lindblad Påsse A, 2002. SFR – Utvärdering av hydrogeology, SKB R-02-14, Svensk Kärnbränslehantering AB.

Carlsson A, 1979. Characteristic features of a superficial rock mass in southern central Sweden – Horizontal and subhorizontal fractures and filling material. Striae 11, Uppsala.

Carlsson L, Carlsten S, Sigurdsson T, Winberg A, 1985. Hydraulic modelling of the final repository for reactor waste (SFR), Compilation and conceptualization of available geological and hydrogeological data, Edition 1, SKB Progress Report SFR 85-06, Svensk Kärnbränslehantering AB.

Curtis P, Elfström M, Markström I, 2004. Rock visualization system. Technical description (RVS v.3.5), SKB R-04-55, Svensk Kärnbränslehantering AB.

Darcel C, Davy P, Bour O, De Dreuzy J-R, 2004. Alternative DFN model based on initial site investigations at Simpevarp, SKB R-04-76, Svensk Kärnbränslehantering AB.

Davy P, Darcel C, Bour O, Munier R, de Dreuzy J R, 2005. Note on the Terzaghi angular correction applied to fracture intensity profile along core, draft manuscript.

Dershowitz W, Winberg A, Hermanson J, Byegård J, Tullborg E-L, Andersson P, Mazurek M, 2003. Äspö Task Force on modelling of groundwater flow and transport of solutes, Task 6C, A semi-synthetic model of block scale conductive structures at the Äspö HRL, SKB IPR-03-13, Svensk Kärnbränslehantering AB.

Elhammer A, Sandkvist Å, 2005. Forsmark site investigation, Detailed marine geological mapping, SKB P-03-101, Svensk Kärnbränslehantering AB.

Follin S, Stigsson M, Berglund S, Svensson U, 2004. Variable-density groundwater flow simulations and particle tracking – Numerical modelling using DarcyTools, Preliminary site description Simpevarp area – version 1.2, SKB R-04-65, Svensk Kärnbränslehantering AB.

Follin S, Stigsson M, Svensson U, 2005. Variable-density groundwater flow simulations and particle tracking – Numerical modelling using DarcyTools, Preliminary site description Simpevarp subarea – version 1.2, SKB R-05-11, Svensk Kärnbränslehantering AB.

Forsman I, Zetterlund M, Rhén I, 2004. Correlation of Posiva Flow Log anomalies to core mapped features in Forsmark (KFM01A to KFM05A), SKB R-04-77, Svensk Kärnbränslehantering AB.

Gustafsson B, 2004. Millennial changes of the Baltic Sea salinity – studies of the salinity to climate change, SKB TR-04-12, Svensk Kärnbränslehantering AB.

Haggerty R, Gorelick S M, 1995. Multi-rate mass transfer for modelling diffusion and surface reactions in media with pore-scale heterogeneity. Water Resources Research, 31(10), 2383–2400.

Harlow F H, Welch J E, 1965. Numerical Calculation of Time-Dependent Viscous Incompressible Flow of Fluid with Free Surface, Phys. Fluids, vol 8, p 2182.

Hartley L, Hoch A, Hunter F, Jackson P, Marsic Niko, 2005. Regional hydrogeological simulations for Forsmark – Numerical modelling using CONNECTFLOW. Preliminary site description of the Forsmark area. SKB R-05-12, Svensk Kärnbränslehantering AB.

Hartley L, Cox I, Hunter F, Jackson P, Joyce S, Swift B, Gylling B, Marsic Niko, 2005. Regional hydrogeological simulations for Forsmark – Numerical modelling using CONNECTFLOW. Preliminary site description of the Forsmark area, SKB R-05-32, Svensk Kärnbränslehantering AB.

Hedenström A, Risberg J, 2003. Shore displacement in northern Uppland during the last 6,500 calendar years, SKB TR-03-17, Svensk Kärnbränslehantering AB.

Hedin A, 2005. An analytical method for estimating the probability of canister/fracture intersections in a KBS-3 respository, SKB R-05-29, Svensk Kärnbränslehantering AB.

Isaksson H, 2003. Forsmark site investigation. Interpretation of topographic lineaments 2002. SKB P-03-40, Svensk Kärnbränslehantering AB.

Isaksson H, Thunehed H, Mattsson H, Keisu M, 2004. Forsmark site investigation. Interpretation of airborne geophysics and integration with topography. Stage 1 (2002). SKB P-04-29, Svensk Kärnbränslehantering AB.

Isaksson H, Keisu M, 2005. Forsmark site investigation. Interpretation of airborne geophysics and integration with topography. Stage 2 (2002–2004). SKB P-04-282, Svensk Kärnbränslehantering AB.

Johansson P-O, 2003. Forsmark site investigation, Drilling and sampling in soil, Installation of groundwater monitoring wells and surface water level gauges, SKB P-03-64, Svensk Kärnbränslehantering AB.

Johansson R, 2005. A comparison of two independent interpretations of lineaments from geophysical and topographic data at the Forsmark site. Preliminary site description. Forsmark area – version 1.2. SKB R-05-23, Svensk Kärnbränslehantering AB.

Johansson P-O, Werner K, Bosson E, Berglund S, Juston J, 2005. Description of climate, surface hydrology, and near-surface hydrogeology for Forsmark 1.2, SKB R-05-06, Svensk Kärnbränslehantering AB.

Juston J, Johansson P-O, 2005. Analysis of meteorological data, surface water level data, and groundwater level data. Forsmark site investigation, SKB P-05-152, Svensk Kärnbränslehantering AB.

Jönsson S, Ludvigson J-E, Svensson T, 2004. Hydraulic interference tests. Boreholes HFM11 and HFM12, Forsmark site investigation, SKB P-04-200, Svensk Kärnbränslehantering AB.

Knutsson G, Morfeldt C-O, 2003. Grundvatten, teori & tillämpning, AB Svensk Byggtjänst.

Korhonen K, Paananen M, Paulamäki S, 2004. Forsmark site investigation. Interpretation of lineaments from airborne geophysical and topographic data. An alternative model within version 1.2 of the Forsmark modelling project. SKB P-04-241, Svensk Kärnbränslehantering AB.

Källgården J, Ludvigson J-E, Hjerne C, 2004a. Single-hole injection tests in borehole KFM03A, Forsmark site investigation, SKB P-04-194, Svensk Kärnbränslehantering AB.

Källgården J, Ludvigson J-E, Jönsson J, 2004b. Single-hole injection tests in borehole KFM02A. Forsmark site investigation, SKB P-04-100, Svensk Kärnbränslehantering AB.

Laaksoharju M, Gimeno M, Auque L, Gómez J, Smellie J, Tullborg E-L, Gurban I, 2004. Hydrogeochemical Evaluation of the Forsmark Site, Model Version 1.1, SKB R-04-05, Svensk Kärnbränslehantering AB.

Laaksoharju M, Auque L, Gimeno M, Gómez J, Gurban I, Hallbeck L, Molinero J, Raposo J, Smellie J, Tullborg E-L, 2005. Hydrogeochemical Evaluation for the Forsmark Model Version 1.2, SKB R-05-17, Svensk Kärnbränslehantering AB.

La Pointe P R, Cladouhos T, Follin S, 1999. Calculation of displacement on fractures-intersecting canister induced by earthquakes: Aberg, Beberg and Ceberg examples, SKB TR-99-03, Svensk Kärnbränslehantering AB.

La Pointe P R, Olofsson I, Hermanson J, 2005. Statistical model of fractures and deformation zones for Forsmark. Preliminary site description. Forsmark area – version 1.2. SKB R-05-26. Svensk Kärnbränslehantering AB.

Levén J, Ludvigson J-E, 2004. Hydraulic interferences during the drilling of borehole KFM01B. Boreholes HFM01, HFM02, HFM03 and KFM01A. Forsmark site investigation, SKB P-04-135, Svensk Kärnbränslehantering AB.

Lindborg T (ed), 2005. Description of the surface systems, Forsmark area – version 1.2, SKB R-05-03, Svensk Kärnbränslehantering AB.

Ludvigson J-E, Levén J, Jönsson S, 2004. Single-hole injection tests in borehole KFM01A, Forsmark site investigation, SKB P-04-95, Svensk Kärnbränslehantering AB.

Ludvigson J-E, Jönsson S, Levén J, 2004. Hydraulic evaluation of pumping activities prior to hydro-geochemical sampling in borehole KFM03A – Comparison with results from difference flow logging, Forsmark site investigation, SKB P-04-96, Svensk Kärnbränslehantering AB.

Ludvigson J-E, Levén, J, 2005. Comparison of measured EC in selected fractures in boreholes KFM02A, KFM03A and KFM04A from difference flow logging and hydrogeochemical characterization – Analysis of observed discrepancies in KFM03A, Forsmark site investigation, SKB P-05-21, Svensk Kärnbränslehantering AB.

Moye D G, 1967. Diamond drilling for foundation exploration. Civ. Eng. Trans. 7th Inst. Eng. Australia, 95–100.

Patankar S V, 1980. Numerical heat transfer and fluid flow. Hemisphere Publishing Corporation, McGraw-Hill Book Company.

Rhén I, Gustafson G, Stanfors R, Wikberg, P, 1997. Äspö HRL – Geoscientific evaluation 1997/5. Models based on site characterization 1986–1995, SKB TR-97-06, Svensk Kärnbränslehantering AB.

Rhén I, Forsmark T, 2001. Äspö Hard Rock Laboratory. Prototype repository, Hydrogeology, Summary report of investigations before the operation phase, SKB IPR-01-65, Svensk Kärnbränslehantering AB.

Rhén I, Follin S, Hermanson, J, 2003. Hydrological Site Descriptive Model – a strategy for its development during Site Investigations, SKB R-03-08, Svensk Kärnbränslehantering AB.

Robertsson A-M, 2004. Forsmark site investigation, Microfossil analyses of till and sediment samples from Forsmark, northern Uppland, SKB P-04-110, Svensk Kärnbränslehantering AB.

SKB, 2002. Metodbeskrivning för BOREMAP-kartering, SKB MD 143.00, Svensk Kärnbränslehantering AB.

SKB, 2004. Preliminary site description. Forsmark area – version 1.1. SKB R-04-15, Svensk Kärnbränslehantering AB.

SKB, 2005a. Preliminary site description. Forsmark area – version 1.2. SKB R-05-18 (preliminary manuscript), Svensk Kärnbränslehantering AB.

SKB, 2005b. Forsmark site investigation. Programme for further investigations of geosphere and biosphere, SKB R-05-14, Svensk Kärnbränslehantering AB.

Sohlenius G, Hedenström A, Rudmark L, 2004. Mapping of unconsolidated Quaternary deposits 2002–2003, Map description, SKB R-04-39, Svensk Kärnbränslehantering AB.

Sundh M, Sohlenius G, Hedenström A, 2004. Stratigraphical investigation of till in machine cut trenches, SKB P-04-34, Svensk Kärnbränslehantering AB.

Svensson U, 1997a. A regional analysis of groundwater flow and salinity distribution in the Äspö area, SKB TR-97-09, Svensk Kärnbränslehantering AB.

Svensson U, 1997b. A site scale analysis of groundwater flow and salinity distribution in the Äspö area, SKB TR-97-17, Svensk Kärnbränslehantering AB.

Svensson U, 1999. A laboratory scale analysis of groundwater flow and salinity distribution in the Äspö area, SKB TR-99-24, Svensk Kärnbränslehantering AB.

Svensson U, 2001a. A continuum representation of fracture networks. Part I: Method and basic test cases. Journal of Hydrology, Volume 250, 170–186.

Svensson U, 2001b. A continuum representation of fracture networks. Part II: Application to the Äspö Hard Rock Laboratory. Journal of Hydrology, Volume 250, 187–205.

Svensson U, 2004a. DarcyTools, Version 2.1. Verification and validation. SKB R-04-21, Svensk Kärnbränslehantering AB.

Svensson U, 2004b. Modelling flow, transport and retension in a 3D fracture network under a natural head gradient, Äspö Task Force, Task 6E, in prep, Svensk Kärnbränslehantering AB.

Svensson U, Ferry M, 2004. DarcyTools, Version 2.1. User's guide. SKB R-04-20, Svensk Kärnbränslehantering AB.

Svensson U, Kuylenstierna H-O, Ferry M, 2004. DarcyTools, Version 2.1. Concepts, methods, equations and demo simulations. SKB R-04-19, Svensk Kärnbränslehantering AB.

Svensson U, Follin S, 2005. Äspö Hard Rock Laboratory, Äspö Task Force – Task 6A, 6B and B2, Simulation of tracer transport considering both experimental and natural time scales, SKB IPR-04-42, Svensk Kärnbränslehantering AB.

Terzaghi R D, 1965. Sources of error in joint surveys, Geotechnique, V.15, 287–304.

Thiem G, 1906. Hydrologishe Methoden, J M Gebhardt, Leipsig.

Vikström M, 2005. Modelling of soil depth and lake sediments. An application of the GeoEditor at the Forsmark site, SKB R-05-07, Svensk Kärnbränslehantering AB.

Werner K, Johansson P-O, 2003. Slug tests in groundwater monitoring wells in soil. Forsmark site investigation, SKB P-03-65, Svensk Kärnbränslehantering AB.

Werner K, 2004. Supplementary slug tests in groundwater monitoring wells in soil. Forsmark site investigation, SKB P-04-140, Svensk Kärnbränslehantering AB.

Werner K, Lundholm L, Johansson P-O, 2004. Drilling and pumping test of wells at Börstilåsen. Forsmark site investigation, SKB P-04-138, Svensk Kärnbränslehantering AB.

Westman P, Wastegård S, Schoning K, Gustafsson B, Omstedt A, 1999. Salinity change in the Baltic Sea during the last 8 500 years: evidence, causes and models. SKB TR-99-38, Svensk Kärnbränslehantering AB.

Winberg A, Andersson P, Byegård J, Poteri A, Cvetkovic V, Dershowitz W, Doe T, Hermansson J, Gómez-Hernandez J, Hautojärvi A, Billaux D, Tullborg E-L,

Appendix A

Geological illustrations

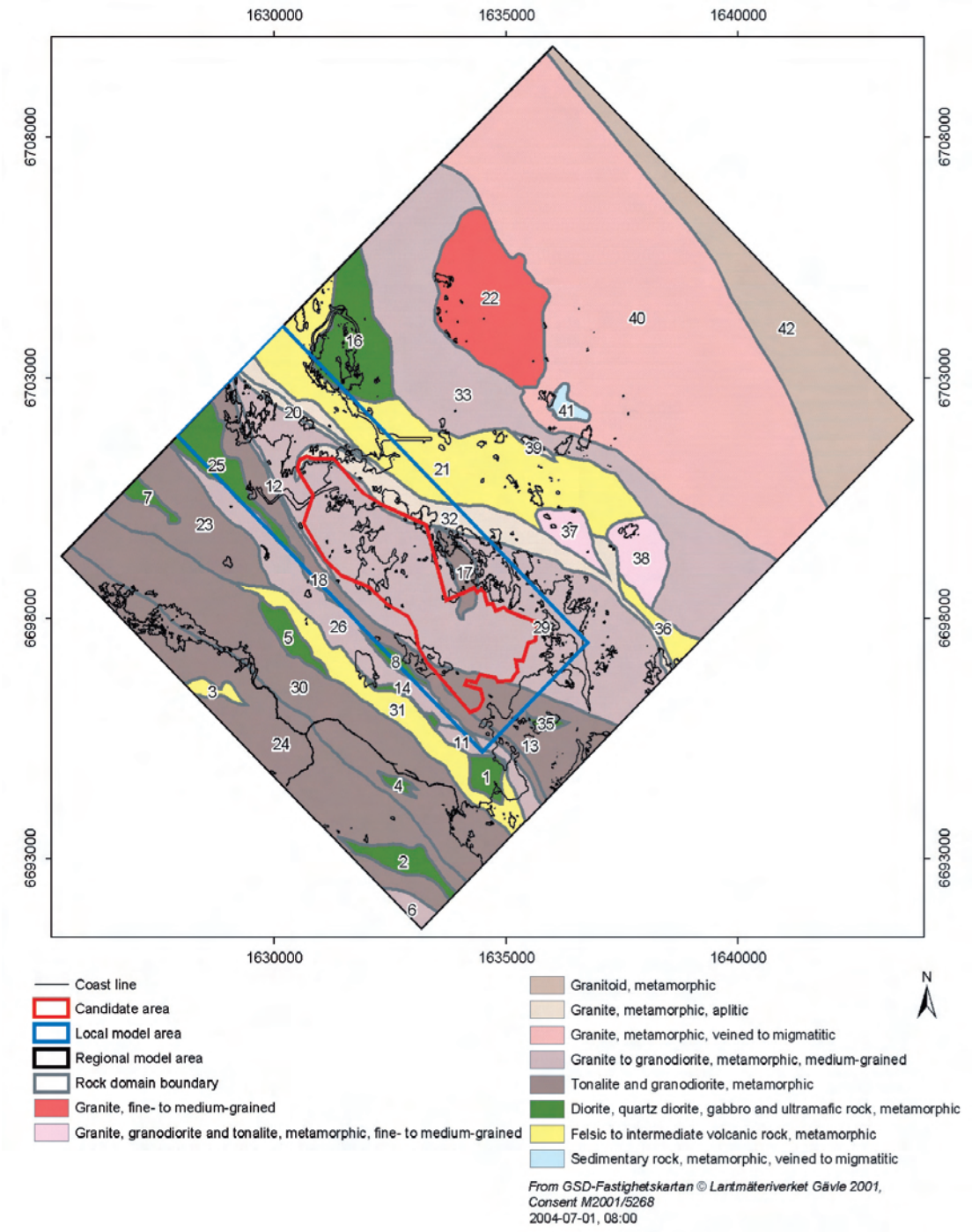

Figure A-1. *Geological map of the bedrock in the Forsmark area, model version 1.2 /SKB 2005a/.*

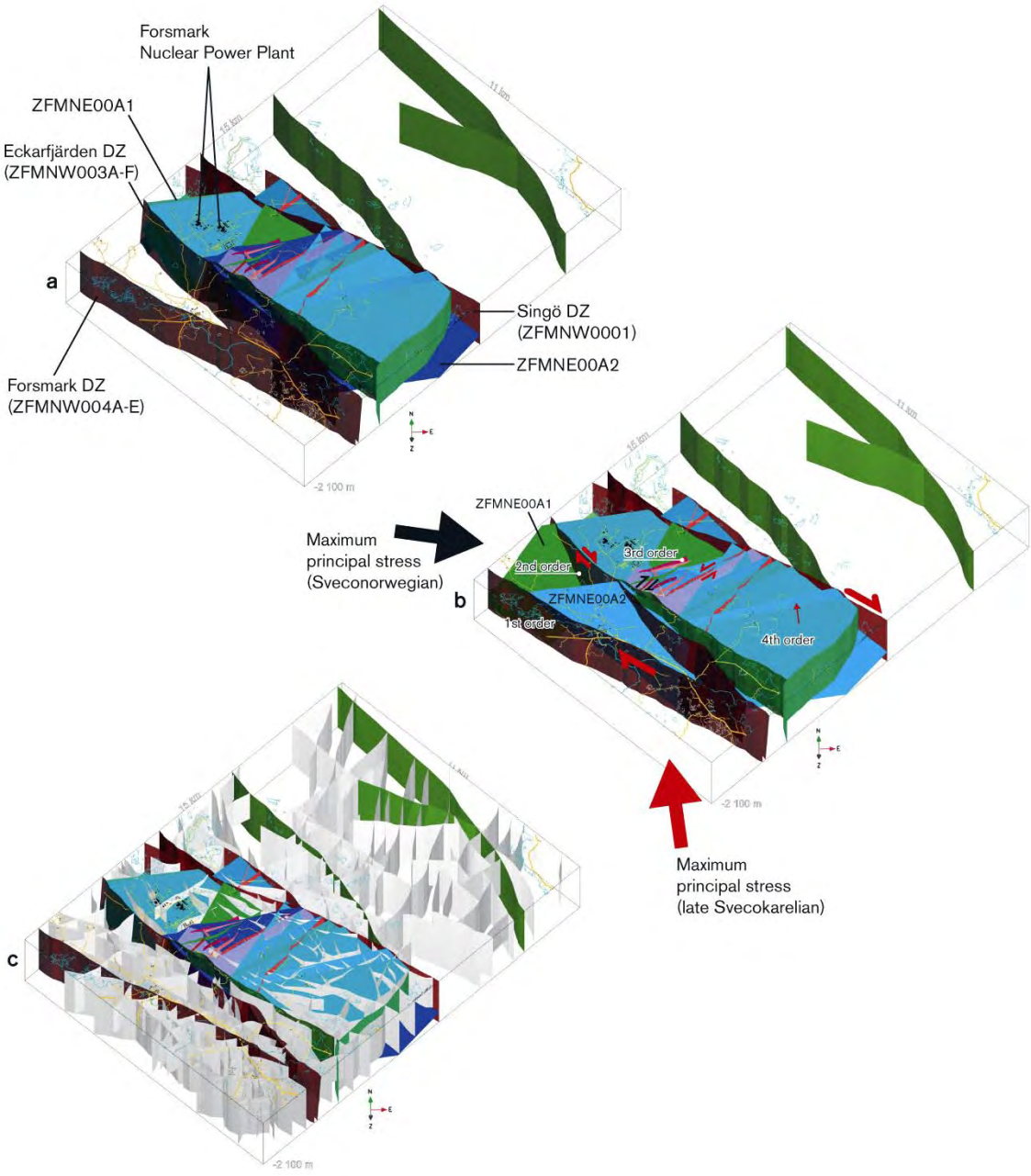

Figure A-2. *Deformation zone models of the bedrock in the Forsmark area, model version 1.2. Top: Base model. Middle: Base variant model. Bottom: Alternative model /SKB 2005a/.*